Electronic Structure of Correlated Materials From First Principles: Hubbard interaction and Hund's exchange

Loig Vaugier

ÉCOLE POLYTECHNIQUE
ParisTech

Thèse présentée pour obtenir le grade de

DOCTEUR DE L'ECOLE POLYTECHNIQUE

Spécialité : Physique des Matériaux et Milieux Denses

LOÏG VAUGIER

Electronic Structure of Correlated Materials from First Principles : Hubbard interaction and Hund's exchange

---

Soutenue publiquement le 8 décembre 2011 à l'Ecole Polytechnique
devant le jury composé de :

Ferdi Aryasetiawan	Chiba University (Japan)	(Rapporteur)
Mark van Schilfgaarde	King's College, London (England)	(Rapporteur)
Silke Biermann	Ecole Polytechnique, Palaiseau (France)	(Directrice de thèse)
Antoine Georges	Ecole Polytechnique, Palaiseau (France)	(Président)
Alexander Lichtenstein	University of Hamburg (Germany)	
Marino Marsi	Laboratoire de Physique des Solides, Orsay (France)	

Electronic Structure of Correlated Materials From First Principles : Hubbard interaction and Hund's exchange

---

Matériaux Corrélés et Structure Electronique *ab initio* : interaction de Hubbard et couplage de Hund

Loïg Vaugier

2011

CENTRE DE PHYSIQUE THÉORIQUE (CPHT)
ECOLE POLYTECHNIQUE
France

Abstract

In this thesis, we present a new implementation of the *constrained Random Phase Approximation* (cRPA) in a density functional code within the linearized augmented plane wave (LAPW) framework. The aim is to calculate – from first principles – the effective Coulomb interaction matrix for correlated solids, opening the way to a *truly ab initio* description within many-body calculations. In particular, we calculate the Hubbard parameter, U, and Hund's exchange, J, as well as their energy dependence arising from dynamical screening effects. As in the Wilson renormalization group, we stress that the effective Coulomb interactions crucially relie on the choice of the correlated subspace for which an effective low-energy Hamiltonian is constructed, although results for physical observables have to be the same at the end. A specific scheme for cRPA, based on a *projection approach* onto the low-energy subspace, is also introduced in order to deal with electronic structures where the target correlated orbitals are strongly entangled with the itinerant ones.

Applications are shown for i) iron-based pnictides, LaOFeAs and $BaFe_2As_2$, and chalcogenides, FeSe (Chapter 6) [Vaugier *et al.* (2012a)], ii) $3d$ transition metals to benchmark the projection scheme (Chapter 6) and iii) $3d$ and $4d$ transition metal perovskites, $SrMO_3$ (M = V, Cr, Mn, Nb, Mo, Tc) and layered perovskites, Sr_2MO_4 (M = Mo, Tc, Ru, Rh) (Chapter 7) [Vaugier *et al.* (2012b)]. The cRPA values for the interaction Hamiltonian are combined with the dynamical mean-field theory (LDA+cRPA+DMFT) for the description of the spin-orbitally ordered Mott insulator Sr_2IrO_4 (in collaboration with [Martins *et al.* (2011)]), and the rare-earth fluorosulfide pigment, CeSF (in collaboration with [Tomczak *et al.* (2012)]).

Résumé

Cette thèse propose une nouvelle implémentation de *"l'approximation de la phase aléatoire avec polarisation contrainte"* (constrained random phase approximation, cRPA). Notre implémentation repose sur la théorie de la fonctionnelle de la densité, développée dans une base d'ondes planes augmentées (linearized augmented plane wave, LAPW). Cette méthode, appliquée à des matériaux fortement corrélés, permet de calculer de facon réaliste la matrice d'interaction coulombienne effective, qui pourra être traitée par la suite au moyen de l'approche à N-corps souhaitée. En particulier, les valeurs de l'interaction de Hubbard, U, et de l'échange de Hund, J, sont déterminées de manière *ab initio*, ainsi que leur dépendance en fréquence qui résulte des effets dynamiques de l'écrantage. Comme dans la théorie du groupe de renormalisation de Wilson, l'interaction coulombienne effective dépend du choix du sous-espace corrélé pour lequel est construit un Hamiltonien effectif de basse énergie, alors que les valeurs des observables physiques n'en dépendent pas. Afin de généraliser la cRPA aux matériaux dont la structure électronique exhibe des orbitales corrélées et itinérantes intriquées, une méthode basée sur la *projection* sur le sous-espace corrélé est également introduite.

Différentes classes de matériaux sont envisagées comme applications : i) pnictides à base de fer, LaOFeAs et $BaFe_2As_2$, et chalcogénides, FeSe (Chapitre 6) [Vaugier *et al.* (2012a)], ii) métaux de transition $3d$ afin de valider notre méthode de projection (Chapitre 6), iii) oxydes de métaux de transition pérovskites, $SrMO_3$ (M = V, Cr, Mn, Nb, Mo, Tc), et pérovskites en couches, Sr_2MO_4 (M = Mo, Tc, Ru, Rh) (Chapitre 7) [Vaugier *et al.* (2012b)]. L'Hamiltonien d'interaction cRPA est également couplé à la théorie du champ moyen dynamique (LDA+cRPA+DMFT) afin de décrire l'isolant de Mott induit par le couplage spin-orbite, Sr_2IrO_4 (en collaboration avec [Martins *et al.* (2011)]), et le pigment à base de terre rare, CeSF (en collaboration avec [Tomczak *et al.* (2012)]).


JEAN-SÉBASTIEN
HONG
JAN
ARMANDO
FADILA
CHARLES
HARTMUT
CYRIL
VÉRONICA
JEANNINE
JEAN-LUC
XIAOYU
SILKE
MÁLIKA
ANTOINE
SHIRO
MARKUS
JAN
ARMANDO
FADILA
LORENZO
XIAOYU
FADILA
SHIRO
IGORDAHN
JERNEJ
MICHÈLE
DAHN
MARKUS
STÉPHANE
EVGENY
IGOR
MARKUS
SILKE
IGOR
JERNEJ
JEAN-SÉBASTIEN
HONG
CYRIL
DAHN
BENJAMIN
JAN
STÉPHANE
SILKE
JERNEJ
MICHÈLE
DAHN
MICHEL
VÉRONICA
CORINNA
XIAOYU
CYRIL
DAHN
MÉLUSINE
ELIE
THOMAS
MANON
ELIE
AMÉLIE
PAULINE
RÉMI
MANUS
DAVID
VARDOURE
ROSANA
DADA
CROUSSET
CÉCILE
EMILIE
LAURA
FLORENCE
DAMIEN
AUGUSTIN
CÉLESTIN
MATHILDE
CASTORS-POIVROTS
VINCENT
CLAIRE
EVOLÈNE
JOSEPH
GENET
DAVID
ROSANA
MARGOT
TOMMY
DAVID
ÉVOLÈNE
RÉMI
CÉCILE
AMÉLIE
MARGOT
GEORGES
KANEL
SIMON
OLIVIER
BENOÎT
DOMINIQUE
CACAHOUÈTE
NICOLAS
SERVANE
CHRISTOPHE
RACHELANNE
GUY
CÉLINE
FABIEN
MGUY
RACHEL
YVES
JACQUES
KANEL
CÉLINE
MARIE-LÉA
MARIE-ANTOINETTE
NICOLAS
VÉRONIQUE
ANNE
YVES
RACHEL
SANNE
MADELEINE
OLIVIER
FERDI
MARK
SILKEFERDIMARK
MARINO
PABLO
ANTOINE
MARINO
SILKE
MARK
PABLO
RUSSEL
WASSYM
CAROLINE
DAVIS
FLORIAN
ROMAN
CAROLE
PAPA
ERIC
JIBERT
YOUSRA
ARNAUD
ANDRÉA
REB
ROJO
ANDRÉAS
FABIAN
DAVIS
JEAN-DAMIEN
LUDIVINE
FLORIAN
JULIEN
MAMAN
PAPA
PAPI
ERIC
PIERRE
ANDRÉA
ROJO
DAVIS
JULIEN
PIERRE
XAVIER
CHARLOTTE
OCTAVE
ROSE
MÈRE
ROSE
ISIDORE
EMMANUELLE
COLINE
ROSE
AURÉLIEN
BILL-PANCRÉAS
ENGUERRAND
PHILIPPE
DOUDOU
DOUDOU
CPHT
TAKASHI
PETER
DONAT
CPHT
DONAT
TAKASHI
PETER
DONAT

Introduction

Naively, the calculation of the Coulomb repulsion between two charges may seem like a simple textbook problem. However, calculating this repulsion for two electrons in a solid is far from being trivial. The electronic polarizability screens the Coulomb potential, leading to a renormalized repulsion strength. The main objective of this thesis is to calculate these renormalized interactions from first principles, that is, without any adjustable parameters. More specifically, we determine the Coulomb interaction matrix for correlated solids in a basis of localized orbitals. These matrices can – under certain conditions – be parametrized by a small number of parameters, Hubbard U and Hund's coupling J, which can then be employed within a lattice Hamiltonian description to model the material of interest.

Electronic screening is a key concept that notably differenciates the behavior of electrons in solids from the one of electrons in isolated atoms. The dielectric function, characterizing the response of a solid to an external perturbation, encodes the different screening processes. They have direct observable consequences in spectroscopic properties such as optical probes or electron energy loss spectroscopy.

In photoemission spectroscopy, a perturbation is caused by the removal or addition of an electron from or into the solid. Adding an electron into a localized orbital on a given atom perturbs the systems and induces a rearrangement of the electronic cloud resulting in a net depletion of electrons around the atom. This process is formally equivalent to the creation of a "screening hole" reducing the effective Coulomb potential. It is dynamical and so must be the effective interaction between the electrons. This is easily seen in two limiting cases: electrons do not respond to a high-frequency oscillating electric field whose frequency exceeds any electronic energy scale, whereas screening is very efficient at low energies, i.e. for excitations that live on large time scales. On intermediate energy scales, different processes, such as particle-hole transitions or collective excitations contribute to the screening. Particularly interesting are collective oscillations, resonant with the perturbation, called plasmons. In the electron gas, such oscillations involve the whole electronic system, while in the solid more exotic plasmon modes can result from the oscillations of a fraction of electrons associated for example with a given set of valence states.

The theoretical description of screening in materials and the calculation of the resulting screened quantities are the topic of the present thesis. To this effect, we use the constrained Random Phase Approximation (cRPA) (which we have implemented in a density functional code

within the full-potential augmented plane wave ((L)APW+lo) electronic structure framework). Since considering screening in an exact way is of paramount difficulty within solids, the problem is simplified such as to neglect the interaction of the created particles and holes. In diagrammatic language, this amounts to a restriction to diagrams involving only single particle-hole bubbles – the random phase approximation (RPA).

These concepts are used for the construction of effective Hamiltonians with a reduced number of degrees of freedom; the effective Hamiltonian is supposed to reproduce the low-energy properties of the material of interest. The identification of screening processes within a given low-energy subspace allows for the calculation of *partially* screened interactions that are interpreted as the bare interactions *within* the low-energy subspace. This scheme can thus be used to construct a *downfolded* lattice Hamiltonian within this subspace.

Correctly accounting for the Coulomb interaction is particularly important in situations where the Coulomb repulsion dominates the behavior of the system. This is typically the case in $3d$ transition metal compounds or rare earth or actinide compounds, which display a panoply of phenomena beyond a simple one-particle picture. Besides being of high technological importance, this class of compounds presents a particular challenge to theory. Effects indeed range from simple renormalisations of quasi-particle band structures in the sense of Landau to the strong coupling case where Coulomb correlations lead to a blocking of electronic motion. These latter materials, Mott insulators, which would be metallic in a band picture, are driven into the insulating state due to large values of the Coulomb repulsion. The failures of the one-body picture can thus be used to define this specific class of materials said to be "strongly correlated".

The description of electronic excitations in correlated materials therefore requires a theoretical treatment that goes beyond the one-particle picture. In particular, the simple approximation that consists in considering the Kohn-Sham eigenvalues of density functional theory (DFT) within the local density approximation (LDA) or generalized gradient approximations (GGA) as excitation energies, is quite generally too poor an approximation. Methods beyond the band picture, such as many-body perturbation theory or the so-called "LDA++" schemes that supplement DFT-LDA with explicit many-body interaction terms are designed to cure these deficiencies.

Dynamical mean-field theory (DMFT), for example, allows for the description of spectral properties around the Mott metal-insulator transition in the Hubbard model. Its realistic extension, the combination with density functional theory LDA+DMFT, has been successfully employed for the description of physical observables, such as photoemission, optics, or transport. Importantly, the predictive power of the combined LDA+DMFT scheme stands or falls with the possibility of reliably assessing the strength of the Coulomb interactions. The *ab initio* calculation of Hubbard U and Hund's J, which is at the heart of the present thesis, is thus a crucial ingredient for any realistic theory of correlated electron systems.

This thesis is divided into three parts. The first part is dedicated to an introduction to popular first principles approaches. In particular, we present the basics of the DFT-LDA and Hedin's framework for many-body perturbation theory (Chapter 2). We then describe the LDA+DMFT scheme, and insist that its combination with cRPA in principle makes this method fully *ab initio* (Chapter 3).

In the second part of the thesis, we first review the various definitions of U found in the literature (Chapter 4). Once we have introduced conceptually the cRPA method, we turn to the technical developments of the implementation within the (L)APW+lo framework (Chapter 5). We discuss the parametrization of the Coulomb interaction matrices in terms of Slater integrals, as well as aspects related to the energy dependence of electronic screening. Finally, we discuss the combined LDA+cRPA+DMFT scheme, that consists in using the calculated interaction parameters within LDA+DMFT calculations. In Chapter 5, we introduce a projection approach for calculating Hubbard and Hund interactions in the case of entangled bands.

The third part of the thesis is devoted to applications of this machinery to interesting correlated materials, such as transition metal oxides. Chapter 6 is devoted to benchmarks on $SrVO_3$ as well as on and iron-based pnictides (LaOFeAs, FeSe, $BaFe_2As_2$, $BaRu_2As_2$). The projection method is tested on the $3d$ transition metal series.

In Chapter 7 we discuss the series of $3d$ and $4d$ perovskite compounds $SrMO_3$ (M = V, Cr, Mn, Nb, Mo, Tc) and Sr_2MO_4 (M = Mo, Tc, Ru, Rh), with particular emphasis on the dependence of the parameters on the choice of the low-energy model. Furthermore, trends for the Hubbard U and Hund's exchange J are identified for $3d$ and $4d$ transition metal oxides. We show that the interplay of the screening and of the localization of the basis that spans the correlated subspace, can induce strong deviations from the expected atomic trends.
Two LDA+cRPA+DMFT studies in which we have contributed with the cRPA calculations, are finally introduced in Chapter 8. The first one elucidates the differences between the layered perovskite paramagnetic metal Sr_2RhO_4 and the isostructural and isoelectronic but Mott insulating Sr_2IrO_4, in collaboration with C. Martins *et al.* [Martins *et al.* (2011)]. The second deals with the rare-earth fluorosulfide CeSF compounds in collaboration with J. Tomczak, L. Pourovskii *et al.* [Tomczak *et al.* (2012)]. The color of these promising pigments can indeed be interpreted now from fully first principles LDA+DMFT calculations.

Contents

List of Figures

Part I

Correlated Materials from the First Principles Point of View

Chapter 1

Introduction to Correlated Materials

1.1 Concepts

A solid is ideally defined as an ordered state of matter, made of nuclei and surrounding electrons. The positions of the nuclei are repeated periodically in space. The knowledge of those inside the primitive unit cell are enough for specifying the crystal. A first approximation, known as the Born-Oppenheimer approximation, consists then in dissociating the dynamics of the electrons from the one of the nuclei : it can be seen as an adiabatic approximation, justified by the several orders of magnitude difference between the electronic and the nuclei masses. In some cases, it may be important to relax this approximation, in order to study the dynamic lattice deviations but this will not be addressed in this work, where we always consider that the Born-Oppenheimer approximation is well-founded. Similarly, we will not deal with any other sources of disorder or surface effects, which would affect the periodicity of the lattice.

Within these approximations, we may write the general Hamiltonian formulation (using Hartree units) for a solid with N_e electrons, as used in first principles approaches (see Chapter 2) :

$$H = \sum_{i=1}^{N_e} \Big[-\frac{\nabla_i^2}{2} + v(\boldsymbol{r}_i) \Big] + \frac{1}{2} \sum_{ij}^{N_e} \frac{1}{|\boldsymbol{r}_i - \boldsymbol{r}_j|}. \tag{1.1}$$

$v(\boldsymbol{r})$ is a static periodic potential that is created by the nuclei and felt by the electrons. The second term is the general formulation of the Coulomb interactions between electrons, which generates the many-body effects. Depending on the materials, these effects can have dramatic consequences on the properties of matter, like (non-exhaustive list) : structure, phase transitions, conductivity, optics, magnetism, phonons, etc.

The simplest model we can think of at the beginning, would consist in merely neglecting all interactions between electrons. Then electrons would only feel the one-body potential that is created by the nuclei. In the so called tight-binding approach, the nuclei generate a local atomic potential that captures most of the electrons, or core electrons, whereas the others, or semicore

and valence electrons, are able to tunnel from one atomic site to another. These electrons are in particular responsible for the chemical bonding that ensures the cohesion in a solid. Even if it appears very crude, this approach tends to be surprisingly successful in some cases. In particular, it creates the picture of bands in solids, which is a very fundamental concept illustrated below.

In the following, Bloch's theorem is introduced as well as band picture which are concepts at the heart of solid state theory.

Bloch's theorem : Bloch's theorem relies only on the periodicity of the lattice and is thus considered as a very foundation of solid-state physics. It states that the translation operator and the Hamiltonian of the system share a common set of eigenstates. It follows that eigenfunctions $\psi_{\boldsymbol{k}}(\boldsymbol{r})$ of the solid can be written as

$$\psi_{\boldsymbol{k}}(\boldsymbol{r}) \quad = \quad \mathrm{e}^{i\boldsymbol{k}\cdot\boldsymbol{r}} u_{\boldsymbol{k}}(\boldsymbol{r}) \quad \text{with} \quad u_{\boldsymbol{k}}(\boldsymbol{r}+\boldsymbol{R}) = u_{\boldsymbol{k}}(\boldsymbol{r}) \quad \forall \boldsymbol{R} \in \text{Bravais},$$

where $\boldsymbol{k}$ is a reciprocal lattice vector inside the first Brillouin Zone (BZ).

Band picture : In the limit of a large crystal, the spacing of the $\boldsymbol{k}$ points tends to zero and $\boldsymbol{k}$ can be considered as a continuous variable. For each $\boldsymbol{k}$, there is a discrete set of eigenvalues $\epsilon_{\boldsymbol{k}\nu}$ that can be labeled by an index ν that defines the band index. A portrait of the spectrum in a solid can be established at this level, involving a set of bands, $\psi^{\sigma}_{\boldsymbol{k}\nu}(\boldsymbol{r})$, of given energies, and regions called gaps where there are no eigenstates for any $\boldsymbol{k}$. The spin-degree of freedom σ has to be added in the definition of the Bloch states, since the filling of the bands will depend on the spin of the electrons. This comes from the Pauli exclusion principle, which states that each band can accommodate no more than two electrons with opposite spin per cell.

Wannier functions

We benefit from the introduction of Bloch states, in order to introduce the concept of Wannier states, which will play a key-role when focusing on the many-body effects in the latter. Introduced by Wannier [Wannier(1937)], in order to get functions centered on the atomic positions of each unit cell of the crystal, the Wannier functions $\phi^{\sigma}_{\boldsymbol{R}L}$ are the Fourier transformation of the Bloch states $\psi^{\sigma}_{\boldsymbol{k}\nu_L}$:

$$\phi^{\sigma}_{\boldsymbol{R}L}(\boldsymbol{r}) \quad = \quad \frac{1}{\sqrt{\mathcal{N}}} \sum_{\boldsymbol{k}} \mathrm{e}^{-i\boldsymbol{k}\cdot\boldsymbol{R}} \psi^{\sigma}_{\boldsymbol{k}\nu_L}(\boldsymbol{r}), \tag{1.2}$$

where $\mathcal{N}$ is the number of $\boldsymbol{k}$ vectors in BZ, $\boldsymbol{R}$ a translation vector of the Bravais lattice, L is a combined index for the orbital character (n, l, m, α) of atom α, ν_L the band index with L character and σ the spin degree of freedom. Wannier functions are not uniquely defined, since any orthogonal linear combination of Wannier functions is again a Wannier function. By calling $U^{\boldsymbol{k}}_{\mu\nu}$ a given unitary transformation matrix from Bloch to Wannier states, this leads to the more general definition :

$$\phi^{\sigma}_{\boldsymbol{R}L}(\boldsymbol{r}) \quad = \quad \frac{1}{\sqrt{\mathcal{N}}} \sum_{\boldsymbol{k}} \mathrm{e}^{-i\boldsymbol{k}\cdot\boldsymbol{R}} \sum_{\nu_L} U^{\boldsymbol{k}}_{L\nu_L} \psi^{\sigma}_{\boldsymbol{k}\nu_L}(\boldsymbol{r}). \tag{1.3}$$

This degree of freedom explains the variety of Wannier bases which we are able to build in electronic structure calculations. We come back to this point in Chapter 3.

1.2 Weakly correlated materials

Weakly correlated materials exhibiting broad energy bands are prototypical systems where the independent-electron picture is a good approximation. The interaction effects can indeed be formulated as a "dressing" of the electrons (or holes), leading to the concept of *quasiparticles* in terms of Landau theory. Within this theory, the quasiparticles are independent entities but with renormalized properties and finite lifetime. For weakly or moderate correlated systems, Landau theory gives a good description of the coherent excitation spectrum, defining the concepts of a Fermi liquid. It is indeed remarkable that the photoemission experiments on such materials gives results that coincide so well with the characteristics predicted for a Fermi liquid.

Weak correlations also allow for perturbative developments around the noninteracting case. Hartree and Hartree-Fock theories give in general not so bad estimations of insulating gaps for atoms or molecules but usually fail when calculating quasiparticle energies in solids. The GW approximation- as a generalization of the Hartree-Fock approximation (see Chapter 2)- has the merit of leading to more reasonable values. It has been applied with success to a large class of materials, e.g. semi-conductors and simple metals [Aryasetiawan and Gunnarsson(1998)].

Nevertheless, the incoherent features of the electronic spectra - like the atomic-like Hubbard satellites - are *intrinsically* beyond Landau theory of Fermi liquids and any band picture. Strong correlations in given systems even cause the breakdown of the concept of quasiparticles [Imada *et al.* (1998)]. This explains why such materials require a point of view that differs from the one-particle picture.

1.3 Strongly correlated materials

According to the independent-electron approximation, there is no ambiguity for a material to be metallic or insulating. Filling the bands with an odd number of electrons would always lead to *metallicity* since the conduction band is partly occupied. However nature behaves differently. Insulating states have been observed for many compounds that were predicted to be metallic because of their odd number of electrons. Such insulating state - whose origin is different from the band insulating one - is called a *Mott insulator* (for a review, see in particular [Imada *et al.* (1998)]).

The Mott insulating state originates from strong electronic correlations and is thus beyond any one-electron descriptions, which oversimplify the interactions. Two processes actually compete for the electronic dynamics within such materials. One emerges from the kinetic energy which makes the valence electrons itinerant along the solid and thus spending a short time

near each atom. Such electrons are well described within a *wave-like* picture. The competing phenomenon is due to the electronic Coulomb repulsion which increases the time spent by valence electrons around the atoms and, if it is large enough, even prevents one electron from occupying an already occupied atomic site. It thus tends to freeze the electronic displacements and is better described within a *particle-like* picture. A pedagogical discussion can be found in [Georges(2004)].
Since the bandwidth gives an estimate of the kinetic energy, narrow bands around the Fermi level correspond to less itinerant states which are therefore subject to strong correlation effects. It is the intermediate situation where electrons struggle between localization and itineracy. Very schematically, beyond a certain critical ratio of interaction over bandwidth, the Coulomb repulsion may triumph over the itineracy of the charge carriers and localize them around their atomic sites, leading to a Mott insulating state. But even for a ratio that is smaller than the critical one, thus in favor of a metal, electronic behavior is expected to be strongly affected by correlation effects. It is indeed important to mention here that scenarios only based on such ratio can oversimplify the reality, as materials can be "strongly correlated" even if the intra-orbital Coulomb repulsion is much smaller than the bandwidth (e.g. due to Hund's coupling, see [Werner *et al.* (2008), de' Medici *et al.* (2011)] and applications for pnictide families [Haule and Kotliar(2009), Aichhorn *et al.* (2010)]). The "strongly correlated" character may also rely on the observables investigated, since two-particle quantities, e.g. magnetic moments in pnictides [Hansmann *et al.* (2010),Toschi *et al.* (2012)], can be more affected by correlations than single-particle ones.

Materials for which any band theory fails are called *strongly correlated*. This means that they can display modified metallic properties or even enter a metal-insulator Mott transition with pressure, temperature or doping. Looking at the Mendeleiev classification (Fig. 1.1), they usually contain valence electrons within d or f-shells, since d or f-atomic orbitals are less extended than the s and p-ones. This naturally makes the d and f-electrons "fighting" between itineracy and localization. For example :

- transition metals : particularly $3d$ elements from titanium (Ti) to nickel (Ni).
- transition metal oxides : d^1 systems such as $LaTiO_3$ or $YTiO_3$ are Mott insulators according to the photoemission experiments, whereas they would be metallic in band theory. Oxides like VO_2 or V_2O_3 display a rich phase-diagram with metal-insulator transitions.
- transition metal chalcogenides : 1T-TaS_2 is an example of a compound exhibiting metal-insulator transition that is driven by an instability of the electron-lattice coupling.
- rare earth ($4f$) and actinide ($5f$) compounds.
- in some cases such as the organic compounds, also the p-shells can be affected.

It thus appears fundamental to build a model that is capable of catching all these features. This is the great merit of the Hubbard-Kanamori-Gutzwiller model [Hubbard(1963), Kanamori(1963), Gutzwiller(1963)] - we will refer to it as the Hubbard model in the following - which, in a sense, contains both, *wave-like* and *particle-like* physics. Originally, this model

only dealt with single orbital cases, but it has been extended to the case of multi-orbital problems as shown below (see for example [Auerbach(1994)] for a pedagogical introduction).

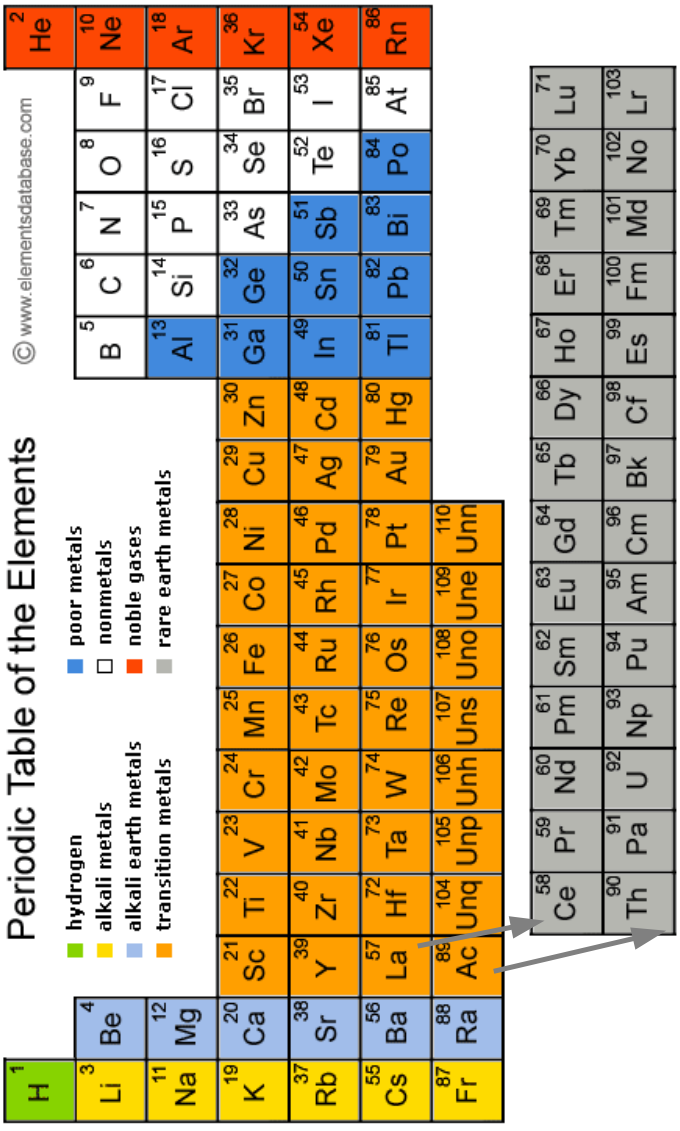

Figure 1.1: Periodic classification of elements.

1.3.1 The Hubbard model

Rewriting the Hamiltonian (Eq. 1.1), but using a field-theory formulation of the solid, it follows :

$$\begin{aligned} H &= \sum_{\sigma} \int d\boldsymbol{r} \Psi_{\sigma}^{\dagger}(\boldsymbol{r}) \Big[-\frac{\nabla^2}{2} + V^{ion}(\boldsymbol{r}) \Big] \Psi_{\sigma}(\boldsymbol{r}) \\ &+ \frac{1}{2} \sum_{\sigma,\sigma'} \int d\boldsymbol{r} d\boldsymbol{r}' \Psi_{\sigma}^{\dagger}(\boldsymbol{r}) \Psi_{\sigma'}^{\dagger}(\boldsymbol{r}') V^{ee}(\boldsymbol{r},\boldsymbol{r}') \Psi_{\sigma'}(\boldsymbol{r}') \Psi_{\sigma}(\boldsymbol{r}), \end{aligned} \tag{1.4}$$

where $\Psi_{\sigma}(\boldsymbol{r}), \Psi_{\sigma}^{\dagger}(\boldsymbol{r})$ are the field operators that respectively annihilate and create an electron with spin σ at $\boldsymbol{r}$. $V^{ion}(\boldsymbol{r})$ corresponds to the one-body potential generated by the nuclei and $V^{ee}(\boldsymbol{r},\boldsymbol{r}') = \frac{1}{|\boldsymbol{r}-\boldsymbol{r}'|}$ is the two-body Coulomb potential. The interacting part (second term) is restricted to a scattering event between two electrons.

It is convenient to absorb the static mean-field potential $v^{\text{eff}}[\rho]$ into the one-particle part of the Hamiltonian. As a mean-field approach, this effective potential is a functional of the charge density $\rho(\boldsymbol{r})$ and has to be determined self-consistently. This is the essence of density functional theory, in which the effective potential $v^{\text{KS}}[\rho]$ is defined as the Hartree plus the exchange-correlation potential (see Chapter 2 for an introduction to density functional theory). It results for the renormalized interaction potential $\tilde{V}^{ee}$ [Auerbach(1994)] :

$$\tilde{V}^{ee}(\boldsymbol{r},\boldsymbol{r}') = V^{ee}(\boldsymbol{r},\boldsymbol{r}') - \frac{1}{N_e}[v^{\text{eff}}[\rho](\boldsymbol{r}) + v^{\text{eff}}[\rho](\boldsymbol{r}')]. \tag{1.5}$$

The Hamiltonian can then be separated into a one-particle part H_0 :

$$H_0 = \sum_{\sigma} \int d\boldsymbol{r} \Psi_{\sigma}^{\dagger}(\boldsymbol{r}) \Big[-\frac{\nabla^2}{2} + V^{ion}(\boldsymbol{r}) + v^{\text{eff}}[\rho](\boldsymbol{r}) \Big] \Psi_{\sigma}(\boldsymbol{r}), \tag{1.6}$$

and an interacting part H_{int} :

$$H_{\text{int}} = \frac{1}{2} \sum_{\sigma,\sigma'} \int d\boldsymbol{r} d\boldsymbol{r}' \Psi_{\sigma}^{\dagger}(\boldsymbol{r}) \Psi_{\sigma'}^{\dagger}(\boldsymbol{r}') \tilde{V}^{ee}(\boldsymbol{r},\boldsymbol{r}') \Psi_{\sigma'}(\boldsymbol{r}') \Psi_{\sigma}(\boldsymbol{r}). \tag{1.7}$$

Expanding the field operators into the Wannier basis $\{\chi_{L\sigma}^{\boldsymbol{R}}(\boldsymbol{r})\}$ previously introduced (where $L = (n,l,m,\alpha)$ is an index for the orbital character (n,l,m) of the atom α in the unit cell) :

$$\Psi_{\sigma}(\boldsymbol{r}) = \sum_{\boldsymbol{R},L} \chi_{L\sigma}^{\boldsymbol{R}}(\boldsymbol{r}) c_{\boldsymbol{R}L}^{\sigma}, \tag{1.8}$$

where $c_{\boldsymbol{R}L}^{\sigma}, c_{\boldsymbol{R}L}^{\sigma\dagger}$ are respectively the annihilation and creation operators of the Wannier states, we can write the Hamiltonian in this Wannier basis as follows :

$$H_0 = \sum_{\boldsymbol{R}\boldsymbol{R}',LL',\sigma} t_{LL'}^{\boldsymbol{R}\boldsymbol{R}',\sigma} c_{\boldsymbol{R}L\sigma}^{\dagger} c_{\boldsymbol{R}'L'\sigma} \tag{1.9}$$

$$H_{\text{int}} = \frac{1}{2} \sum_{\boldsymbol{R}_1\boldsymbol{R}_2\boldsymbol{R}_3\boldsymbol{R}_4} \sum_{L_1L_2L_3L_4} \sum_{\sigma\sigma'} U_{L_1L_2L_3L_4}^{\boldsymbol{R}_1\boldsymbol{R}_2\boldsymbol{R}_3\boldsymbol{R}_4,\sigma\sigma'} c_{\boldsymbol{R}_1L_1\sigma}^{\dagger} c_{\boldsymbol{R}_3L_3\sigma} c_{R_4L_4\sigma'}^{\dagger} c_{R_2L_2\sigma'}. \tag{1.10}$$

The real space hopping amplitudes are defined as

$$t_{LL'}^{\boldsymbol{R}\boldsymbol{R}',\sigma} = \int d\boldsymbol{r}[\chi_{L\sigma}^{\boldsymbol{R}}(\boldsymbol{r})]^* \Big[\frac{\nabla^2}{2} + V^{ion}(\boldsymbol{r}) + v^{\text{eff}}[\rho](\boldsymbol{r})\Big]\chi_{L\sigma}^{\boldsymbol{R}}(\boldsymbol{r}), \tag{1.11}$$

and the well-known Hubbard parameters as

$$U_{L_1L_2L_3L_4}^{\boldsymbol{R}_1\boldsymbol{R}_2\boldsymbol{R}_3\boldsymbol{R}_4,\sigma\sigma'} = \int d\boldsymbol{r}d\boldsymbol{r}'[\chi_{L_1\sigma}^{R_1}(\boldsymbol{r})]^*[\chi_{L_2\sigma'}^{R_2}(\boldsymbol{r}')]^*\tilde{V}^{ee}(\boldsymbol{r},\boldsymbol{r}')\chi_{L_4\sigma'}^{R_4}(\boldsymbol{r}')\chi_{L_3\sigma}^{R_3}(\boldsymbol{r}). \tag{1.12}$$

The calculation of $U_{L_1L_2L_3L_4}^{\boldsymbol{R}_1\boldsymbol{R}_2\boldsymbol{R}_3\boldsymbol{R}_4,\sigma\sigma'}$ is at the heart of this work. In the following, the spin indices (σ,σ') for $U_{L_1L_2L_3L_4}^{\boldsymbol{R}_1\boldsymbol{R}_2\boldsymbol{R}_3\boldsymbol{R}_4,\sigma\sigma'}$ will be omitted, because only spin unpolarized calculations will be carried out throughout this thesis.

Such formulation is the most general one, but much simpler Hamiltonians are considered in general. In the case of the Hubbard model, the real space hopping amplitudes are restricted to nearest and next-nearest-neighbor hopping terms and only the *local intra-atomic* part of the interacting Hamiltonian is treated. If, furthermore, one only keeps density-density interaction terms, the Hubbard model (easily generalized from the original single-orbital Hubbard-Kanamori-Gutzwiller model) reads as :

$$H_0 = \sum_{\langle ij\rangle,\sigma}\sum_{LL'} t_{LL'}^{ij,\sigma} c_{iL}^{\sigma\dagger} c_{jL'}^{\sigma} \tag{1.13}$$

$$H_{\text{int}} = \sum_{i}\sum_{LL',\sigma\sigma'} U_{LL'}^{\sigma\sigma'} n_{iL}^{\sigma} n_{iL'}^{\sigma'} \tag{1.14}$$

$$U_{LL'}^{\sigma\sigma'} \equiv U_{LL'LL'}^{\mathbf{0000},\sigma\sigma'}, \tag{1.15}$$

where i,j run over all atomic sites and $n_{iL}^{\sigma} = c_{iL}^{\sigma\dagger}c_{iL}^{\sigma}$. $U_{LL'}^{\sigma\sigma'}$ are defined as the reduced interaction matrices. Common many-body methods (e.g. LDA+DMFT, see Chapter 3) explicitly deal with such local interacting Hamiltonian, whereas the long-range Coulomb interactions are assumed to be reasonably taken into account by the band structure approaches to H_0. The interaction Hamiltonian can also be extended to non-density-density terms as given in Chapter 5 (Eqs. 5.83 and 5.84).

In a nutshell, the picture of the interaction processes within the Hubbard model is the following : electrons with opposite spins on the same orbital are sanctioned by $U = U_{LL}^{\sigma\bar{\sigma}}$ (local intra-orbital interaction), whereas the inter-orbital interaction, $U_{L\neq L'}^{\sigma\sigma'}$, is lowered by Hund's exchange and implicitly spin-dependent because of the Pauli principle (see Chapter 4 and Chapter 5 for further developments, in particular Fig. 5.2). The interacting part of the Hubbard Hamiltonian is diagonalized in a *particle-like* localized Wannier basis whereas the kinetic part requires a *wave-like* basis. This proves the ability of the Hubbard model to deal with the electronic *hesitation* between itineracy and localization.

Before concluding this part, we would like to add a remark about the renormalized Coulomb potential $\tilde{V}^{ee}(\boldsymbol{r},\boldsymbol{r}')$ introduced in Eq. 1.5. The matrix elements of $\tilde{V}^{ee}(\boldsymbol{r},\boldsymbol{r}')$ expanded into

a localized basis of the lattice, lead to the Hubbard parameters as shown in Eq. 1.12. In this scheme, the static screening effects of the high-energy excitations have been integrated out. In a sense, this will have similarities with the constrained-Random Phase Approximation (cRPA) method in Chapter 4. The screening is a key quantity to investigate. Without any screening, the typical order of magnitude of the Coulomb interaction would be around 20 eV, thus several times bigger than any typical kinetic energy. Nature in this case would not be able to generate metallic phases!
We illustrate this point in the next paragraph employing the homogeneous interacting electron gas in the Random Phase Approximation (RPA) - such system is a general starting point for modeling solids.

1.3.2 Homogeneous interacting electron gas

The idea that solids can be reasonably approximated by an homogeneous electron gas, is at the heart of numerous developments in the field of condensed matter, in particular in the density functional theory of Kohn and Sham [Kohn and Sham(1965)]. The homogeneous interacting electron gas is thus an excellent starting point for the introduction of concepts that are developed throughout this work, especially for the screening polarization in the Random Phase Approximation (for a textbook, see [Bruus and Flensberg(2003)]).

The simplest model for the interacting electron gas is the jellium model. In the limit of high electronic density, it is possible to perform a perturbation expansion of the ground state energy around the non-interacting solution, but the divergent behavior of the second order implies to consider an infinite order of perturbation. Green's functions formalism provides a very powerful machinery for studying the problem. A self-energy quantity is introduced that links the bare Green's functions to the interacting ones via a Dyson equation. Using Feynman's rules, a diagrammatic expansion of the self-energy involving bare propagators $G^0(\boldsymbol{k}, i\omega_n)$ and bare Coulomb interaction lines $v(\boldsymbol{q})$, can be constructed. For each given order, the diagrams with the highest divergence numbers are the most relevant.

Random Phase Approximation (RPA)

The Random Phase Approximation (RPA) consists in approximating the self-energy by an infinite sum of diagrams of all orders, but only the most divergent one for each order is kept [Bruus and Flensberg(2003)]. In other words, all the interactions that are felt by the electrons, average out because of their "random phases", except the Hartree term (Eq. 2.3). This leads to the effective potential which is given below. As shown in Fig. 1.3, the sum is factorized by the pair-bubble that corresponds to the polarization $P^0(\boldsymbol{q}, i\nu_n)$ at finite temperature ($i\nu_n(i\omega_n)$ are bosonic (fermionic) Matsubara frequencies) :

$$P^0(\boldsymbol{q}, i\nu_n) \quad = \quad \Big[G^0 G^0\Big](\boldsymbol{q}, i\nu_n) = \frac{2}{\beta}\sum_{i\omega_n}\int d\boldsymbol{k}\frac{1}{i\omega_n + i\nu_n - \xi_{\boldsymbol{k}+\boldsymbol{q}}}\frac{1}{i\omega_n - \xi_{\boldsymbol{k}}}, \tag{1.16}$$

where $G^0(\boldsymbol{k}, i\omega_n) = \frac{1}{i\omega_n - \xi_{\boldsymbol{k}}}$ is the bare Green's function of momentum $\boldsymbol{k}$ with the energy $\xi_{\boldsymbol{k}}$ with respect to the Fermi level and we note that the spin summation leads to a factor 2.

At this level, it is rather intuitive to introduce a renormalized interaction line $W^{\text{RPA}}(\boldsymbol{q}, i\nu_n)$ that connects the self-energy Σ^{RPA} to the bare Green's functions. Such reformulation of the interaction is at the basis of Hedin's equations introduced in Chapter 2. Using a Dyson-like equation approach (Fig. 1.4), it follows :

$$W^{\text{RPA}}(\boldsymbol{q}, i\nu_n) = \frac{v(\boldsymbol{q})}{1 - v(\boldsymbol{q})P^0(\boldsymbol{q}, i\nu)} = \frac{4\pi}{\boldsymbol{q}^2 - 4\pi P^0(\boldsymbol{q}, i\nu_n)}. \tag{1.17}$$

In the static, long-wavelength limit $\boldsymbol{q} \to 0$, it is interesting to observe that the screened interaction W^{RPA} has a Yukawa form with the so called Thomas-Fermi screening wavenumber k_s :

$$W^{\text{RPA}}(\boldsymbol{q} \to 0, 0) \to \frac{4\pi}{\boldsymbol{q}^2 + k_s^2}, \quad k_s^2 \equiv -4\pi P^0(0, 0), \tag{1.18}$$

which leads to the screened potential in the real-space :

$$W^{\text{RPA}}(\boldsymbol{r}, \boldsymbol{r}') = \frac{\mathrm{e}^{-k_s|\boldsymbol{r}-\boldsymbol{r}'|}}{|\boldsymbol{r} - \boldsymbol{r}'|}. \tag{1.19}$$

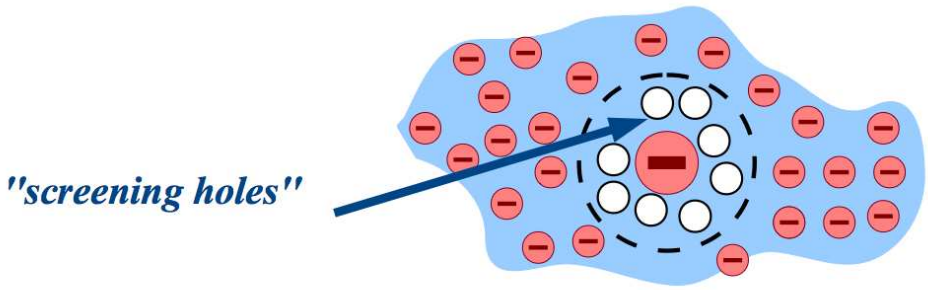

Figure 1.2: Schematic view of the electronic rearrangement when adding an extra negative charge, as simulated in the linear response theory. The local depletion of the surrounding negative charges induces an effective "hole screening" which lowers the effective electron-electron interaction.

Interpretation of the RPA polarization

The polarization is defined as a response function of the charge density upon a change in the total field applied. It is easier to visualize it at the static limit in the real-space (see Fig. 1.2).
The introduction of an extra charge, e.g. an additional electron, locally induces a potential that generates a depletion of the surrounding negative charges which is compensated by an increase of

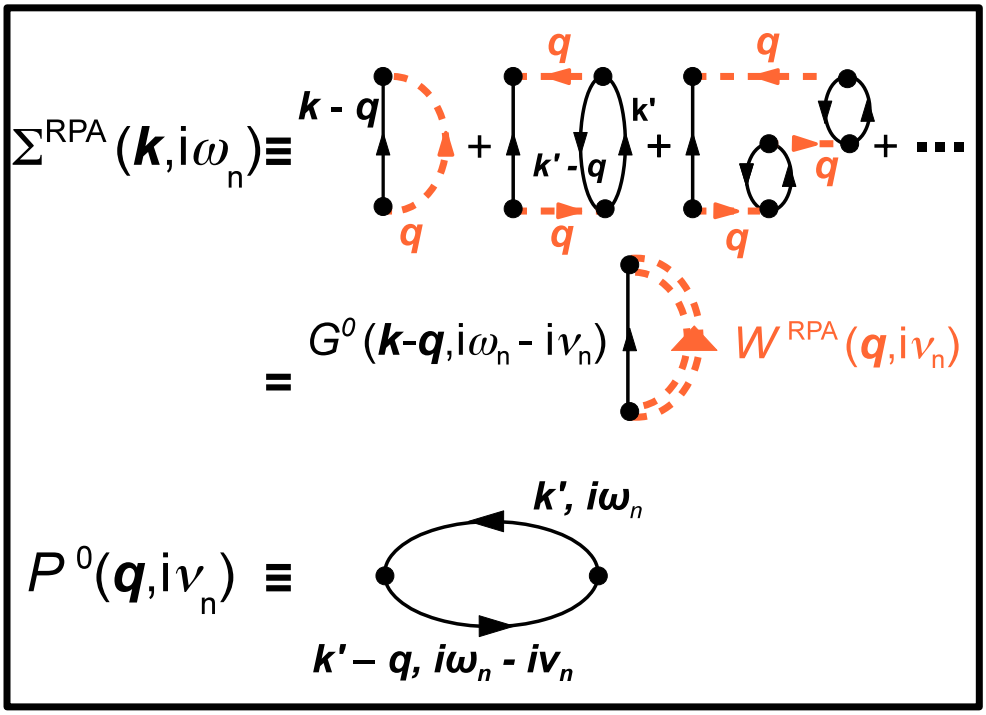

Figure 1.3: Diagrammatic interpretation of the RPA approximation. The sum in the self-energy is factorized by the pair-bubble corresponding to the RPA polarization $P^0(\boldsymbol{q}, i\nu_n)$ where ν_n are bosonic Matsubara frequencies. The self-energy in RPA then reads as the bare Green's functions times the fully screened interaction W^{RPA}. This gives a kind of introduction to the GW method described in Chapter 2.

positive charges. The effective repulsion between this trial charge and the other negative charges is lowered due to the screening induced by the (opposite sign) positive charges.
This picture then needs to be extended to the dynamical case, where charges in solids can form excited electron-hole pairs. The hole left by the excitation of an electron induces a hole-screening among the electrons. This effect tends to disappear when the frequency is so high that charge fluctuations become frozen. It follows that the polarization goes to zero at high frequency and the repulsion goes to its unscreened value.

For the homogeneous electron gas, the RPA polarization from Eq. 1.16 is obtained by traditional frequency summations [Mahan(1990)] :

$$P^0(\boldsymbol{q}, i\nu_n) \;=\; 2\int d\boldsymbol{k} \frac{f(\xi_{\boldsymbol{k}+\boldsymbol{q}} - f(\xi_{\boldsymbol{k}}))}{\xi_{\boldsymbol{k}+\boldsymbol{q}} - \xi_{\boldsymbol{k}} - i\nu_n}, \tag{1.20}$$

where $f(\xi)$ is the Fermi-Dirac distribution. In the static, long-wavelength limit $\boldsymbol{q} \to 0$ and at low temperature, it follows :

$$P^0(\boldsymbol{q} \to 0, 0) \;\to\; -\rho(\epsilon_F) \quad \text{for} \quad k_B T \ll \epsilon_F. \tag{1.21}$$

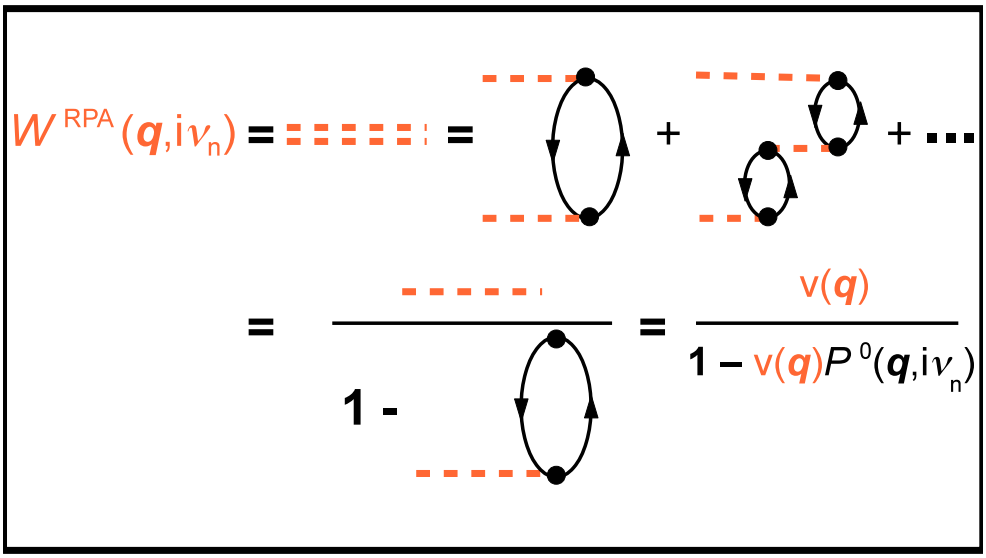

Figure 1.4: Diagrammatic interpretation of the Dyson-like relation that connects the fully screened interaction W in RPA to the bare interaction v *via* the RPA polarization. Further details can be found in [Bruus and Flensberg(2003)].

$\rho(\epsilon_F)$ is the electronic density at the Fermi level. Injecting it to Eq. 1.18

$$W^{\mathrm{RPA}}(\boldsymbol{q} \to 0, 0) \quad \to \quad \frac{1}{\rho(\epsilon_F)}. \tag{1.22}$$

A static long-range screening is thus induced by a finite number of carriers at the Fermi level. Extrapolating to solids, the long-range interaction in metals is quickly screened by electron-hole transitions around the Fermi level, with a range of the order of the inverse of the Thomas-Fermi screening wavenumber. This is not the case for insulators where the effective interaction is longer-range.
We mention that an approach based on the evaluation of a screened Yukawa-type Coulomb interaction with Hartree-Fock wavefunctions in solids was introduced by [Norman(1995),Brooks(2001)]. By selecting the Thomas-Fermi wavevector of the Yukawa potential, left as an adjustable parameter, in order to fit the photoemission spectra for NiO, a good agreement can be obtained with experiments.

Chapter 2

First Principles Approaches for Materials

A great motivation for first principles approaches is to calculate the properties of a system without introducing any bias. Such approaches indeed solve the Hamiltonian of Eq. 1.1 within the Born-Oppenheimer approximation only. Several schemes can be found in both quantum chemistry and condensed matter physics. We start with the description of density functional theory (DFT) - a very popular and powerful framework. We then give a short description of wavefunction-based approaches like Hartree-Fock, which give reasonable results for molecules but miss the screening effects in solids. The problem of screening is explicitly addressed in the GW approximation to Hedin's equations, described at the end of the chapter.

2.1 Ground Zero : Density Functional Theory (DFT) picture

A first density functional theory of quantum systems has been proposed in 1927 by Thomas and Fermi. Both derived an energy functional for electrons in an external potential, but making crude approximations for the electronic interactions. Their approach thus appeared unadapted for the description of electrons in matter. The great merit of the work of Hohenberg and Kohn in 1964 was to formulate density functional theory as an *exact theory of many-body systems* via two theorems given below [Hohenberg and Kohn(1964)]. The demonstrations of these theorems can be found in the textbook of [Martin(2004)]. Later, an alternative and also more general formulation was proposed by [Levy(1982)] and [Lieb(1983)], which makes the formalism for deriving energy functionals more intuitive. In 1965, Kohn and Sham introduced an *ansatz* - leading to the set of Kohn-Sham equations - which allowed for approximate functionals for real systems [Kohn and Sham(1965)]. More details about DFT and applications can be found in the reviews [Jones and Gunnarsson(1989), Kohn(1999)].

2.1.1 The Hohenberg-Kohn theorem

The Hohenberg-Kohn theorem asserts that

- it exists a one-to-one mapping between any external potential $v^{\text{ext}}(\boldsymbol{r})$ and the ground state density $\rho_0(\boldsymbol{r})$.
- all properties of any interacting system are *exactly* determined through the knowledge of the ground state density $\rho_0(\boldsymbol{r})$.
- a *universal functional* for the energy $E[\rho]$ in terms of the density ρ can be defined, for any external potential. The ground state energy $E_0 = E[\rho_0]$ of any interacting system is then obtained by a Rayleigh-Ritz variational principle, such that : $\forall \rho,\ E_0 \leq E[\rho]$ and the density ρ_0 is the exact ground state density.

These theorems lead to the following statement : for ground state properties, the many-body problem can be *exactly* cast into a one-particle effective potential.

However, it is far from being the end of the story. The Hohenberg-Kohn theorems only prove that such one-particle potential exists, without indicating how to calculate it. This is the major bottleneck of DFT. In practice, one needs to formulate approximations in order to estimate this potential. Various approximations have been formulated and are reviewed, e.g. in [Capelle(2006)].

We conclude with the following energy functional, as it is usually introduced within DFT [Martin(2004)] :

$$E[\rho] = F[\rho] + \int d^3\boldsymbol{r} v^{\text{ext}}(\boldsymbol{r})\rho(\boldsymbol{r}), \tag{2.1}$$

where $F[\rho]$ is a *universal functional* that includes the kinetic energy of the interacting system as well as the potential energy of the interacting electrons. In particular, it contains the Hartree term E^{Hartree} of the interactions, which is a static mean-field approximation where an electron feels the potential v^{Hartree} induced by all the other electrons (in Hartree units) :

$$E^{\text{Hartree}}[\rho] = \frac{1}{2}\int d^3\boldsymbol{r} d^3\boldsymbol{r}' \frac{\rho(\boldsymbol{r})\rho(\boldsymbol{r}')}{|\boldsymbol{r}-\boldsymbol{r}'|} \tag{2.2}$$

$$v^{\text{Hartree}}(\boldsymbol{r}) = \int d^3\boldsymbol{r}' \frac{\rho(\boldsymbol{r}')}{|\boldsymbol{r}-\boldsymbol{r}'|}. \tag{2.3}$$

2.1.2 The Kohn-Sham equations

In 1965, an important step for first principles approaches was reached with the development of the Kohn-Sham equations [Kohn and Sham(1965)]. This development has also enjoyed a great popularity. Kohn and Sham, indeed, proposed a scheme for replacing the many-body problem

by an equivalent non-interacting one. Their idea is based on the mapping of the interacting electronic system into an effective model of independent particles, subject to an external Kohn-Sham potential v^{KS}, but with the same ground-state density as the original system. Such *ansatz*, in a nutshell, involves independent particles but with an interacting density. This approach brings back into play a set of Schrödinger-like equations, but employing now the one-body potential v^{KS}.

Assuming the existence of such fictitious non-interacting system with the same density ρ as the original interacting one, the energy functional from Eq. 2.1 can be written as follows :

$$E[\rho] \quad = \quad T_{\text{ni}}[\rho] + \int d^3\boldsymbol{r} v^{\text{ext}}(\boldsymbol{r})\rho(\boldsymbol{r}) + E^{\text{Hartree}}[\rho] + E_{xc}[\rho], \tag{2.4}$$

where $T_{\text{ni}}[\rho]$ is the independent-particle kinetic energy and E^{Hartree} is the self-interaction energy with density ρ (Eq. 2.2). All many-body effects comprising exchange and correlation events, are grouped into the exchange-correlation energy $E_{xc}[\rho]$. Comparing Eq. 2.1 from Hohenberg-Kohn functional with Eq. 2.4, the following relation for $E_{xc}[\rho]$ can be extracted :

$$E_{xc}[\rho] \quad = \quad F[\rho] - T_{\text{ni}}[\rho] - E^{\text{Hartree}}[\rho]. \tag{2.5}$$

Due to the stationary of the total energy functional $E[\rho]$ with respect to the density, the Kohn-Sham potential v^{KS} can be introduced as

$$v^{\text{KS}}[\rho](\boldsymbol{r}) \quad = \quad v^{\text{ext}}(\boldsymbol{r}) + v^{\text{Hartree}}(\boldsymbol{r}) + v^{xc}[\rho](\boldsymbol{r}), \tag{2.6}$$

where $v^{\text{Hartree}} = \int d^3\boldsymbol{r}' \frac{\rho(\boldsymbol{r}')}{|\boldsymbol{r}-\boldsymbol{r}'|}$ is the Hartree potential (Eq. 2.3) and $v^{xc}[\rho]$ is the exchange-correlation potential defined as follows :

$$v^{xc}[\rho](\boldsymbol{r}) \quad = \quad \frac{\delta E_{xc}[\rho]}{\delta\rho(\boldsymbol{r})}. \tag{2.7}$$

The many-body problem is therefore simplified to the following independent Schrödinger-like equations - or Kohn-Sham equations :

$$\Big[-\frac{\hbar^2}{2m}\nabla^2 + v^{\text{KS}}[\rho](\boldsymbol{r})\Big]\psi_{n\boldsymbol{k}}(\boldsymbol{r}) \quad = \quad \epsilon_{n\boldsymbol{k}}\psi_{n\boldsymbol{k}}(\boldsymbol{r}), \tag{2.8}$$

where $\psi_{n\boldsymbol{k}}(\boldsymbol{r})$ are the Kohn-Sham eigenfunctions of the one-particle fictitious system and $\epsilon_{n\boldsymbol{k}}$, the Kohn-Sham eigenstates. It is important to insist on the fact that no approximations were introduced so far by describing the interacting system within such an effective model. If an expression for $v^{xc}[\rho]$ or $E^{xc}[\rho]$ was explicitly known, this mapping would even be *exact*. Approximations are however required for the exchange-correlation functionals and are described in the next paragraph.
Once a choice for calculating v^{xc} has been done, the set of Kohn-Sham equations (Eq. 2.8) has to be solved self-consistently, since the Kohn-Sham potential is a functional of the density (Eq. 2.6). The self-consistency condition reads as :

$$\rho(\boldsymbol{r}) \quad = \quad \sum_{\epsilon_{n\boldsymbol{k}} \leq \epsilon_F} |\psi_{n\boldsymbol{k}}(\boldsymbol{r})|^2. \tag{2.9}$$

We conclude this part with a remark on the physical meaning of the Kohn-Sham eigenstates. The only thing that the original interacting system and the fictitious non-interacting model have in common is the ground-state density. It implies that the Kohn-Sham eigenfunctions are only auxiliary quantities and are not supposed to describe the excitations of the system. Their spectra have therefore no reason to have any physical meaning. Furthermore, approaches identifying these wavefunctions to the "true" states of the interacting system, are in principle not well-founded. However, such approaches give surprisingly good results compared to experiments. This justifies their popularity.

2.1.3 The Local Density Approximation (LDA)

As explained previously, approximations to the exchange-correlation functional $E_{xc}[\rho]$ are necessary, in order to solve the Kohn-Sham equations. Several procedures have been developed, but none of them are fully satisfactory. The task is especially hard, when electronic correlations are strong.

In this thesis, we will always use the approximation called local density approximation (LDA), which may be one of the most popular approximations to the exchange-correlation functional. Even if it is not a well controlled approximation - and this will have consequences on the double-counting problem (see Chapter 3) when going beyond DFT-LDA - it is the easiest one. Other approximations to the exchange-correlation functional are reviewed in [Capelle(2006)].

The local density approximation (LDA) consists in making the following assumption

$$E_{xc}^{\mathrm{LDA}}[\rho] = \int d^3\boldsymbol{r}\rho(\boldsymbol{r})\epsilon_{xc}^{\mathrm{LDA}}(\rho(\boldsymbol{r})), \tag{2.10}$$

where $\epsilon_{xc}^{\mathrm{LDA}}(\rho)$ is the exchange-correlation energy density of an homogeneous electron gas with density ρ. It means that the exchange-correlation energy with density $\rho(\boldsymbol{r})$ is *locally* approximated to the exchange-correlation energy of the homogeneous electron gas, whose density is uniform and equal to $\rho(\boldsymbol{r})$. The consequence is that $\epsilon_{xc}^{\mathrm{LDA}}$ becomes a function of $\rho(\boldsymbol{r})$ and is not a functional anymore, even if it does not have an analytical expression. Using Quantum Monte Carlo algorithms, Ceperley and Adler have calculated the exchange-correlation energy of the homogeneous electron gas with different densities. This leads to interpolation formulas for any density [Ceperley and Alder(1980)]. Such formulas are very practical to use and justify the popularity of the LDA approximation. In quantum chemistry, efforts have also been addressed to design material-adapted functionals, in order to get DFT results that are closer to experiments, but theoretical justifications are missing and we will not use any of these functionals in this work.

We finally mention the extension of DFT-LDA to spin-polarized calculations in order to include non-homogeneous spin densities. This is called DFT-LSDA. Hohenberg-Kohn theorems and Kohn-Sham equations are easily supplemented with a spin index. It is more subtle for the local approximation of the exchange-correlation functional. The exchange energy $E_x^{\mathrm{LDA}}[\rho]$ is straightforwardly given by

$$E_x^{\mathrm{LDA}}[\rho_\uparrow(\boldsymbol{r}),\rho_\downarrow(\boldsymbol{r})] = \frac{1}{2}(E_x^{\mathrm{LDA}}[2\rho_\uparrow(\boldsymbol{r})] + E_x^{\mathrm{LDA}}[2\rho_\downarrow(\boldsymbol{r})]), \tag{2.11}$$

but there is no such formal expression for the correlation part. The correlation part, in practice, can be directly constructed from the spin-densities or defined in a similar manner than the exchange energy but without well-founded justification.

2.1.4 Basis sets : Linearized Augmented Plane Waves (L)APW+lo

Density functional theory has been implemented in numerous bases, differing from each other by their cost at the numerical level and by their accuracy. Localized functions emerging from the tight-binding approaches, are extensively used in quantum chemistry and give an intuitive description of the electronic structure and bonding, but the orbitals must be *chosen* for each given system in order to be effective. There is therefore a loss of generality that goes against the *ab initio* engineering. Pseudopotential approaches, by replacing the strong Coulomb potential of the nucleus by an effective ionic potential applied to the valence electrons, are very promising but are still not as much accurate as the *augmented* approaches, which rely on the partition of the space into muffin-tin spheres (MTS) centered on the nuclei and interstitial regions. Such augmented methods have been originally introduced by Slater [Slater(1953)], who proposed an augmentation of the interstitial regions by plane-waves (IPW). They gave birth to the two popular basis sets which are commonly used in first principles calculations :

- the muffin-tin orbital basis in its linear version, linear muffin-tin orbitals (LMTO) [Andersen(1975)] and its Nth-order version (NMTO) [Andersen and Saha-Dasgupta(2000)].
- the augmented plane waves (APW) and their descendants. Such approaches are reviewed in [Singh(1994)].

The main advantage of APW bases resides in the plane wave representation between the atoms for the smooth varying part of the wavefunctions, and in radial functions times spherical harmonics inside the muffin-tin spheres for the rapidly varying part close to the nuclei. In contrast, the great disadvantage is that the basis functions are energy-dependent and thus the equations for matching the functions at sphere boundaries are non-linear. This drawback is avoided when using the *linearized* augmented plane wave (LAPW) framework, which consists in building augmentation functions as linear combinations of a radial function and its energy derivative at a chosen fixed energy [Singh(1994)].

It exists other improvements (see below and Appendix A for details) that are currently used in modern electronic structure codes like WIEN2K [Blaha *et al.* (2001)]. These methods are usually said *all electron* : although the core and valence electrons are not treated in the same way, their density are both calculated self-consistently along the DFT cycles and they are both used for evaluating the Hartree and the exchange-correlation potentials.

The division of the unit cell in muffin-tin spheres (MTS) S^{α}_{MT}, where α denotes an atom of the unit cell, and interstitial regions (IPW) between the spheres (Fig. 2.1), generates a dual

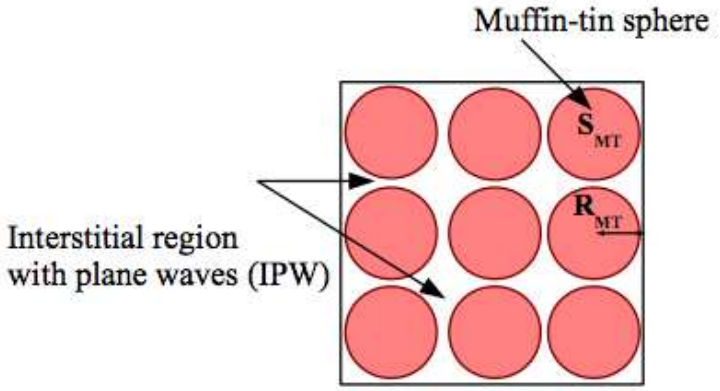

Figure 2.1: Schematic representation of the (L)APW+lo space partition. The space is divided into the muffin-tin spheres S^{α}_{MT} around each atom α, whereas the interstitial regions between the spheres are filled with plane waves.

representation for the potential $v^{\mathrm{KS}}(\boldsymbol{r})$:

$$v^{\mathrm{KS}}(\boldsymbol{r}) = \begin{cases} \sum_{\boldsymbol{G}} \mathrm{e}^{i\boldsymbol{G}\cdot\boldsymbol{r}}\, v_{\boldsymbol{G}} & \text{if } \boldsymbol{r} \in \text{IPW} \\ \sum_{L=0}^{L_{max}} \sum_{M=-L}^{L} V_{LM} Y_{LM}(\boldsymbol{r}) & \text{if } \boldsymbol{r} \in S^{\alpha}_{MT}. \end{cases}$$

$\boldsymbol{G}$ are reciprocal vectors of the lattice and Y_{LM} refer to spherical harmonics. In contrast to the pseudopotential approaches, there is no approximation to the potential here, hence leading to the *full potential* qualification of the method.

The eigenfunctions $\psi^{\sigma}_{\boldsymbol{k}\nu}(\boldsymbol{r})$ of the Kohn-Sham Hamiltonian are then expanded into the (L)APW+lo bases as follows. We add that the (L)APW basis functions can be supplemented by a set of local orbitals (indexed by lo and LO letters, see below). More details are given in Appendix A.

$$\begin{aligned} \psi^{\sigma}_{\boldsymbol{k}\nu}(\boldsymbol{r}) &= \frac{1}{\sqrt{\Omega}} \sum_{\boldsymbol{G}}^{N_{\mathrm{PW}}} c^{\nu\sigma}_{\boldsymbol{G}}(\boldsymbol{k}) \mathrm{e}^{i(\boldsymbol{k}+\boldsymbol{G})\cdot\boldsymbol{r}} \quad \text{if } \boldsymbol{r} \in \text{IPW} \\ &= \sum_{\boldsymbol{G}}^{N_{\mathrm{PW}}} c^{\nu\sigma}_{\boldsymbol{G}}(\boldsymbol{k}) \sum_{lm} A^{\alpha,\boldsymbol{k}+\boldsymbol{G}}_{lm} u^{\alpha,\sigma}_{l}(r, E^{\alpha}_{1l}) Y_{lm}(\theta,\phi) \quad \text{if } \boldsymbol{r} \in S^{\alpha}_{MT} \\ &\quad + \sum_{n_{\mathrm{lo}}=1}^{N_{\mathrm{lo}}} c^{\nu,\sigma}_{\mathrm{lo}} [A^{\alpha,\mathrm{lo}}_{lm} u^{\alpha,\sigma}_{l}(r, E^{\alpha}_{1l}) + B^{\alpha,\mathrm{lo}}_{lm} \dot{u}^{\alpha,\sigma}_{l}(r, E^{\alpha}_{1l})] Y_{lm}(\theta,\phi) \\ &\quad + \sum_{n_{\mathrm{LO}}=1}^{N_{\mathrm{LO}}} c^{\nu,\sigma}_{\mathrm{LO}} [A^{\alpha,\mathrm{LO}}_{lm} u^{\alpha,\sigma}_{l}(r, E^{\alpha}_{1l}) + C^{\alpha,\mathrm{LO}}_{lm} u^{\alpha,\sigma}_{l}(r, E^{\alpha}_{2l})] Y_{lm}(\theta,\phi). \end{aligned} \tag{2.12}$$

The expressions for the coefficients A_{lm}, B_{lm}, C_{lm} can be found in Appendix A. (ν, σ) refer to the band and spin indices, respectively. Ω is the volume of the unit cell and $\boldsymbol{G}$ are reciprocal

vectors of the lattice. N_{PW} is the total number of plane waves for representing interstitial regions, whereas $N_{\text{lo}}(N_{\text{LO}})$ is the number of local (Local) orbitals (Orbitals). $(E_{1l}^{\alpha}, E_{2l}^{\alpha})$ are linearization energies that depend on the atom α and the orbital index l. The matching at the sphere boundaries for the (L)APW+lo basis functions is done with a linear combination of radial functions at a reference energy E_{1l}^{α}. Such procedure is not convenient for semicore states. A method employing Local Orbitals (LO) with two linearization energies $(E_{1l}^{\alpha}, E_{2l}^{\alpha})$ and only for these semicore states, was introduced by [Singh(1991)] and leads to a better accuracy.
In 2000, APW methods have been revisited by [Sjöstedt *et al.* (2000)] : the introduction of a set of local orbitals (lo) involving radial functions and their energy derivative, allows for a better flexibility of the APW bases.
Generally, in full-potential augmented plane-wave frameworks (e.g. in WIEN2K code), the LAPW, APW+lo and LO types of orbitals can be used simultaneously.

2.1.5 Merits and failures of DFT-LDA

The popularity of DFT-LDA approaches resides in the results obtained for a wide class of materials that are surprisingly good with respect to experiments. In particular, the lattice parameters of simple crystals can be obtained with high accuracies (errors of the order of $2-3\%$) [Imada and Miyake(2010)]. Another example is the determination of the ionization energy in molecules and the cohesive energy in solids with errors of the order of $10-20\%$. Another great advantage of such approaches is their high computational feasibility, which makes possible to consider more and more complex systems with growing computer power.

However, the energy functional, which is formulated from the Hohenberg-Kohn theorems, is only valid for the ground-state. No information is thus directly given for the excitations - except for the highest occupied state that has to correspond with the ionization energy - whereas experiments, like photoemission, transport or optics, are used as probes of the excitation spectra. Even if it is tempting to identify the Kohn-Sham energies with the true excitations of the system, it is not well-founded theoretically. However, many DFT-based approaches usually make such correspondence. Nevertheless, the Kohn-Sham eigenvalues and eigenfunctions can be used as auxiliary quantities for constructing physically meaningful quantities, as in the fixed-node diffusion Monte Carlo and many-body perturbations calculations [Foulkes *et al.* (2001)].

The main bottleneck of DFT remains the approximations that have to be made for evaluating the exchange-correlation energy. In the case of strongly correlated materials, like transition metals and their oxides or rare-earth compounds, DFT-LDA spectra (or any other general approximation than LDA) do not qualitatively agree with experiments. For these systems including, for instance, open d or f-shells, electrons may struggle between itineracy and localization, whereas DFT-LDA spectra generally exhibit a metallic electronic structure because of the partial filling of the Kohn-Sham bands. DFT-LDA spectra are in particular unable to simulate the Mott insulating spectra of materials like V_2O_3 [Imada *et al.* (1998)] or Sr_2IrO_4 (see Chapter 8) : the electronic correlations in these systems require a treatment that goes beyond the local density approximation of the exchange-correlation functional.

Some of the other LDA drawbacks can be attributed to the presence of a spurious self-interaction term in the local approximation to the exchange. It would require a proper cancellation whereas it is roughly approximated [Martin(2004)]. This motivated methods e.g. called self-interaction correction (SIC) which are reviewed in [Svane and Gunnarsson(1990)].

2.2 Wavefunction-based approaches

Hartree and Hartree-Fock theories are two wavefunction-based approaches, that are often used in quantum chemistry calculations for atoms and short molecules. They usually give reasonable results, especially the post-Hartree-Fock methods [Martin(2004)]. However, their huge computational cost is a shortcoming when dealing with solids, in contrast to DFT. The point here is not to present in details the technical developments of these approaches. We only plan to give their essence for two reasons : they historically are at the basis of the treatment of the many-body problems and they introduce some concepts like the exchange-correlation energy, which play an important role in DFT. They both employ an effective potential that incorporates a part of the real interactions.

Hartree approximation

Hartree proposed the easiest trial many-body wavefunction which corresponds to the product of the single-particle wave functions $\psi_i(\boldsymbol{r})$. According to the variational principle, the many-body problem is then reduced to a set of independent Scrödinger-like equations h_i^{eff} :

$$h_i^{eff} = \Big[-\frac{\nabla^2}{2} + v^{\text{Hartree}}(\boldsymbol{r}) + v_i^{\text{SIC}}(\boldsymbol{r}) \Big] \tag{2.13}$$

$$v_i^{\text{SIC}}(\boldsymbol{r}) = -\int d\boldsymbol{r}' \frac{|\psi_i(\boldsymbol{r}')|^2}{|\boldsymbol{r}-\boldsymbol{r}'|}, \tag{2.14}$$

where $v^{\text{Hartree}}(\boldsymbol{r})$ refer to the Hartree potential (Eq. 2.3) and we have incorporated the self-interaction correction v_i^{SIC}, in order to cancel the unphysical part of the Hartree potential. Indeed, a major drawback of the Hartree approximation comes from the fact that it does not include the Pauli exclusion principle when building the many-body wavefunction. Therefore, the average distance between electrons are usually underestimated leading to an overestimation of the ground-state energy.

Hartree-Fock approximation (HFA)

The easiest way of fulfilling the Pauli principle when starting from the single-particle wavefunctions, is to build their anti-symmetrized product or Slater determinant, denoted Φ. This leads to

the following expectation value of the Hamiltonian, with an explicit reference to the spin degree of freedom :

$$\begin{aligned}\langle\Phi|H|\Phi\rangle &= \sum_{i=1}^{N_e}\sum_{\sigma} d\boldsymbol{r}\psi_i^{\sigma *}(\boldsymbol{r})[-\frac{\nabla^2}{2}]\psi_i^{\sigma}(\boldsymbol{r}) \\ &+\frac{1}{2}\sum_{i,j}^{N_e}\sum_{\sigma_i,\sigma_j}\int d\boldsymbol{r}d\boldsymbol{r}'\psi_i^{\sigma_i *}(\boldsymbol{r})\psi_j^{\sigma_j *}(\boldsymbol{r}')\frac{1}{|\boldsymbol{r}-\boldsymbol{r}'|}\psi_i^{\sigma_i}(\boldsymbol{r})\psi_j^{\sigma_j}(\boldsymbol{r}') \\ &-\frac{1}{2}\sum_{i,j}^{N_e}\sum_{\sigma}\int d\boldsymbol{r}d\boldsymbol{r}'\psi_i^{\sigma *}(\boldsymbol{r})\psi_j^{\sigma *}(\boldsymbol{r}')\frac{1}{|\boldsymbol{r}-\boldsymbol{r}'|}\psi_j^{\sigma}(\boldsymbol{r})\psi_i^{\sigma}(\boldsymbol{r}'). \qquad (2.15)\end{aligned}$$

The second term is the direct interaction, whereas the last one is the exchange interaction. Since the case $i = j$ is included in the exchange interaction, it nicely cancels the self-interaction coming from the direct term. We remark that keeping only the direct interaction and its correction from the exchange term would lead to the same results as in the Hartree approximation. By means of the variational principle, an effective one-body potential (orbital and spin-dependent) is obtained :

$$\begin{aligned}v_{eff}^{i,\sigma} &= v^{\text{Hartree}}(\boldsymbol{r}) + v_{xc}^{i,\sigma}(\boldsymbol{r}) \\ v_{xc}^{i,\sigma}(\boldsymbol{r}) &= -\sum_{j=1}^{N_e}\int d\boldsymbol{r}'\psi_j^{\sigma *}(\boldsymbol{r}')\psi_i^{\sigma}(\boldsymbol{r}')\frac{1}{|\boldsymbol{r}-\boldsymbol{r}'|}\frac{\psi_j^{\sigma}(\boldsymbol{r})}{\psi_i^{\sigma}(\boldsymbol{r})}. \qquad (2.16)\end{aligned}$$

In the Hartree-Fock approximation (HFA), the only considered correlation comes from the Pauli principle and leads to the exchange potential v_{xc} which lowers the energy interaction for parallel spin electrons (Eq. 2.16) and does not affect the interaction between opposite spin electrons. Such effect is known as the exchange-hole interaction, resulting from the impossibility for same spin electrons to occupy the same state. Formally, this is equivalent to a screening involving holes. It is hence remarkable that actually even non-interacting independent parallel spin electrons are subject to electronic screening. However, such screening is missed for electrons of opposite spins.

Approaches beyond HFA propose to estimate a correlation energy able to lower the energy computed in Hartree-Fock according to a theorem attributed to MacDonald [Martin(2004)]. Correlation energy is a quantity that is more difficult to calculate than the exchange energy, which is analytically known in cases like the homogeneous electron gas (for a discussion about exchange-correlation energy, see LDA approximation in section 2.1.3).

For atoms, HFA usually works quite well [Aryasetiawan(2000)]. However, it is more problematic for solids : the gaps of insulating solids are severely overestimated because of the poor treatment of the screening. For metals, HFA even predicts a vanishing density of states at the Fermi energy. The problem of screening is addressed in a more rigorous way in Hedin's equations and in the GW approximation which can be considered as a generalization of HFA but with a screened Coulomb interaction.

2.3 Hedin's equations and GW approximation

2.3.1 Hedin's equations

Using a Green's function formalism, Hedin derived a closed set of equations that would provide an exact solution to the many-body problem [Hedin(1965)]. The many-body effects are contained in the self-energy operator which is non-local and energy dependent and is deduced from screened interacting scatterings. The derivation of Hedin's equations - using Green's functions or the Schwinger functional formalism - can be found in [Aryasetiawan and Gunnarsson(1998)]. We will content ourselves with the general expressions of the equations. In the following, all space-time dependencies are written in terms of the combined index $1 = (\boldsymbol{r}_1, t_1)$.

$$G(1,2) = G_0(1,2) + \int d(34) G_0(1,3)\Sigma(3,4)G(4,2) \tag{2.17}$$

$$\Lambda(1,2,3) = \delta(1,2)\delta(1,3) + \int d(4567)\frac{\delta\Sigma(1,2)}{\delta G(4,5)}G(4,6)G(7,5)\Lambda(6,7,3) \tag{2.18}$$

$$P(1,2) = -i\int d(34) G(1,3)\Lambda(3,4,2)G(4,1^+) \tag{2.19}$$

$$W(1,2) = v(1,2) + \int d(34) v(1,3)P(3,4)W(4,2) \tag{2.20}$$

$$\Sigma(1,2) = i\int d(34) G(1,3^+)W(1,4)\Lambda(3,2,4). \tag{2.21}$$

G_0 represents the bare Green's function whereas G is the interacting one. P is the polarization defined as the variation of the charge density ρ with respect to the total potential applied $V = V^{\text{Hartree}} + V^{\text{ext}}$:

$$P(1,2) = \frac{\delta\rho(1)}{\delta V(2)}. \tag{2.22}$$

The polarization is seen as a scattering between electron propagators via the vertex function Λ :

$$\Lambda(1,2,3) = \delta(1-2)\delta(2-3) + \int d(4567)\frac{\delta\Sigma(1,2)}{\delta G(4,5)}G(4,6)G(7,5)\Lambda(6,7,3). \tag{2.23}$$

W is the Coulomb interaction screened by the polarization. It relies on the inverse dielectric function $\epsilon^{-1}(1,2) = \frac{\delta V(1)}{\delta V^{\text{ext}}}$ and the bare Coulomb operator as follows :

$$W(1,2) = \int d3\, \epsilon^{-1}(1,3)v(3-2). \tag{2.24}$$

The self-energy Σ is finally deduced from the time-product of G, W and Λ.

Even if the above coupled equations are *exact*, they are practically useless under such form, because we do not know how to solve them brutally. It is not clear neither whether we should use an iterative procedure. Appropriate approximations are thus highly desirable.

2.3.2 The GW Approximation

The GW approximation (GWA) is the simplest approximation that can be used for solving Hedin's equations [Hedin(1965)]. It consists in starting from the bare Green's functions to compute the polarization as done in RPA and then consider the interactions at a mean-field level. Only one cycle is usually performed. It follows that :

$$G(1,2) = G_0(1,2) \tag{2.25}$$
$$\Lambda(1,2,3) = \delta(1,2)\delta(1,3) \tag{2.26}$$
$$P(1,2) = -iG(1,2)G(2,1^+) \tag{2.27}$$
$$W(1,2) = v(1,2) + \int d(3,4)v(1,3)P(3,4)W(4,2) \tag{2.28}$$
$$\Sigma(1,2) = iG(1,2)W(2,1^+). \tag{2.29}$$

The last equation leading to the self-energy is the one that gives the name to the method. It is given by a Hartree-Fock-like expression, with the major difference that the screened interaction W is involved instead of the bare interaction. GWA may thus be regarded as a generalization of HFA, but with a *dynamically screened shorter-range* Coulomb interaction. This is a clear improvement in terms of diagrammatic expansion, since the longer-range behavior of the Coulomb potential would dramatically affect the convergence.

There is however no rigorous proof of the well-founding of such scheme and it is usually used because of its ability to yield reasonable results with respect to experiments. LDA Kohn-Sham Green's functions are often considered as initial guesses for G_0 and then a "quasiparticle" correction to the LDA exchange-correlation potential is estimated from the calculated self-energy. It follows a correction to the spectra, which appears to be surprisingly good for a wide range of systems like simple metals and weakly correlated semiconductors and insulators [Aryasetiawan and Gunnarsson(1998), Aryasetiawan(2000)]. The description of strongly correlated systems is however not accessible by this method.

It exists several proposals that explore ways beyond GWA. We think in particular of a quasiparticle self-consistent scheme by [van Schilfgaarde *et al.* (2006)]. Some efforts have also been addressed in order to couple the merits of GWA with those of the dynamical mean-field theory [Biermann *et al.* (2003), Sun and Kotliar(2002)].
Recently, the GW method has been implemented in a linearized augmented plane wave framework ((L)APW+lo) [Jiang *et al.* (2012)] and has been coupled to LDA+U in order to open a gap for magnetic phases [Gomez-Abal *et al.* (2008), Jiang *et al.* (2009)]. The combination with LDA+U (for an introduction to LDA+U, see Chapter 3) can be seen as an approximation to the GW+DMFT combination which is still some way into the future. In this procedure, the authors first employ the LDA+U solution as the starting point and then apply GWA in order to calculate the quasiparticle corrections. This scheme was able to reproduce, for instance, the trends of the optical gaps along the lanthanide sesquioxide series [Jiang *et al.* (2009)].

Chapter 3

Dynamical Mean Field Theory (DMFT) within DFT-LDA

First principles approaches based on density functional theory turn out to be very efficient for materials without significant electronic correlations. However, these approaches contain too drastic approximations to describe adequately strongly correlated systems. Indeed, the many-body system within these frameworks is mapped into a non-interacting homogeneous electron gas, exposed to an effective external potential, or exchange-correlation potential in DFT-LDA.

Several improvements over DFT-LDA have been proposed in order to take into account the strong electronic correlations in a more rigorous way. In particular, there are several attempts to treat the self-interaction problem better. A self-interaction correction (SIC) method [Svane and Gunnarsson(1990)] reproduces quite well the localized nature of d/f electrons. However the one-electron part does not agree with spectroscopy measurements. Hartree-Fock theories, by explicitly containing a self-interaction cancellation, should be more adapted but they miss the screening that strongly renormalizes the bare Coulomb repulsion [Aryasetiawan(2000)]. The question of screening is then more rigorously addressed in the GW approximation which can be considered as a generalization of Hartree-Fock with a frequency and orbital-dependent screened interaction [Aryasetiawan and Gunnarsson(1998)]. Even if such a method appears quite successful for simple metals and semi-conductors, it still fails for the description of strongly correlated systems, because of the oversimplification of the vertex in Hedin's equations (see Chapter 2 for a description of Hedin's equations and GW approximation). Furthermore, the calculation of the screened interaction is based on response functions that usually rely on LDA wavefunctions. This point can be improved by a self-energy calculated in a self-consistent procedure [van Schilfgaarde *et al.* (2006)]. However, these methods still fail for Mott-insulating systems.

The LDA+U method, on the other hand, allowed for major advances, especially to describe the Mott insulating phase [Anisimov *et al.* (1997a)]. In this method, a functional is introduced which treats the interactions among localized d/f electrons at the Hartree-Fock level, whereas itinerant s/p are described by a one-electron LDA potential. The interaction U becomes an adjustable parameter that is commonly set by hand in order to reproduce experimental data like

the gap of the Mott insulator. A limitation of the LDA+U framework is that it starts from an artificial magnetic structure in order to reproduce a Mott insulator.

Concerning many-body physics and correlated electrons from the model side, the Hubbard model benefited a lot from the major improvements that have been put forward by the dynamical mean-field theory (DMFT) [Georges *et al.* (1996)]. The combination of the DFT-LDA treatment of the itinerant states with the DMFT solution of the Hubbard model for the localized ones - as a generalization of LDA+U- turned out to be very successful for strongly correlated materials. Starting from a paramagnetic DFT-LDA calculation, LDA+DMFT approaches are able to catch the correct electronic nature of a correlated compound and make quantitative predictions about their properties, in reasonable agreement with experiments [Lichtenstein and Katsnelson(1998), Biermann(2006)]. Nevertheless, the adaptability of the Hubbard parameters still appears as a subtle issue. The first principles determination of the Hubbard parameters as done in this work, therefore makes LDA+DMFT a truly first principles approach, as well as other semi-*ab initio* approaches based on lattice Hamiltonians. Approaches that go beyond the DMFT approximation, such as the GW+DMFT combination which unifies the accurate local DMFT treatment of the self-energy with the non-local one by GW (see [Biermann *et al.* (2003), Sun and Kotliar(2002)] for detailed reviews), will not be described below.

We start with a brief overview of the dynamical mean-field theory and its application for solving the half-filled one-band Hubbard model. In particular, Fermi liquid and Mott insulating regimes are reviewed for the Bethe lattice in infinite dimensions. We then turn to the LDA+DMFT method and its implementation within the (L)APW+lo framework - thus fully consistent with the framework used for the first principles determination of the Hubbard parameters.

3.1 DMFT : introduction and application to the Mott transition

3.1.1 From the lattice to the quantum impurity model

Generalization of the Weiss mean-field

A mean-field approach for lattice models conceptually consists in replacing the complicated lattice problem by a single-site effective one. All the non-local interactions from the lattice are cast into an external bath - or Weiss mean-field - that is felt by each single site. The Weiss mean-field is introduced in a way that it reproduces accurately the expectation value of a given local observable of the lattice model. A mean-field approximation is then invoked in order to determine the Weiss field self-consistently.

It is enlightening to refer to the original approach that has been introduced by Pierre Weiss for classical interacting spins (Ising model) : the Weiss field in this context is set in order to reproduce the thermal average of the magnetization. The classical mean-field approximation then consists in identifying this field with the thermal average of the local field that is applied

to each spin. In classical models, such mean-field approximation even becomes *exact* above a critical dimension. In the extreme case of an infinite connectivity, treating the neighbors of a given spin as an external bath actually appears quite intuitive.
The dynamical mean-field theory (DMFT) can be seen as a generalization of such ideas, but applied to the quantum case [Georges *et al.* (1996), Georges(2004), Kotliar and Vollhardt(2004)].

A first step towards the elaboration of DMFT was accomplished by Metzner and Vollhardt [Metzner and Vollhardt(1989)], who showed that an infinite-dimension limit can be defined for lattice fermion models, under the condition that the model parameters are appropriately scaled with the dimension. In the case of the single-band Hubbard model, only the hopping parameters have to be scaled by $t = t^*/\sqrt{2d}$, where t^* is fixed, whereas the local Coulomb repulsion U is unchanged. In this limit, the self-energy becomes completely local, thus independent of momenta [Müller-Hartmann(1989)]. The final and important step that leads to the DMFT framework, was introduced by Georges and Kotliar [Georges and Kotliar(1992)], when mapping the lattice problem into a self-consistent quantum impurity problem. In the DMFT framework, the solid is replaced by an atom that is dynamically coupled to a bath of free electrons. As in the classical mean-field approximation, an approximation- namely the dynamical mean-field approximation- has to be introduced in order to determine this bath self-consistently.

DMFT framework

The DMFT construction (for extensive reviews see [Georges *et al.* (1996), Kotliar *et al.* (2006), Bulla(2006), Georges(2004)]) can be explained on the basis of the single-band Hubbard model (Eqs. 1.13 and 1.15). With simplified notations and writing explicitly the single-electron atomic level $\epsilon_0 - \mu$, the lattice Hamiltonian reads as :

$$H = -\sum_{\langle ij\rangle,\sigma} t_{ij} c_i^{\dagger\sigma} c_j^{\sigma} + U \sum_i n_{i\uparrow} n_{i\downarrow} + (\epsilon_0 - \mu) \sum_{i,\sigma} n_{i\sigma}. \tag{3.1}$$

The key quantity of DMFT is the local on-site Green's function of the lattice :

$$G_\sigma(\tau - \tau') \equiv -\langle T c_i^{\sigma}(\tau) c_i^{\dagger\sigma}(\tau')\rangle, \tag{3.2}$$

where the index i is omitted because of the translation invariance of the lattice.

In the classical mean-field theory of the Ising model, this quantity plays the role of the local magnetization, which is described by the coupling of a spin on site i with an effective Weiss field. In complete analogy, we introduce the local Green's function for a single atom coupled to an effective bath. This corresponds to the single-impurity Anderson model [Anderson(1961)], where an interacting impurity is coupled to a set of non-interacting fermions via the hybridization function Δ. The effective impurity action S_{eff} is the appropriate quantity for taking into account the retardation effects of the electrons hopping between the single site and the bath :

$$S_{eff} = -\int_0^\beta d\tau \int_0^\beta d\tau' \sum_\sigma c_\sigma^\dagger(\tau) \mathcal{G}_0^{-1}(\tau - \tau') c_\sigma(\tau') + U \int_0^\beta d\tau n_\uparrow(\tau) n_\downarrow(\tau), \tag{3.3}$$

where $c_\sigma^\dagger, c_\sigma$ are the Grassmann variables associated with the impurity creation and annihilation operators and $n_\sigma = c_\sigma^\dagger c_\sigma$ is the corresponding occupation. $\mathcal{G}_0$ plays the role of a bare propagator for a fermion created on the impurity at time τ and destroyed at time τ'.

The Matsubara spectral representation of this propagator is given by :

$$\mathcal{G}_0^{-1}(i\omega_n) = i\omega_n + \mu - \epsilon_0 - \Delta(i\omega_n). \tag{3.4}$$

This is interpreted as the quantum generalization of the Weiss effective field in the classical case, but with the difference that it is a *dynamical mean-field*, i.e. depending on the energy. It therefore takes into account the local quantum fluctuations of the impurity state due to the coupling with the reservoirs of charges.

Applying such *dynamical mean-field approximation* within DMFT consists in identifying the impurity self-energy Σ_{imp}- that is related to the impurity bare $\mathcal{G}_0$ and interacting G propagators : [1]

$$\Sigma_{\text{imp}}(i\omega_n) = \mathcal{G}_0^{-1}(i\omega_n) - G^{-1}(i\omega_n), \tag{3.5}$$

with the *lattice* self-energy $\Sigma(\boldsymbol{k}, i\omega_n)$ defined as follows :

$$\Sigma(\boldsymbol{k}, i\omega_n) = i\omega_n + \mu - \epsilon_0 - \epsilon_{\boldsymbol{k}} - G^{-1}(\boldsymbol{k}, i\omega_n), \tag{3.6}$$

where $\epsilon_{\boldsymbol{k}}$ is the Fourier transformation of the hopping integrals t_{ij}.

As the impurity self-energy is a local quantity, the DMFT approximation means the following. First, all the non-local components of the lattice self-energy are neglected, and second the local component is approximated by Σ_{imp},

$$\Sigma(\boldsymbol{k}, i\omega_n) = \Sigma_{\text{imp}}(i\omega_n). \tag{3.7}$$

The self-consistency condition, by construction, requires that the local lattice Green's function $G(i\omega_n) = \sum_{\boldsymbol{k}} G(\boldsymbol{k}, i\omega_n)$ coincides with the Green's function of the impurity and thus reads as :

$$G(i\omega_n) = \sum_{\boldsymbol{k}} \left[i\omega_n + \mu - \epsilon_0 - \epsilon_{\boldsymbol{k}} + G^{-1}(i\omega_n) - \mathcal{G}_0^{-1}(i\omega_n) \right]^{-1}. \tag{3.8}$$

The DMFT scheme is illustrated in Fig 3.1. The Anderson model for the impurity (Eq. 3.5) has to be solved in this scheme and is the main technical part. Many powerful approaches have been elaborated so far, in particular in the context of Kondo physics (see [Hewson(1993)] as textbook and below for examples of impurity solvers). Since DMFT is a non-perturbative construction [2], it is valid in the whole parameter space of the lattice model.

Analogously to classical mean-field theories, DMFT is exact in the infinite dimension limit. It is usually considered as a good approximation for finite-dimensional systems, even if it neglects the non-local fluctuations. A variety of cluster DMFT that go beyond the local approximation, have been developed [Kotliar *et al.* (2001), Biroli and Kotliar(2002), Parcollet *et al.* (2004)].

[1] For a reason that is intrinsic to the mean-field theory and that becomes more clear when deriving the DMFT self-consistency relation, we keep the same notation for both the impurity and the local lattice Green's functions.

[2] see for example the derivation of the DMFT equations within the cavity method [Georges *et al.* (1996), Kotliar *et al.* (2006)]

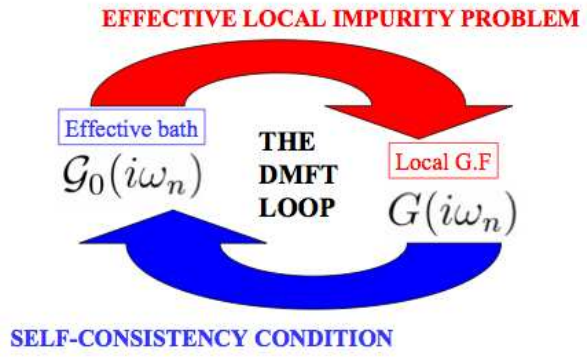

Figure 3.1: The DMFT iterative loop (from [Georges(2004)]). Starting from an initial guess for $\mathcal{G}_0$, the impurity Anderson model is solved with a given solver and leads to the impurity self-energy Σ_{imp} (top arrow). The DMFT approximation then consists in identifying Σ_{imp} with the lattice self-energy such that the local lattice Green's function reads as Eq. 3.8. This leads to an updated Weiss function $\mathcal{G}_0^{-1} = G^{-1} + \Sigma_{\text{imp}}$ (bottom arrow) which is injected again into the impurity solver.

Limits in which DMFT becomes exact

In addition to the infinite dimension limit, DMFT equations yield the exact solution in two simple limits.

- **In the non-interacting limit** $U = 0$, the self-energy vanishes and this makes the DMFT approximation trivially exact. Solving the effective action (Eq. 3.3) leads to $G(i\omega_n) = \mathcal{G}_0(i\omega_n)$. The self-consistency condition 3.8 exactly reproduces the local non-interacting Green's function.

- **In the atomic limit** $t_{ij} = 0$, the Hubbard model consists in a collection of independent atoms. By definition, the lattice self-energy has only on-site components. It follows that the DMFT approximation is exact.

DMFT approximation is thus exact in the two limits of non-interacting bands and of isolated atoms. One may expect that it is still a reasonable approximation in the intermediate regime.

We conclude with the remark that a clue of the popularity of DMFT resides in its ability to catch features of multiple energy scales. This point will be illustrated below within the DMFT solution of the single-band Hubbard model for a Bethe lattice.

Quantum impurity solvers

It is not the point here to describe all the quantum impurity solvers that are employed for solving the impurity Anderson model.
Several solvers are well reviewed in [Hewson(1993)] in the context of the Kondo problem, and

also in [Georges *et al.* (1996)] in the context of DMFT. Approximate schemes like iterated perturbation theory (IPT) [Georges and Kotliar(1992)] or non-crossing-approximation (NCA) [Pruschke *et al.* (1995)] are usually replaced by efficient numerical procedures, like the Wilson numerical renormalization group (NRG) [Bulla *et al.* (2008)], adaptive exact diagonalization methods [Georges *et al.* (1996)] or quantum Monte Carlo (QMC) schemes [Georges and Krauth(1992), Rozenberg *et al.* (1992)] based on the Hirsh-Fye algorithm [Hirsch(1983),Hirsch and Fye(1986)]. Recently, continuous time quantum Monte Carlo (CTQMC) algorithms have demonstrated to be particularly efficient and accurate [Rubtsov *et al.* (2005), Werner *et al.* (2006), Gull(2008)]. They in particular solve the Anderson model at much lower temperatures and stronger interactions than Hirsh-Fye QMC. Furthermore, they are free of systematic errors related to the time discretization. All the LDA+DMFT calculations carried out in this work will employ the hybridization expansion CTQMC method as quantum impurity solver.

3.1.2 The Mott transition in the half-filled one-band Hubbard model

DMFT allowed for an important progress in the understanding of the Mott transition from a metallic to an insulating state. This transition cannot be understood within independent-particle theories. The ability of DMFT to describe accurately both the low-energy part of the spectra (quasiparticles) and the high-energy one (Hubbard satellites) for a given ratio of Coulomb repulsion and kinetic energy, justifies its wide success. For reviews on the Mott transition, see for example [Georges *et al.* (1996), Kotliar and Vollhardt(2004), Imada *et al.* (1998), Rozenberg *et al.* (1994), Aligia *et al.* (1995)].

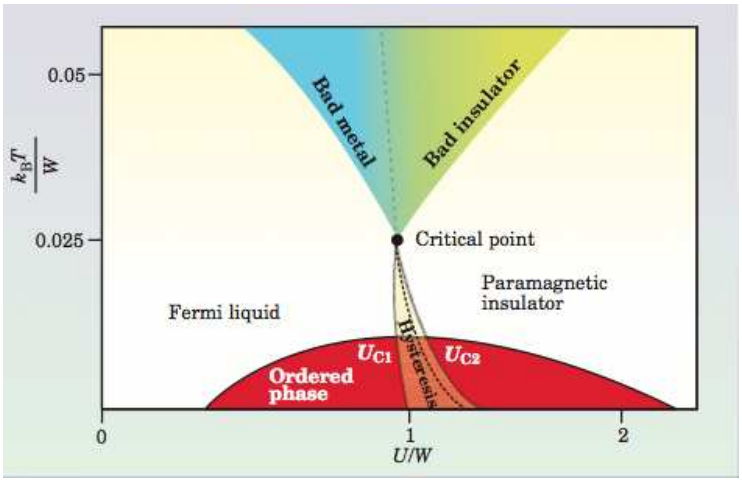

Figure 3.2: Phase diagram of the one-band half-filled Hubbard model within DMFT, representing a material undergoing a Mott metal-insulator transition (from [Kotliar and Vollhardt(2004)]). Temperature (y-axis) and strength of the Coulomb repulsion over the bandwidth D (x-axis) are plotted.

We present below, as an illustration, the DMFT calculation for the half-filled single-band Hubbard model (Eq. 3.1) for the $d = \infty$ Bethe lattice (Fig. 3.3). The phase diagram of this

model is represented in Fig 3.2. As already pointed out, the competition between itineracy and localization of electrons in such models is set by the ratio U/D (at the x-axis of the phase diagram), where U denotes a generic Coulomb repulsion and D the bandwidth of the model. The y-axis of this phase diagram is the temperature expressed in the units of the bandwidth. Thermal excitations break up the quantum coherence of the quasiparticles and, hence, induce an incoherent "bad-metal" or "bad-insulator" state.

In the absence of correlations (thus $U/D = 0$), the Hubbard Hamiltonian simplifies to the one-body hopping term that is diagonal in the momentum space. The system is described by a non-interacting Green's function and the self-energy is zero. It follows that the spectral function at given momentum, $A(\boldsymbol{k}, \omega)$, is a Dirac δ-function,

$$A(\boldsymbol{k}, \omega) \quad = \quad -\frac{1}{\pi}\mathrm{Im}[G(\boldsymbol{k}, \omega)] = \delta(\omega - \epsilon_k), \tag{3.9}$$

and the total local spectral function coincides with the Bethe density of states.

Turning on correlations, the spectral function has a Lorentzian profile :

$$A(\boldsymbol{k}, \omega) \quad = \quad -\frac{1}{\pi}\left[\frac{\mathrm{Im}\Sigma(\omega)}{(\omega + \mu - H_0(\boldsymbol{k}) - \mathrm{Re}[\Sigma(\omega)])^2 + \mathrm{Im}[\Sigma(\omega)]^2}\right]. \tag{3.10}$$

In the Fermi liquid regime, the real part of the self-energy leads to a shift of the non-interacting excitations, whereas the imaginary part is responsible for the broadening of the quasiparticle excitations. It is far away from being the end of the story, since the self-energy strongly depends on the frequency and in the case of the Mott insulator, it will lead to a notable transfer of spectral weights.

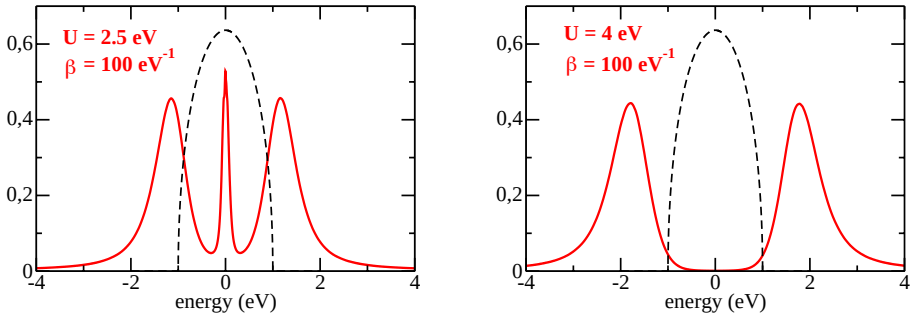

Figure 3.3: Spectral density (in red) for the Bethe lattice within DMFT. The quantum impurity problem is solved with the continuous time Monte-Carlo algorithm (CTQMC) in its strong coupling regime at $\beta = 100$ eV^{-1}. A stochastic maximum entropy method has been employed for the analytical continuation on the real axis. The non-interacting density of states (DOS) is shown for comparison. (left) $U = 2.5$ eV induces a correlated metal with quasiparticle excitations around the Fermi level as well as atomic-like excitations around $U/2$. The pinning at the Fermi level is missed by the maximum entropy method. (right) $U = 4$ eV leads to a Mott insulator with a gap $\approx U$.

Fermi liquid regime

At low temperature and moderate interaction strength, the system exhibits an intermediate regime which is still metallic but affected by correlations. It corresponds to a Fermi liquid regime which is interpreted in terms of quasiparticle excitations with finite lifetime at low-energies, and atomic-like excitations or Hubbard bands at higher energies. These Hubbard bands correspond to the adding and removal of an electron, respectively (see left panel of Fig 3.3 for the corresponding spectral density). These quasiparticles have an enhanced effective mass $m/m^* = Z$ where Z is defined as the quasiparticle renormalization factor which also corresponds to the spectral weight renormalization :

$$Z = \left(1 - \frac{\partial \mathrm{Re}\Sigma}{\partial \omega}\bigg|_{\omega=0}\right)^{-1}. \tag{3.11}$$

Z is equal to 1 for a non-interacting system whereas $Z < 1$ for a correlated one. As observed in Fig. 3.3, $Z < 1$ induces in particular a reduced bandwidth, $Z \cdot D \sim 2\epsilon_F^*$, which gives an estimation of the coherence scale.
The complementary weight $1 - Z$ is transferred from the low-energy part of the spectrum to the incoherent Hubbard satellites that are reminiscent from the atomic limit of the Hubbard model. Since the correlations do not modify the Fermi surface, the spectral density $A(\omega = 0)$ is also pinned to its non-interacting value, i.e. the density of states at the Fermi level [Müller-Hartmann(1989)]. The self-energy around the Fermi level displays Fermi liquid characteristics [Pines and Nozière(1965)] : its real part is linear with respect to the frequency whereas its imaginary part shows an ω^2 behavior. For higher frequencies, it considerably deviates from this low-energy behavior and then match the atomic limit behavior, $\Sigma(\omega \to \infty) \sim \frac{U^2}{4\omega}$ at large frequency. The real part goes to the constant Hartree term which is zero at half-filling. With a temperature above the coherent energy scale, thermal fluctuations induce a scattering rate, even at the Fermi level. This invalidates the quasiparticle interpretation. The phase called “bad metal” is reached at this point.

Mott insulator

Above a critical value for the ratio U/D, it is energetically favorable for the electrons to localize around atomic sites, mimicking the atomic limit situation. This corresponds to the Mott insulator with a gap around U, since excitations are now only atomic-like.

Furthermore, there is no more spectral weight at the Fermi level. Since the real part of the self-energy must be zero by antisymmetry at half-filling, the elimination of the spectral weight must come from a divergence in the imaginary part of the self-energy [Brinkman and Rice(1970)].

The absence of fluctuations, on the other hand, lead to unscreened local moments following a Curie-like law, and these moments can even order antiferromagnetically at very low temperatures, driven by the super-exchange mechanism.

An increase of the temperature then induces a thermal filling of the insulating gap and a "less" divergent imaginary self-energy. The system enters the phase called "bad insulator" (Fig. 3.2).

In realistic multi-band systems, the problem is much more complex but also richer in terms of possible phenomena. The crystal field splitting is enhanced by correlations [Poteryaev *et al.* (2008)] and charge transfers between orbitals may be allowed by self-energies leading to modifications of the Fermi surface. Other parameters enter the characterization of the Mott insulating state : we think for example of the Zaanen-Sawatzky-Allen classification established for transition-metal oxides [Zaanen *et al.* (1985), Imada *et al.* (1998)]. Such classification relies on the comparison between the charge transfer energy Δ between the ligand and metal orbitals and U, in order to differenciate a charge-transfer insulator (gap around Δ) from a Mott insulator (gap around U). However, Hund's coupling is missing in this classification although it is expected to play a significant role [de' Medici *et al.* (2011)].

We turn to realistic extensions of DMFT in order to deal with the electronic structure calculations of strongly correlated materials. One of the most popular extensions is the LDA+DMFT approximation, that couples DMFT to DFT-LDA.
We first summarize the motivations of such approach and its historical background and we detail its formalism, in particular within the (L)APW+lo framework.

3.2 LDA+DMFT

3.2.1 General introduction : from LDA+U to LDA+DMFT

The LDA+DMFT approximation [Anisimov *et al.* (1997b), Lichtenstein and Katsnelson(1998)] can be motivated from two main perspectives. The first arises from the LDA+U approximation as a natural improvement, whereas the second can be viewed as a way to upgrade the DMFT approach from model Hamiltonians to realistic systems. We only mention below the first point, as it is enlightening for the following. Historically, the elaborations of LDA+U functionals are indeed closely related to the first principles determinations of interaction parameters within constrained-LDA (cLDA), as detailed at the end of Chapter 4.

The LDA+U approach was introduced as an extension to the local spin density approximation (LSDA) (see Chapter 2) by [Anisimov *et al.* (1991), Lichtenstein *et al.* (1995), Anisimov *et al.* (1997a)]. The motivation was to focus on the ordered phases of the Mott insulating states, since they were poorly described within DFT-LSDA.

The idea of LDA+U consists in constructing a generalized functional of the density that explicitly takes into account, as in Hartree-Fock approximation, the Coulomb repulsion on a chosen set of correlated orbitals. Correlated orbitals are identified with the projection of the Bloch states onto a set of atomic local orbitals of the linear muffin-tin orbital (LMTO) basis. A correction $E_U[\{n^\sigma\}]$ to the LSDA functional can be obtained [Anisimov *et al.* (1997a)], where n^σ is the occupation of the correlated orbitals.

Since correlations are already treated at the DFT-LSDA level, it is necessary to subtract from the LSDA functional, the correlation terms that would be counted twice. This leads to the well-known double-counting functional $E_{dc}[\{n^\sigma\}]$. It then follows that :

$$E^{LDA+U}[\rho^\sigma(\boldsymbol{r}),\{n^\sigma\}] \;=\; E^{LSDA}[\rho^\sigma(\boldsymbol{r})] + E_U[\{n^\sigma\}] - E_{dc}[\{n^\sigma\}]. \tag{3.12}$$

The orbital-dependent interaction matrix that is involved in $E_U[\{n^\sigma\}]$ is usually expressed in terms of Slater integrals (see Appendix B) - e.g. $(\mathrm{F}^0,\mathrm{F}^2,\mathrm{F}^4)$ for d orbitals [Anisimov *et al.* (1997a)]. Efforts have been addressed to calculate them from first principles. This leads to the constrained-LDA (cLDA) methods (see Chapter 4), which are naturally combined with LDA+U. There are even methods that explicitly start from a LDA+U reformulation [Pickett *et al.* (1998), Cococcioni and de Gironcoli(2005)].

The double counting problem is a subtle issue and various forms of double counting functionals were proposed. One of the most popular choices is the following [Anisimov *et al.* (1997a)] :

$$E_{dc}[\{n^\sigma\}] \;=\; \frac{U}{2}N(N-1) - \frac{J}{2}\left[N^\uparrow(N^\uparrow-1) + N^\downarrow(N^\downarrow-1)\right], \tag{3.13}$$

where $N^\sigma \equiv \mathrm{Tr}[n^\sigma_{mm'}]$ and $N = N^\uparrow + N^\downarrow$. U and J are respectively the Coulomb on-site and exchange parameters that are related to the Slater integrals by $U = \mathrm{F}^0$ and $J = (\mathrm{F}^2+\mathrm{F}^4)/14$ for d shells (see Appendix B).

Major advances have been achieved by LDA+U for the description of magnetically-ordered Mott insulators, since the spectra with Hubbard bands separated by U, are correctly reproduced. However, LDA+U approaches do not treat Hubbard atomic-like excitations and quasiparticle excitations on an equal footing. More dramatically, in the absence of broken orbital symmetry, they do not improve the DFT-LDA results. The LDA+U approaches have actually similar drawbacks than the static Hartree-Fock approximation on which they rely. LDA+U can also be seen as a static approximation to LDA+DMFT [Anisimov *et al.* (1997b), Lichtenstein and Katsnelson(1998)].

In its basic version, LDA+DMFT consists in tackling the one-particle part of the electronic Hamiltonian within DFT-LDA whereas a chosen set of correlated orbitals is treated by DMFT. The starting point is thus rather similar than in LDA+U, in the difference that the many-body problem is considered beyond the Hartree-Fock approximation. An illuminating functional-based presentation of DFT-LDA, GW, DMFT, LDA+U, LDA+DMFT and the conceptual similarities of these theories can be found in [Kotliar *et al.* (2006)]. DMFT appears as an approximation to the more general spectral density functional theory (SDFT), at the same level as LDA to DFT. In SDFT, a local reference system is introduced and the true local Green's functions are correctly reproduced thanks to a self-consistent bath Green's function. Although it is an exact representation, one needs to apply approximations like DMFT in practical schemes. SDFT-DMFT then allows for the calculation of one-particle observables, whereas DFT-LDA yields ground-state properties.

LDA+DMFT thus appears as a reasonable approximation to an exact functional of both density and local Green's function. The self-consistency in this scheme has to be performed via

a double iteration loop, one over the DMFT cycle and another one over the total charge density which affects the one-electron LDA Hamiltonian.

In the following, we give a short overview of the LDA+DMFT approximation and we present a recent implementation within the (L)APW+lo framework. Further details about LDA+DMFT can be found in the reviews [Kotliar et al. (2006), Georges(2004), Biermann(2006), Lechermann et al. (2006), Aichhorn et al. (2009)].

3.2.2 Overview of the method

We review below the main steps of the LDA+DMFT approximation. The starting point is a converged DFT-LDA calculation which gives a set of Kohn-Sham eigenstates $\{|\psi^{\sigma}_{\boldsymbol{k}\nu}\rangle\}$ with energies $\epsilon_{\boldsymbol{k}\nu}$ for spanning the Hilbert space.

Projection onto the correlated subspace : Projected Wannier functions

In a similar manner than in LDA+U, one has to first identify the correlated orbitals in a localized or Wannier basis set, in order to tackle them within DMFT (instead of Hartree-Fock in LDA+U). We call $\{|\phi^{\alpha\sigma}_{\boldsymbol{k}m}\rangle\}$ such basis. The expression in real space can be obtained within the Fourier transformation defined in Chapter 1 (Eq. 1.2). The index m is an orbital index and α denotes an atom in the unit cell. The construction consists in a projection onto the correlated subspace $\mathcal{C}$ which is defined by the localized orbitals labeled by m and centered on the atom α :

$$\Pi^{\boldsymbol{k}}_{\alpha,\sigma} \quad = \quad \sum_{m\in\mathcal{C}} |\phi^{\alpha\sigma}_{\boldsymbol{k}m}\rangle\langle\phi^{\alpha\sigma}_{\boldsymbol{k}m}|. \tag{3.14}$$

Historically, the Wannier basis was directly identified with the LMTO basis [Andersen(1975)] like in the LDA+U method, since the LMTO basis orbitals are atom-centered and can (approximatively) be associated with a particular angular momentum. Several approaches for constructing Wannier functions from local orbitals have then been proposed. Through a N$^{\text{th}}$-order version of muffin-tin orbitals (NMTO) [Andersen and Saha-Dasgupta(2000)], Wannier functions have been designed by using a projection procedure and successfully applied within LDA+DMFT to the Mott transition in orthorhombic $3d^1$ perovskites.
Another important improvement came from the maximally localized Wannier function framework by [Marzari and Vanderbilt(1997), Souza *et al.* (2001)]. Referring to the definition of the Wannier functions as introduced in Chapter 1 (Eq. 1.3), Marzari and co-workers derived a condition of *maximum localization* in order to determine the transformation $U^{k}_{\mu\nu}$. This condition is based on the minimization of the quadratic spreads of the probability distributions for the Wannier functions. This scheme was first coupled to LDA+DMFT by [Lechermann *et al.* (2006)].

In this thesis, we prefer the alternative projection procedure as it was implemented by [Anisimov *et al.* (2005)] and applied to LDA+DMFT within the (L)APW+lo framework by [Aichhorn *et al.* (2009)]. It was shown that the projected functions are Wannier functions (and close to maximally localized Wannier functions) when dealing with correlated bands that do not energetically

overlap with the rest of the band structure [Lechermann *et al.* (2006)]. In the case of entangled correlated and itinerant states, the projected orbitals are not rigorously Wannier and it is *only empirically* believed that they are equivalent to MLWF.

The Wannier projection procedure roughly consists in considering atomic orbitals $\{|\chi_m^{\alpha\sigma}\rangle\}$ that are promoted to Wannier functions by a truncated expansion over Bloch states and then orthonormalized. In all the following, m refers to an orbital index of the correlated subspace and α denotes the corresponding atom in the unit cell. By expanding the atomic orbitals $|\chi_m^{\alpha\sigma}\rangle$ over the full Bloch basis set $\{\psi_{\boldsymbol{k}\nu}^{\sigma}\}$, it follows that

$$|\chi_{\boldsymbol{k}m}^{\alpha\sigma}\rangle = \sum_{\text{all }\nu} \langle\psi_{\boldsymbol{k}\nu}^{\sigma}|\chi_m^{\alpha\sigma}\rangle|\psi_{\boldsymbol{k}\nu}^{\sigma}\rangle. \tag{3.15}$$

An energy window $\mathbb{W}$ for selecting the Bloch states that are physically relevant for generating the correlated subspace, is then defined and the summation in Eq. 3.15 is restricted to the Bloch states inside this energy window $\mathbb{W}$. The number of included bands - identified with their band indices or with their energy - depends in general on $\boldsymbol{k}$ (and σ). The set of orbitals that is produced after the truncation is called $\{|\tilde{\chi}_{\boldsymbol{k}m}^{\alpha\sigma}\rangle\}$ and is not orthonormal :

$$|\tilde{\chi}_{\boldsymbol{k}m}^{\alpha\sigma}\rangle = \sum_{\nu\in\mathbb{W}} \langle\psi_{\boldsymbol{k}\nu}^{\sigma}|\chi_m^{\alpha\sigma}\rangle|\psi_{\boldsymbol{k}\nu}^{\sigma}\rangle. \tag{3.16}$$

The second step of the procedure then consists in orthonormalizing this set of orbitals with a standard numerical routine in order to produce a Wannier basis $\{|\phi_{\boldsymbol{k}m}^{\alpha\sigma}\rangle\}$. The computational task is not very high, since only a subset of Bloch states is involved in the construction of $\{\tilde{\chi}_{\boldsymbol{k}m}^{\alpha\sigma}\}$ orbitals.

We finally define *"Wannier" projectors* $P_{m\nu}^{\alpha,\sigma}(\boldsymbol{k})$ that connect the Bloch basis to the Wannier basis :

$$P_{m,\nu}^{\alpha,\sigma}(\boldsymbol{k}) \equiv \langle\phi_{\boldsymbol{k}m}^{\alpha\sigma}|\psi_{\boldsymbol{k}\nu}^{\sigma}\rangle. \tag{3.17}$$

We will refer to these projectors throughout this work. As they will play an important role later, we add the following expressions :

$$|\phi_{\boldsymbol{k}L}\rangle = \sum_{\nu\in\mathbb{W}} P_{L\nu}^{*}(\boldsymbol{k})|\psi_{\boldsymbol{k}\nu}\rangle, \tag{3.18}$$

and also the Fourier transformation from the reciprocal to the direct space (see Chapter 1, Eq.1.2) :

$$|\phi_{\boldsymbol{R}L}\rangle = \frac{1}{\sqrt{\mathcal{N}}}\sum_{\boldsymbol{k}} \mathrm{e}^{-i\boldsymbol{k}\cdot\boldsymbol{R}}|\phi_{\boldsymbol{k}L}\rangle, \tag{3.19}$$

where we have condensed the indices (m,α) into L. As we will always consider paramagnetic DFT-LDA calculations, the spin degree of freedom will be omitted from the notations. It is easy to introduce it back for further applications.

DMFT self-consistent loop

For the sake of clarity, we mention that we have to consider as many impurity models as inequivalent correlated atoms α per unit cell. We remind the reader that the compact index L replaces (m, α) for a shorter notation. The spin index is still omitted, since paramagnetic DFT-LDA calculations are considered.

The Anderson effective impurity model for the correlated subspace $\mathcal{C}$ is defined by its bare propagator $[\mathcal{G}^0]_{LL'}$ and by the local Hubbard interactions considered as known for the moment. It is one of the objective of this work to investigate in details their determination.
Considering the Kohn-Sham wavefunctions as initial guesses for $\mathcal{G}^0$, it follows that :

$$\mathcal{G}^0(i\omega_n) \;=\; \Pi^{\boldsymbol{k}}_{\alpha}\left[\frac{\delta_{\nu\nu'}}{i\omega_n+\mu-\epsilon_{\boldsymbol{k}\nu}}\right]\Pi^{\boldsymbol{k}}_{\alpha}. \tag{3.20}$$

The solution of the impurity model leads to the impurity Green's function $G^{\text{imp}}(i\omega_n)$ as well as to the impurity self-energy $\Sigma_{\text{imp}}(i\omega_n)$ satisfying the Dyson equation :

$$[\Sigma_{\text{imp}}(i\omega_n)]_{mm'} \;=\; [\mathcal{G}^0(i\omega_n)]^{-1}_{mm'} - [G^{\text{imp}}(i\omega_n)]^{-1}_{mm'}. \tag{3.21}$$

According to the DMFT approximation (Eq. 3.8) which relates the effective impurity model to the lattice, the lattice self-energy $\Sigma(\boldsymbol{k}, i\omega_n)$ for the correlated states is approximated by the impurity self-energy. As in LDA+U, it is also necessary, at this step, to deal with a double-counting correction Σ_{dc} discussed later :

$$\Sigma_{\nu\nu'}(\boldsymbol{k}, i\omega_n) \;=\; \sum_{\alpha,mm'} [P^{\alpha}_{m\nu}(\boldsymbol{k})]^* \Delta\Sigma^{\text{imp}}_{mm'}(i\omega_n) P^{\alpha}_{m'\nu'}(\boldsymbol{k}), \tag{3.22}$$

where $\Delta\Sigma^{\text{imp}}_{mm'}(i\omega_n) = \Sigma_{\text{imp}}(i\omega_n) - \Sigma_{\text{dc}}(i\omega_n)$. The projectors $P^{\alpha}_{m\nu}(\boldsymbol{k})$ from Eq. 3.17 are employed for treating only the correlated states within DMFT. The lattice self-energy enters the lattice Green's function through the Dyson equation and hence :

$$[G(\boldsymbol{k}, i\omega_n)]^{-1}_{\nu\nu'} \;=\; (i\omega_n + \mu - \epsilon_{\boldsymbol{k}\nu})\delta_{\nu\nu'} - \Sigma_{\nu\nu'}(\boldsymbol{k}, i\omega_n). \tag{3.23}$$

The local Green's function is then obtained by projecting the lattice Green's function onto the set of correlated orbitals m of the correlated atom α and by summing over the full Brillouin zone :

$$G^{\text{loc}}_{mm'}(i\omega_n) \;=\; \sum_{\boldsymbol{k}} \sum_{\nu\nu'\in\mathbb{W}} P^{\alpha}_{m\nu}(\boldsymbol{k}) G_{\nu\nu'}(\boldsymbol{k}, i\omega_n) [P^{\alpha}_{m'\nu'}(\boldsymbol{k})]^*. \tag{3.24}$$

By definition, the DMFT self-consistency imposes that the lattice local Green's function coincides with the impurity one :

$$G^{\text{loc}}(i\omega_n) \;=\; G^{\text{imp}}(i\omega_n). \tag{3.25}$$

This implies an upfolding of the Weiss field $\mathcal{G}^0$ via the Dyson equation :

$$\mathcal{G}_0^{-1}(i\omega_n) \;=\; \Sigma_{\text{imp}}(i\omega_n) + G^{-1}_{\text{loc}}(i\omega_n). \tag{3.26}$$

It leads to a new impurity model. This cycle is repeated until convergence is reached.

Double-counting correction

In a similar manner than in LDA+U, one has to correct for the correlations that have already been taken into account in DFT-LDA (or any other exchange-correlation approximation) in order to avoid accounting these effects twice. Since DFT itself is not an orbital-resolved theory and LDA is not a well-controlled approximation, such double-counting correction appears to be quite tricky. Several approaches have been proposed (for a review see [Karolak *et al.* (2010)]). We introduce below three of these approaches :

- **fully localized limit** already introduced in Eq. 3.13 in the context of LDA+U [Anisimov *et al.* (1993), Anisimov *et al.* (1997a)]

$$[\Sigma^{\sigma}_{\rm dc}]_{mm'} = \left[U\,(N-\frac{1}{2}) - J(N^{\sigma}-\frac{1}{2})\right]\delta_{mm'}, \tag{3.27}$$

  where $N = N^{\uparrow} + N^{\downarrow}$. In the case of paramagnetic calculations, $N^{\uparrow} = N^{\downarrow} = \frac{N}{2}$.

- **around mean-field** also originates from LDA+U [Anisimov *et al.* (1991)] :

$$[\Sigma^{\sigma}_{\rm dc}]_{mm'} = \left[U\,(N-n^{\sigma}) - J(N^{\sigma}-n^{\sigma})\right]\delta_{mm'}, \tag{3.28}$$

  where n^{σ} is the electron density *per spin and orbital*, i.e. 0.5 for a half-filled system.

- **Held's correction** that is especially adapted for t_{2g} correlated orbitals [Held(2007)] and hence for t_{2g} lattice Hamiltonians (see Chapter 5, Eq. 5.86) :

$$[\Sigma^{\sigma}_{\rm dc}]_{mm'} = (U-2J)(N-\frac{1}{2})\delta_{mm'} \tag{3.29}$$

In all these corrections, U and J are parameters that need to be defined properly (see Chapter 5).

Update of the total charge density

Once the convergence of the DMFT loop is reached, the charge density is deduced from the Fourier transformation of the lattice Green's function [Mahan(1990)] :

$$\rho(\boldsymbol{r}) = \frac{1}{\beta}\sum_{n}\langle \boldsymbol{r}|G(i\omega_n)|\boldsymbol{r}\rangle \mathrm{e}^{i\omega_n\cdot 0^+} \tag{3.30}$$

and the chemical potential is set in order to fulfill the total electron number. A new Kohn-Sham potential is generated from this upfolded density and the whole cycle is performed again until the convergences of the density ρ, the chemical potential and all DMFT quantities, are reached.

In practice, there exists rather few implementations of the whole LDA+DMFT loop including the charge self-consistency because of the numerical difficulties : we mention the implementation

within the LMTO framework by [Savrasov *et al.* (2001), Savrasov and Kotliar(2004), Pourovskii *et al.* (2007)], within Korringa-Kohn-Rostoker (RKK) method by [Minár *et al.* (2005)] and recently within the (L)APW+lo framework by [Haule *et al.* (2010), Aichhorn *et al.* (2011)]. A lighter *"one-shot"'* approach is usually adopted. This approach is validated by the good results with respect to photoemission experiments. It consists in starting from a converged DFT-LDA calculation and stopping once the convergence of the DMFT loop is reached.

3.2.3 Achievements and limitations within the (L)APW+lo framework

Since the pioneering works by [Anisimov *et al.* (1997b), Lichtenstein and Katsnelson(1998)], many materials have been investigated with *"one-shot"* LDA+DMFT calculations, with a successful comparison to experiments, in particular photoemission spectroscopies (PES) and angle-resolved photoemission spectroscopies (ARPES). Applications for classes of materials are reviewed for example in [Kotliar *et al.* (2006), Biermann(2006)].
Recently, the LDA+DMFT combination was implemented by [Aichhorn *et al.* (2009)] within the (L)APW+lo framework provided by the electronic structure code WIEN2K [Blaha *et al.* (2001)]. The full-potential (L)APW+lo framework provides a high level of accuracy for representing the Hilbert space. The implementation, for instance, has been successfully applied to the family of iron-based superconductors like LaOFeAs [Aichhorn *et al.* (2009)] and FeSe [Aichhorn *et al.* (2010)], and also to the layered perovskite Sr_2RuO_4 [Mravlje *et al.* (2011)].

However, rather intrinsic limitations are still on the table, in particular the arbitrariness in the choice of the correlated orbitals, the interaction parameters and the double-counting correction. We will not elaborate much on the double-counting problem but we shall mention that its evaluation usually requires the knowledge of the Hubbard parameters U and J.
One application of this work (see Chapter 8) is to combine within LDA+DMFT in the (L)APW+lo framework (or any other lattice Hamiltonian solvers in the future), a systematic procedure to construct low-energy Hamiltonians and the corresponding interaction parameters from first principles. The chosen procedure is the constrained-Random Phase Approximation (cRPA) method which was invented by [Aryasetiawan *et al.* (2004)]. We insist on the fact that our implementation of cRPA is fully consistent with the LDA+DMFT implementation by [Aichhorn *et al.* (2009)].

Part II

Hubbard U Calculation : Constrained Random Phase Approximation (cRPA)

Chapter 4

What is U in Solids ?

As a first observation, one may note that the problem of electronic interactions highly differs from an isolated atom to atoms in solids. The major difference comes from the possibility of non-local and long-range screening within solids, which strongly lowers the effective Coulomb repulsion between electrons (for a schematic view, see Fig. 1.2). How strong the screening is and how to take it into account in models, are fundamental questions for condensed matter theories.

Early attempts arise from the introduction of the well-known Hubbard parameter U in the single-orbital Hubbard-Kanamori-Gutzwiller model [Hubbard(1963),Kanamori(1963),Gutzwiller(1963)]. U is an effective Coulomb interaction usually turned by hand in such model. Due to screening in solids, it is set to an order of magnitude less than the bare atomic interaction. This U parameter corresponds to the Coulomb energy cost for placing two electrons at the same atomic site, or equivalently to the affinity and ionization energy difference (Fig. 4.1) when respectively adding and removing one electron on a given shell, as summarized by the following equation

$$U = E(d^{n+1}) + E(d^{n-1}) - 2E(d^n). \tag{4.1}$$

$E(d^n)$ is the total energy of a system for which n electrons fill a given d shell on a given atom. With the multi-orbital generalization of the original single-orbital Hubbard model - and other extensions, necessary for taking into account the charge, orbital and/or spin degrees of freedom (see Chapter 1) - the Hubbard U changed its shape from a simple local intra-orbital parameter to a more general on- and inter-site, intra- and inter-orbital interaction parameter.

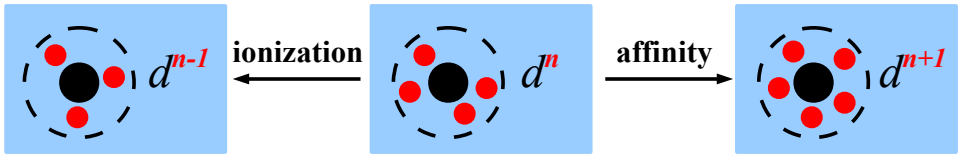

Figure 4.1: Schematic representation of the affinity and ionization when respectively adding and removing one electron on a given shell of an atom (from H. Jiang's talk).

An important step in the determination of U was achieved with the pioneering work of Sawatzky and co-workers which consisted in fitting the spectra from X-ray photoemission, absorption and Auger experiments by a set of Slater integrals (see Appendix B for an introduction to Slater integrals) in a configuration-interaction model [Antonides *et al.* (1977), Sawatzky and Allen(1984), van der Marel(1985)]. By cluster-configuration calculations and comparison with experiments, they were able to extract detailed information about the local electronic structure. An example is given in Fig. 4.2 for copper monoxide (CuO) showing a combination of photoemission (PES) and inverse photoemission (BIS) spectra. An estimation of U is deduced from the multiplet structure of Cu d states.

The method of Sawatzky and co-workers thus affords an experimental determination of the Hubbard U in relation to a configuration-interaction model. Furthermore, in such approach, the monopole part of the Coulomb interaction represented by the Slater integral F^0, is shown to be strongly dependent on the screening in solids, whereas the parameters describing the multiplet splitting of the ground and excited states ($F^k, k > 0$) are in good agreement with Hartree-Fock calculations for free ions [Antonides *et al.* (1977), van der Marel(1985)]. A limitation of this approach is the knowledge of the initial and final states of the system. The dimension of the configuration-interaction basis is hence limited by the computational capacities.

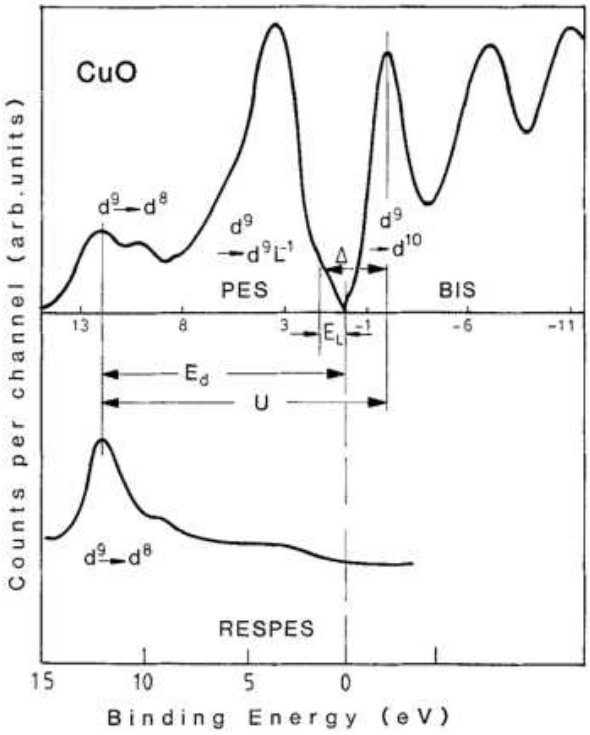

Figure 4.2: Electronic structure data of CuO extracted from the photoemission (PES) and inverse photoemission (BIS) spectra (upper part). The resonance photoemission spectrum is shown in the lower part in order to enhance the $d^9 \rightarrow d^8$ final states. (from [Hüfner(1994)])

Many-body solvers, on the other hand, have been developed for solving Hubbard models dealing with correlated degrees of freedom close to the Fermi level (see for example [Georges *et al.* (1996), Sorella(2001), Tahara and Imada(2008)]). Such models are usually constructed on the basis of physical intuition and the Hubbard interaction U as well as Hund's coupling J are left as adjustable parameters. A severe shortcoming is that without a judicious choice of these interaction parameters, the low-energy model may yield confusing results and even miss important physical features. Such considerations have motivated the development of systematic - or *ab initio* - ways of constructing low-energy effective Hamiltonians involving parameters that are calculated from first principles. The *constrained-Random Phase Approximation (cRPA)* is one of these methods.

Another important motivation concerns the precise evaluation of the dynamical electronic screening and its treatment by the many-body solver. Since screening is a dynamical event, the effective Coulomb repulsion due to the retarded character of the interaction, is expected to be strongly dependent on the frequency. In particular, the Hubbard parameters should yield the unscreened bare Coulomb values in the infinite frequency limit, which is an order of magnitude larger than the static screened value. The treatment of dynamical Hubbard interactions implies a serious challenge for the actual many-body solvers.

We start with a conceptual description of the constrained-Random Phase Approximation (cRPA), which we have implemented in the electronic structure code WIEN2K *[Blaha et al. (2001)]. cRPA provides a consistent way for modeling the Coulomb interactions.*
At the beginning, we include the cRPA method in the more general framework of downfolding. Then we describe the essence of the approach, the achievements and the limitations. We leave for Chapter 5 the technicalities of the implementation in WIEN2K *and the improvements.*
We conclude the chapter with a short presentation of the alternative approaches to determine the Hubbard U in materials. Although they are not ab initio, we first present the cluster-configuration calculations that rely on photoemission experiments. We then give a description of the density functional-based methods (cLDA and linear response formalism).

4.1 The constrained Random Phase Approximation (cRPA) : Concepts

4.1.1 The concept of downfolding

The aim of the following sections is to explain how to build low-energy effective Hamiltonians without any adjustable parameters and include this procedure in the larger context of first principles calculations, between the electronic structure and the many-body solver operations. This point of view gives a general introduction to the downfolding procedure.

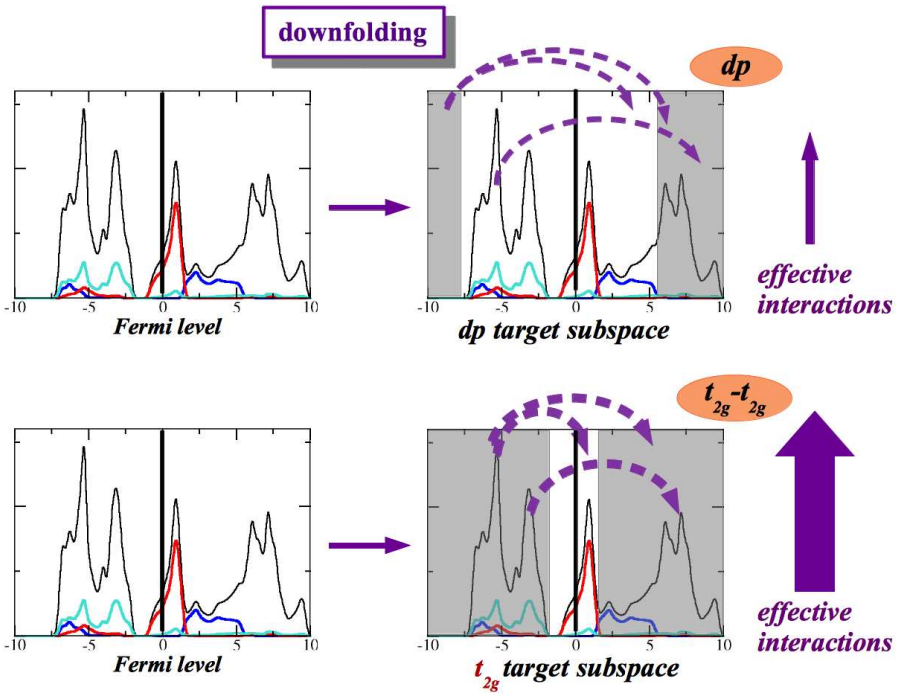

Figure 4.3: Downfolding of the effective interactions for two given low-energy Hamiltonians, called dp (on the top right) and t_{2g}-t_{2g} (on the bottom right) (see also Fig. 4.6), based on the density of states of $SrVO_3$. The total density (on the left) is shown in black, whereas the partial densities for t_{2g}, e_g and O-p are shown in red, blue and turquoise, respectively (Fig. 4.4). The grey areas (on the right) correspond to the higher-energy states that are not included in the downfolded low-energy model. The purple arrows indicate the contributions of the excluded higher-energy states to the total polarization. These effects have to be integrated out to yield effective interactions within the low-energy model, which thus increase with the number of excluded screening channels. The effective interactions are thus scale-dependent as in Wilson renormalization group's philosophy.

Effective low-energy Hamiltonians from first principles : general framework

The main purpose of downfolding is to build an effective Hamiltonian that only accounts for the degrees of freedom near the Fermi level that should be relevant for the physical properties. Therefore, the degrees of freedom at higher energies have to be integrated out in such a way that only a small number of *target* bands survive.
In the case of strongly correlated materials, such target bands can be listed : they are usually d orbitals in transition metal oxides (TMO) and f orbitals in rare-earth compounds.

Following the ideas of the Wilson renormalization group, the price to pay for such operation is the renormalization of the interaction energies on these target bands (Fig. 4.3). The renormalized interaction leads to an effective repulsion which is symbolized by U in the single-orbital Hubbard model. The renormalization is caused by the interaction between low and high-energy electrons : the polarization of the high-energy electrons - typically from s and p states - creates a screening that reduces by about an order of magnitude the bare repulsion v on these target bands close to the Fermi level. Such effect is well highlighted in the Dyson-like equation that connects

the fully screened interaction W to the bare interaction v via the polarization response function (see Hedin's equations in Chapter 2, Eq. 2.20). For a more specific presentation of downfolding in electronic structure, see [Aryasetiawan *et al.* (2009)].

The choice of the low-energy model is obviously not unique. Looking at the early $3d$-TMO, one may wonder whether only t_{2g} degrees of freedom should be retained instead of the whole d manifold (for the band structure of early TMO, see Chapter 7, Fig. 7.2). Two different "down-folded" Hamiltonians clearly will not lead to the same Hubbard interactions U or J, since the low-energy part will differ and the high-energy part will be integrated out differently. However, both models should yield the same results for physical observables at the end, under the condition that both models are appropriate for catching the physical properties. This leads to the following statement and we will insist on this throughout this thesis : *in order to be meaningful, values for the Coulomb interactions have to be accompanied by a precise definition of the model they are referring to.*

4.1.2 The partially screened interaction W^r alias U

In the following, we focus on the cRPA procedure. As we will see, cRPA employs the Kohn-Sham states coming from an electronic structure calculation and yields effective Coulomb parameters for an Hamiltonian that needs to be defined. These parameters can enter low-energy solvers (like DMFT, diagrammatic Monte-Carlo, etc). In a sense, cRPA makes LDA+DMFT or LDA+U first principles approaches (Fig. 4.7).

The idea of cRPA as introduced by [Aryasetiawan *et al.* (2004)] resides in the interpretation of a *partially* screened interaction as the effective Coulomb U, via a systematic *ab initio* procedure for constructing low-energy effective Hamiltonians (see Fig. 4.5).
cRPA relies on the calculation of the polarization and the dielectric function at the RPA level, as done in the GW approximation to Hedin's equations (see Chapter 2 for a presentation of these equations). The starting point is the one for downfolding : one needs to choose first a set of adequate degrees of freedom around the Fermi level. This set defines a correlated subspace of the full Hilbert space and is called $\mathcal{C}$.

In the following, we introduce in our notations the indices "d" in order to specify the contribution of the *chosen* degrees of freedom or to refer to any quantity that is calculated within $\mathcal{C}$ subspace.

Projection onto the correlated subspace $\mathcal{C}$

In this section, we assume that the *chosen* correlated orbitals do *not* energetically overlap with the itinerant ones, as observed for example in the band structure of $SrVO_3$ (Fig. 4.4). In $SrVO_3$, the d bands could be chosen as target bands for cRPA whereas the oxygen p would be part of the itinerant states. The more general case of bands with correlated character that are entangled with ones with itinerant character, requires more care and is considered later in this chapter.

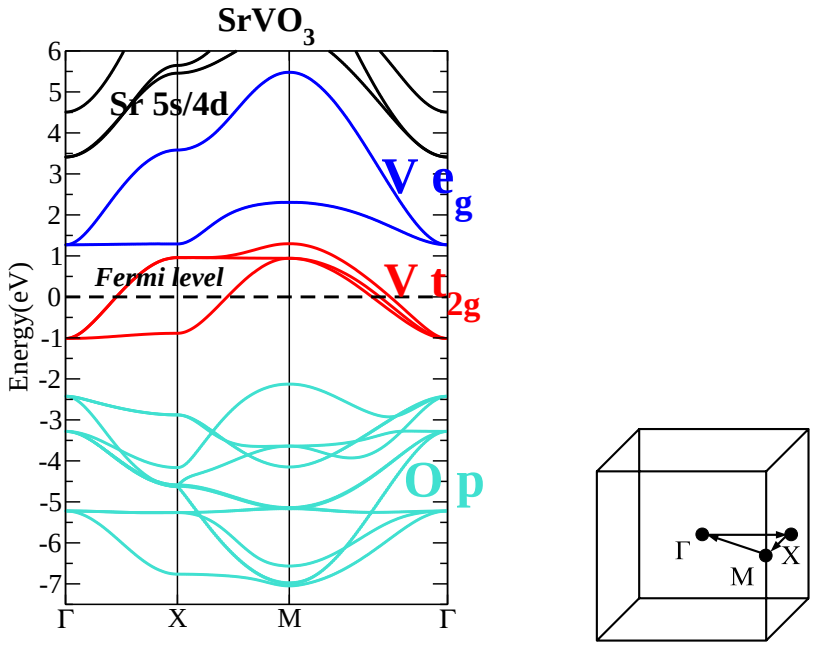

Figure 4.4: (left panel) DFT-LDA band structure of $SrVO_3$. The three degenerate t_{2g} bands are highlighted in red, the e_g in blue and the oxygen p in turquoise. (right panel) Brillouin zone meshes considered.

The bare Green's functions G_d^0 are constructed within the correlated subspace $\mathcal{C}$ as follows :

$$G_d^0(\boldsymbol{r},\boldsymbol{r}';\omega) \;=\; \sum_{\boldsymbol{k}} \left\{ \sum_{d}^{\text{occ}} \frac{\psi_{d\boldsymbol{k}}(\boldsymbol{r})\psi^*_{d\boldsymbol{k}}(\boldsymbol{r}')}{\omega-\epsilon_{d\boldsymbol{k}}-i\eta} + \sum_{d}^{\text{unocc}} \frac{\psi_{d\boldsymbol{k}}(\boldsymbol{r})\psi^*_{d\boldsymbol{k}}(\boldsymbol{r}')}{\omega-\epsilon_{d\boldsymbol{k}}+i\eta} \right\}, \tag{4.2}$$

where $\epsilon_{d\boldsymbol{k}}$ are the energies of the Bloch states $\psi_{d\boldsymbol{k}}$ spanning $\mathcal{C}$. For the simplicity of the notations, we omit the spin degree of freedom.

The starting point of the cRPA method then consists in extending the conceptual division of the Hilbert space to the total polarization P (Fig. 4.5) :

$$P \;=\; P^d + P^r, \tag{4.3}$$

where P^d corresponds to the polarization restricted to the transitions from d to d states, whereas $P^r = P - P^d$ takes into account all other transitions. In other words, the contributions of the d electrons have been projected out in the polarization P^r. At the RPA level, one can calculate the

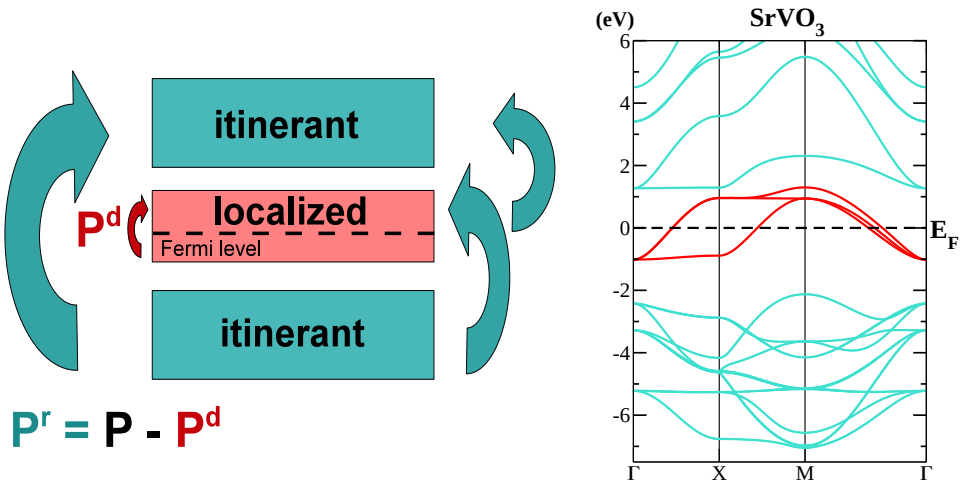

Figure 4.5: Illustration of the cRPA method for a prototypical band structure of a correlated material. We assume that as in the band structure of $SrVO_3$ in the right part of the graph, the *chosen* localized states (in red) do not overlap within the other states (e_g and p in turquoise). In the left part of the graph, P^d (in red) is the polarization that only involves the transitions from and to the *chosen* localized states (t_{2g} for example here), whereas $P^r = P - P^d$ (in turquoise) is the polarization that is left. P^r leads to the partially screened interaction W^r which can be interpreted as the bare interaction but within the low-energy subspace $\mathcal{C}$ that is the Hubbard interaction U (see derivations in the text).

spectral representation of P^d as generated by the Green's functions G^0_d :

$$P^d(\boldsymbol{r},\boldsymbol{r}';\omega) \equiv \int d\omega' G^0_d(\boldsymbol{r},\boldsymbol{r}';\omega-\omega')G^0_d(\boldsymbol{r}',\boldsymbol{r};\omega') \tag{4.4}$$

$$= \sum_{\boldsymbol{k},d}^{\text{occ}} \sum_{\boldsymbol{k}',d'}^{\text{unocc}} \psi^*_{d\boldsymbol{k}}(\boldsymbol{r})\psi_{d'\boldsymbol{k}'}(\boldsymbol{r})\psi^*_{d'\boldsymbol{k}'}(\boldsymbol{r}')\psi_{d\boldsymbol{k}}(\boldsymbol{r}') \times\Big\{\frac{1}{\omega-\epsilon_{d'\boldsymbol{k}'}+\epsilon_{d\boldsymbol{k}}+i\eta}-\frac{1}{\omega+\epsilon_{d'\boldsymbol{k}'}-\epsilon_{d\boldsymbol{k}}-i\eta}\Big\}. \tag{4.5}$$

Such derivation at the RPA level can be found in many textbooks, e.g. [Mahan(1990)]. For the diagrammatic interpretation of the RPA polarization, see the last section of Chapter 1, where RPA has been developed for the homogeneous electron gas.

Practically, one computes the total polarization P as well as the $\mathcal{C}$-restricted- or *constrained*-polarization P^d. The polarization P^r is then deduced from Eq. 4.3.

Identity relations that lead to an interpretation of W^r as U

Following [Aryasetiawan *et al.* (2004)], the expression in Eq. 4.3 which defines P^r, can be further used in the Dyson-like equation (see Hedin's equations in Chapter 2, Eq. 2.20) to obtain

the *partially* screened interaction W^r :

$$\begin{aligned} W &= [1-vP]^{-1}v = [1-vP^d-vP^r]^{-1}v \\ &= \frac{v/[1-vP^r]}{1-\Big[v/[1-P^rv]\Big]P^d} \\ &= [1-W^rP^d]^{-1}W^r. \end{aligned} \tag{4.6}$$

We have defined the key quantity W^r as it follows from Hedin's equations with shorthand notation ($\boldsymbol{r}\,\tau$) represented by a number [Aryasetiawan and Gunnarsson(1998)] :

$$W^r(1,2) \equiv \int d3\,\epsilon_r^{-1}(1,3)v(3,2), \tag{4.7}$$

where ϵ_r is the constrained dielectric function

$$\epsilon^r(1,2) = \delta(1-2) - \int d3\,P^r(1,3)v(3,2). \tag{4.8}$$

Omitting the indices, this leads to :

$$W^r = \frac{v}{1-P^rv}, \tag{4.9}$$

which is interpreted as the *partially* screened interaction where all the screening channels *except the (d to d) ones*, screen the bare Coulomb interaction v.

According to the last expression in Eq. 4.6, W^r is further screened by the polarization P^d to give back the fully screened interaction W. The recovering of W suggests that W^r can be interpreted as the bare interaction but within the low-energy subspace $\mathcal{C}$ – or U in the Hubbard model. In other words, the cRPA method consists in setting that $\langle \dots | W^r | \dots \rangle = U$ (see Chapter 5 for further technical details).

We add that it is called *constrained* RPA since the transitions in the RPA polarization leading to U are constrained to all transitions except the transitions from the *chosen* target bands to the *chosen* target bands.

In addition, relation 4.9 gives a *frequency-dependent* U coming from the energy dependence of the polarization P^r. This leads to a physical effect arising from response theory : since electrons do not respond to the high-frequency variations of an external electric field, any electronic polarization like P or P^r has to vanish at high frequency. In this limit, the particle-hole excitations are ineffective for screening the bare Coulomb potential, whereas they are close to the static limit.

Eq. 4.9 is valid in any basis, as it involves operators. For practical reasons, the interactions are expanded into a localized basis $\{\phi_{\boldsymbol{R}L}(\boldsymbol{r})\}$ (we remind the reader that $L=(n,l,m,\alpha)$ and $\boldsymbol{R}$ refers to the unit cell index, see Chapter 3 for further details) :

$$U^{\boldsymbol{R}_1\boldsymbol{R}_2\boldsymbol{R}_3\boldsymbol{R}_4}_{L_1L_2L_3L_4}(\omega) \equiv \langle \phi_{\boldsymbol{R}_1L_1}\phi_{\boldsymbol{R}_2L_2}|W^r(\omega)|\phi_{\boldsymbol{R}_3L_3}\phi_{\boldsymbol{R}_4L_4}\rangle \tag{4.10}$$

$$= \int d\boldsymbol{r}d\boldsymbol{r}'\phi^*_{\boldsymbol{R}_1L_1}(\boldsymbol{r})\phi_{\boldsymbol{R}_3L_3}(\boldsymbol{r})W^r(\boldsymbol{r},\boldsymbol{r}';\omega)\phi^*_{\boldsymbol{R}_2L_2}(\boldsymbol{r}')\phi_{\boldsymbol{R}_4L_4}(\boldsymbol{r}'). \tag{4.11}$$

The Fourier transformation leads to the retarded interaction matrix elements $U^{\boldsymbol{R}_1\boldsymbol{R}_2\boldsymbol{R}_3\boldsymbol{R}_4}_{L_1L_2L_3L_4}(\tau-\tau')$.

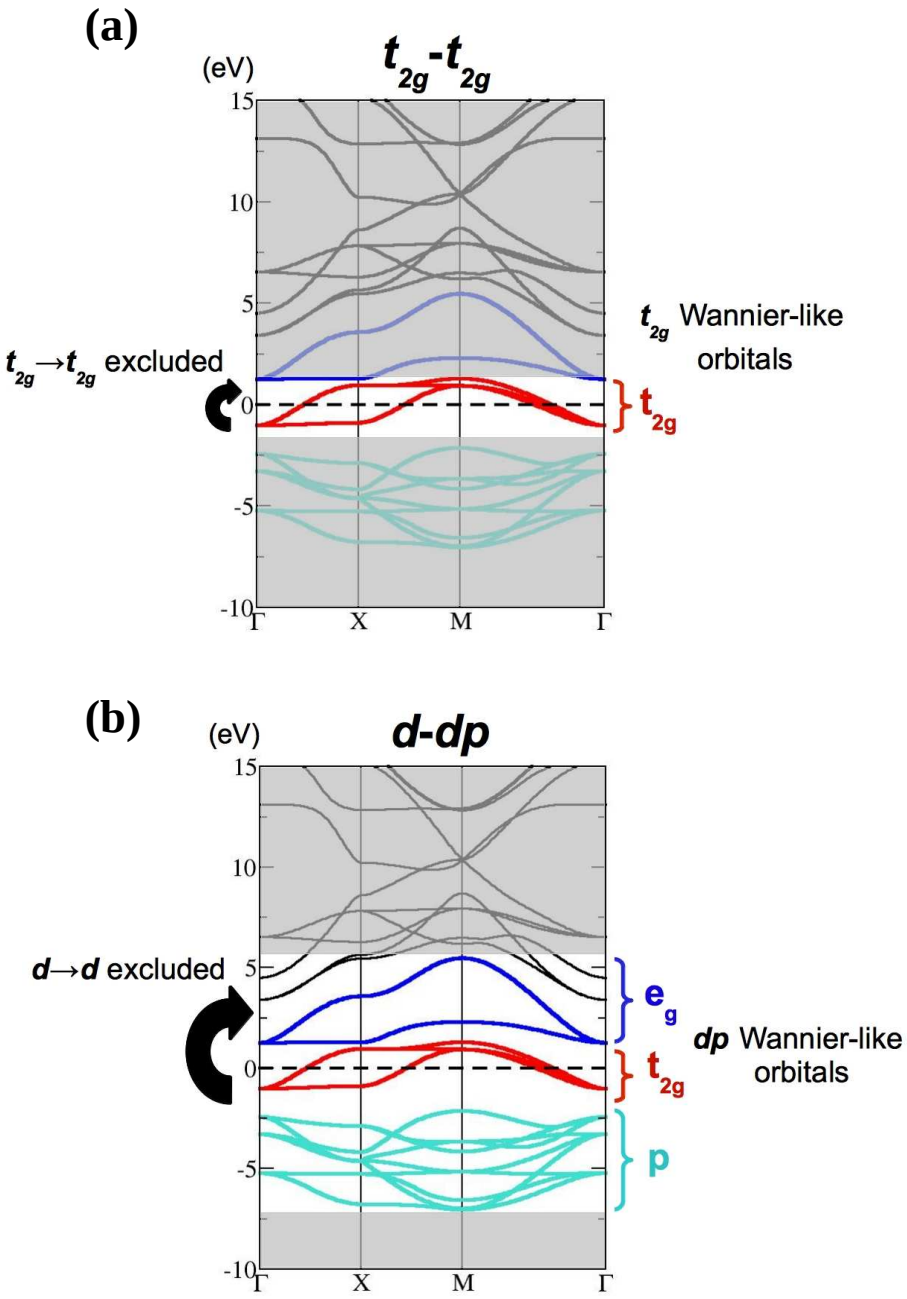

Figure 4.6: Illustration of low-energy Hamiltonians constructed for $SrVO_3$ (taken as an example). (a) t_{2g}-t_{2g} Hamiltonian : the t_{2g} Wannier functions are constructed out of t_{2g} Kohn-Sham bands within an energy window $\mathbb{W}_{t_{2g}}$. In cRPA, the transitions from and to the t_{2g} states included in $\mathbb{W}_{t_{2g}}$ have to be removed from the total polarization to get the constrained polarization P^r. A $\mathcal{C}_{t_{2g}}$-restricted lattice Hamiltonian is then obtained. (b) d-dp Hamiltonian : the dp Wannier functions are constructed out of dp Kohn-Sham bands within an energy window $\mathbb{W}_{dp}$. The oxygen-like p states are included because of the hybridization with the e_g states. In cRPA, the transitions from and to the d states included in $\mathbb{W}_{dp}$ have to be removed from the total polarization to get the constrained polarization P^r. A $\mathcal{C}_{dp}$-restricted lattice Hamiltonian is obtained, where both d and p degrees of freedom are present but only the double occupation on d costs U.

Notations for the low-energy Hamiltonians : t_{2g}-t_{2g} and d-dp

We illustrate the cRPA procedure on the benchmark system $SrVO_3$ in order to discuss our notations employed throughout the thesis. Further details on $SrVO_3$ are given in Chapter 6 and Chapter 7. We adopted the same notations for low-energy *downfolded* models as [Miyake *et al.* (2008)].
In our cRPA implementation, the Bloch states $\psi_{\nu \boldsymbol{k}}(\boldsymbol{r})$ are always approximated by the Kohn-Sham eigenstates resulting from a paramagnetic DFT-LDA calculation (for a discussion of such approximation, see the section 4.1.3). The energies $\epsilon_{\nu \boldsymbol{k}}$ correspond to the Kohn-Sham eigenvalues.

From a chemical point a view, vanadium (V) has 4^+ oxidation state in $SrVO_3$ whose the nominal valence is d^1 because of the respective electronegativities of the elements. Since $SrVO_3$ is a cubic perovskite, the crystal field splits the d orbitals into a set of non-bonding t_{2g}-like bands, which are filled by one electron, and e_g forming bonding and anti-bonding bands with oxygen p orbitals (see Fig. 4.4).

In a quite intuitive way, one can choose the t_{2g} bands as the low-energy degrees of freedom for the cRPA downfolding procedure. The correlated subspace, $\mathcal{C}_{t_{2g}}$, that only includes the t_{2g} degrees of freedom (see Fig. 4.6, part (a)), needs to be generated.
To this effect, a set of projected Wannier functions with t_{2g} character is constructed out of Kohn-Sham bands within the energy window $\mathbb{W}_{t_{2g}}$. The energy window $\mathbb{W}_{t_{2g}}$ is chosen such as only t_{2g} bands are included, following the procedure indicated in Chapter 3. In that case, the subspace so generated within $\mathbb{W}_{t_{2g}}$ equals the correlated subspace $\mathcal{C}_{t_{2g}}$. The so constructed Wannier basis will be employed for representating W^r.

The constrained polarization P^r (Eq. 4.5) has then to be calculated. The transitions from and to the t_{2g} bands within $\mathbb{W}_{t_{2g}}$ have to be removed from the total polarization to get P^r. A method based on the Kohn-Sham indices or on an energy window can be employed for labeling the transitions that have to be eliminated.

We finally get the interaction parameters that correspond to a $\mathcal{C}_{t_{2g}}$-restricted lattice Hamiltonian, where the t_{2g} orbitals are subject to strong correlations via the Coulomb interactions. We call this model, the t_{2g}-t_{2g} model (Fig. 4.6).

Alternatively, the correlated subspace $\mathcal{C}_{dp}$ that keeps also the e_g degrees of freedom in addition to the t_{2g} ones (see Fig. 4.6, part (b)), could be chosen.
Because of the hybridization effects between e_g and oxygen p orbitals, an extended dp energy window $\mathbb{W}_{dp}$ that includes the whole d as well as the p manifold, has to be considered for constructing localized d orbitals.

Although both d and p states are kept for the downfolding of the interaction Hamiltonian within $\mathcal{C}_{dp}$, only the double occupation on d has to cost an energy corresponding to the Hubbard interaction for the model we have in mind. We thus need to calculate the constrained polarization P^r corresponding to the total polarization in which the transitions from and to the d bands within $\mathbb{W}_{dp}$ have to be cut off.

We finally get the interaction parameters that correspond to a $\mathcal{C}_{dp}$-restricted lattice Hamiltonian, where only the d orbitals are subject to strong correlations via the Coulomb interactions. We call this hybrid model, the d-dp model (Fig. 4.6).

4.1.3 Achievements and limitations

History and implementations of cRPA

Since the pioneering work by [Springer and Aryasetiawan(1998)], theoreticians have attempted to compute screened interactions based on density response functions in order to construct Hubbard models. Springer and Aryasetiawan promoted the head of the linear muffin-tin orbital basis (LMTO) in the atomic sphere approximation (ASA) to Wannier-like functions but did not recognize the importance of constraining transitions in the total polarization. This was the merit of Kotani who mentioned that the d-d polarization should be projected out of the total polarization in order to avoid double counting in the calculation of self-energies [Kotani(2000)]. A systematic procedure corresponding to the formulation of cRPA was finally established by [Aryasetiawan *et al.* (2004)].

Since 2004, the cRPA method has been implemented within the head of LMTO-ASA framework [Aryasetiawan *et al.* (2004), Solovyev and Imada(2005)] and within the maximally localized Wannier function (MLWF) framework using the full-potential (FP) LMTO basis [Miyake and Aryasetiawan(2008)] and the (L)APW+lo basis [Şaşıoğlu *et al.* (2011)].
The Coulomb interactions in the pnictide families have been widely investigated with cRPA in the MLWF framework [Miyake *et al.* (2010)]. The $3d$, $4d$ and $5d$ transition metals have also received much attention in cRPA employing the head of LMTO-ASA [Aryasetiawan *et al.* (2006)] or MLWF [Miyake *et al.* (2009), Şaşıoğlu *et al.* (2011)] as local orbitals.

cRPA has been coupled to LDA+DMFT in several works. Such combination (Tab. 4.1) was able to reproduce experimental features for correlated metals, such as iron-based pnictides, LaOFeAs [Aichhorn *et al.* (2009)] and FeSe [Aichhorn *et al.* (2010)], transition metal oxide $SrVO_3$ [Aichhorn *et al.* (2009), Lechermann *et al.* (2006)] and layered perovskite Sr_2RuO_4 [Mravlje *et al.* (2011)]. In the case of $SrVO_3$, it was shown that the energy-dependent Hubbard interactions from cRPA coupled to an extended DMFT approach lead to experimental agreement [Casula *et al.* (2012a)]. However, the approach of these authors was not fully consistent : cRPA calculations were carried out within MLWF whereas LDA+DMFT used projected localized functions. It was shown by [Lechermann *et al.* (2006)] that the projected localized functions constructed with the projection procedure (see Chapter 3) are Wannier functions if the correlated bands are not entangled with itinerant ones. In the case of entangled systems, the projected functions can be considered as localized functions but not rigorously Wannier-like. We show in Chapter 8 that the combination of cRPA with LDA+DMFT also successfully describes the spin-orbitally ordered paramagnetic Mott insulator, Sr_2IrO_4 [Martins *et al.* (2011)].

Interestingly, the pressure dependence of the Coulomb interactions is accessible within cRPA as done in the MLWF framework [Tomczak *et al.* (2009)]. The cRPA method was also combined

	t_{2g}-t_{2g}	d-dp
$SrVO_3$	$\mathcal{U} = 4.0^{a,b}, 5.5^{c}(3.2)$ eV $\mathcal{J} = 0.65^{a,b}, 1.00^{c}(0.46)$ eV	$U_{mm} = 6.0^{a,b}(4.0)$ eV $J_m = 0.65^{a,b}(0.57)$ eV
Sr_2RuO_4	$\mathcal{U} = 2.3^{d}(2.6)$ eV $\mathcal{J} = 0.40^{d}(0.25)$ eV	
Sr_2RhO_4	$\mathcal{U} = 1.7$ eV^{e} $\mathcal{J} = 0.23$ eV^{e}	
LaOFeAs		$U = 2.7^{a}(2.4)$ eV $J = 0.80^{a}(0.73)$ eV
FeSe		$U = 4.0^{f}(3.9)$ eV $J = 0.90^{f}(0.9)$ eV
$SrMnO_3$	$\mathcal{U} = 3.5^{g}(1.8)$ eV $\mathcal{J} = 0.60^{g}(0.39)$ eV	$U = 2.8$ eV $J = 0.89$ eV
Sr_2IrO_4	$\mathcal{U} = 2.1$ eV^{e} $\mathcal{J} = 0.23$ eV^{e}	

[a] [Aichhorn *et al.* (2009)], [b] [Lechermann *et al.* (2006)], [c] [Sekiyama *et al.* (2004)]
[d] [Mravlje *et al.* (2011)],[e] [Martins *et al.* (2011)], [f] [Aichhorn *et al.* (2010)]
[g] [Mravlje *et al.* (2012)]

Table 4.1: Hubbard parameter and Hund's exchange employed in LDA+DMFT calculations to reproduce experimental features such as quasiparticule renormalizations for correlated metals. $(\mathcal{U}, \mathcal{J})$ refer to the Hubbard-Kanamori interactions (Figs. 5.1 and 5.2), whereas (U, J) correspond to F^0, $(F^2+F^4)/14$, respectively (Eqs. 5.67 and 5.68), and (U_{mm}, J_{mm}) are the interactions between the t_{2g} orbitals within the d-dp Hamiltonian (Fig. 5.1). In red parentheses, we show our values from cRPA (see Chapter 6 and 7). For $SrVO_3$, considering the energy-dependent Hubbard interactions from cRPA within an extended DMFT scheme lead to experimental agreement [Casula *et al.* (2012a),Casula *et al.* (2012b)]. The case of Mott insulators is illustrated for $SrMnO_3$ (see Chapter 7) and Sr_2IrO_4 (see Chapter 8) materials. We mention that the antiferromagnetic phase of $SrMnO_3$ was described within GGA+U using $U = 2.7$ eV and $J = 1.0$ eV [Hee Lee and Rabe(2010)].

with LDA+U leading to a truly first principles approach by [Karlsson *et al.* (2010)], and applied to NiO and to gadolinium (Gd) element (for a further discussion, see below).

The main advantages provided by cRPA with respect to the alternative first principles methods (such as constrained-LDA, see below) and despite the numerical cost, are summarized below :

- the four-index interaction matrix elements $U^{\boldsymbol{R}_1\boldsymbol{R}_2\boldsymbol{R}_3\boldsymbol{R}_4}_{L_1L_2L_3L_4}$ are simultaneously obtained : on- and off-site, intra and inter-orbital and exchange components of the effective Coulomb interaction.
- cRPA is a Wilson-like renormalization method in which one can choose the low-energy degrees of freedom for downfolding the corresponding low-energy interaction Hamiltonian.
- cRPA gives the energy dependence of the effective Coulomb interaction. The issue of a

dynamical Hubbard $U(\omega)$ in solvers like LDA+DMFT is currently receiving much attention [Casula *et al.* (2012a), Werner *et al.* (2012), Casula *et al.* (2012b)].

Beyond cRPA as a perspective

It is a well-known statement that the random phase approximation (RPA) is not appropriate to describe correlated systems subject to strong Coulomb interactions. In the cRPA method, only the itinerant states are treated at the level of RPA when calculating the constrained polarization and for these states, such approximation is usually well founded. The correlated states that were chosen for downfolding, on the other hand, will be treated in a second time by a given many-body solver.

Approximations to the polarization beyond RPA are always desirable even for itinerant states. This question has already received much attention in the context of self-consistent GW schemes to solve Hedin's equations [van Schilfgaarde *et al.* (2006)]. To our knowledge, there is only one attempt by [Kutepov *et al.* (2010)] to combine with cRPA the interaction W from a self-consistent GW calculation. However, it is usually believed that the polarization obtained from these self-consistent approaches, is underestimated and may be even worse than the RPA one. Underestimations of the polarization induce overestimated values for U. Kutepov and coworkers, indeed, get larger values for the pnictide $BaFe_2As_2$ than the ones from standard cRPA which are given in Chapter 6 or in the literature [Miyake *et al.* (2010)].

One could improve the standard cRPA method by a self-consistent cRPA illustrated in Fig. 4.7 which can be seen as an approximation to the GW+DMFT method [Biermann *et al.* (2003)]. It would consist in combining cRPA with any many-body solver of a lattice Hamiltonian and then performing an update of the polarization. In Fig. 4.7, we consider for example the combination with DMFT. In chapter 8, a *"one-shot"* LDA+DMFT approach based on the cRPA interaction Hamiltonian, is applied to layered oxides and to rare-earth compounds. A combination with other solvers like diagrammatic Monte-Carlo [Kozik *et al.* (2011)] is currently in development. At the first iteration of this self-consistent loop, cRPA would provide electron-electron interaction parameters for the lattice Hamiltonian solver chosen. Within the updated polarization and the updated charge density, one would obtain an updated screening polarization. New interaction parameters would then be produced by cRPA and given to the many-body solver until convergence is reached.

One would add that, at first glance, it seems puzzling to employ the DFT-LDA spectrum for approximating the screening of a strongly correlated material which could be a Mott insulator. For such materials in particular, the electronic structure is subject to a strong rearrangement because of the strength of the correlations. This rearrangement is especially dramatic for the correlated bands but these bands are usually the *target* bands which are chosen for downfolding in cRPA. The transitions from and to these bands are hence removed from the total polarization. It would be still interesting to evaluate the effective Coulomb interactions for a Mott insulator like $SrMnO_3$ (see Chapter 7) within a scheme combining cRPA with a many-body solver and an updated polarization arising from the Hubbard bands in the spirit of Fig. 4.7.

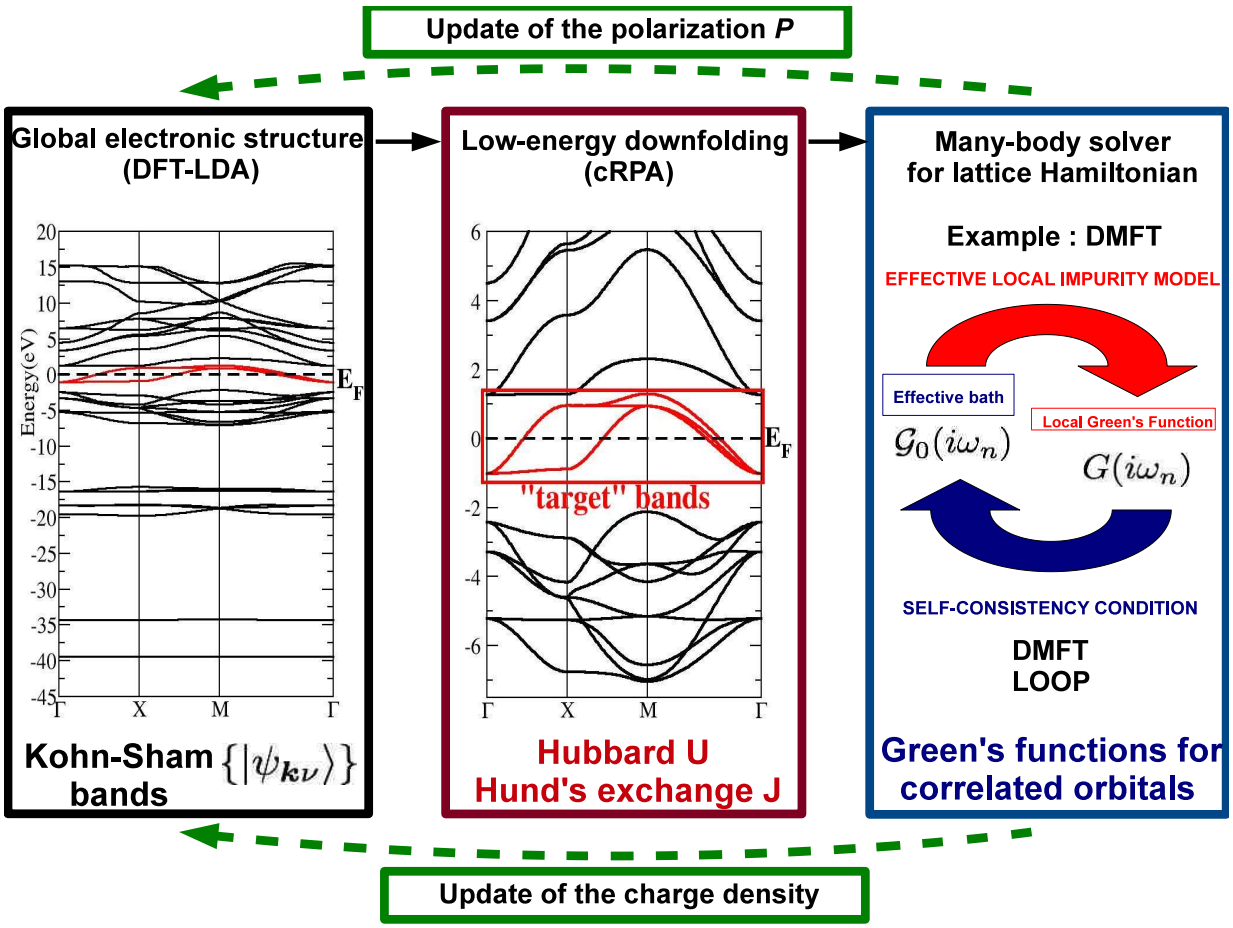

Figure 4.7: Schematic self-consistent procedure in order to describe strongly correlated systems. A so constructed LDA+DMFT on top of cRPA interaction Hamiltonian, in its *one-shot* version, is employed in Chapter 8 for interpreting the spectral properties of layered oxides and rare-earth compounds. This scheme can be seen as an approximation to GW+DMFT [Biermann *et al.* (2003), Sun and Kotliar(2002)]. Updating the polarization P after the many-body solver treatment, would allow for going beyond the RPA approximation and better accounting for the screening in strongly correlated materials.

Recently, a truly first principles calculation of the Hubbard U based on LDA+U was addressed by [Karlsson *et al.* (2010)]. In this work, the authors calculated U with cRPA and then employed LDA+U to get a new set of Kohn-Sham wavefunctions. Remarkably, a convergence is reached in such scheme, which was tested on NiO and gadolinium (Gd). In Gd, a difference of about 5 eV for U after the first and the last loop is reported. At convergence, the $4f$ exchange splitting is increased compared to the one from LDA but is too large by about $1-2$ eV compared to experiments. Furthermore, the spectrum of the dynamical Hubbard $U(\omega)$ is much more "flat" at convergence than after the first loop, as if the high-frequency tail of $U(\omega)$ was taken into account to renormalize the static interaction. For NiO, the value of the charge-transfer gap (around 2.5 eV) is improved compared to LDA but is still much smaller than the experimental one (around 4 eV). The remaining discrepancies could be due to LDA+U.

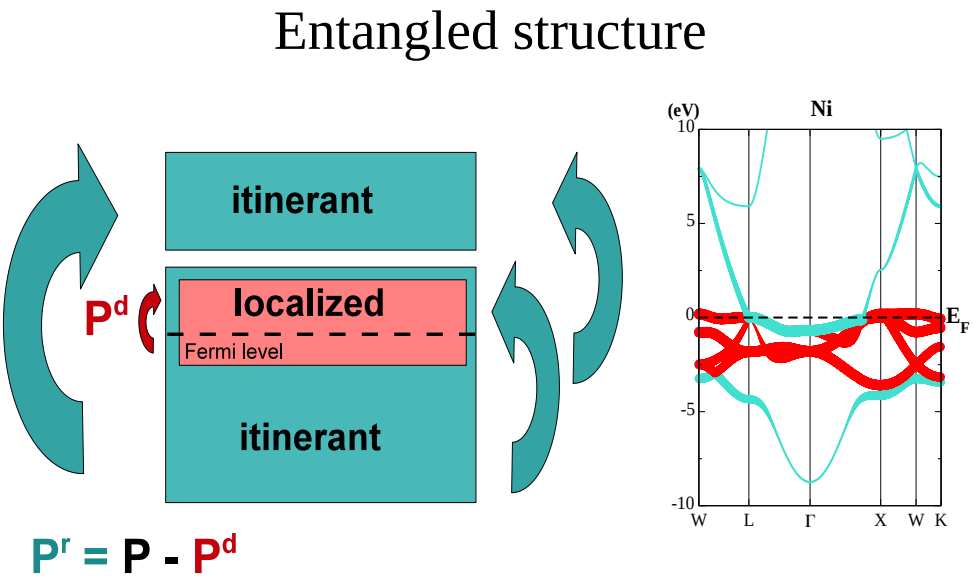

Figure 4.8: Schematic cRPA method (left part of the graph) for a material exhibiting a set of correlated bands (in red) that are entangled with itinerant ones (in turquoise). As an example, we show on the right part of the graph the paramagnetic DFT-LDA band structure of nickel where the d bands are entangled with the sp ones.

Entangled correlated bands

When introducing the polarization P^d in Eq. 4.5, we made the assumption that the correlated *target* bands do not energetically overlap with the itinerant ones. In this case, there was no ambiguity to specify the transitions which have to be removed from the total polarization : methods using band indices or an energy window coincide. Such a situation appeared in $SrVO_3$ for example.

However this is far from being the end of the story. In many cases, correlated states are entangled with itinerant ones (Fig. 4.8). The paramagnetic DFT-LDA band structure of nickel

(Ni) is such a caricature : the $3d$ states around the Fermi level are mixed with a $4sp$-like band that lies on a larger energy scale. It becomes then extremely inappropriate to exclude only the transitions from and to the d states with band indices or an energy window.

Let us for example consider a prototypical Kohn-Sham band that crosses the Fermi level. We suppose that this band has a mixed orbital character with 60% d and 40% sp. Removing from the total polarization all the transitions from and to this band because it has a significant d-character, would not be well founded, since we would also eliminate a part of the sp-screening channels which should *not* be eliminated. The situation can be even trickier when the bands are so entangled that it is not possible any more to identify a proper set of bands with correlated character. In cerium (Ce) element for instance, the d states are notably entangled with the f states, and therefore asking whether a low-energy "f" model is reliable, is highly relevant.
It follows that using band indices or energy windows for such systems would severely approximate P^r and thus the effective electron-electron interactions.

An improvement of the standard cRPA approach devoted to entangled systems is a challenging problem that already received attention. In [Miyake *et al.* (2009)], the authors introduced a disentanglement scheme that generates an isolated set of d bands from the diagonalization of the Hamiltonian expanded into the MLWF basis. For $3d$ transition metals [Miyake *et al.* (2009)] and for some iron-based superconductors [Miyake *et al.* (2010)], the combination with LDA+DMFT was able to catch experimental features. However, in some other cases such as Cerium, the method may lead to unphysical values of the Coulomb interactions because of the artificial system that is constructed by the diagonalization [T. Miyake (private communications)].
Recently, an other method was discussed [Şaşıoğlu *et al.* (2011)]. In this method, the polarization P^d for the correlated subspace is defined as the density correlation function :

$$P^d(\boldsymbol{r},t;\boldsymbol{r}',t') \equiv -i\langle\Psi_0|T[n_d(\boldsymbol{r},t)n_d(\boldsymbol{r}',t')]|\Psi_0\rangle,$$

with the Kohn-Sham determinant Ψ_0, the time-ordering operator T and the Heisenberg density operator $n(\boldsymbol{r},t) = n^d(\boldsymbol{r},t) + n^r(\boldsymbol{r},t)$ (decomposed according to the d subspace and the rest).
In Chapter 5, we present another method to calculate the polarization P^d which is defined as the projection of the total polarization to the correlated subspace $\mathcal{C} = \{d\}$. We call this method, the projection method.

Dynamical Hubbard $U(\omega)$

It is well known that the high-frequency tail of $U(\omega)$ should impact the low-energy part of the spectrum. In particular, since the infinite frequency limit corresponds to the unscreened (bare) interaction v, the system is expected to be more correlated. Between the static and the infinite frequency limits, the spectrum of $U(\omega)$ (see Fig. 4.9 for $SrVO_3$ and other examples in Chapter 6 and 7) is made of plasmonic excitations, which correspond to specific screening processes [Aryasetiawan *et al.* (2006)]. Such dynamical effects are most of the time neglected but sometimes taken into account only via a renormalization of the static value of U in the Hubbard model.

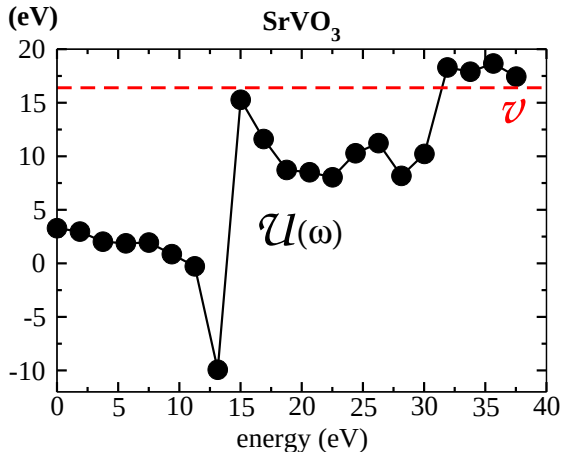

Figure 4.9: Real-part of the dynamical Hubbard interaction $\mathcal{U}(\omega)$ for the t_{2g}-t_{2g} Hamiltonian in $SrVO_3$. $\mathcal{U}(\omega)$ varies from around 3.5 eV in the static limit to the unscreened (bare) interaction $\mathcal{V} \approx 16.5$ eV. It exhibits a strong plasmon pole around 15 eV that notably screens the Coulomb repulsion.

The main difficulty that prevents us from directly using the dynamical $U(\omega)$ is the lack of reliable quantum impurity solvers : because of the order of magnitude of difference between the static and the bare interaction, traditional weak coupling expansion methods cannot be employed. Furthermore, the many poles structure of $U(\omega)$ prohibits a simple extension of the Hubbard-Holstein model. A Green's function *ansatz* in an extended DMFT scheme has been recently introduced in order to handle with the dynamical interaction effects [Casula *et al.* (2012a), Werner *et al.* (2012), Casula *et al.* (2012b)]. These effects appear to be quite significant in the low-energy properties.

Consequently, a first principles determination of $U(\omega)$ is an important piece of information. Further investigations on the combination of such dynamical Hubbard interaction with LDA+DMFT are currently in development.

4.2 Alternative approaches

In the following, we give a short description of other methods employed for calculating effective electron-electron interactions.
We start with the configuration-interaction method which is not ab initio but affords a determination of Coulomb interactions in agreement with spectroscopy experiments. Other density-functional theory-based methods than cRPA are then reviewed (cLDA and linear response formalism).

4.2.1 Configuration-interaction cluster calculations from spectroscopy

Configuration-interaction cluster-model approaches are powerful methods to fit the data from spectroscopy experiments, e.g. $2p$ X-ray absorption spectra (XAS), photoemission spectra (PES, BIS), Auger spectra, etc. For an interpretation of the charge-transfer gap in NiO with such cluster-theory, see for example [Sawatzky and Allen(1984)].

Spectroscopy experiments can give detailed information on the local electronic structure : in the case of $3d$ transition metals, the allowed dipole excitations in XAS experiments from $2p$-core to $3d$ atomic shell can be selected and hence probe the $3d$ states. For an exhaustive presentation of cluster-theory coupled to XAS, see [Haverkort(2005)].
However, configuration-interaction theories can not be classified as *ab initio* methods since they rely on cluster models involving a set of adjustable parameters. In Fig. 4.10, we show for a typical cluster model, the three main parameters that need to be adjusted in agreement with the experimental spectra, namely the charge-transfer energy Δ, the on-site Coulomb energy U and the transfer-integral t_{pd}.

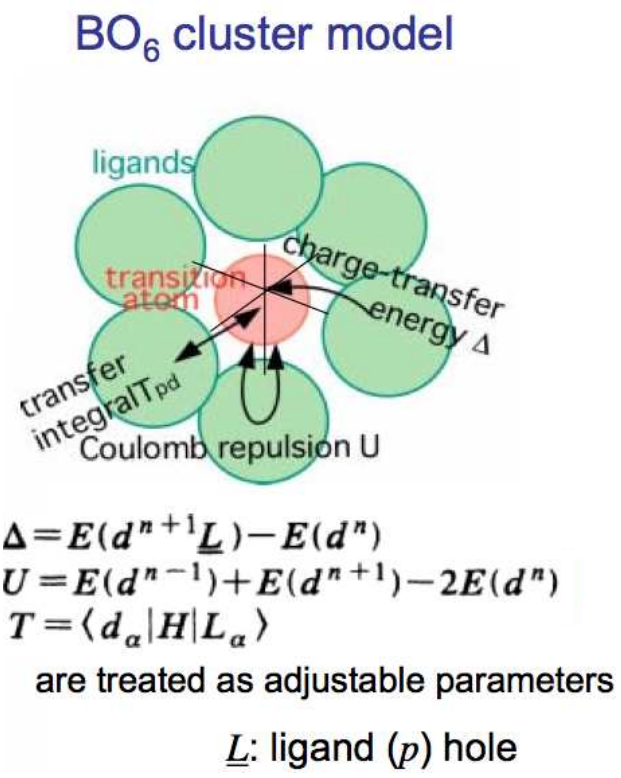

Figure 4.10: Schematic representation of a cluster model for a perovskite structure, involving the charge-transfer energy Δ, the on-site Coulomb energy $U = \mathrm{F}^0$ and the transfer-integral t_{pd} as parameters that need to be adjusted within spectroscopy experiments (from A. Fujimori's talk).

In contrast to density functional-based approaches, the initial and final states are treated on a equal footing in configuration-interaction methods, simulating the spectroscopy experiment. An

Hamiltonian for both the initial and the final states have to be built and diagonalized by Lanczos-type routines [Sugano *et al.* (1970)]. The electron-electron repulsion Hamiltonian is usually parametrized by a set of Slater integrals $\{F^k\}$ (see Appendix B). A tight-binding approach is employed for describing the electronic hopping inside the cluster. It is important to construct an appropriate many-particles basis for both the initial and final states. This means that a sufficient number of electronic configurations has to be taken into account. The dimension of these bases may therefore drastically increase.

According to Auger spectroscopies on transition metals [Antonides *et al.* (1977), van der Marel(1985)], only the monopole part of the repulsion corresponding to the Slater integral F^0 is notably affected by the screening of the surrounding charges. On the other hand, the multiplet splittings in the spectra can be described by Slater integrals $F^k, k > 0$ as determined by Hartree-Fock calculations in atomic systems. These effects are attributed to the different shapes of the local electronic cloud which are not easily screened by the charges located externally.

In configuration-interaction cluster calculations, $U = F^0$ is hence extracted as a fitting parameter from the spectroscopy experiments. Other Slater integrals are deduced from atomic Hartree-Fock calculations with same number of electrons. Applications for $3d$ transition metals and their oxides can be found in [Bocquet *et al.* (1992),Bocquet *et al.* (1996),Saitoh *et al.* (1995), Mizokawa and Fujimori(1996)].

4.2.2 constrained LDA (cLDA)

The constrained-LDA (cLDA) method is based on the density functional theory (DFT) that is extended to arbitrary constraints [Dederichs *et al.* (1984)]. In cLDA, it is the local d or f charge occupation in a single cell which is constrained in order to mimic the definition of U from Eq. 4.1 (see also Fig. 4.1). The original idea is hence to isolate a given shell such that it is not hybridized with others and then constrain its electronic occupation (see [McMahan *et al.* (1988), Hybertsen *et al.* (1989), Gunnarsson *et al.* (1989), Gunnarsson(1990), Anisimov and Gunnarsson(1991)] for pioneering works).

The method practically consists in considering a supercell around an atom which can be seen as an impurity (Fig. 4.11) and then perform a self-consistent total energy calculation $E(n_d)$ with a constrained n_d occupancy on the d shell for example. The cLDA approaches are usually implemented within the linear muffin-tin orbital (LMTO) framework assuming that the LMTO basis functions are able to describe both the Hilbert space in DFT as well as the Hubbard model. The hopping terms connecting a d or f orbital with all other orbitals can be identified within LMTO and hence set to zero [Anisimov and Gunnarsson(1991)]. The method was extended to (L)APW+lo framework by putting the d or f shell into the core in order to remove the hybridization for this shell [Madsen and Novák(2005)]. Such methods are sometimes denoted "hard"-cLDA.

The Hubbard parameter U^{cLDA} can be related to the second derivative of the total energy

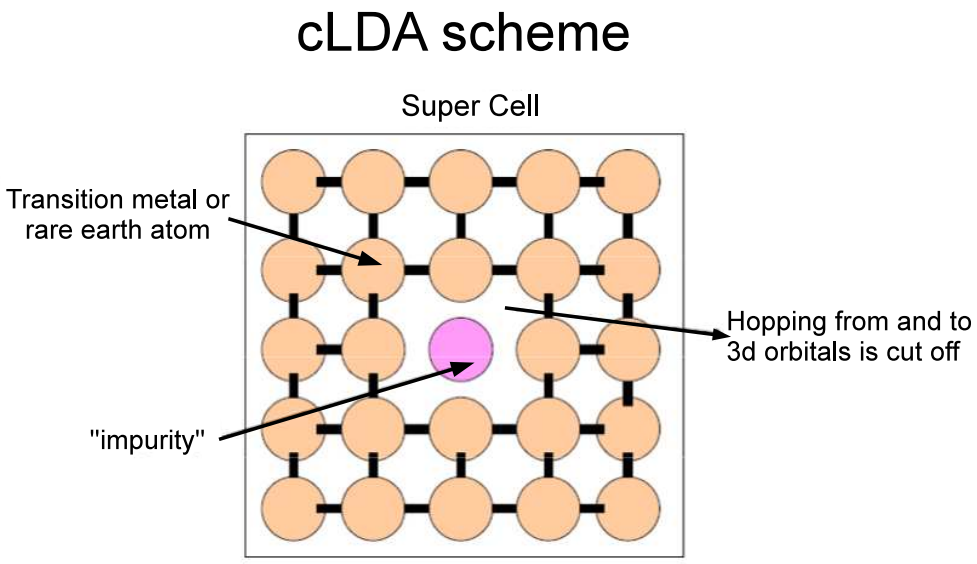

Figure 4.11: Illustration of the "hard"-cLDA method (from F. Aryasetiawan's talk).

$E(n_{d\uparrow}, n_{d\downarrow})$ with respect to the number of localized d electrons (Eq. 4.1) :

$$U^{\text{cLDA}} = \frac{\partial^2 E(n_{d\uparrow}, n_{d\downarrow})}{\partial n_d^2} = \frac{\partial C_d}{\partial n_d}, \tag{4.12}$$

and equivalently to the change in the d level with respect to the number of localized d electrons. C_d corresponds to the center of the d band [Aryasetiawan *et al.* (2006), Gunnarsson *et al.* (1989)]. Within the method of Anisimov and co-workers, one deduces in a supercell calculation that [Anisimov *et al.* (1991), Anisimov and Gunnarsson(1991)] :

$$U^{\text{cLDA}} = \epsilon_{d\uparrow}\left[n_{d\uparrow} = \frac{n}{2} + \frac{1}{2}, n_{d\downarrow} = \frac{n}{2}\right] - \epsilon_{d\uparrow}\left[n_{d\uparrow} = \frac{n}{2} + \frac{1}{2}, n_{d\downarrow} = \frac{n}{2} - 1\right], \tag{4.13}$$

and

$$J^{\text{cLDA}} = \epsilon_{d\uparrow}\left[n_{d\uparrow} = \frac{n}{2} + \frac{1}{2}, n_{d\downarrow} = \frac{n}{2} - \frac{1}{2}\right] - \epsilon_{d\downarrow}\left[n_{d\uparrow} = \frac{n}{2} + \frac{1}{2}, n_{d\downarrow} = \frac{n}{2} - \frac{1}{2}\right], \tag{4.14}$$

where $\epsilon_{d\sigma}$ are the d eigenvalues at the impurity atom calculated at given occupancies with respect to the Fermi energy, which also needs to be adjusted with these occupancies. n is the total number of d electrons.

Such cLDA method has been widely coupled to LDA+U [Anisimov *et al.* (1997a)] and also (to a lesser extent) to LDA+DMFT [Anisimov *et al.* (2009a)].

Recently, cLDA was also formulated in terms of maximally localized Wannier functions (MLWF) and applied to the $3d$ transition metal series [Nakamura *et al.* (2006)]. This scheme is sometimes denoted "soft"-cLDA.

However, the question whether screening is correctly taken into account is a major problem in the cLDA approaches. The calculations of the electron-electron interactions from [Anisimov and Gunnarsson(1991), Anisimov *et al.* (1991), Solovyev *et al.* (1994)] are for example suspected of being overestimated by [Pickett *et al.* (1998)], who indicates that screening may be underestimated. It is usually known that only the screening from the charges inside the atomic sphere is treated with good accuracy [Aryasetiawan *et al.* (2006)]. The systems filling this condition should be reasonably described by "hard"-cLDA methods whereas it may be more problematic for other systems, where only half of the screening charge is included in the Wigner-Seitz cell [Anisimov and Gunnarsson(1991)]. A notable dependence on the muffin-tin sphere radius has also been reported in an early work on La_2CuO_4 [McMahan *et al.* (1988)].

Comparison between cLDA and cRPA

The comparison between cRPA and cLDA is usually rather subtle. The discrepancies reported in the literature (see for example $SrVO_3$ in Chapter 6) may be understood in terms of screening channels. The values from "hard"-cLDA are usually bigger than the ones from cRPA but the methods are not straightforwardly comparable since screening is not considered in an equivalent way. According to a study on $3d$ transition metals [Nakamura *et al.* (2006)], there might be a better agreement between "soft"-cLDA and cRPA (see Chapter 6).

By construction of cLDA, the hopping terms between a given shell and the rest are turned to zero. As proposed by [Aryasetiawan *et al.* (2006)], a fair comparison may consist in removing from the total polarization in cRPA *all the transitions involving this shell*. For $SrVO_3$ for example, the values within the dp model for which the transitions from oxygen-p to d are removed in addition to the dd transitions, agree with the ones from cLDA (Tab. 6.1).

4.2.3 Linear response formalism

The cLDA approaches benefited from the reformulation of the LDA+U functionals within a local orbital basis instead of LMTO [Pickett *et al.* (1998)]. Using a generalized constrained density functional, Pickett and co-workers evaluated the change in energy when constraining a set of local orbital densities in the linear combination of atomic orbital (LCAO) basis. The minimization of such functional involves Lagrange potential shifts applied to these local orbitals and their variations with the changes in the charge lead to an interaction matrix U in the linear response formalism. Their results for the diagonal interaction U_{dd} for transition metal monoxides are about $40 - 65\%$ smaller than the ones by [Anisimov *et al.* (1991)]. They also mention a significant dependence on the choice of the local orbitals. For example, they indicate that U_{dd} in FeO shifts from 4.6 to 7.8 eV when the atomic d orbitals of Fe^{2+} are chosen instead of the ones of the neutral element.

Cococcioni and co-workers have extended the formalism of [Pickett *et al.* (1998)] to get an interpretation of the Hubbard U that relies on the *energy correction* of the DFT-LDA functional in the LDA+U framework (Fig. 4.12) [Cococcioni and de Gironcoli(2005)]. In a nutshell, such

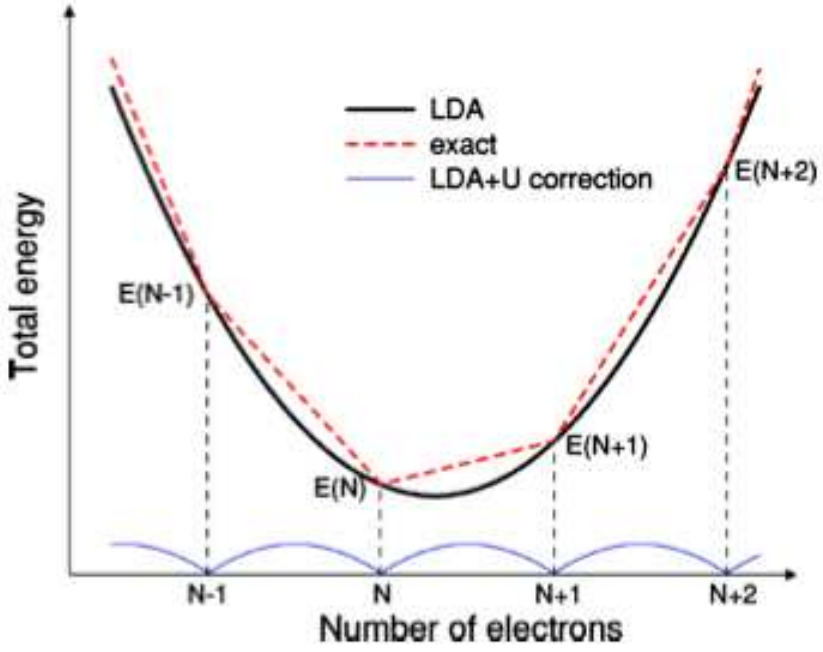

Figure 4.12: Total energy vs. the number of electrons in a generic atomic system in contact with a reservoir (From [Cococcioni and de Gironcoli(2005)]). U is seen as the correction that has to be applied to the LDA energy functional in order to eliminate the unphysical curvature of the LDA energy profile compared to the straight-line segments in the exact calculation.

U would be zero if the exchange-correlation functional within DFT was exact. They introduce a set of projection operators in a plane wave pseudopotential basis. This allows them to select the degrees of freedom I (with the occupation number $n_m^{I\sigma}$) on which the Hubbard U will apply. Starting from the LDA+U framework by [Lichtenstein *et al.* (1995)], the energy correction $E_U[\{n_{mm'}^{I\sigma}\}]$ reads as :

$$E_U[\{n_{mm'}^{I\sigma}\}] = \frac{U}{2}\sum_{I\sigma}\sum_{i}\mathrm{Tr}[n^{I\sigma}(1-n^{I\sigma})], \tag{4.15}$$

and hence this correction does not affect fully occupied or empty states. Since the total energy of an open atomic system with fractional occupation E_n can be seen as $E_n = (1-\omega)E_N + \omega E_{N+1}$, where ω is the statistical weight of the state with $N+1$ electrons, the exact profile of the total energy with the number of electrons is made of segments joining the states with integer occupations. An unphysical curvature between these states is produced by DFT-LDA (or any other exchange-correlation approximation) but can be eliminated by an appropriate energy correction.

It follows that the Hubbard U should correct for this curvature. Such curvature was already known from DFT community and is usually associated to the fractional electron self-interaction error induced by any exchange-correlation approximation [Perdew *et al.* (1982)].

Such analysis leads to the following procedure introduced by Cococcioni and de Gironcoli. As in cLDA, they start with a supercell approach in the constrained DFT framework :

$$E[\{q_I\}] = \min_{n(\boldsymbol{r}),\alpha_I} \left\{ E[n(\boldsymbol{r})] + \sum_I \alpha_I (n_I - q_I) \right\}, \tag{4.16}$$

where the occupation numbers n_I for the atomic site I are constrained to the occupations q_I by the Lagrange multipliers α_I. Via a Legendre transformation, α_I can be seen as the strength of a single particle potential that is applied to the localized orbitals I. They deduce :

$$U = \frac{\partial \alpha_I^{\mathrm{KS}}}{\partial q_I} - \frac{\partial \alpha_I}{\partial q_I} = (\chi_0^{-1} - \chi^{-1})_{II}, \tag{4.17}$$

where $\chi_{IJ} = \frac{\partial n_I}{\partial \alpha_J}$ is the interacting density response function within the variation of q_I. The non-interacting one χ^0_{IJ} is introduced in order to subtract the curvature arising from the noninteracting band structure.

The procedure practically consists in adding small positive and negative potential shifts to each localized site J and compute the variation of the occupation number n_I for the site I in the supercell. Their results for iron and cerium elements as well as for some transition metal monoxides are in reasonable agreement with the ones from the literature. Recently, this method was extended to the calculation of inter-site interactions [Campo Jr and Cococcioni(2010)] but Hund's exchange is still missing. Another important issue is the derivation of an orbital-dependent Hubbard U. Since the formalism relies significantly on LDA+U functionals, one may worry about the choice of double counting functionals.

4.3 Conclusions

Several ways of treating the electron-electron interactions have been introduced in this chapter and consequently several definitions of the parameter U have been given. This may lead to confusion. Our opinion is that this confusion can be enlightened by the following statement : U *itself* is not a physical observable, but U *and the considered model*, become well-defined. Therefore, addressing values of U without mentioning the employed model, does not have any meaning. We illustrate this point with various examples in Chapter 6 and Chapter 7.

In configuration-interaction cluster models, Coulomb interactions are determined as fitting parameters of experimental spectra. On the other hand, in constrained density functional-based approaches like cLDA, the low-energy model that is constructed is not transparent. This explains the subtlety of the comparison between cLDA and cRPA. The discrepancies may be solved by a better knowledge of the screening channels that are involved. Furthermore, the extensions of constrained DFT like the linear response formalism crucially relies on the formulation of LDA+U functionals, since U is used as a correction to DFT-LDA.

In the cRPA method, a systematic Wilson-like procedure to downfold low-energy Hamiltonians is introduced. It relies on the calculation of response functions and leads to the matrix

elements of the effective Coulomb interaction in a localized basis. Furthermore, it gives the spectrum of the dynamical interaction whose combination with many-body solvers is currently receiving high attention.

In this thesis, we have focused our attention on the cRPA method, which we have implemented in the density functional theory electronic structure code WIEN2K *[Blaha et al. (2001)] within the (L)APW+lo framework (see Chapter 2 for an introduction to (L)APW+lo bases). A more technical presentation of cRPA is given in Chapter 5.*

Chapter 5

cRPA in Linearized Augmented Plane-Waves ((L)APW+lo): Technical Advances

This chapter is devoted to the implementation of the cRPA method in the (L)APW+lo framework of the electronic structure code WIEN2K *[Blaha et al. (2001)]. In order to make the text as clear as possible, the main results are first reviewed. More details about the technicalities of the procedure can be found in Section 5.1.5.*
In this work, we benefited from the GW implementation in (L)APW+lo by [Jiang et al. (2012), Gomez-Abal et al. (2008), Jiang et al. (2009)]. The projected Wannier-like functions which we employ for representating Coulomb interactions, were introduced in Chapter 3 : we have followed the implementation in WIEN2K *by [Aichhorn et al. (2009)]. A parametrization for the Coulomb interaction matrix that is based on the Slater integrals, was also developed. Such method makes rather practical the further combination with lattice Hamiltonian solvers like LDA+DMFT.*
We finish the chapter with two last points : first, an improvement of the standard cRPA approach dedicated to materials exhibiting bands with correlated character that are entangled with itinerant ones. Our approach relies on the projection of the polarization into the correlated subspace and is hence denoted d-projection. Second, we derive an interaction parameter that would be adapted to an impurity-like model mapping the lattice like in the DMFT transformation. This can be seen as an effort to the GW+DMFT combination.

5.1 General formalism

We start below with a presentation of the formulas for the Hubbard interaction matrix U, the (fully) screened interaction matrix W and the bare interaction matrix v within the (L)APW+lo framework. Demonstrations and technicalities can be found in Section 5.1.5.

5.1.1 Product mixed basis in (L)APW+lo

In the (L)APW+lo framework, the real space is divided into muffin-tin sphere (MTS) regions and interstitial regions filled with plane waves (IPW) (see Fig. 2.1 for an illustration). As already described in Chapter 2, such approach combines the advantages of the plane waves expansion for the itinerant states with those of the atomic sphere decomposition around the nuclei for the localized ones. A natural question is then how to represent the two-particle bare, fully and partially screened interaction operators, respectively v, W and W^r within this framework . This is done by the construction of an optimized product mixed basis that relies on the space partition between the MTS and IPW regions [Aryasetiawan and Gunnarsson(1998), Kotani and van Schilfgaarde(2002)].

The Kohn-Sham eigenstates can be written as linear combinations of the (L)APW+lo basis functions (Eq. 2.12). Such mixed expansion involves spherical harmonics in the MTS regions and plane waves in the IPW regions.
Let us first consider the MTS part. Spherical harmonics involve a radial and an orthoradial part. The product of spherical harmonics can still be expanded into spherical harmonics using Clebsch-Gordan coefficients. We can therefore define the product basis functions $\{\gamma_{\alpha NLM}(\boldsymbol{r})\}$ in the MTS regions as :

$$\gamma_{\alpha NLM}(\boldsymbol{r}) \quad = \quad v^{\alpha}_{NL}(r) Y^{\alpha}_{LM}(\theta,\phi), \tag{5.1}$$

where (N, L, M) indices correspond to quantum orbital numbers and α to the atomic index. $Y^{\alpha}_{LM}(\theta,\phi)$ are spherical harmonics that are centered on the atom α in MTS. An optimal set of radial functions $v^{\alpha}_{NL}(r)$ is obtained by diagonalizing the overlap matrices of the (L)APW+lo radial functions. More details can be found in the work related to the GW implementation within the (L)APW+lo framework by [Jiang *et al.* (2012),Li(2008)]. So defined, the functions $\{\gamma_{\alpha NLM}(\boldsymbol{r})\}$ constitute an orthonormal basis set. The translational symmetry of the lattice is then imposed by taking the Bloch summation which leads to the basis functions $\{\gamma^{\boldsymbol{q}}_{\alpha NLM}(\boldsymbol{r})\}$ for the MTS regions :

$$\gamma^{\boldsymbol{q}}_{\alpha NLM}(\boldsymbol{r}) \quad = \quad \frac{1}{\sqrt{\mathcal{N}}} \sum_{\boldsymbol{R}} \mathrm{e}^{i\boldsymbol{q}\cdot\boldsymbol{R}} \gamma_{\alpha NLM}(\boldsymbol{r}). \tag{5.2}$$

In the IPW regions on the other hand, one knows that the product of plane waves is still a plane wave. We call $\{\tilde{P}^{\boldsymbol{q}}_{\boldsymbol{G}}(\boldsymbol{r})\}$ such an orthonormalized set of interstitial plane waves.
The orthonormal product mixed basis finally reads as

$$\{\chi^{\boldsymbol{q}}_{i}(\boldsymbol{r})\} \quad \equiv \quad \left\{\gamma^{\boldsymbol{q}}_{\alpha NLM}(\boldsymbol{r}), \tilde{P}^{\boldsymbol{q}}_{\boldsymbol{G}}(\boldsymbol{r})\right\}. \tag{5.3}$$

At this step, it may be convenient to discuss about the plane waves expansion of the bare Coulomb operator v, since this will actually improve the product mixed basis set $\{\chi^{\boldsymbol{q}}_{i}(\boldsymbol{r})\}$ as introduced above.

A plane wave basis set, such as $\{\tilde{\chi}^{\boldsymbol{q}}_{\boldsymbol{G}}(\boldsymbol{r}) = \frac{e^{i(\boldsymbol{q}+\boldsymbol{G})\cdot\boldsymbol{r}}}{\sqrt{\Omega}}\}$, is not suitable for realistic calculations, as a huge number of plane waves would be required. However, it has a major advantage, which is the diagonal representation of v :

$$v_{\boldsymbol{G}\boldsymbol{G}'}(\boldsymbol{q}) = \frac{4\pi}{|\boldsymbol{q}+\boldsymbol{G}|^2}\delta_{\boldsymbol{G}\boldsymbol{G}'}. \tag{5.4}$$

The divergence at $\boldsymbol{q} = 0$ is hence concentrated at the Γ point : $\boldsymbol{G} = \boldsymbol{G}' = 0$. In the $\boldsymbol{q} \to 0$ limit, we may formulate the previous Eq. 5.4 as follows :

$$v_{\boldsymbol{G}\boldsymbol{G}'}(\boldsymbol{q} \to 0) = \frac{4\pi}{q^2}\delta_{\boldsymbol{G}0}\delta_{\boldsymbol{G}'0} + \tilde{v}_{\boldsymbol{G}}\delta_{\boldsymbol{G}\boldsymbol{G}'}(1-\delta_{\boldsymbol{G}0}) \tag{5.5}$$

$$\tilde{v}_{\boldsymbol{G}} \equiv \frac{4\pi}{|\boldsymbol{G}|^2}, \tag{5.6}$$

where $\tilde{v}$ represents the regular part of $v(\boldsymbol{q} \to 0)$.

When v is expanded into another basis than plane waves, the problem induced by the $\boldsymbol{q} \to 0$ limit is not well-defined, since the divergence is not concentrated to a single point anymore. Furthermore, the representation of v is not diagonal neither.

Our scheme then consists in using as a basis, the eigenvectors of v but expanded into the original product mixed basis from Eq. 5.3. Let us call $\{\chi^{\boldsymbol{q}}_{\mu}(\boldsymbol{r})\}$ such basis, while we reserve the (i,j) notations for the original mixed basis $\{\chi^{\boldsymbol{q}}_{i}(\boldsymbol{r})\}$ (Eq. 5.3).

One can relate the plane waves expansion to the original mixed basis *via* the transformation matrices $\mathcal{W}^{i}_{\boldsymbol{G}} \equiv \langle\chi^0_i|\tilde{\chi}^0_{\boldsymbol{G}}\rangle$:

$$\begin{aligned} v_{ij}(\boldsymbol{q} \to 0) &= \langle\chi^0_i|v|\chi^0_j\rangle \\ &= \sum_{\boldsymbol{G}\boldsymbol{G}'} \mathcal{W}^{i}_{\boldsymbol{G}} v_{\boldsymbol{G}\boldsymbol{G}'}(\boldsymbol{q} \to 0)[\mathcal{W}^{j}_{\boldsymbol{G}'}]^* \\ &= \frac{v^s_{ij}}{\boldsymbol{q}^2} + \tilde{v}_{ij}, \end{aligned} \tag{5.7}$$

where $v^s_{ij} \equiv 4\pi\mathcal{W}^{i}_{0}[\mathcal{W}^{j}_{0}]^*$ and $\tilde{v}_{ij} \equiv \sum_{\boldsymbol{G}} \mathcal{W}^{i}_{\boldsymbol{G}}\tilde{v}_{\boldsymbol{G}}[\mathcal{W}^{j}_{\boldsymbol{G}}]^*$.

By diagonalizing the regular part of the Coulomb interaction $\tilde{v}$ at $\boldsymbol{q} \to 0$ (which equals v for all $\boldsymbol{q} \neq 0$), the eigenvectors $\{\chi^{\boldsymbol{q}}_{\mu}(\boldsymbol{r})\}$ read as

$$\chi^{\boldsymbol{q}}_{\mu}(\boldsymbol{r}) = \sum_{i} \mathcal{T}^{\boldsymbol{q}}_{\mu i}\chi^{\boldsymbol{q}}_{i}(\boldsymbol{r}), \tag{5.8}$$

and generate a product mixed basis that is equivalent to the plane wave basis and almost as accurate as the original product mixed basis [Jiang *et al.* (2012)]. Rigorously, we note that the singular part $v^s_{\mu\nu} = \langle\chi^0_\mu|v^s|\chi^0_\nu\rangle$ is not diagonal but as a reasonable approximation, one assumes that it is the case (see also Appendix C) :

$$v^s_{\mu\nu} = 4\pi\delta_{\mu 0}\delta_{\nu 0}. \tag{5.9}$$

In conclusion, $\{\chi^{\boldsymbol{q}}_{\mu}(\boldsymbol{r})\}$ is the product mixed basis used for expanding within our implementation any two-particle operator, e.g. the polarization, the dielectric function and the interactions. In particular, the bare interaction v is diagonal in this basis.
In the following, we replace the indices (μ,ν) by the indices (i,j). These indices thus run over the size of the complete product mixed basis.

5.1.2 Hubbard U

The key ideas of the cRPA method rely on the identity relations 4.6 and 4.9, which lead to interpret the partially screened interaction matrix W^r as the Hubbard interaction matrix U within a given correlated subspace, $\mathcal{C}$. Referring to Eq. 4.11 that involves the matrix elements of W^r in the projected Wannier basis $\{|\phi_{\boldsymbol{R}L}\phi_{\boldsymbol{R}'L'}\rangle\}$ (where $\{|\phi_{\boldsymbol{R}L}\rangle\}$ spans $\mathcal{C}$ subspace), we get the following expression for the matrix elements of U within the (L)APW+lo framework :

$$\begin{aligned} U^{\boldsymbol{R}_1\boldsymbol{R}_2\boldsymbol{R}_3\boldsymbol{R}_4}_{L_1L_2L_3L_4}(\omega) &= \langle\phi_{\boldsymbol{R}_1L_1}\phi_{\boldsymbol{R}_2L_2}|W^r|\phi_{\boldsymbol{R}_3L_3}\phi_{\boldsymbol{R}_4L_4}\rangle \\ &= \frac{1}{\mathcal{N}}\sum_{\boldsymbol{q}} \mathrm{e}^{i\boldsymbol{q}\cdot(\boldsymbol{R}_3-\boldsymbol{R}_2)} \sum_{ij} [M^i_{L_1\boldsymbol{R}_1,L_3\boldsymbol{R}_3}(\boldsymbol{q})]^* v_i^{\frac{1}{2}}(\boldsymbol{q}) [\varepsilon^r(\boldsymbol{q},\omega)]^{-1}_{ij} v_j^{\frac{1}{2}}(\boldsymbol{q}) M^j_{L_4\boldsymbol{R}_4,L_2\boldsymbol{R}_2}(\boldsymbol{q}), \end{aligned} \tag{5.10}$$

where we remind the reader that $L=(n,l,m,\alpha)$ corresponds to (n,l,m) orbital quantum numbers of a correlated state in $\mathcal{C}$, for an atom α in the unit cell. R is the unit cell index. The sum (of size $\mathcal{N}$) over $\boldsymbol{q}$ is performed over the first Brillouin zone. ε^r is the partial symmetrized dielectric function that includes the screening effects reducing the bare Coulomb repulsion v into $W^r \equiv U$. A proper definition of ε^r is given below (Eq. 5.33). Both v and ε^r are expanded into the (L)APW+lo product mixed basis $\{\chi^{\boldsymbol{q}}_i(\boldsymbol{r})\}$ introduced earlier (Eq. 5.8).

$M^i_{L\boldsymbol{R},L'\boldsymbol{R}'}(\boldsymbol{q})$ are auxiliary quantities that correspond to the overlaps between the product mixed basis functions $\chi^{\boldsymbol{q}}_i(\boldsymbol{r})$ and the Kohn-Sham wavefunctions $\psi_{\boldsymbol{k}n}(\boldsymbol{r})$ *via* the Wannier-like projectors $P_{Ln}(\boldsymbol{k})$ onto the correlated subspace (which we have already introduced in Chapter 3, Eq. 3.17) :

$$\begin{aligned} M^i_{L\boldsymbol{R},L'\boldsymbol{R}'}(\boldsymbol{q}) &= \frac{1}{\mathcal{N}}\sum_{\boldsymbol{k}} \mathrm{e}^{-i\boldsymbol{k}\cdot(\boldsymbol{R}-\boldsymbol{R}')} \sum_{n,n'\in\mathbb{W}} [P_{Ln}(\boldsymbol{k})]^* \left(\int_\Omega d\boldsymbol{r}\psi_{\boldsymbol{k}n}(\boldsymbol{r}) [\chi^{\boldsymbol{q}}_i(\boldsymbol{r})\psi_{\boldsymbol{k}-\boldsymbol{q},n'}]^* \right) P_{L'n'}(\boldsymbol{k}-\boldsymbol{q}) \\ &= \frac{1}{\mathcal{N}}\sum_{\boldsymbol{k}} \mathrm{e}^{-i\boldsymbol{k}\cdot(\boldsymbol{R}-\boldsymbol{R}')} \sum_{n,n'\in\mathbb{W}} [P_{Ln}(\boldsymbol{k})]^* M^i_{nn'}(\boldsymbol{k},\boldsymbol{q}) P_{L'n'}(\boldsymbol{k}-\boldsymbol{q}) \end{aligned} \tag{5.11}$$

$$M^i_{nn'}(\boldsymbol{k},\boldsymbol{q}) = \int_\Omega d\boldsymbol{r}\psi_{\boldsymbol{k}n}(\boldsymbol{r}) [\chi^{\boldsymbol{q}}_i(\boldsymbol{r})\psi_{\boldsymbol{k}-\boldsymbol{q},n'}]^* \tag{5.12}$$

The sum over the Kohn-Sham states (n,n') is restricted to the energy window $\mathbb{W}$ by construction of the Wannier functions : the projectors $P_{Ln}(\boldsymbol{k})$ are indeed set to zero if $n \notin \mathbb{W}$.

The relation 5.10 is rather general. The matrix elements are frequency-dependent because of the frequency-dependence of the polarization (see Chapter 4). For further applications, one gives below the expressions for the on-site and off-site interactions.

On-site interactions

The local on-site interaction at an atomic site α inside a given unit cell reads as :

$$U^{\text{on-site}}_{L_1L_2L_3L_4}(\omega) = \frac{1}{\mathcal{N}}\sum_{\boldsymbol{q}}\sum_{ij}[M^i_{L_1,L_3}(\boldsymbol{q})]^* v_i^{\frac{1}{2}}(\boldsymbol{q})[\varepsilon^r(\boldsymbol{q},\omega)]^{-1}_{ij} v_j^{\frac{1}{2}}(\boldsymbol{q}) M^j_{L_4,L_2}(\boldsymbol{q}), \quad (5.13)$$

where we omit the index $\boldsymbol{R}$ to make the notations shorter. An example of such on-site interaction is given by the intra-orbital interaction, which corresponds to the energy cost for the double electronic occupation of an orbital m.

Off-site interactions

We restrict the off-site Coulomb repulsion between electrons to the neighboring unit cells defined by $\boldsymbol{R}_1 = \boldsymbol{R}_3 = \boldsymbol{R}$ and $\boldsymbol{R}_2 = \boldsymbol{R}_4 = \boldsymbol{0}$. The expression 5.10 leads to :

$$U^{\text{off-site},\boldsymbol{R}}_{L_1L_2L_3L_4}(\omega) = \frac{1}{\mathcal{N}}\sum_{\boldsymbol{q}} e^{i\boldsymbol{q}\cdot\boldsymbol{R}}\sum_{ij}[M^i_{L_1\boldsymbol{R},L_3\boldsymbol{R}}(\boldsymbol{q})]^* v_i^{\frac{1}{2}}(\boldsymbol{q})[\varepsilon^r(\boldsymbol{q},\omega)]^{-1}_{ij} v_j^{\frac{1}{2}}(\boldsymbol{q}) M^j_{L_4\boldsymbol{0},L_2\boldsymbol{0}}(\boldsymbol{q}). \quad (5.14)$$

The phase factor includes the relative distance $\boldsymbol{R}$ between the unit cells. Such parameters would be necessary for an extended model which deals with the nearest-neighbor and next-nearest-neighbor interactions for example.

5.1.3 Fully screened W and unscreened (bare) v

$W^{\boldsymbol{R}_1\boldsymbol{R}_2\boldsymbol{R}_3\boldsymbol{R}_4}_{L_1L_2L_3L_4}(\omega)$: general expression

The matrix elements of W in the Wannier basis $\{|\phi_{L\boldsymbol{R}}\phi_{L'\boldsymbol{R}'}\rangle\}$ are defined in a similar manner than for W^r. The difference is that the whole screening of the bare repulsion has to be taken into account. The total symmetrized dielectric function, ε, has therefore to be employed.

It follows that $W^{\boldsymbol{R}_1\boldsymbol{R}_2\boldsymbol{R}_3\boldsymbol{R}_4}_{L_1L_2L_3L_4}(\omega) = \langle\phi_{L_1\boldsymbol{R}_1}\phi_{L_2\boldsymbol{R}_2}|W|\phi_{L_3\boldsymbol{R}_3}\phi_{L_4\boldsymbol{R}_4}\rangle$:

$$W^{\boldsymbol{R}_1\boldsymbol{R}_2\boldsymbol{R}_3\boldsymbol{R}_4}_{L_1L_2L_3L_4}(\omega) = \frac{1}{\mathcal{N}}\sum_{\boldsymbol{q}} e^{i\boldsymbol{q}\cdot(\boldsymbol{R}_3-\boldsymbol{R}_2)}\sum_{ij}[M^i_{L_1\boldsymbol{R}_1,L_3\boldsymbol{R}_3}(\boldsymbol{q})]^* v_i^{\frac{1}{2}}(\boldsymbol{q})\varepsilon^{-1}_{ij}(\boldsymbol{q},\omega) v_j^{\frac{1}{2}}(\boldsymbol{q}) M^j_{L_4\boldsymbol{R}_4,L_2\boldsymbol{R}_2}(\boldsymbol{q}). \quad (5.15)$$

$v^{\boldsymbol{R}_1\boldsymbol{R}_2\boldsymbol{R}_3\boldsymbol{R}_4}_{L_1L_2L_3L_4}$: general expression

For the unscreened (bare) Coulomb v, there is no screening at all. The dielectric function has to be replaced by the identity. v is therefore not frequency-dependent as W^r and W. The matrix

elements $v^{\boldsymbol{R}_1\boldsymbol{R}_2\boldsymbol{R}_3\boldsymbol{R}_4}_{L_1L_2L_3L_4} = \langle \phi_{L_1\boldsymbol{R}_1}\phi_{L_2\boldsymbol{R}_2}|v|\phi_{L_3\boldsymbol{R}_3}\phi_{L_4\boldsymbol{R}_4}\rangle$ read as :

$$v^{\boldsymbol{R}_1\boldsymbol{R}_2\boldsymbol{R}_3\boldsymbol{R}_4}_{L_1L_2L_3L_4} = \frac{1}{\mathcal{N}}\sum_{\boldsymbol{q}} \mathrm{e}^{i\boldsymbol{q}\cdot(\boldsymbol{R}_3-\boldsymbol{R}_2)} \sum_{ij} [M^i_{L_1\boldsymbol{R}_1,L_3\boldsymbol{R}_3}(\boldsymbol{q})]^* v_i^{\frac{1}{2}}(\boldsymbol{q}) v_j^{\frac{1}{2}}(\boldsymbol{q}) M^j_{4\boldsymbol{R}_4,L_2\boldsymbol{R}_2}(\boldsymbol{q}). \tag{5.16}$$

$M^i_{L\boldsymbol{R},L'\boldsymbol{R}'}(\boldsymbol{q})$ quantities were defined in Eq. 5.11.

5.1.4 What about metallic transitions?

Metallic systems are characterized by the existence of a Drude singularity when the frequency tends to zero. Such Drude peak is observed in all metallic response functions, like electrical conductivity, optics or dielectric function. Practically, one gets a Drude peak when $\boldsymbol{q} \to 0$ and $\omega \to 0$: the metallic transitions then fully screen the long-range part of the Coulomb repulsion.

This point is enlightened below with the total dielectric function ε expanded into the product mixed basis. [1]
One first notes that the product mixed basis (labeled by (i,j) indices) does not have a straightforward physical interpretation, in contrast to the plane wave basis. We have to admit for the moment the following decomposition into the product mixed basis of the symmetrized dielectric function in the $\boldsymbol{q} \to 0$ limit (see Eq. 5.40 and Appendix C for details) :

$$\varepsilon_{ij}(\boldsymbol{q}\to 0,\omega) = \left(\begin{array}{c|c} \varepsilon^H(\omega) = \varepsilon_{\boldsymbol{G}=0,\boldsymbol{G}'=0}(\omega) & \varepsilon^{W_1}_{0j}(\omega) \\ \hline \varepsilon^{W_2}_{i0}(\omega) & \varepsilon^B_{i\neq 0,j\neq 0}(\omega) \end{array}\right)$$

Only the $i = j = 0$ component has a clear interpretation as it equals the dielectric function $\varepsilon_{\boldsymbol{G}=0,\boldsymbol{G}'=0}$ in the plane wave basis with infinite wavelength corresponding to the long-range screening. Using a standard block-wise inversion, we can compute the inverse of the dielectric function, as it is required by the Dyson-like equation (Eq. 2.20 in Hedin's equations or Fig. 1.4) :

$$\varepsilon^{-1}_{ij}(\boldsymbol{q}\to 0,\omega) = \left(\begin{array}{c|c} [\varepsilon_H - \varepsilon_{W_1}\cdot\varepsilon_B^{-1}\cdot\varepsilon_{W_2}]^{-1} \equiv \text{headinv} & -\text{headinv}\cdot\varepsilon_{W_1}\cdot\varepsilon_B^{-1} \\ \hline -\varepsilon_B^{-1}\cdot\varepsilon_{W_2}\cdot\text{headinv} & \varepsilon_B^{-1} + \varepsilon_B^{-1}\cdot\varepsilon_{W_2}\cdot\text{headinv}\cdot\varepsilon_{W_1}\cdot\varepsilon_B^{-1} \end{array}\right)$$

For a metallic system and in the static limit $\omega \to 0$, we can show that $\varepsilon^H \to \infty$ because of some intra-band transitions (Eq. 5.41). This makes the scalar $\varepsilon^{-1}_{00}(0,0)$ going to zero. It thus simplifies the inverse dielectric function as follows :

$$\varepsilon^{-1}_{ij}(\boldsymbol{q}\to 0,\omega\to 0) \sim \left(\begin{array}{c|c} 0 & 0 \\ \hline 0 & \varepsilon_B^{-1} \end{array}\right) \tag{5.17}$$

[1] It would be absolutely equivalent for the partial dielectric function ε^r that leads to U.

From this expression, we deduce that the static long-range part of the bare Coulomb repulsion $v_{i=0,j=0}$ is canceled out by the metallic screening contained in $\varepsilon^{-1}_{00} \approx 0$. Only a short-range repulsion can then subsist for metallic systems. We had rather similar conclusions when we calculated the Yukawa-like screened interaction W^{RPA} for an homogeneous electron gas (Eq. 1.18).

In the following section, we add technical details about the derivation of $U^{\boldsymbol{R}_1\boldsymbol{R}_2\boldsymbol{R}_3\boldsymbol{R}_4}_{L_1L_2L_3L_4}(\omega)$ *within the (L)APW+lo framework.*

5.1.5 Technical details

The total polarization P and the restricted polarizations P^d, P^r

As already mentioned, a product basis is well-adapted for expanding the polarization P and interactions v, W and $W^r = U$. This is usually done in GW implementations [Aryasetiawan and Gunnarsson(1998)]. Defining $\Phi_{n\boldsymbol{k},n'\boldsymbol{k}'}(\boldsymbol{r}) = \psi_{n\boldsymbol{k}}(\boldsymbol{r})\psi^*_{n'\boldsymbol{k}'}(\boldsymbol{r})$ as a product of Bloch wavefunctions, the total polarization reads as :

$$P(\boldsymbol{r},\boldsymbol{r}';\omega) = \sum_{n}^{\text{occ}}\sum_{n'}^{\text{unocc}}\sum_{\boldsymbol{k},\boldsymbol{k}'}\Phi_{n\boldsymbol{k},n'\boldsymbol{k}'}(\boldsymbol{r})\Phi^*_{n\boldsymbol{k}\,n'\boldsymbol{k}'}(\boldsymbol{r}')\Big(\frac{1}{\omega-\omega_{n\boldsymbol{k},n'\boldsymbol{k}'}+i\eta}-\frac{1}{\omega+\omega_{n\boldsymbol{k},n'\boldsymbol{k}'}-i\eta}\Big). \tag{5.18}$$

The product function $\Phi_{n\boldsymbol{k},n'\boldsymbol{k}'}(\boldsymbol{r})$ is still a Bloch function, but with the wavevector $\boldsymbol{k}-\boldsymbol{k}'$:

$$\begin{aligned}\Phi_{n\boldsymbol{k},n'\boldsymbol{k}'}(\boldsymbol{r}+\boldsymbol{R}) &= \psi_{\boldsymbol{k}n}(\boldsymbol{r}+\boldsymbol{R})\psi^*_{\boldsymbol{k}'n'}(\boldsymbol{r}+\boldsymbol{R})\\ &= \mathrm{e}^{i(\boldsymbol{k}-\boldsymbol{k}')\cdot\boldsymbol{R}}\psi_{\boldsymbol{k}n}(\boldsymbol{r})\psi^*_{\boldsymbol{k}'n'}(\boldsymbol{r})\\ &= \mathrm{e}^{i(\boldsymbol{k}-\boldsymbol{k}')\cdot\boldsymbol{R}}\Phi_{n\boldsymbol{k},n'\boldsymbol{k}'}(\boldsymbol{r}),\end{aligned} \tag{5.19}$$

and thus all quantities like the polarization can be expanded into an appropriate product mixed basis (like $\{\chi^{\boldsymbol{q}}_i(\boldsymbol{r})\}$ introduced in Eq. 5.8) as follows :

$$P(\boldsymbol{r},\boldsymbol{r}';\omega) = \frac{1}{\mathcal{N}}\sum_{\boldsymbol{q}}\sum_{ij}[\chi^{\boldsymbol{q}}_i(\boldsymbol{r})]^*P_{ij}(\boldsymbol{q},\omega)\chi^{\boldsymbol{q}}_j(\boldsymbol{r}'), \tag{5.20}$$

where the sum over the vectors $\boldsymbol{q}$ is performed over the first Brillouin zone. The polarization matrix elements in the product basis, P_{ij}, read as :

$$P_{ij}(\boldsymbol{q},\omega) = \frac{1}{\mathcal{N}}\sum_{\boldsymbol{k}}\sum_{n}^{\text{occ}}\sum_{n'}^{\text{unocc}}M^i_{nn'}(\boldsymbol{k},\boldsymbol{q})F_{nn'\boldsymbol{k}}(\boldsymbol{q},\omega)[M^j_{nn'}(\boldsymbol{k},\boldsymbol{q})]^*, \tag{5.21}$$

where we have introduced the overlap between the Bloch wavefunctions (or Kohn-Sham eigenstates in practice) and the product mixed basis functions, $M^i_{nn'}(\boldsymbol{k},\boldsymbol{q})$:

$$M^i_{nn'}(\boldsymbol{k},\boldsymbol{q}) = \int_\Omega d\boldsymbol{r}\psi_{\boldsymbol{k}n}(\boldsymbol{r})[\chi^{\boldsymbol{q}}_i(\boldsymbol{r})\psi_{\boldsymbol{k}-\boldsymbol{q},n'}(\boldsymbol{r})]^*, \tag{5.22}$$

and the following quantities :

$$\omega_{n\boldsymbol{k},n'\boldsymbol{k}-\boldsymbol{q}} = \epsilon_{n'\boldsymbol{k}-\boldsymbol{q}} - \epsilon_{n\boldsymbol{k}} \tag{5.23}$$

$$F_{nn'\boldsymbol{k}}(\boldsymbol{q},\omega) = \frac{1}{\omega - \omega_{n\boldsymbol{k},n'\boldsymbol{k}-\boldsymbol{q}} + i\eta} - \frac{1}{\omega + \omega_{n\boldsymbol{k},n'\boldsymbol{k}-\boldsymbol{q}} - i\eta}. \tag{5.24}$$

As a remark, we note that when using the Matsubara frequencies, the occupied to unoccupied transitions in $F_{nn'\boldsymbol{k}}(\boldsymbol{q}, i\nu)$ simplify as follows :

$$F_{nn'\boldsymbol{k}}(\boldsymbol{q}, i\nu) = \frac{-2\omega_{n\boldsymbol{k},n'\boldsymbol{k}-\boldsymbol{q}}}{\nu^2 + \omega^2_{n\boldsymbol{k},n'\boldsymbol{k}-\boldsymbol{q}}}. \tag{5.25}$$

Assuming for the moment that the correlated subspace $\mathcal{C}$ is unambiguously defined since the correlated bands do not energetically overlap with the itinerant ones, we can define the d-restricted polarization P^d (Eq. 4.5) expanded into the product mixed basis :

$$P^d_{ij}(\boldsymbol{q},\omega) = \frac{1}{\mathcal{N}} \sum_{\boldsymbol{k}} \sum_{d}^{\text{occ}} \sum_{d'}^{\text{unocc}} M^i_{dd'}(\boldsymbol{k},\boldsymbol{q}) F_{dd'\boldsymbol{k}}(\boldsymbol{q},\omega) [M^j_{dd'}(\boldsymbol{k},\boldsymbol{q})]^*, \tag{5.26}$$

and hence for the constrained polarization P^r :

$$P^r_{ij}(\boldsymbol{q},\omega) = P_{ij}(\boldsymbol{q},\omega) - P^d_{ij}(\boldsymbol{q},\omega). \tag{5.27}$$

The total and restricted dielectric functions ε and ε^r

The total dielectric function ϵ is defined in the reciprocal space by :

$$\epsilon(\boldsymbol{q},\omega) = 1 - v(\boldsymbol{q}) P(\boldsymbol{q},\omega). \tag{5.28}$$

When performing calculations in GW or in cRPA, it is more convenient to make use of a symmetrized dielectric function ε that has the same eigenvalues as ϵ but simplifies the $\boldsymbol{q} \to 0$ limit [Jiang *et al.* (2012)] :

$$\varepsilon(\boldsymbol{q},\omega) \equiv v^{-\frac{1}{2}}(\boldsymbol{q}) \epsilon(\boldsymbol{q},\omega) v^{\frac{1}{2}}(\boldsymbol{q}). \tag{5.29}$$

In the following, ε will be referred as the dielectric function in order to make the notations shorter. v in the product mixed basis is diagonal by construction of this basis. It implies for the total ε :

$$\begin{aligned} \varepsilon_{ij}(\boldsymbol{q},\omega) &= \delta_{ij} - v_i^{\frac{1}{2}}(\boldsymbol{q}) P_{ij}(\boldsymbol{q},\omega) v_j^{\frac{1}{2}}(\boldsymbol{q}) \\ &= \delta_{ij} - \frac{1}{\mathcal{N}} \sum_{\boldsymbol{k}} \sum_{n}^{\text{occ}} \sum_{n'}^{\text{unocc}} v_i^{\frac{1}{2}}(\boldsymbol{q}) M^i_{nn'}(\boldsymbol{k},\boldsymbol{q}) F_{nn'\boldsymbol{k}}(\boldsymbol{q},\omega) [v_j^{\frac{1}{2}}(\boldsymbol{q}) M^j_{nn'}(\boldsymbol{k},\boldsymbol{q})]^*. \end{aligned} \tag{5.30}$$

In an equivalent way, one can define the function $\kappa^d \equiv -v^{\frac{1}{2}} P^d v^{\frac{1}{2}}$ that relies on the d-restricted polarization :

$$\kappa^d_{ij}(\boldsymbol{q},\omega) = -v_i^{\frac{1}{2}}(\boldsymbol{q}) P^d_{ij}(\boldsymbol{q},\omega) v_j^{\frac{1}{2}}(\boldsymbol{q}). \tag{5.31}$$

The *constrained* dielectric function ε^r reads as

$$\varepsilon^r_{ij}(\boldsymbol{q},\omega) = \varepsilon_{ij}(\boldsymbol{q},\omega) - \kappa^d_{ij}(\boldsymbol{q},\omega) \tag{5.32}$$

$$= \delta_{ij} - v_i^{\frac{1}{2}}(\boldsymbol{q}) P^r_{ij}(\boldsymbol{q},\omega) v_j^{\frac{1}{2}}(\boldsymbol{q}). \tag{5.33}$$

The screened interactions W and W^r

From the Dyson-like equation for the screened interaction (Eq. 2.20 in Hedin's equations and Eq. 2.28 in the GW method), it follows for W, W^r in the product mixed basis :

$$W_{ij}(\boldsymbol{q},\omega) = v_i^{\frac{1}{2}}(\boldsymbol{q}) \varepsilon^{-1}_{ij}(\boldsymbol{q},\omega) v_j^{\frac{1}{2}}(\boldsymbol{q}) \tag{5.34}$$

$$W^r_{ij}(\boldsymbol{q},\omega) = v_i^{\frac{1}{2}}(\boldsymbol{q}) [\varepsilon^r(\boldsymbol{q},\omega)]^{-1}_{ij} v_j^{\frac{1}{2}}(\boldsymbol{q}). \tag{5.35}$$

In the cRPA method, the Hubbard interactions are interpreted as the matrix elements of W^r expanded into a localized basis (see Chapter 4). Atomic projected functions can be promoted to Wannier functions as recently implemented in WIEN2K by [Aichhorn *et al.* (2009)] in the context of LDA+DMFT. We therefore need the projectors $P_{Ln}(\boldsymbol{k})$ (Eq. 3.17) that connect the Kohn-Sham eigenstates $\psi_{\boldsymbol{k}n}(\boldsymbol{r})$ within a given energy window $\mathbb{W}$, to the Wannier orbitals $\phi_{\boldsymbol{R}L}(\boldsymbol{r})$ spanning the correlated subspace, $\mathcal{C}$. In passing, we point out here the consistency of our implementation : everything from the Wannier implementation to the cRPA implementation relies on the same electronic structure code. In addition, this also makes truly consistent the combination of cRPA with LDA+DMFT (see Chapter 8 for applications).

We remind the reader our definition $U^{\boldsymbol{R}_1\boldsymbol{R}_2\boldsymbol{R}_3\boldsymbol{R}_4}_{L_1L_2L_3L_4} = \langle \phi_{\boldsymbol{R}_1 L_1} \phi_{\boldsymbol{R}_2 L_2} | W^r | \phi_{\boldsymbol{R}_3 L_3} \phi_{\boldsymbol{R}_4 L_4} \rangle$ (Eq. 5.10). The Wannier functions can be Fourier transformed (Eq. 1.2). We then get :

$$U^{\boldsymbol{R}_1\boldsymbol{R}_2\boldsymbol{R}_3\boldsymbol{R}_4}_{L_1L_2L_3L_4}(\omega) = \frac{1}{\mathcal{N}^2} \sum_{\boldsymbol{k}_1\boldsymbol{k}_2\boldsymbol{k}_3\boldsymbol{k}_4} \mathrm{e}^{i(\boldsymbol{k}_1\cdot\boldsymbol{R}_1 + \boldsymbol{k}_2\cdot\boldsymbol{R}_2 - \boldsymbol{k}_3\cdot\boldsymbol{R}_3 - \boldsymbol{k}_4\cdot\boldsymbol{R}_4)} \langle \phi_{\boldsymbol{k}_1 L_1} \phi_{\boldsymbol{k}_2 L_2} | W^r | \phi_{\boldsymbol{k}_3 L_3} \phi_{\boldsymbol{k}_4 L_4} \rangle. \tag{5.36}$$

At this step, the projectors $P_{Ln}(\boldsymbol{k})$ can be introduced. They lead to the matrix elements of W^r in a product Kohn-Sham representation $|\psi_{\boldsymbol{k}n}\psi_{\boldsymbol{k}'n'}\rangle$:

$$U^{\boldsymbol{R}_1\boldsymbol{R}_2\boldsymbol{R}_3\boldsymbol{R}_4}_{L_1L_2L_3L_4}(\omega) = \frac{1}{\mathcal{N}^2} \sum_{\boldsymbol{k}_1\boldsymbol{k}_2\boldsymbol{k}_3\boldsymbol{k}_4} \mathrm{e}^{i(\boldsymbol{k}_1\cdot\boldsymbol{R}_1 + \boldsymbol{k}_2\cdot\boldsymbol{R}_2 - \boldsymbol{k}_3\cdot\boldsymbol{R}_3 - \boldsymbol{k}_4\cdot\boldsymbol{R}_4)}$$
$$\times \sum_{n_1n_2n_3n_4} P_{L_1n_1}(\boldsymbol{k}_1) [P_{L_3n_3}(\boldsymbol{k}_3)]^* \langle \psi_{\boldsymbol{k}_1 n_1} \psi_{\boldsymbol{k}_2 n_2} | W^r | \psi_{\boldsymbol{k}_3 n_3} \psi_{\boldsymbol{k}_4 n_4} \rangle [P_{L_4n_4}(\boldsymbol{k}_4)]^* P_{L_2n_2}(\boldsymbol{k}_2), \tag{5.37}$$

where the sum over (n_1, n_2, n_3, n_4) indices is restricted, by construction, to the Kohn-Sham states that are included in $\mathbb{W}$ at a given $\boldsymbol{k}$ point. The product Kohn-Sham representation of W^r can be expanded into the product mixed basis *via* the overlap quantities $M^i_{nn'}(\boldsymbol{k}, \boldsymbol{q})$ (Eq. 5.22) :

$$\langle \psi_{\boldsymbol{k}_1 n_1} \psi_{\boldsymbol{k}_2 n_2} | W^r | \psi_{\boldsymbol{k}_3 n_3} \psi_{\boldsymbol{k}_4 n_4} \rangle = \frac{1}{\mathcal{N}} \sum_{\boldsymbol{q}} \sum_{ij} [M^i_{n_1 n_3}(\boldsymbol{k}_1, \boldsymbol{q})]^* W^r_{ij}(\boldsymbol{q}, \omega) M^j_{n_4 n_2}(\boldsymbol{k}_4, \boldsymbol{q}) \delta_{\boldsymbol{k}_3, \boldsymbol{k}_1 - \boldsymbol{q}} \delta_{\boldsymbol{k}_2, \boldsymbol{k}_4 - \boldsymbol{q}}. \tag{5.38}$$

When inserting Eq. 5.38 into Eq. 5.37, it follows for the Hubbard interactions :

$$\begin{aligned} U^{\boldsymbol{R}_1 \boldsymbol{R}_2 \boldsymbol{R}_3 \boldsymbol{R}_4}_{L_1 L_2 L_3 L_4}(\omega) &= \frac{1}{\mathcal{N}} \sum_{\boldsymbol{q}} \mathrm{e}^{i\boldsymbol{q}\cdot(\boldsymbol{R}_3 - \boldsymbol{R}_2)} \sum_{ij} W^r_{ij}(\boldsymbol{q}, \omega) \\ &\times \frac{1}{\mathcal{N}} \sum_{\boldsymbol{k}_1} \mathrm{e}^{i\boldsymbol{k}_1\cdot(\boldsymbol{R}_1 - \boldsymbol{R}_3)} \Big(\sum_{n_1 n_3} P_{L_1 n_1}(\boldsymbol{k}_1) [M^i_{n_1 n_3}(\boldsymbol{k}_1, \boldsymbol{q}) P_{L_3 n_3}(\boldsymbol{k}_1 - \boldsymbol{q})]^* \Big) \\ &\times \frac{1}{\mathcal{N}} \sum_{\boldsymbol{k}_2} \mathrm{e}^{-i\boldsymbol{k}_2\cdot(\boldsymbol{R}_4 - \boldsymbol{R}_2)} \Big(\sum_{n_2 n_4} [P_{L_4 n_4}(\boldsymbol{k}_2)]^* P_{L_2 n_2}(\boldsymbol{k}_2 - \boldsymbol{q}) M^j_{n_4 n_2}(\boldsymbol{k}_2, \boldsymbol{q}) \Big) \\ &= \frac{1}{\mathcal{N}} \sum_{\boldsymbol{q}} \mathrm{e}^{i\boldsymbol{q}\cdot(\boldsymbol{R}_3 - \boldsymbol{R}_2)} \sum_{ij} [M^i_{L_1 \boldsymbol{R}_1, L_3 \boldsymbol{R}_3}(\boldsymbol{q})]^* W^r_{ij}(\boldsymbol{q}, \omega) M^j_{L_4 \boldsymbol{R}_4, L_2 \boldsymbol{R}_2}(\boldsymbol{q}). \end{aligned} \tag{5.39}$$

The reader will recognize the relations 5.10 and 5.11 which were given at the beginning of this chapter.

The dielectric functions in the limit $\boldsymbol{q} \to 0$

A $\boldsymbol{q} \to 0$ singularity arises from v but can be ingeniously regularized in the total and constrained symmetrized dielectric functions [Gomez-Abal *et al.* (2008), Jiang *et al.* (2009), Li(2008)]. We proceed by expanding at $\boldsymbol{q} = 0$ the dielectric functions first into a plane wave basis and then by transforming back into the product mixed basis $\{\chi^0_i(\boldsymbol{r})\}$. More details are given in appendix C.

In the plane wave basis, the total symmetrized dielectric function can be divided into three terms around the singularity of $v_{\boldsymbol{G}\boldsymbol{G}'}(\boldsymbol{q} \to 0)$: [2]

$$\begin{aligned} &\varepsilon_{\boldsymbol{G}=0, \boldsymbol{G}'=0}(\boldsymbol{q} \to 0, \omega) \quad \text{head} \\ &\varepsilon_{\boldsymbol{G}\neq 0, \boldsymbol{G}'=0}(\boldsymbol{q} \to 0, \omega) \quad \text{wings} \\ &\varepsilon_{\boldsymbol{G}\neq 0, \boldsymbol{G}'\neq 0}(\boldsymbol{q} \to 0, \omega) \quad \text{body} \end{aligned}$$

Singularities are concentrated in the so called head and wings parts. An approach based on the $\boldsymbol{k} \cdot \boldsymbol{p}$ perturbation theory, where $\boldsymbol{p}$ refers to the momentum matrix, is appropriate for treating

[2] This would be absolutely equivalent for the partial dielectric function ε^r.

the divergences of $\varepsilon_{\boldsymbol{GG'}}(\boldsymbol{q} \to 0)$ [Ambrosch-Draxl and Sofo(2004)]. The divergence may have physical meaning on the other hand, as the metallic Drude peak can appear when $\omega \to 0$ due intra-band transitions of the head part at zero energy.

Transforming the dielectric function from the plane wave basis into the product mixed basis leads to (see Appendix C) :

$$\varepsilon_{ij}(\boldsymbol{q} \to 0, \omega) \quad = \quad \varepsilon_{ij}^{H}(\omega) + \varepsilon_{ij}^{W}(\omega) + \varepsilon_{ij}^{B}(\omega), \tag{5.40}$$

where ($\tilde{\delta_{ij}} \equiv 1 - \delta_{ij}$)

$$\varepsilon_{ij}^{H}(\omega) = \delta_{i0}\delta_{j0}\Bigg\{1 - \frac{4\pi}{\Omega\mathcal{N}} \lim_{\boldsymbol{q}\to 0} \sum_{\boldsymbol{k}} \Bigg(\sum_{n} \frac{-\delta(\epsilon_{n\boldsymbol{k}} - \epsilon_F)}{\omega^2} |\boldsymbol{p}_{nn\boldsymbol{k}} \cdot \boldsymbol{q}|^2 \tag{5.41}$$

$$+ \sum_{n\neq n'} F_{nn'\boldsymbol{k}}(0,\omega) |\frac{\boldsymbol{p}_{nn'k} \cdot \boldsymbol{q}}{\epsilon_{n\boldsymbol{k}} - \epsilon_{n'\boldsymbol{k}}}|^2 \Bigg) \Bigg\} \tag{5.42}$$

$$\varepsilon_{ij}^{W_1}(\omega) = -\tilde{\delta}_{i0}\delta_{j0}\sqrt{\frac{4\pi}{\Omega}}\frac{1}{\mathcal{N}} \lim_{\boldsymbol{q}\to 0} \sum_{\boldsymbol{k}} \sum_{n\neq n'} F_{nn'\boldsymbol{k}}(0,\omega) \frac{\boldsymbol{p}_{nn'\boldsymbol{k}} \cdot \boldsymbol{q}}{\epsilon_{n\boldsymbol{k}} - \epsilon_{n'\boldsymbol{k}}} \tilde{v}_i^{\frac{1}{2}} M_{nn'}^{i}(\boldsymbol{k}, 0) \tag{5.43}$$

$$\varepsilon_{ij}^{W_2}(\omega) = -\delta_{i0}\tilde{\delta}_{j0}\sqrt{\frac{4\pi}{\Omega}}\frac{1}{\mathcal{N}} \lim_{\boldsymbol{q}\to 0} \sum_{\boldsymbol{k}} \sum_{n\neq n'} F_{nn'\boldsymbol{k}}(0,\omega) \frac{\boldsymbol{p}_{nn'\boldsymbol{k}} \cdot \boldsymbol{q}}{\epsilon_{n\boldsymbol{k}} - \epsilon_{n'\boldsymbol{k}}} [\tilde{v}_j^{\frac{1}{2}} M_{nn'}^{j}(\boldsymbol{k}, 0)]^* \tag{5.44}$$

$$\varepsilon_{ij}^{B}(\omega) = \tilde{\delta}_{i0}\tilde{\delta}_{j0}\Big(\delta_{ij} - \frac{1}{\mathcal{N}} \sum_{\boldsymbol{k}} \sum_{n\neq n'} F_{nn'\boldsymbol{k}}(0,\omega) \tilde{v}_i^{\frac{1}{2}} M_{nn'}^{i}(\boldsymbol{k}, 0) [\tilde{v}_j^{\frac{1}{2}} M_{nn'}^{j}(\boldsymbol{k}, 0)]^*\Big). \tag{5.45}$$

We remind the reader that $p_{nn'\boldsymbol{k}} \equiv \langle \psi_{n\boldsymbol{k}} | p | \psi_{n'\boldsymbol{k}} \rangle$ are the momentum matrix elements, whereas $\tilde{v}_i$ are the eigenvalues of the regular Coulomb interaction defined in Eqs. 5.6 and 5.7.

The intra-band transitions in Eq. 5.41 lead to the Drude peak for metallic systems. The weight of this Drude peak increases with the density of states at the Fermi level. In a sense, one can see an analogy with the metallic screening in the homogeneous electron gas which makes the screened Coulomb interaction proportional to the inverse of the density of states at the Fermi level (see Chapter 1, Eq. 1.22).

The Γ point treatment in the Brillouin-Zone summation

According to Eq. 5.10, one needs to sum over the vectors $\boldsymbol{q}$ of the first Brillouin zone. This sum is integrable but the $\boldsymbol{q} \to 0$ limit again requires a careful treatment due to the behavior of $v(\boldsymbol{q} \to 0)$. According to Eqs. 5.7 and 5.9 within the product mixed basis :

$$v_{ij}^{\frac{1}{2}}(\boldsymbol{q} \to 0) = \left(\begin{array}{c|c} \frac{\sqrt{4\pi}}{|\boldsymbol{q}|} + \tilde{v}_0^{\frac{1}{2}} & 0 \\ \hline 0 & \tilde{v}_{i\neq 0}^{\frac{1}{2}} \end{array}\right)$$

In Appendix D, one can show that it follows for W^r :

$$W^r_{ij}(\boldsymbol{q}\to 0,\omega) = \frac{1}{|\boldsymbol{q}|^2}W^{rs2}_{ij}(\omega)+\frac{1}{|\boldsymbol{q}|}W^{rs1}_{ij}(\omega)+\tilde{W}^r_{ij}(\omega), \tag{5.46}$$

where ($\tilde{\delta}_{ij}\equiv 1-\delta_{ij}$)

$$W^{rs2}_{ij}(\omega) = 4\pi[\varepsilon^r(0,\omega)]^{-1}_{00}\delta_{i0}\delta_{j0} \tag{5.47}$$

$$W^{rs1}_{ij}(\omega) = \sqrt{4\pi}\Big\{\delta_{i0}[\varepsilon^r(0,\omega)]^{-1}_{0j}\tilde{v}^{\frac{1}{2}}_j\tilde{\delta}_{j0}+\tilde{\delta}_{i0}[\varepsilon^r(0,\omega)]^{-1}_{i0}\tilde{v}^{\frac{1}{2}}_i\delta_{j0}\Big\} \tag{5.48}$$

$$\tilde{W}^r_{ij}(\omega) = \tilde{v}^{\frac{1}{2}}_i[\varepsilon^r(0,\omega)]^{-1}_{ij}\tilde{v}^{\frac{1}{2}}_j. \tag{5.49}$$

The expressions of $\varepsilon^r_{ij}(\boldsymbol{q}=0,\omega)$ have been given earlier when replacing ε by ε^r in Eq. 5.40.

Once we have injected Eq. 5.46 into Eq. 5.39, the following expression for the Hubbard interactions is deduced, where $\lambda\equiv(L,\boldsymbol{R})$:

$$U^{\boldsymbol{R}_1\boldsymbol{R}_2\boldsymbol{R}_3\boldsymbol{R}_4}_{L_1L_2L_3L_4}(\omega) = \tilde{U}^{\boldsymbol{R}_1\boldsymbol{R}_2\boldsymbol{R}_3\boldsymbol{R}_4}_{L_1L_2L_3L_4}(\omega)+C_{s2}U^{s2}_{\lambda_1\lambda_2\lambda_3\lambda_4}(\omega)+C_{s1}U^{s1}_{\lambda_1\lambda_2\lambda_3\lambda_4}(\omega), \tag{5.50}$$

and

$$\tilde{U}^{\boldsymbol{R}_1\boldsymbol{R}_2\boldsymbol{R}_3\boldsymbol{R}_4}_{L_1L_2L_3L_4}(\omega) = \frac{1}{\mathcal{N}}\sum_{\boldsymbol{q}}\mathrm{e}^{i\boldsymbol{q}\cdot(\boldsymbol{R}_3-\boldsymbol{R}_2)}\sum_{ij}[M^i_{L_1\boldsymbol{R}_1,L_3\boldsymbol{R}_3}(\boldsymbol{q})]^*\tilde{v}^{\frac{1}{2}}_i(\boldsymbol{q})[\varepsilon^r(\boldsymbol{q},\omega)]^{-1}_{ij}\tilde{v}^{\frac{1}{2}}_j(\boldsymbol{q})M^j_{L_4\boldsymbol{R}_4,L_2\boldsymbol{R}_2}(\boldsymbol{q}) \tag{5.51}$$

$$U^{s2}_{\lambda_1\lambda_2\lambda_3\lambda_4}(\omega) = \frac{4\pi}{\Omega}[\varepsilon^r(0,\omega)]^{-1}_{00}\delta_{\lambda_1\lambda_3}\delta_{\lambda_4\lambda_2} \tag{5.52}$$

$$U^{s1}_{\lambda_1\lambda_2\lambda_3\lambda_4}(\omega) = \sqrt{\frac{4\pi}{\Omega}}\sum_{i\neq 0}\Big\{[\varepsilon^r(0,\omega)]^{-1}_{0i}M^i_{L_4\boldsymbol{R}_4,L_2\boldsymbol{R}_2}(0)\tilde{v}^{\frac{1}{2}}_i\delta_{\lambda_1\lambda_3}+[\varepsilon^r(0,\omega)]^{-1}_{i0}[M^i_{L_1\boldsymbol{R}_1,L_3\boldsymbol{R}_3}(0)]^*\tilde{v}^{\frac{1}{2}}_i\delta_{\lambda_4\lambda_2}\Big\} \tag{5.53}$$

The coefficients C_{s2}, C_{s1} come from traditional Brillouin-zone integrations of singular functions and are given in Appendix D.

In the following, we make use of a simplified notation $U_{m_1m_2m_3m_4}$ for the Hubbard interactions, where m replaces $(m, \alpha, \boldsymbol{R})$.

5.2 Coulomb interactions for low-energy Hamiltonians

The four-index interaction matrix $U_{m_1m_2m_3m_4}$ (Eq. 5.10) is the most general representation of the screened Coulomb interaction into a localized basis set : all density-density as well as non-density-density, intra as well as inter-orbital interactions are included. However, for further combination with a many-body solver, one needs to parametrize this matrix with a reasonable number of parameters. These parameters are then employed for reconstructing the interacting lattice Hamiltonian which has to be solved. For example, the t_{2g}-restricted Hubbard model is usually written in terms of only three Hubbard-Kanamori parameters, $\mathcal{U}, \mathcal{U}'$ and $\mathcal{J}$ and only two of them are independent in a perfect cubic symmetry because of the relation $\mathcal{U}' = \mathcal{U} - 2\mathcal{J}$ (see below and Appendix B for more details). These parameters have to be extracted from the matrix $U^{\text{cubic}}_{m_1m_2m_3m_4}$, as explained below. Another approach has to be considered for d-dp Hubbard Hamiltonians.
We develop an accurate parametrization of $U^{(\mathcal{S})}_{m_1m_2m_3m_4}$ that relies on an optimal set of calculated Slater integrals for d-dp Hamiltonians. Hubbard U and Hund's exchange J are introduced as function of these integrals (see also Appendix B for more details). Hubbard-Kanamori parameters for the parametrization of t_{2g}-t_{2g} Hamiltonians are introduced in a second time. Applications for oxides [Vaugier *et al.* (2012b)] and iron-based pnictides and chalcogenides [Vaugier *et al.* (2012a)] are treated in Chapter 6.

5.2.1 Slater integrals parametrization

Introduction

It is well-known that the Coulomb potential $v^{\text{at}}(\boldsymbol{r}, \boldsymbol{r}') = \frac{1}{|\boldsymbol{r}-\boldsymbol{r}'|}$ for an atom can be expanded in terms of Legendre polynomials (see as textbooks [Slater(1960), Sugano *et al.* (1970)]). It follows that :

$$v^{\text{at}}(\boldsymbol{r}, \boldsymbol{r}') = \sum_{k=0}^{\infty} \frac{4\pi}{2k+1} \frac{r_<^k}{r_>^{k+1}} \sum_{q=-k}^{k} Y_{kq}(\theta, \phi) Y^*_{kq}(\theta', \phi'), \tag{5.54}$$

where $r_<(r_>)$ is the lesser (greater) of $(|r|, |r'|)$ and $Y_{lm}(\theta, \phi)$ are spherical harmonics. Slater showed that the matrix elements of v^{at} in the spherical harmonic basis $\{\phi_m(\boldsymbol{r}) = R_{nl}(r)Y_{lm}(\theta, \phi)\}$ can be decomposed into an angular part with well-established numbers- namely the Racah-Wigner numbers- and a radial part which he expressed in terms of Slater integrals [Slater(1960),

Sugano *et al.* (1970)] :

$$v^{\text{at}}_{m_1m_2m_3m_4} \equiv \langle\phi_{m_1}\phi_{m_2}|\frac{1}{|\boldsymbol{r}-\boldsymbol{r}'|}|\phi_{m_3}\phi_{m_4}\rangle \tag{5.55}$$

$$= \sum_{k=0}^{2l}\alpha_k(m_1,m_2,m_3,m_4)\mathrm{F}^k_{\text{at}}, \tag{5.56}$$

where the indices m correspond to the angular quantum numbers. $\{\mathrm{F}^k_{\text{at}}\}$ are the *atomic* Slater integrals which are defined as follows :

$$\mathrm{F}^k_{\text{at}} = \int_0^\infty r^2dr\int_0^\infty r'^2dr'\frac{r^k_<}{r^{k+1}_>}R^2_{nl}(r)R^2_{nl}(r') \tag{5.57}$$

and α_k are the Racah-Wigner numbers :

$$\alpha_k(m_1,m_2,m_3,m_4) = \frac{4\pi}{2k+1}\sum_{q=-k}^{k}\langle Y_{lm_1}|Y_{kq}Y_{lm_3}\rangle\langle Y_{lm_2}Y_{kq}|Y_{lm_4}\rangle, \tag{5.58}$$

where $\langle Y_{l_1m_1}|Y_{l_2m_2}Y_{l_3m_3}\rangle$ corresponds to a Gaunt coefficient (see Appendix B for a more detailed introduction).

In the expansion of Eq. 5.56, one can show that only a finite number of Slater integrals are required, because the sphericity of the atom makes non-vanishing only a small subset of Racah-Wigner coefficients [Sugano *et al.* (1970)]. This number equals $l+1$, where l is the orbital quantum number : for d-shells, we therefore need only three Slater integrals ($\mathrm{F}^0_{\text{at}}, \mathrm{F}^2_{\text{at}}, \mathrm{F}^4_{\text{at}}$) and only four ($\mathrm{F}^0_{\text{at}}, \mathrm{F}^2_{\text{at}}, \mathrm{F}^4_{\text{at}}, \mathrm{F}^6_{\text{at}}$) for f-shells.

The Slater integral F^0_{at} corresponds to the monopole part of the Coulomb interaction : it is thus a quantity that notably varies with atomic shells. The Slater integrals with $k>0$ on the other hand, correspond to the multipole parts of the interaction. As a consequence, their ratio are weakly dependent on the atomic shells. An approximate value is usually known for the ratio $\mathrm{F}^4_{\text{at}}/\mathrm{F}^2_{\text{at}}$ in d-shells, as well as for the ratio $\mathrm{F}^6_{\text{at}}/\mathrm{F}^2_{\text{at}}$ in f-shells. With hydrogen-like wavefunctions, one gets approximately for these ratios [Anisimov *et al.* (1997a), Haverkort(2005)] :

$$\mathrm{F}^4_{\text{at}}/\mathrm{F}^2_{\text{at}} \approx 0.625 \quad (3d \text{ shells}) \tag{5.59}$$

$$\mathrm{F}^4_{\text{at}}/\mathrm{F}^2_{\text{at}} \approx 0.67,\ \mathrm{F}^6_{\text{at}}/\mathrm{F}^2_{\text{at}} \approx 0.49 \quad (4f \text{ shells}) \tag{5.60}$$

The values slightly depend on the principal quantum number n and on the oxidation state of the atom considered. An exhaustive list of atomic Slater integrals is given in [Haverkort(2005)].

Extension to solids

An extension of the Slater integrals to the effective screened Coulomb potential in solids is presented below. Screening, and Wannier orbitals instead of atomic wavefunctions, are major

differences between solids and atoms. However, one can still define a set of Slater integrals $\{\mathrm{F}^k\}$ for parametrizing the screened interaction matrix $U_{m_1m_2m_3m_4}$. The Slater integrals can then be employed as input parameters for many-body solvers in order to construct the interacting part of the lattice Hamiltonian in the appropriate symmetry of the crystal field.

A method based on a spherical average of $U^{(\mathcal{S})}_{m_1m_2m_3m_4}$ and on the atomic ratios (Eqs. 5.59 and 5.60), has been commonly employed in the past, e.g. [Anisimov *et al.* (1997a)]. A disadvantage of such method is that it employs only two independent parameters and relies on an atomic ratio whose validity is not well-controlled.

In the following, we develop another approach that consists in calculating *an optimal set* of Slater integrals from the interaction matrix $U^{(\text{spheric})}_{m_1m_2m_3m_4}$ within the Wannier local orbitals, $\{|\phi_{m,-2\leq m\leq 2}\rangle\}$ which are said "spheric". Indeed, such basis of the correlated subspace $\mathcal{C}$ contains all the d manifold. This explains why $U^{(\text{spheric})}_{m_1m_2m_3m_4}$ are denoted "spheric". The demonstration is given in Appendix B.

The main approximation of our approach consists in assuming that the relation 5.56 can be extended to solids with an angular part that is still expressed in terms of Racah-Wigner numbers (hence set by spherical harmonics combinations), but a radial part that is proper to solids and deduced from $U^{(\text{spheric})}_{m_1m_2m_3m_4}$:

$$U^{(\text{spheric})}_{m_1m_2m_3m_4} = \sum_{k=0}^{2l} \alpha_k(m_1,m_2,m_3,m_4)\mathrm{F}^k. \tag{5.61}$$

In Appendix B, we demonstrate that relation 5.61 can be inverted and the optimal set of Slater integrals $\{\mathrm{F}^k\}$ is obtained as follows :

$$\mathrm{F}^k(\omega) = \mathcal{C}_{l,k} \sum_{m_1,m_2,m_3,m_4} (-1)^{m_1+m_4} U^{(\text{spheric})}_{m_1m_2m_3m_4}(\omega) \begin{pmatrix} l & k & l \\ -m_1 & m_1-m_3 & m_3 \end{pmatrix} \begin{pmatrix} l & k & l \\ -m_2 & m_2-m_4 & m_4 \end{pmatrix}, \tag{5.62}$$

where the parentheses correspond to the Wigner 3j-symbols and the coefficients $\mathcal{C}_{l,k}$ are defined as follows :

$$\mathcal{C}_{l,k} = \frac{2k+1}{(2l+1)^2 \begin{pmatrix} l & k & l \\ 0 & 0 & 0 \end{pmatrix}^2}. \tag{5.63}$$

The frequency dependence of the Slater integrals arises from the frequency dependence of the interaction matrix elements induced by the dynamical screening (see Chapter 4). When using the Matsubara frequencies $(i\nu)$, $U^{(\text{spheric})}_{m_1m_2m_3m_4}(i\nu)$ as well as $\mathrm{F}^k(i\nu)$ are real numbers. (see also [Kutepov *et al.* (2010)] for an analogous expression of $\{\mathrm{F}^k\}$).

The Slater integrals $\mathrm{F}^k(\omega)$ can then be employed for building the Slater average interaction matrix $\bar{U}^{(\mathcal{S})}_{m_1m_2m_3m_4}(\omega)$ in the symmetry $\mathcal{S}$ of the crystal and ligand field (also the one that is

appropriate for the many-body solver) :

$$\bar{U}^{(\mathcal{S})}_{m_1m_2m_3m_4}(\omega) = \sum_{m'_1m'_2m'_3m'_4} \mathcal{S}_{m_1m'_1}\mathcal{S}_{m_2m'_2}\left\{\sum_{k=0}^{2l}\alpha_k(m'_1,m'_2,m'_3,m'_4)\mathrm{F}^k(\omega)\right\}\mathcal{S}^{-1}_{m'_3m_3}\mathcal{S}^{-1}_{m'_4m_4}. \tag{5.64}$$

Selecting $\mathcal{S}$ as the identity transformation leads to an evaluation of the efficiency of the parametrization since we can compare the reconstructed interaction matrix elements with the original ones. This will be discussed for $SrVO_3$ in Chapter 6. Since the Racah-Wigner numbers vanish for given spherical harmonics combinations, we are not able to reconstruct the entire interaction matrix. The non-vanishing interaction matrix elements to which we have access, are the reduced interactions such as $\bar{U}^{(\mathcal{S})}_{mm'mm'}$ and $\bar{U}^{(\mathcal{S})}_{mm'm'm}$.

Hubbard U and Hund's coupling J

The Hubbard U parameter is defined as the following average over all possible pairs (m,m') [Anisimov *et al.* (1993), Anisimov *et al.* (1997a)] :

$$U \equiv \frac{1}{(2l+1)^2}\sum_{mm'}\sum_{k=0}^{2l}\alpha_k(m,m',m,m')\mathrm{F}^k. \tag{5.65}$$

On the other hand, it follows for Hund's exchange J [Anisimov *et al.* (1993)] :

$$J \equiv \frac{1}{2l(2l+1)}\sum_{m\neq m'}\sum_{k}\alpha_k(m,m',m',m)\mathrm{F}^k. \tag{5.66}$$

In Appendix B, we show that both U and J can be deduced from the Slater integrals $\{\mathrm{F}^k\}$ as follows :

$$U = \mathrm{F}^0 \tag{5.67}$$

$$J = \frac{\mathrm{F}^2+\mathrm{F}^4}{14} \quad \text{for } d \text{ shells} \tag{5.68}$$

$$= \frac{286\mathrm{F}^2+195\mathrm{F}^4+250\mathrm{F}^6}{6435} \quad \text{for } f \text{ shells} \tag{5.69}$$

Interactions between t_{2g} orbitals within the d-dp Hamiltonian from the Slater parametrization

Within Eq. 5.64 (where $\mathcal{S}$ corresponds to the transformation from a spherical to a cubic orbital basis), one can deduce from the Slater integrals $\{\mathrm{F}^k\}$, a set of Hubbard interaction matrix elements with cubic symmetry for the t_{2g} and e_g subspaces and between t_{2g} and e_g. We will restrict

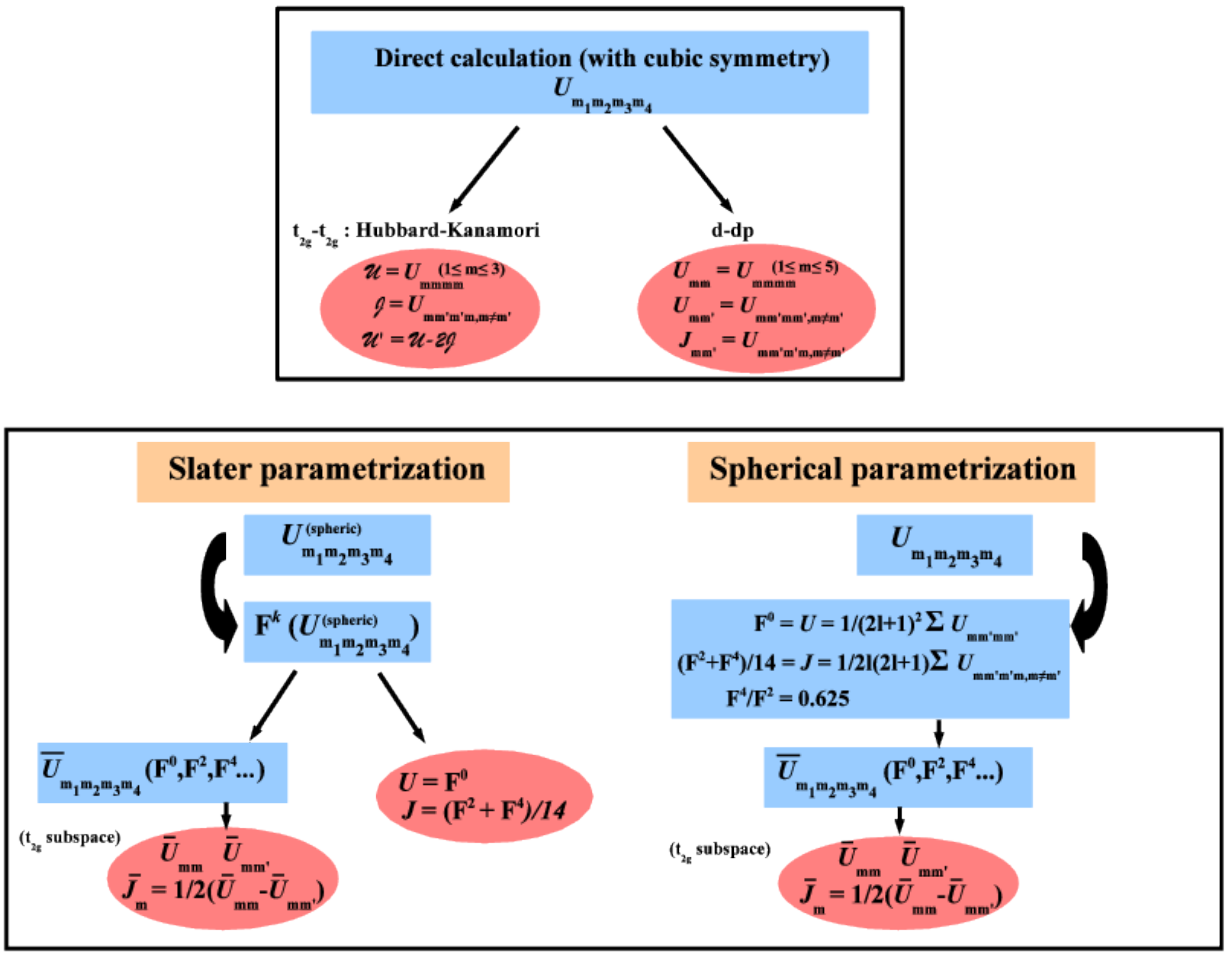

Figure 5.1: Schematic view for parametrizing the four-index Hubbard interaction matrix. (top panel) Direct calculation : Hubbard-Kanamori parameters within the t_{2g}-t_{2g} Hamiltonian, see Eqs. 5.75, 5.76 and 5.77. *d-dp* Hamiltonian, see Eqs 5.78 and 5.79. (bottom panel, left) Slater parametrization with the Slater integrals calculated with Eq. 5.62. Interactions between t_{2g} orbitals are deduced from Eqs. 5.70 and 5.71. (bottom, right) Spherical parametrization (see Eqs. 5.73 and 5.74). In this method, one needs to set the ratio F^4/F^2 to the empirical atomic value around 0.63 for $3d$ shells.

ourselves to the interactions between the t_{2g} orbitals for further comparison within the t_{2g}-t_{2g} Hamiltonian. In the case of cubic symmetry, they are defined as follows (see also Appendix B) :

$$\bar{U}_{mm} = \mathrm{F}^0 + \frac{4}{49}\mathrm{F}^2 + \frac{4}{49}\mathrm{F}^4 \tag{5.70}$$

$$\bar{U}_{mm'} = \mathrm{F}^0 - \frac{2}{49}\mathrm{F}^2 - \frac{4}{441}\mathrm{F}^4 \tag{5.71}$$

$$\bar{J}_m = \frac{1}{2}(\bar{U}_{mm} - \bar{U}_{mm'}) = \frac{3}{49}\mathrm{F}^2 + \frac{20}{441}\mathrm{F}^4 \tag{5.72}$$

Interactions between e_g orbitals or between t_{2g} and e_g orbitals can also be deduced from the Slater integrals (see Appendix B and [Sugano *et al.* (1970)]).

Interactions between t_{2g} orbitals within the d-dp Hamiltonian from a spherical parametrization

In the usual determination of the Slater integrals one finds in the literature [Anisimov *et al.* (1997a), Aichhorn *et al.* (2009)], one needs to refer to an empirical value of the ratio $\mathrm{F}^4/\mathrm{F}^2$ in order to deduce the complete set of Slater integrals. Starting with the spherical average of $U_{m_1m_2m_3m_4}$ in order to deduce the Hubbard U and Hund's exchange J, we get :

$$U = \frac{1}{(2l+1)^2}\sum_{mm'} U^{(\mathcal{S})}_{mm'mm'} \equiv \mathrm{F}^0 \tag{5.73}$$

$$J = \frac{1}{2l(2l+1)}\sum_{mm',m\neq m'} U^{(\mathcal{S})}_{mm'm'm} \equiv (\mathrm{F}^2+\mathrm{F}^4)/14, \tag{5.74}$$

This leads to F^0 and $(\mathrm{F}^2+\mathrm{F}^4)/14$ but one condition is still missing to get the whole set $\{\mathrm{F}^k\}$. The ratio $\mathrm{F}^4/\mathrm{F}^2$ is usually set to the atomic value around 0.63 for $3d$ shells.
Once we have $(\mathrm{F}^0,\mathrm{F}^2,\mathrm{F}^4)$, we are able to deduce values for the interactions between the t_{2g} orbitals *via* Eqs. 5.70, 5.71 and 5.72.

5.2.2 Hubbard-Kanamori parametrization

The Coulomb interaction matrix within the t_{2g}-t_{2g} Hamiltonian – hence with cubic symmetry – is fitted with Hubbard-Kanamori parameters instead of Slater integrals. The Hubbard-Kanamori parameters are defined as follows :

$$\mathcal{U} = \frac{1}{N}\sum_{m=1}^{N=3} U^{(\mathrm{cubic})}_{mmmm} \tag{5.75}$$

$$\mathcal{J} = \frac{1}{N(N-1)}\sum_{m\neq m'}^{N=3} U^{(\mathrm{cubic})}_{mm'm'm} \tag{5.76}$$

$$\mathcal{U}' = \frac{1}{N(N-1)}\sum_{m\neq m'}^{N=3} U^{(\mathrm{cubic})}_{mm'mm'} \tag{5.77}$$

With cubic symmetry, one easily verifies that $\mathcal{U}' = \mathcal{U} - 2\mathcal{J}$.

In Fig. 5.1, we have summarized the three methods that lead to effective interactions between t_{2g} orbitals, but with different choices of the one-body Hamiltonian. The comparison with the direct calculation for the d-dp Hamiltonian gives an estimation of the efficiency of the Slater and spherical parametrization methods (see Chapter 6 for application on $SrVO_3$).

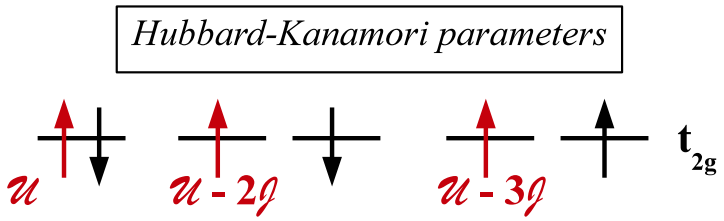

Figure 5.2: Hubbard-Kanamori interactions between t_{2g} orbitals with cubic symmetry.

5.2.3 Many-body interactions : application to the t_{2g}-t_{2g} and d-dp models

The reduced interaction matrices $U^{\sigma\sigma'}_{mm'}$ and $J_{mm'}$ with given symmetry $\mathcal{S}$ are defined as follows:

$$U^{\sigma\bar{\sigma}}_{mm'} \equiv U^{(\mathcal{S})}_{mm'mm'} = \langle \phi_{0m}\phi_{0m'}|W^r(0)|\phi_{0m}\phi_{0m'}\rangle \quad (5.78)$$

$$J_{mm'} \equiv U^{(\mathcal{S})}_{mm'm'm} = \langle \phi_{0m}\phi_{0m'}|W^r(0)|\phi_{0m'}\phi_{0m}\rangle \quad (5.79)$$

$$U^{\sigma\sigma}_{mm'} \equiv U^{(\mathcal{S})}_{mm'mm'} - J_{mm'}. \quad (5.80)$$

The interacting part of the multi-orbital Hubbard model (Eq. 1.10) reads

$$H_{\text{int}} = H_{\text{dens-dens}} + H_{\text{ndens-dens}}, \quad (5.81)$$

where the density-density ($H_{\text{dens-dens}}$) and the non-density-density ($H_{\text{ndens-dens}}$) terms for the correlated subspace $\mathcal{C}$ are defined as

$$H_{\text{dens-dens}} = \frac{1}{2}\sum_{mm'\in\mathcal{C},\sigma} U^{\sigma\sigma}_{mm'} n_{m\sigma} n_{m'\sigma} + \frac{1}{2}\sum_{mm'\in\mathcal{C}} U^{\sigma\bar{\sigma}}_{mm'}(n_{m\uparrow}n_{m'\downarrow} + n_{m\downarrow}n_{m'\uparrow}) \quad (5.82)$$

$$H_{\text{ndens-dens}} = -\frac{1}{2}\sum_{mm'\in\mathcal{C}} J_{mm'}(c^\dagger_{m\uparrow}c_{m\downarrow}c^\dagger_{m'\downarrow}c_{m'\uparrow} + \text{h.c.}) \quad \text{spin flip} \quad (5.83)$$

$$-\frac{1}{2}\sum_{mm'\in\mathcal{C}} J_{mm'}(c^\dagger_{m\uparrow}c^\dagger_{m\downarrow}c_{m'\uparrow}c_{m'\downarrow} + \text{h.c.}) \quad \text{pair hopping.} \quad (5.84)$$

We discuss below the t_{2g}-t_{2g} and d-dp models introduced in Chapter 4.

t_{2g}-t_{2g} Hamiltonian

In the t_{2g}-t_{2g} model, extended t_{2g} Wannier functions are constructed and e_g orbitals are not included in the low-energy Hamiltonian. We therefore can not calculate the set of Slater integrals within relation 5.62, since the spherical relations shown in Appendix B do not hold in this case. The Hubbard-Kanamori parameters $\mathcal{U}, \mathcal{J}, \mathcal{U}'$ (Eqs. 5.75, 5.76 and 5.77) have to be evaluated directly from the interaction matrix $U^{\text{(cubic)}}_{m_1 m_2 m_3 m_4}$ with cubic symmetry. With these parameters, we can build the interacting Hubbard model for the t_{2g} correlated subspace :

$$H^{t_{2g}}_{\text{int}} = \sum_{m \in \mathcal{C}} \mathcal{U}\, n_{m\uparrow} n_{m\downarrow} + \sum_{m > m' \in \mathcal{C}, \sigma} (\mathcal{U} - 2\mathcal{J})\, n_{m\sigma} n_{m'\bar{\sigma}} + (\mathcal{U} - 3\mathcal{J})\, n_{m\sigma} n_{m'\sigma} \quad (5.85)$$

$$- \mathcal{J}\, c^{\dagger}_{m\sigma} c_{m\bar{\sigma}} c^{\dagger}_{m'\bar{\sigma}} c_{m'\sigma} - \mathcal{J}\, c^{\dagger}_{m\sigma} c^{\dagger}_{m\bar{\sigma}} c_{m'\sigma} c_{m'\bar{\sigma}} \quad (5.86)$$

The exchange interaction $\mathcal{J}$ lowers the repulsion between electrons on two different orbitals. The inter-orbital interaction is hence implicitly spin-dependent : the Pauli exclusion principle induces a reduced repulsion between electrons with same spin.

d-dp Hamiltonian

The hybrid d-dp model is a direct application of the Slater integrals parametrization. Within the spherical-like Wannier functions representation, the Slater integrals $(\mathrm{F}^0, \mathrm{F}^2, \mathrm{F}^4)$ are deduced from Eq. 5.62. They are then employed as input parameters for the many-body solver in order to construct the interacting Hubbard Hamiltonian in the appropriate symmetry (Eq. 5.64).

5.3 The projection approach for entangled correlated bands

Until now, we have not explained how to compute the polarization P^d (Eq. 4.5), which is the total polarization but restricted to the correlated subspace $\mathcal{C}$. This is the aim of this section.

It may happen for some systems that the correlated *target* (e.g. d/f) states around the Fermi level do not energetically overlap with the other more itinerant ones. Cubic perovskite $SrVO_3$ (Fig. 4.4) displays such electronic structure : an energy window $\mathbb{W}_{t_{2g}}$ that only includes t_{2g}-like bands clearly emerges from e_g and p states. We already mentioned that a low-energy t_{2g}-t_{2g} model is appropriate for $SrVO_3$ (see Chapter 4). In this case, as the correlated subspace, $\mathcal{C}_{t_{2g}}$, equals the one generated with $\mathbb{W}_{t_{2g}}$, the projection transformation (introduced in Chapter 3, see Eq. 3.14) is a unitary transformation : for all $\boldsymbol{k}$'s in the Brillouin zone, the Kohn-Sham eigenstates within $\mathbb{W}_{t_{2g}}$ and the t_{2g} Wannier orbitals are in one to one correspondance. The restricted polarization P^d can be directly calculated in that case from Eq. 4.5 : band indices or an energy window can refer *without ambiguity* to the "correlated" Kohn-Sham states within $\mathbb{W}_{t_{2g}}$, in order to exclude from the total polarization only the transitions from occupied to empty t_{2g}. Such approach is denoted *the mask approach* (see also Fig. 4.5).

A majority of systems, however, are rather far away from this situation and prevent us from using the mask approach. For example, fcc nickel (Ni) (Fig. 6.8 and see also Fig. 4.8) displays a set of correlated d bands that are entangled with itinerant sp states. The d correlated subspace in this case, differs from the one constructed within any energy window. Referring only to the d states for constraining the polarization in RPA is hence not possible anymore within the mask approach. Nor is it clear how close to Wannier functions the localized orbitals built by the projection procedure (Eq. 3.14) are in that case. We will thus refer to these orbitals as localized orbitals instead of Wannier functions.
It becomes clear that such systems- said "entangled"- require a special care in order to apply the cRPA scheme. In Chapter 4, we already quoted two methods : one consists in a disentanglement of the correlated states [Miyake *et al.* (2009)] whereas the other is based on the evaluation of a density correlation function [Şaşıoğlu *et al.* (2011)]. Below, we propose to start from the polarization P^d that is obtained by the *projection of the total polarization into the correlated subspace*. Applications on $3d$ transition metals are given in Chapter 6.

5.3.1 The d-projected polarization P^d : definition

We remind the reader the definition 3.14 of the projector $\Pi_d^{\boldsymbol{k}}$ that projects a Kohn-Sham eigenstate $|\psi_{\boldsymbol{k}n}\rangle$ within an energy window $\mathbb{W}$ onto a localized state $|\phi_{\boldsymbol{k}m}^d\rangle$. Here, the index α for a correlated atom is replaced by d index as follows :

$$\Pi_d^{\boldsymbol{k}} = \sum_{m\in\mathcal{C}} |\phi_{\boldsymbol{k}m}^d\rangle\langle\phi_{\boldsymbol{k}m}^d|. \tag{5.87}$$

When applying this operation to the total Green's function $G(\boldsymbol{r},\boldsymbol{r}';\omega)$, it gives a definition of the Green's function G^d that is restricted to the correlated subspace $\mathcal{C}$:

$$G_d^0(\boldsymbol{r},\boldsymbol{r}';\omega) = \sum_{\boldsymbol{k}}\sum_{n\in\mathbb{W}} \frac{\langle\boldsymbol{r}|\Pi_d^{\boldsymbol{k}}\psi_{n\boldsymbol{k}}\rangle\langle\psi_{n\boldsymbol{k}}\Pi_d^{\boldsymbol{k}}|\boldsymbol{r}'\rangle}{\omega-\epsilon_{n\boldsymbol{k}}-i\eta\,\mathrm{sign}(\epsilon_F-\epsilon_{n\boldsymbol{k}})}. \tag{5.88}$$

The sum over the Kohn-Sham eigenstates labeled by n is limited to the energy window $\mathbb{W}$ by construction of the projectors. Within the definition $P^d \equiv G_d^0 G_d^0$ (Eq. 4.4), it follows that :

$$\begin{aligned} P^d(\boldsymbol{r},\boldsymbol{r}';\omega) = & \sum_{\boldsymbol{k},\,n\in\mathbb{W}}^{\text{occ}} \sum_{\boldsymbol{k}',\,n'\in\mathbb{W}}^{\text{unocc}} \langle\boldsymbol{r}|\Pi_d^{\boldsymbol{k}'}\psi_{n'\boldsymbol{k}'}\rangle\langle\psi_{n\boldsymbol{k}}\Pi_d^{\boldsymbol{k}}|\boldsymbol{r}\rangle\langle\boldsymbol{r}'|\Pi_d^{\boldsymbol{k}}\psi_{n\boldsymbol{k}}\rangle\langle\psi_{n'\boldsymbol{k}'}\Pi_d^{\boldsymbol{k}'}|\boldsymbol{r}'\rangle \\ & \times\left\{\frac{1}{\omega-\epsilon_{n'\boldsymbol{k}'}+\epsilon_{n\boldsymbol{k}}+i\eta}-\frac{1}{\omega+\epsilon_{n'\boldsymbol{k}'}-\epsilon_{n\boldsymbol{k}}-i\eta}\right\}. \end{aligned} \tag{5.89}$$

The correlated-restricted polarization thus involves the same Kohn-Sham energies $\epsilon_{n\boldsymbol{k}}$ as the total polarization. The projection only affects the Kohn-Sham wavefunctions by projecting them onto the localized subspace. Another interpretation of the formula 5.89 can be established within the introduction of the *modified Kohn-Sham functions* $|\tilde{\psi}_{\boldsymbol{k}n}\rangle$

$$|\tilde{\psi}_{\boldsymbol{k}n}\rangle \equiv \sum_{L\in\mathcal{C}} P_{Ln}(\boldsymbol{k})|\phi_{\boldsymbol{k}L}\rangle, \tag{5.90}$$

where $P_{Ln}(\boldsymbol{k})$ are the projectors onto the correlated subspace $\mathcal{C}$ (Eq. 3.17) with $L = (n, l, m, \alpha)$. Replacing the Kohn-Sham functions in the total polarization (Eq. 5.18) by these modified $\tilde{\psi}_{\boldsymbol{k}n}(\boldsymbol{r})$ leads to the polarization P^d that is equivalent to the d-projected polarization established above (Eq. 5.89)

$$\begin{aligned} P^d(\boldsymbol{r},\boldsymbol{r}';\omega) &= \sum_{\boldsymbol{k},\, n\in\mathbb{W}}^{\text{occ}} \sum_{\boldsymbol{k}',\, n'\in\mathbb{W}}^{\text{unocc}} \tilde{\psi}_{n'\boldsymbol{k}'}(\boldsymbol{r})\tilde{\psi}^*_{n\boldsymbol{k}}(\boldsymbol{r})\tilde{\psi}_{n\boldsymbol{k}}(\boldsymbol{r}')\tilde{\psi}^*_{n'\boldsymbol{k}'}(\boldsymbol{r}') \\ &\quad \times\left\{\frac{1}{\omega-\epsilon_{n'\boldsymbol{k}'}+\epsilon_{n\boldsymbol{k}}+i\eta}-\frac{1}{\omega+\epsilon_{n'\boldsymbol{k}'}-\epsilon_{n\boldsymbol{k}}-i\eta}\right\} \end{aligned} \tag{5.91}$$

The interpretation with *modified Kohn-Sham functions* will be useful when considering the $\boldsymbol{q}\to 0$ limit in our cRPA implementation. We may relate them to the original Kohn-Sham states by :

$$|\tilde{\psi}_{\boldsymbol{k}n}\rangle = \sum_{L\in\mathcal{C}}\sum_{n'\in\mathbb{W}} P_{Ln}(\boldsymbol{k})[P_{Ln'}(\boldsymbol{k})]^*|\psi_{\boldsymbol{k}n'}\rangle. \tag{5.92}$$

Bijective Wannier transformation

The Kohn-Sham states with correlated character lying on the energy window $\mathbb{W}$ are now supposed to be separated from the rest of the band structure. We thus consider here that they do not energetically overlap with itinerant states anymore. The projection procedure in this case is bijective and thus invertible. It is then straightforward to establish that :

$$\sum_{L\in\mathcal{C}} P_{Ln}(\boldsymbol{k})[P_{Ln'}(\boldsymbol{k})]^* = \delta_{nn'}. \tag{5.93}$$

Referring to Eq. 5.92, we identify $\tilde{\psi}_{\boldsymbol{k}n}(\boldsymbol{r})$ with the original Kohn-Sham functions $\psi_{\boldsymbol{k}n}(\boldsymbol{r})$. This leads back to Eq. 4.5 (see Chapter 4) :

$$\begin{aligned} P^d(\boldsymbol{r},\boldsymbol{r}';\omega) &= \sum_{\boldsymbol{k},\, n\in\mathbb{W}}^{\text{occ}} \sum_{\boldsymbol{k}',\, n'\in\mathbb{W}}^{\text{unocc}} \psi_{n'\boldsymbol{k}'}(\boldsymbol{r})\psi^*_{n\boldsymbol{k}}(\boldsymbol{r})\psi_{n\boldsymbol{k}}(\boldsymbol{r}')\psi^*_{n'\boldsymbol{k}'}(\boldsymbol{r}') \\ &\quad \times\left\{\frac{1}{\omega-\epsilon_{n'\boldsymbol{k}'}+\epsilon_{n\boldsymbol{k}}+i\eta}-\frac{1}{\omega+\epsilon_{n'\boldsymbol{k}'}-\epsilon_{n\boldsymbol{k}}-i\eta}\right\}. \end{aligned} \tag{5.94}$$

5.3.2 Formalism within (L)APW+lo

As mentioned in the introduction of this chapter, one needs to expand the polarization into the product mixed basis $\{\chi^{\boldsymbol{q}}_i(\boldsymbol{r})\}$. Using Eq. 5.20 but starting from Eq. 5.89, we get for $P^d_{ij}(\boldsymbol{q},\omega)$:

$$P^d_{ij}(\boldsymbol{q},\omega) = \frac{1}{\mathcal{N}}\sum_{\boldsymbol{k}}\sum_{n\in\mathbb{W}}^{\text{occ}}\sum_{n'\in\mathbb{W}}^{\text{unocc}} \tilde{M}^i_{nn'}(\boldsymbol{k},\boldsymbol{q})F_{nn'\boldsymbol{k}}(\boldsymbol{q},\omega)[\tilde{M}^j_{nn'}(\boldsymbol{k},\boldsymbol{q})]^*, \tag{5.95}$$

where we have introduced the quantity $\tilde{M}^i_{nn'}(\boldsymbol{k},\boldsymbol{q})$ which is similar to the overlap between the Kohn-Sham eigenstates and the product mixed basis, $M^i_{nn'}(\boldsymbol{k},\boldsymbol{q})$ (Eq. 5.22), but is now specific for the correlated subspace :

$$\tilde{M}^i_{nn'}(\boldsymbol{k},\boldsymbol{q}) \equiv \int_\Omega d\boldsymbol{r}\, \tilde{\psi}_{\boldsymbol{k}n}(\boldsymbol{r})[\chi^{\boldsymbol{q}}_i(\boldsymbol{r})\tilde{\psi}_{\boldsymbol{k}-\boldsymbol{q},n'}(\boldsymbol{r})]^* \tag{5.96}$$

$$= \sum_{L_1L_3\in\mathcal{C}} P_{L_1n}(\boldsymbol{k})\Big[\sum_{n_1n_3\in\mathbb{W}}[P_{L_1n_1}(\boldsymbol{k})]^* M^i_{n_1n_3}(\boldsymbol{k},\boldsymbol{q})P_{L_3n_3}(\boldsymbol{k}-\boldsymbol{q})\Big][P_{L_3n'}(\boldsymbol{k}-\boldsymbol{q})]^*. \tag{5.97}$$

It is then straightforward to compute the polarization $P^r_{ij} = P_{ij} - P^d_{ij}$ and the corresponding dielectric function $\varepsilon^r_{ij} = \varepsilon_{ij} - \kappa^d_{ij}$, following the cRPA scheme. We remind the reader that κ^d_{ij} is defined as (Eq. 5.31) :

$$\kappa^d_{ij}(\boldsymbol{q},\omega) \equiv -v^{\frac{1}{2}}_i(\boldsymbol{q})P^d_{ij}(\boldsymbol{q},\omega)v^{\frac{1}{2}}_j(\boldsymbol{q}). \tag{5.98}$$

Long wavelength $\boldsymbol{q}\to 0$ limit

As already mentioned in Section 5.1.5 dedicated to the technicalities, one needs to be careful with the $\boldsymbol{q}\to 0$ limit in the dielectric functions ϵ, ϵ^r and in the function κ^d. In a similar manner, head, wings and body parts in the plane wave basis within $\boldsymbol{k}\cdot\boldsymbol{p}$ perturbation theory are identified. The dielectric function is then transformed from the plane wave basis into the product mixed basis.

An important difference appears when considering the momentum matrix elements in the calculation of $\kappa^d_{ij}(\boldsymbol{q}\to 0,\omega)$: following the interpretation of P^d that involves the modified Kohn-Sham functions $\tilde{\psi}_{\boldsymbol{k}n}(\boldsymbol{r})$, we can build the *modified momentum matrix elements* $\tilde{\boldsymbol{p}}_{nn'\boldsymbol{k}}$ as follows :

$$\tilde{\boldsymbol{p}}_{nn'\boldsymbol{k}} \equiv \langle\tilde{\psi}_{\boldsymbol{k}n}|\boldsymbol{p}|\tilde{\psi}_{\boldsymbol{k}n'}\rangle \tag{5.99}$$

$$= \sum_{L_1L_3}[P_{L_1n}(\boldsymbol{k})]^*\Big[\sum_{n_1n_3} P_{L_1n_1}(\boldsymbol{k})\langle\psi_{\boldsymbol{k}n_1}|\boldsymbol{p}|\psi_{\boldsymbol{k}n_3}\rangle[P_{L_3n_3}(\boldsymbol{k})]^*\Big]P_{L_3n'}(\boldsymbol{k}). \tag{5.100}$$

Such expressions can be injected into the head and wings for κ^d, following Eqs. 5.41, 5.42 and 5.45. We get a set of equations that looks very similar to the one for the total dielectric

function, but with $\tilde{\boldsymbol{p}}_{nn'\boldsymbol{k}}$ instead of $\boldsymbol{p}_{nn'\boldsymbol{k}}$ and $\tilde{M}^i_{nn'}(\boldsymbol{k},\boldsymbol{q})$ instead of $M^i_{nn'}(\boldsymbol{k},\boldsymbol{q})$ ($\tilde{\delta_{ij}} \equiv 1-\delta_{ij}$) :

$$\kappa^{d,H}_{ij}(\omega) = -\delta_{i0}\delta_{j0}\frac{4\pi}{\Omega\mathcal{N}}\lim_{\boldsymbol{q}\to 0}\sum_{\boldsymbol{k}}\Big(\sum_{n\in\mathbb{W}}\frac{-\delta(\epsilon_{n\boldsymbol{k}}-\epsilon_F)}{\omega^2}|\tilde{\boldsymbol{p}}_{nn\boldsymbol{k}}\cdot\boldsymbol{q}|^2 \tag{5.101}$$

$$+\sum_{n\neq n'\in\mathbb{W}}F_{nn'\boldsymbol{k}}(0,\omega)|\frac{\tilde{\boldsymbol{p}}_{nn'k}\cdot\boldsymbol{q}}{\epsilon_{n\boldsymbol{k}}-\epsilon_{n'\boldsymbol{k}}}|^2\Big) \tag{5.102}$$

$$\kappa^{d,W_1}_{i,j}(\omega) = -\tilde{\delta}_{i0}\delta_{j0}\sqrt{\frac{4\pi}{\Omega}}\frac{1}{\mathcal{N}}\lim_{\boldsymbol{q}\to 0}\sum_{\boldsymbol{k}}\sum_{n\neq n'\in\mathbb{W}}F_{nn'\boldsymbol{k}}(0,\omega)\frac{\tilde{\boldsymbol{p}}_{nn'\boldsymbol{k}}\cdot\boldsymbol{q}}{\epsilon_{n\boldsymbol{k}}-\epsilon_{n'\boldsymbol{k}}}\tilde{v}_i^{\frac{1}{2}}\tilde{M}^i_{nn'}(\boldsymbol{k},0) \tag{5.103}$$

$$\kappa^{d,W_2}_{i,j}(\omega) = -\delta_{i0}\tilde{\delta}_{j0}\sqrt{\frac{4\pi}{\Omega}}\frac{1}{\mathcal{N}}\lim_{\boldsymbol{q}\to 0}\sum_{\boldsymbol{k}}\sum_{n\neq n'\in\mathbb{W}}F_{nn'\boldsymbol{k}}(0,\omega)\frac{\tilde{\boldsymbol{p}}_{nn'\boldsymbol{k}}\cdot\boldsymbol{q}}{\epsilon_{n\boldsymbol{k}}-\epsilon_{n'\boldsymbol{k}}}[\tilde{v}_j^{\frac{1}{2}}\tilde{M}^j_{nn'}(\boldsymbol{k},0)]^*$$

$$\kappa^{d,B}_{ij}(\omega) = -\tilde{\delta}_{i0}\tilde{\delta}_{j0}\frac{1}{\mathcal{N}}\sum_{\boldsymbol{k}}\sum_{n\neq n'\in\mathbb{W}}F_{nn'\boldsymbol{k}}(0,\omega)\tilde{v}_i^{\frac{1}{2}}\tilde{M}^i_{nn'}(\boldsymbol{k},0)[\tilde{v}_j^{\frac{1}{2}}\tilde{M}^j_{nn'}(\boldsymbol{k},0)]^*. \tag{5.104}$$

We focus in the next paragraph on the impact of the first term (Eq. 5.101) for metallic systems.

5.3.3 Metallic systems

We already mentioned at the beginning of this chapter that metallic systems are characterized by intra-orbital transitions at zero frequency that lead to a Drude singular peak in the response functions. Such transitions have been identified in the head part of the dielectric function (Eq. 5.41). The system considered now exhibits a band structure where the bands at the Fermi level have both a correlated (e.g. d) and an itinerant (e.g. sp) character. Within the cRPA method, we have to exclude from the polarization only the transitions between the correlated states.

Because of the strong hybridization between d and sp states, excluding only d-d transitions will *not necessarily* eliminate the metallicity. Indeed, the system can still have intra-band sp-sp or sp-d transitions at zero frequency, since the band has a mixed sp-d character. This again points out the inadequacy of band indices for constraining the RPA polarization within entangled systems.

A Drude peak in the partial dielectric function ε^r can be obtained but with a weight that has to be reduced with respect to the one we would obtain in the total dielectric function. The subtraction of the head part of ε (Eq. 5.41) with the head part of κ^d (Eq. 5.101) leads to the head of ε^r and hence :

$$\varepsilon^{r,H}_{ij}(\omega) = \delta_{i0}\delta_{j0}\Big\{1+\varepsilon^{r,\text{Drude}}(\omega)+\varepsilon^{r,inter}(\omega)\Big\}, \tag{5.105}$$

where

$$\varepsilon^{r,\text{Drude}}(\omega) = -\frac{4\pi}{\Omega\mathcal{N}} \lim_{\boldsymbol{q}\to 0} \sum_{\boldsymbol{k}} \sum_{n\in\mathbb{W}} \frac{-\delta(\epsilon_{n\boldsymbol{k}} - \epsilon_F)}{\omega^2} \left[|\boldsymbol{p}_{nn\boldsymbol{k}} \cdot \boldsymbol{q}|^2 - |\tilde{\boldsymbol{p}}_{nn\boldsymbol{k}} \cdot \boldsymbol{q}|^2 \right] \tag{5.106}$$

$$\begin{aligned} \varepsilon^{r,\text{inter}}(\omega) = -\frac{4\pi}{\Omega\mathcal{N}} \lim_{\boldsymbol{q}\to 0} \sum_{\boldsymbol{k}} \Bigg(& \sum_{n\neq n'\in\mathbb{W}} F_{nn'\boldsymbol{k}}(0,\omega) \left[\left| \frac{\boldsymbol{p}_{nn'k} \cdot \boldsymbol{q}}{\epsilon_{n\boldsymbol{k}} - \epsilon_{n'\boldsymbol{k}}} \right|^2 - \left| \frac{\tilde{\boldsymbol{p}}_{nn'\boldsymbol{k}} \cdot \boldsymbol{q}}{\epsilon_{n\boldsymbol{k}} - \epsilon_{n'\boldsymbol{k}}} \right|^2 \right] \\ & + \sum_{n\neq n'\notin\mathbb{W}} F_{nn'\boldsymbol{k}}(0,\omega) \left| \frac{\boldsymbol{p}_{nn'k} \cdot \boldsymbol{q}}{\epsilon_{n\boldsymbol{k}} - \epsilon_{n'\boldsymbol{k}}} \right|^2 \Bigg). \end{aligned} \tag{5.107}$$

We can identify in Eq. 5.106 the *reduced* Drude peak that makes the system still metallic, although the contributions from the d-d transitions have been removed.

5.4 From a lattice to an impurity interaction

5.4.1 General idea

Within the cRPA method, Hubbard interactions and Hund's couplings for lattice Hamiltonians were constructed from first principles. We have indicated how to parametrize the four-index interaction matrix $U^{(\text{spheric})}_{m_1m_2m_3m_4}$ with an optimal set of Slater integrals, which are practical to combine with a many-body solver. The DMFT scheme is one possible choice and its LDA+DMFT combination a popular and efficient method for strongly correlated materials.

As explained in Chapter 3, DMFT relies on the mapping of the lattice model into a single interacting impurity model that is coupled to a non-interacting fermionic bath. One may ask whether the effective local Coulomb interaction employed in DMFT differs from the interactions calculated previously for a lattice Hamiltonian. This question has connections with the GW+DMFT combination. Once we are able to identify the local polarization from the GW part, we could replace it by the DMFT local polarization [Biermann *et al.* (2003)].

For the moment, we get back to the foundations of the cRPA method consisting in interpreting the partially screened interaction matrix W^r expanded into a localized basis set, as the Hubbard interaction $U^{(\text{lattice})}$ for a lattice Hamiltonian. Such interpretation is based on the identity relations (Eqs. 4.6 and 4.9) between W and W^r. The transitions between the *target* correlated states only, generate a screening that reduces W^r to W. W^r is the interaction remaining once all the degrees of freedom except the *target* ones have been integrated out.

The constrained polarization $P^r = P - P^d$ is then employed for screening the bare interaction, leading to the effective *lattice interaction* $U^{(\text{lattice})}$: *only the transitions from and to the target correlated states* have to be removed from the total polarization. In the perspective of constructing an effective *local impurity-like interaction* U^{imp} that does not depend on the lattice anymore, we would have to employ a constrained polarization P^r_{imp}, where *only the local transitions from and to the target correlated states* have to be removed.

One can define the polarization P^r_{imp} as follows :

$$P^r_{\text{imp}} \equiv P - P^d_{\text{loc}}, \tag{5.108}$$

where P^d_{loc} only includes the local part of the polarization P^d :

$$P^d = P^d_{\text{loc}} + P^d_{\text{nloc}}. \tag{5.109}$$

We then get the local impurity-like interaction U^{imp} :

$$U^{\text{imp}} = \frac{v}{1 - P^r_{\text{imp}} v} = [\epsilon^r_{\text{imp}}]^{-1} v. \tag{5.110}$$

We find enlightening to show below how $U^{(\text{imp})}$ connects to $U^{(\text{lattice})} = [1 - vP^r]^{-1}v$:

$$\begin{aligned} U^{\text{lattice}} &= \frac{v}{1 - [P - P^d_{\text{loc}} - P^d_{\text{nloc}}]v} = \frac{v/(1 - [P - P^d_{\text{loc}}]v)}{1 + P^d_{\text{nloc}} \frac{v}{1-[P-P^d_{\text{loc}}]v}} \\ U^{\text{imp}} &= \frac{U^{\text{lattice}}}{1 - P^d_{\text{nloc}} U^{\text{lattice}}}. \end{aligned} \tag{5.111}$$

The non-local polarization of the *target* correlated states hence generates a screening of U^{lattice} that leads to U^{imp}.
In the following, we focus on the calculation of the local polarization P^d_{loc} for the correlated subspace $\mathcal{C}$.

5.4.2 Local polarization for the correlated subspace

One first expands the bare Green's functions into the localized basis set $\{|\phi_{\boldsymbol{R}L}\rangle\}$:

$$G^0(\boldsymbol{r}, \boldsymbol{r}'; \omega) = \sum_{\boldsymbol{R},\boldsymbol{R}'} \sum_{LL'} \langle \boldsymbol{r}|\phi_{\boldsymbol{R}L}\rangle G^{\boldsymbol{R}\boldsymbol{R}'}_{LL'}(\omega) \langle \phi_{\boldsymbol{R}'L'}|\boldsymbol{r}'\rangle, \tag{5.112}$$

where as previously, $L = (n, l, m, \alpha)$, and the localized representation of the Green's functions $G^{\boldsymbol{R}\boldsymbol{R}'}_{LL'}$ is defined as follows :

$$G^{\boldsymbol{R}\boldsymbol{R}'}_{LL'}(\omega) = \sum_{\boldsymbol{k}} \sum_{n} \frac{\langle \phi_{\boldsymbol{R}L}|\psi_{\boldsymbol{k}n}\rangle \langle \psi_{\boldsymbol{k}n}|\phi_{\boldsymbol{R}'L'}\rangle}{\omega + \mu - \epsilon_{n\boldsymbol{k}} - i\eta\, \text{sign}(\epsilon_F - \epsilon_{n\boldsymbol{k}})} \tag{5.113}$$

$$= \sum_{\boldsymbol{k}} \sum_{n \in \mathbb{W}} \frac{\mathrm{e}^{i\boldsymbol{k}\cdot(\boldsymbol{R}-\boldsymbol{R}')} P_{Ln}(\boldsymbol{k}) [P_{L'n}(\boldsymbol{k})]^*}{\omega + \mu - \epsilon_{n\boldsymbol{k}} - i\eta\, \text{sign}(\epsilon_F - \epsilon_{n\boldsymbol{k}})}. \tag{5.114}$$

We have used in particular the Fourier transformation defined in Eq. 1.3 (see Chapter 1). The *local* non-interacting Green's function in the real-space representation then reads as :

$$G^{\text{loc}}(\boldsymbol{r}, \boldsymbol{r}'; \omega) = \sum_{LL'} \langle \boldsymbol{r}|\phi_{\boldsymbol{0}L}\rangle G^{\boldsymbol{0}\boldsymbol{0}}_{LL'}(\omega) \langle \phi_{\boldsymbol{0}L'}|\boldsymbol{r}'\rangle. \tag{5.115}$$

An analogous expression but in the interacting case can be found in the LDA+DMFT framework (see Chapter 3, Eq. 3.24).

We propose, as a definition, the following expression for the *local polarization* :

$$P^{\text{loc}}(\boldsymbol{r},\boldsymbol{r}';\omega) \equiv \int d\omega' G^{\text{loc}}(\boldsymbol{r},\boldsymbol{r}';\omega-\omega')G^{\text{loc}}(\boldsymbol{r}',\boldsymbol{r};\omega') \tag{5.116}$$

$$\begin{aligned} &= \sum_{L_1L_3}\sum_{L_2L_4}\phi_{\mathbf{0}L_1}(\boldsymbol{r})\phi^*_{\mathbf{0}L_3}(\boldsymbol{r}')\left[\int d\omega' G^{\mathbf{00}}_{L_1L_3}(\omega-\omega')G^{\mathbf{00}}_{L_2L_4}(\omega')\right]\phi_{\mathbf{0}L_2}(\boldsymbol{r}')\phi^*_{\mathbf{0}L_4}(\boldsymbol{r}) \\ &= \sum_{L_1L_3}\sum_{L_2L_4}\phi_{\mathbf{0}L_1}(\boldsymbol{r})\phi^*_{\mathbf{0}L_3}(\boldsymbol{r}')P_{L_1L_2L_3L_4}(\omega)\phi_{\mathbf{0}L_2}(\boldsymbol{r}')\phi^*_{\mathbf{0}L_4}(\boldsymbol{r}), \end{aligned} \tag{5.117}$$

where the auxiliary quantity $P_{L_1L_2L_3L_4}$ reads as :

$$\begin{aligned} P_{L_1L_2L_3L_4}(\omega) \equiv &\sum_{\boldsymbol{k},\,n\in\mathbb{W}}\sum_{\boldsymbol{k}',n'\in\mathbb{W}} P_{L_1n}(\boldsymbol{k})[P_{L_3n}(\boldsymbol{k})]^*P_{L_2n'}(\boldsymbol{k}')[P_{L_4n'}(\boldsymbol{k}')]^* \\ &\times\left\{\frac{1}{\omega-\epsilon_{n'\boldsymbol{k}'}+\epsilon_{n\boldsymbol{k}}+i\eta}-\frac{1}{\omega+\epsilon_{n'\boldsymbol{k}'}-\epsilon_{n\boldsymbol{k}}-i\eta}\right\}. \end{aligned} \tag{5.118}$$

5.4.3 Formalism within (L)APW+lo

Local polarization

In the (L)APW+lo framework, one can expand the local polarization P^{loc} into the product mixed basis $\{\chi^{\boldsymbol{q}}_i(\boldsymbol{r})\}$ as follows :

$$P^{\text{loc}}_{ij}(\boldsymbol{q},\omega) = \frac{1}{\mathcal{N}^2}\sum_{L_1L_3\in\mathcal{C}}\sum_{L_2L_4\in\mathcal{C}}\langle\chi^{\boldsymbol{q}}_i\phi_{\mathbf{0}L_3}|\phi_{\mathbf{0}L_1}\rangle P_{L_1L_2L_3L_4}(\omega)\langle\phi_{\mathbf{0}L_4}|\phi_{\mathbf{0}L_2}\chi^{\boldsymbol{q}}_j\rangle. \tag{5.119}$$

In order to benefit from the properties of the product basis, we find more appropriate to transform the localized basis $|\phi_{\mathbf{0}L}\rangle$ into the Kohn-Sham basis $|\psi_{\boldsymbol{k}n}\rangle$:

$$\begin{aligned} P^{\text{loc}}_{ij}(\boldsymbol{q},\omega) &= \frac{1}{\mathcal{N}^2}\sum_{L_1L_3,L_2L_4\in\mathcal{C}}\sum_{\boldsymbol{k}_1\boldsymbol{k}_3,\boldsymbol{k}_2\boldsymbol{k}_4}\langle\chi^{\boldsymbol{q}}_i\phi_{\boldsymbol{k}_3L_3}|\phi_{\boldsymbol{k}_1L_1}\rangle P_{L_1L_2L_3L_4}(\omega)\langle\phi_{\boldsymbol{k}_4L_4}|\phi_{\boldsymbol{k}_2L_2}\chi^{\boldsymbol{q}}_j\rangle \\ &= \frac{1}{\mathcal{N}^2}\sum_{L_1L_3,L_2L_4\in\mathcal{C}}\sum_{\boldsymbol{k}_1\boldsymbol{k}_3,\boldsymbol{k}_2\boldsymbol{k}_4}\sum_{n_1n_3,n_2n_4\in\mathbb{W}}[P_{L_1n_1}(\boldsymbol{k}_1)]^*P_{L_3n_3}(\boldsymbol{k}_3)[P_{L_2n_2}(\boldsymbol{k}_2)]^*P_{L_4n_4}(\boldsymbol{k}_4) \\ &\quad\times\langle\chi^{\boldsymbol{q}}_i\psi_{\boldsymbol{k}_3n_3}|\psi_{\boldsymbol{k}_1n_1}\rangle P_{L_1L_2L_3L_4}(\omega)\langle\psi_{\boldsymbol{k}_4L_4}|\psi_{\boldsymbol{k}_2L_2}\chi^{\boldsymbol{q}}_j\rangle. \end{aligned} \tag{5.120}$$

One can then employ the following property of the product basis :

$$\langle\chi^{\boldsymbol{q}}_i\psi_{\boldsymbol{k}_3n_3}|\psi_{\boldsymbol{k}_1n_1}\rangle = \int_\Omega d\boldsymbol{r}\psi_{\boldsymbol{k}_1n_1}(\boldsymbol{r})[\psi_{\boldsymbol{k}_3n_3}(\boldsymbol{r})\chi^{\boldsymbol{q}}_i(\boldsymbol{r})]^* = M^i_{n_1n_3}(\boldsymbol{k}_1,\boldsymbol{q})\delta_{\boldsymbol{k}_3,\boldsymbol{k}_1-\boldsymbol{q}}.$$

The expression for the local polarization is then simplified as follows :

$$P^{\text{loc}}_{ij}(\boldsymbol{q},\omega) = \sum_{L_1L_3\in\mathcal{C}}\sum_{L_2L_4\in\mathcal{C}} M^i_{L_1\mathbf{0},L_3\mathbf{0}}(\boldsymbol{q})P_{L_1L_2L_3L_4}(\omega)[M^j_{L_4\mathbf{0},L_2\mathbf{0}}(\boldsymbol{q})]^*, \tag{5.121}$$

where we remind the reader that quantities $M_{L\boldsymbol{R},L'\boldsymbol{R}'}$ (Eq. 5.11) were defined as (setting $\boldsymbol{R} = \boldsymbol{R}' = \mathbf{0}$) :

$$M^i_{L_1\mathbf{0},L_3\mathbf{0}}(\boldsymbol{q}) = \frac{1}{\sqrt{\mathcal{N}}}\sum_{\boldsymbol{k}}\sum_{n_1n_3\in\mathbb{W}}[P_{L_1n_1}(\boldsymbol{k})]^* M^i_{n_1n_3}(\boldsymbol{k},\boldsymbol{q})P_{L_3n_3}(\boldsymbol{k}-\boldsymbol{q}). \tag{5.122}$$

Impurity dielectric function

Following the ideas of the cRPA method as detailed in Eqs. 5.108 and 5.110, we can construct the restricted polarization that should be appropriate for an impurity model :

$$[P^r_{\text{imp}}(\boldsymbol{q},\omega)]_{ij} = P_{ij}(\boldsymbol{q},\omega) - P^{\text{loc}}_{ij}(\boldsymbol{q},\omega). \tag{5.123}$$

It is equivalent to think of an auxiliary quantity κ^{loc} as introduced earlier for the d-projection procedure. In the product mixed basis, it follows for κ^{loc} :

$$\kappa^{\text{loc}}_{ij}(\boldsymbol{q},\omega) = -v_i^{\frac{1}{2}}(\boldsymbol{q})P^{\text{loc}}_{ij}(\boldsymbol{q},\omega)v_j^{\frac{1}{2}}(\boldsymbol{q}), \tag{5.124}$$

and for the partial symmetrized dielectric function of the impurity model :

$$[\varepsilon^r_{\text{imp}}(\boldsymbol{q},\omega)]_{ij} = \varepsilon_{ij}(\boldsymbol{q},\omega) - \kappa^{\text{loc}}_{ij}(\boldsymbol{q},\omega). \tag{5.125}$$

U impurity

Applying Eq. 5.10 but with the partial dielectric function $\varepsilon^r_{\text{imp}}$, we deduce the interaction matrix elements of the impurity model mapping the lattice :

$$U^{\text{imp}}_{L_1L_2L_3L_4}(\omega) = \frac{1}{\mathcal{N}}\sum_{\boldsymbol{q}}\sum_{ij}[M^i_{L_1\mathbf{0},L_3\mathbf{0}}(\boldsymbol{q})]^* v_i^{\frac{1}{2}}(\boldsymbol{q})[\varepsilon^r_{\text{imp}}(\boldsymbol{q},\omega)]^{-1}_{ij} v_j^{\frac{1}{2}}(\boldsymbol{q})M^j_{L_4\mathbf{0},L_2\mathbf{0}}(\boldsymbol{q}). \tag{5.126}$$

We have finished with the presentation of the cRPA method implemented within the (L)APW+lo framework. In the next part, we focus on applications to strongly correlated materials, like 3d and 4d transition metal oxides (see Chapter 6 and Chapter 7) and iron-based pnictides (see Chapter 6). The d-projection method is benchmarked on the 3d transition metal series (see Chapter 6). A combination of cRPA with LDA+DMFT is shown in Chapter 8 for the layered perovskites Sr_2IrO_4 and Sr_2RhO_4, and for the lanthanide CeSF compounds.

5.5 Calculated quantities: summary of notations

To summarize our notations :

- $U^{(\mathcal{S})}_{m_1 m_2 m_3 m_4}$ are the matrix elements of the interaction matrix in the localized basis set $\{|\phi_m\rangle\}$ with $\mathcal{S}$ symmetry of the crystal field.
- $U^{\sigma\bar{\sigma}}_{mm'} \equiv \langle\phi_m\phi_{m'}|W^r(0)|\phi_m\phi_{m'}\rangle$, $J_{mm'} \equiv \langle\phi_m\phi_{m'}|W^r(0)|\phi_{m'}\phi_m\rangle$ and $U^{\sigma\sigma}_{mm'} = U^{\sigma\bar{\sigma}}_{mm'} - J_{mm'}$ are the reduced interaction matrices that are directly calculated with $\mathcal{S}$ symmetry.
- Within the d-dp Hamiltonian, the average interaction matrix elements between t_{2g} orbitals that are directly calculated with cubic symmetry are denoted $U_{mm}, U_{mm'}$ and J_m for the on-site intra-t_{2g}, inter-t_{2g} and exchange interaction, respectively. Analogous quantities, but for the *bare* situation, $v_{mm}, J^{\text{bare}}_m$, and for the *fully screened* situation, $W_{mm}, J^{\text{screened}}_m$, can be introduced.
- U and J are the Hubbard parameter and Hund's coupling, respectively. By definition, $U = \text{F}^0$ and $J = (\text{F}^2 + \text{F}^4)/14$ (for d shells) in our notations.
- Employing Eqs. 5.70, 5.71 and 5.72, Slater-average on-site, $\bar{U}_{mm}$, and exchange, $\bar{J}_m$, interactions between t_{2g} orbitals within the d-dp Hamiltonian, can be extracted – and analogously for the *bare*, $\bar{v}_{mm}, \bar{J}^{\text{bare}}_m$ and the *fully screened* $\bar{W}_{mm}, \bar{J}^{\text{screened}}_m$ cases. They correspond to a part only – the t_{2g} one – of the d-dp low-energy Hamiltonian and therefore, should not be taken for parametrizing this Hamiltonian.
- $(\mathcal{U}, \mathcal{U}', \mathcal{J})$ are the Hubbard-Kanamori interactions between t_{2g} orbitals within the t_{2g}=t_{2g} Hamiltonian (Fig. 5.2). They are the appropriate parameters for mapping the low-energy Hamiltonian downfolded into the t_{2g} subspace. Analogous parameters but within *bare* repulsions, $\mathcal{V}, \mathcal{J}_{\text{bare}}$, or within *fully screened* repulsions, $\mathcal{W}, \mathcal{J}_{\text{screened}}$, are also introduced.

Part III

Applications

Chapter 6

cRPA Calculations on Benchmarks

We start this chapter with the cubic perovskite oxide $SrVO_3$. It is indeed a well-known benchmark for first principles calculations. Here, only the Hubbard parameters are reported. We compare in particular our cRPA calculations with the values of U found in the literature. The electronic properties of this material are more extensively considered in Chapter 7.
Some iron-based pnictide and chalcogenide compounds (LaOFeAs, FeSe, $BaFe_2As_2$ and $BaRu_2As_2$) are then investigated. The cRPA values within projected Wannier-like functions are in agreement with the ones within the maximally localized Wannier function (MLWF) framework.
Finally, we test the projection method (see Chapter 5) on the $3d$ transition metal series. Indeed, in these materials, the target correlated d bands are entangled with the itinerant sp ones. The standard cRPA approach employing band indices or energy window for constraining the polarization, is hence not appropriate in these cases.

6.1 $SrVO_3$

6.1.1 Hubbard U from the literature

The DFT-LDA band structure of $SrVO_3$ (Fig. 6.1) exhibits a set of t_{2g} bands that do not energetically overlap with the other bands. Hubbard models keeping only the t_{2g} degrees of freedom instead of the whole d set, are hence reasonable models. In the literature, a quantitative agreement between LDA+DMFT calculations and photoemission spectra was already reported (see Chapter 7 for details and Tab. 4.1). In particular, Sekiyama and co-workers considered a t_{2g} Hubbard model which they solved within DMFT [Sekiyama *et al.* (2004)]. For this model, they employed the constrained-LDA (cLDA) method from [Gunnarsson(1990)] to deduce the Hubbard-Kanamori interaction parameters adapted to a t_{2g}-restricted Hubbard model (Fig. 5.2). They got : $\mathcal{U} = 5.5$ eV and $\mathcal{J} = 1$ eV. With these values, they were able to reproduce the photoemission spectrum.
Many estimates of the Hubbard interactions can be found in the literature which we enumerate below (Tab. 6.1).

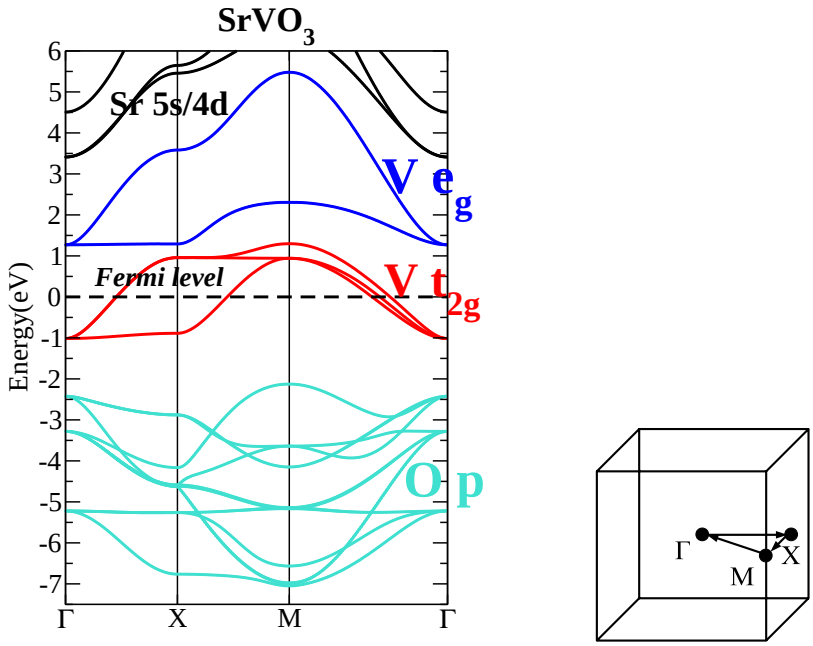

Figure 6.1: (left panel) DFT-LDA band structure of $SrVO_3$. The three bands (in red) around the Fermi level form the set of degenerate t_{2g} bands. The two bands above (in blue) are composed of the e_g orbitals which make bonding-anti-bonding states with the six oxygen p-orbitals (in turquoise) below. (right panel) Brillouin zone meshes considered.

cLDA calculations

In principle, it is not straightforward to deduce the interaction parameters needed in a t_{2g} model from cLDA approaches. As mentioned in Chapter 4, the "hard"-cLDA approach consists in considering an impurity atom inside a supercell and then suppressing all hopping terms from and to the d orbitals of this impurity. Within this framework, it is not possible to perform a similar operation for a restricted number of orbitals like t_{2g}'s. Consequently, the low-energy model that is constructed in "hard"-cLDA, is not transparent. In passing, we note that it would be interesting to employ the "soft"-cLDA method (see Chapter 4) but to the best of our knowledge, there are not published results for $SrVO_3$.

Using the head of the linear muffin-tin orbitals (LMTO) in the atomic sphere approximation (ASA) as local orbitals, Aryasetiawan and co-workers give for the effective Coulomb interaction, $U^{\mathrm{cLDA}} = 9.5$ eV [Aryasetiawan *et al.* (2006)]. Another implementation in LMTO-ASA by [Solovyev(2006)] reports $U^{\mathrm{cLDA}} = 10.1$ eV and $J^{\mathrm{cLDA}} = 1$ eV. Employing the atomic orbitals within a linearized augmented plane wave framework ((L)APW+lo), $U^{\mathrm{cLDA}} = 7.3$ eV and $J^{\mathrm{cLDA}} = 1$ eV [H. Jiang (private communications)]. The discrepancies between LMTO-ASA and the atomic orbitals in (L)APW+lo may originate from the higher localization of the head of the LMTO-ASA wavefunctions.

cRPA			cLDA
t_{2g}-t_{2g}	d-dp	dp	
$\mathcal{U} = 3.2, \mathcal{J} = 0.46$ eV	$U_{mm} = 4.0, J_m = 0.57$ eV	$U = 9.9, J = 0.88$ eV	$U_{mm} = 5.5, J_m = 1.0$ eV[c]
$\mathcal{U} = 3.5$ eV[a]		$U = 9.5$ eV[a]	$U = 9.5$ eV[a]
$\mathcal{U} = 3.0, \mathcal{J} = 0.43$ eV[b]			$U = 10.1, J = 1.0$ eV[d]

[a] [Aryasetiawan *et al.* (2006)] [b] [Miyake and Aryasetiawan(2008)] [c] [Sekiyama *et al.* (2004)]
[d] [Solovyev(2006)]

Table 6.1: Comparison of the Hubbard interactions obtained for $SrVO_3$ within cRPA and cLDA. $(\mathcal{U}, \mathcal{J})$ refer to the Hubbard-Kanamori interactions between t_{2g} orbitals (Fig. 5.2), whereas $U = F^0$ and $J = (F^2 + F^4)/14$ and (U_{mm}, J_m) refer to the interactions between t_{2g} orbitals within the d-dp subspace (Fig. 5.1). The results within cRPA are almost the same within different implementations and frameworks. The cRPA values within the dp Hamiltonian (for which all transitions between p and d orbitals were removed) agree with the ones from cLDA (for which all hopping terms between d shells and the rest were suppressed).

cRPA calculations

As mentioned in Chapter 4, the cRPA method is a systematic procedure for downfolding a low-energy Hamiltonian. One has therefore the flexibility of selecting the number of degrees of freedom included in the low-energy model.

Using the head of the t_{2g} LMTO-ASA wavefunctions as local orbitals, Aryasetiawan and co-workers obtained $\mathcal{U} = 3.5$ eV for the on-site intra-orbital interaction in the t_{2g}-restricted model [Aryasetiawan *et al.* (2006)].
On the other hand, using the head of the d LMTO-ASA wavefunctions but removing the $dp \rightarrow dp$ transitions from the total polarization, they got around $U \approx 9.5$ eV. The values are bigger in the latter since the screening has been notably reduced by the elimination of the transitions from p to d. Within our notation [1], the model so constructed is denoted the "dp" model.

Aryasetiawan and co-workers observed that the cRPA values within the dp model are rather close to the cLDA ones. They mention that further excluding transitions from the occupied t_{2g} to all non-e_g empty states, do not change the value around 9.5 eV. They hence suggest a way to compare cRPA with "hard"-cLDA. By construction of cLDA, the hopping terms between the d shell and the rest have to be turned to zero. A fair comparison would consist in removing from the total RPA polarization all the transitions that involve the d shell. One must say that such comparison is still an open issue, because of the discrepancies in the results of different implementations of cLDA (see Tab. 6.1).

The cRPA method was also implemented within the maximally localized Wannier function (MLWF) framework by [Miyake and Aryasetiawan(2008)]. Miyake and Aryasetiawan got $\mathcal{U} = 3$ eV and $\mathcal{J} = 0.43$ eV in the model they denoted t_{2g}-t_{2g}. The MLWF are expected to be less localized than the head of the LMTO-ASA. This explains that the values within MLWF are smaller than within LMTO-ASA. They also introduced a method that consists in maximizing the

[1] In this work, we have adapted our notations to the ones of Miyake and co-workers [Miyake *et al.* (2008)].

on-site interaction or in other words, in minimizing the off-site interactions. They gave $\mathcal{U} = 3.4$ eV within this approach.

6.1.2 The "t_{2g}-t_{2g} Hamiltonian"

Localized basis

According to the band structure of $SrVO_3$ (Fig. 6.1), one can construct a model that includes the t_{2g} degrees of freedom only. This motivates the choice of the t_{2g}-t_{2g} model (see Chapter 4 for the definition of the model, Fig. 4.6). The energy window $\mathbb{W} = [-1.8, 1.8]$ eV is used for constructing the t_{2g} Wannier orbitals out of the t_{2g} Kohn-Sham states. This window mostly includes t_{2g} bands. One or both of the e_g bands are also included at given $\boldsymbol{k}$ points since the energy window is not $\boldsymbol{k}$-dependent. This should not be problematic since e_g's are orthogonal to t_{2g}'s and hence should not overlap with them after the orthonormalization procedure. The correlated subspace so obtained is a t_{2g} subspace.

One should mention here that usually, such projected Wannier functions are known as extended Wannier functions [Lechermann *et al.* (2006)]. The extension of these functions is due to the "leakage" on the oxygen atomic sites induced by hybridization effects. Since the pd charge transfer energy is larger in $SrVO_3$ than in $SrMnO_3$ (see Chapter 4), the Wannier orbitals within the t_{2g}-t_{2g} model are more localized in $SrVO_3$.

On-site interactions

In Fig. 6.2, one shows the cRPA results on the imaginary frequency axis employing a 4x4x4 $\boldsymbol{k}$-mesh for the Brillouin zone integration. Such mesh is enough to yield converged values. Indeed, a deviation of about 5% is reported with a 2x2x2 $\boldsymbol{k}$-mesh.

From the calculation of the Hubbard interaction matrix $U^{(\text{cubic})}_{m_1 m_2 m_3 m_4}$ with cubic symmetry (see Chapter 5, Fig. 5.1), one can deduce values for the Hubbard-Kanamori parameters $\mathcal{U}, \mathcal{U}'$ and $\mathcal{J}$ (Eqs. 5.75, 5.76 and 5.77). Employing Kohn-Sham indices, the transitions from the occupied to the empty t_{2g} bands are excluded from the total polarization in order to calculate the Hubbard interaction matrix U. On the other hand, all transitions are taken into account to calculate the fully screened interaction matrix W.

We get for the Hubbard-Kanamori parameters : $\mathcal{U} = 3.2$ eV, $\mathcal{U}' = 2.3$ eV and $\mathcal{J} = 0.46$ eV. These values are extracted from the static limit of the averaged $U^{(\text{cubic})}_{mmmm}(i\nu \to 0)$, $U^{(\text{cubic})}_{mm'mm',m\neq m'}(i\nu \to 0)$ and $U^{(\text{cubic})}_{mm'm'm,m\neq m'}(i\nu \to 0)$. These results are in agreement with the ones reported in the literature [Aryasetiawan *et al.* (2006),Miyake and Aryasetiawan(2008)]. We also verify that $\mathcal{U}' \approx \mathcal{U} - 2\mathcal{J} = 2.38$ eV as expected with cubic symmetry.

As discussed earlier in Chapter 4, Coulomb interactions in solids strongly depends on the screening. The screening is a dynamical quantity which can be extremely efficient at low fre-

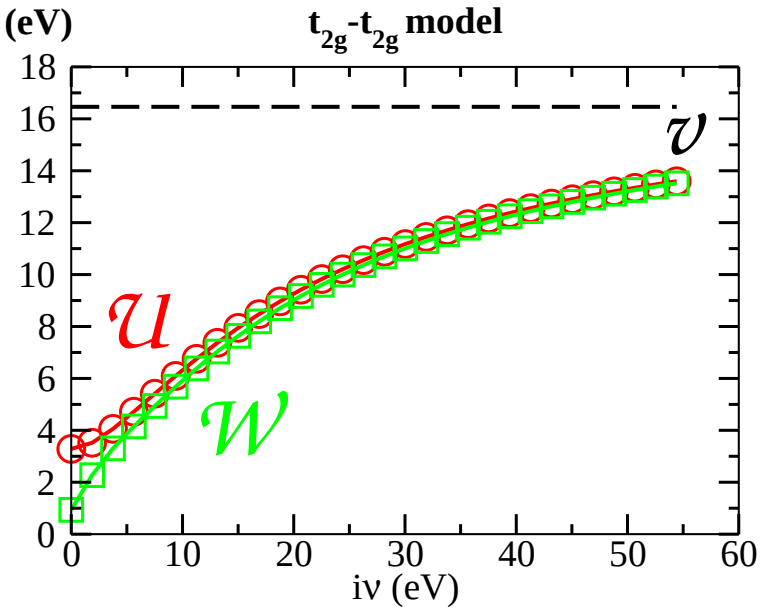

Figure 6.2: Coulomb interaction parameters calculated on the imaginary frequency axis for the t_{2g}-t_{2g} model in $SrVO_3$. $\mathcal{U}$ (in red) corresponds to the Hubbard-Kanamori interaction between t_{2g} orbitals, whereas $\mathcal{W}$ (in green) denotes the fully screened interaction and $\mathcal{V}$ (in black) the unscreened (bare) one.

quency but has to vanish in the infinite frequency limit when the electronic reactivity becomes "frozen". Consequently, Coulomb interactions have to be frequency-dependent.

This is evident in Fig. 6.2 which shows the effective Coulomb interaction $\mathcal{U}(i\nu)$ on the imaginary frequency axis. In the static limit, the screening induced by the creation of electron-hole pairs, strongly reduces the bare Coulomb repulsion from $\mathcal{V} = 16.4$ eV to $\mathcal{W} = 0.9$ eV. A partial screening without t_{2g}-t_{2g} transitions is also rather effective since it leads to $\mathcal{U} = 3.2$ eV.

$\mathcal{U}(i\nu)$ and $\mathcal{W}(i\nu)$ then merge around 5 eV to yield the same asymptotic behavior toward $\mathcal{V}$. The deviation between $\mathcal{U}(i\nu)$ and $\mathcal{W}(i\nu)$ is attributed to the t_{2g}-t_{2g} transitions in a range of the order of the t_{2g} bandwidth.

On the other hand, Hund's exchange $\mathcal{J}$ is weakly dependent on the screening since it varies from 0.46 eV to $\mathcal{J}_{\text{bare}} = 0.57$ eV.This weak dependence is usually interpreted with the fact that the shapes of the electronic clouds are not significantly affected by the multipole part of the interactions [Antonides *et al.* (1977), Sawatzky and Allen(1984), van der Marel(1985)].

As illustrated in Fig. 6.3, the frequency-dependent Hubbard interaction exhibits more pronounced structures on the real-axis. One finds a clear pole around 15 eV in the real-part of $\mathcal{U}(\omega)$ in both the t_{2g}-t_{2g} and d-dp models. Such structure can be attributed to a plasmonic excitation corresponding to collective oscillations of electrons (see Chapter 4).

In the homogeneous electron gas, the plasmon frequency ω_p can be related to the electronic

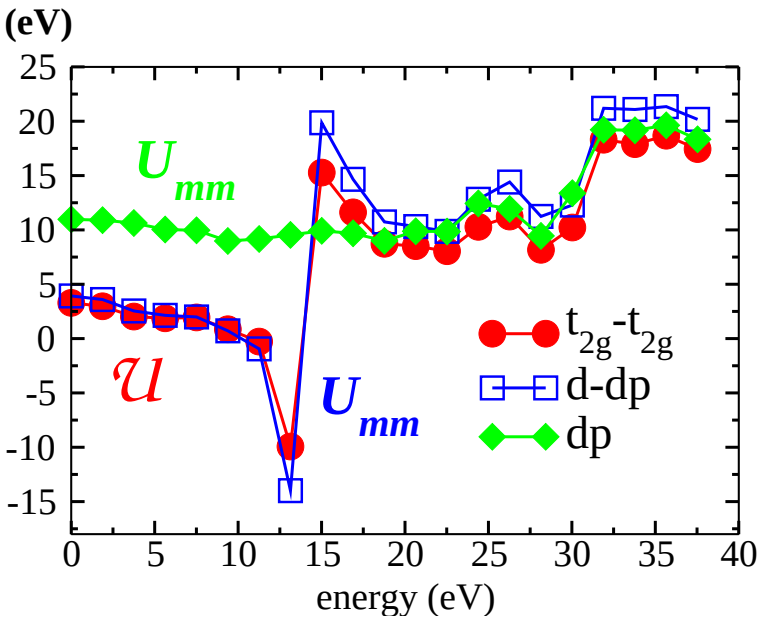

Figure 6.3: Real-part of the dynamical Hubbard interaction $\mathcal{U}(\omega)$ for the t_{2g}-t_{2g} Hamiltonian, and $U_{mm}(\omega)$ for the d-dp and dp Hamiltonians. Only the t_{2g}-t_{2g} transitions and the d-d transitions have been excluded from the total polarization in the t_{2g}-t_{2g} and d-dp Hamiltonians, respectively. In the dp Hamiltonian, the p-d transitions have been also eliminated from the screening. In the static limit, $\mathcal{U}^{t_{2g}-t_{2g}} \approx U_{mm}^{d-dp}$ but is almost three times smaller than U_{mm}^{dp}. This shows the importance of the pd transitions in the total screening. Other transitions of higher energies lead to a reduction by a factor 2 of the bare Coulomb repulsion within the dp model. The pole around 15 eV is interpreted in terms of a plasmonic excitation which is induced by the p-d transitions since the divergence disappears in the dp model.

density N/Ω involved in the oscillation :

$$\omega_p \;=\; \sqrt{\frac{Ne^2}{\Omega m \epsilon_0}} = \sqrt{\frac{4\pi N}{\Omega}} \quad \text{(Hartree)}, \tag{6.1}$$

where we made use in the last expression of the atomic units ($e = m = \hbar = 1$).
The density $1/7.26^3$ (a.u.) fits relatively well with $\omega_p \approx 5$ eV (in $SrVO_3$ $a = 7.26$ Bohr, see Chapter 7, Tab. 7.1), corresponding to an oscillation of one electron from the d shell. A small structure emerges around 5 eV in $\mathcal{U}(\omega)$ but a better resolution is desirable.

On the other hand, considering $N = 19$ in formula 6.1, which corresponds to one electron from the d shell and 18 electrons from the filled oxygen p's, lead to $\omega_p \approx 22$ eV. This does not perfectly fit with the feature around 15 eV of $\mathcal{U}(\omega)$ but it is not so bad neither since a formula that is valid for an homogeneous electron gas was employed.

The comparison between the effective dynamical intra-t_{2g} interactions within the t_{2g}-t_{2g} and dp models supports another way of interpreting the plasmon around 15 eV. In the dp model, the transitions from the occupied oxygen p to the empty d states are cut off. The corresponding

(eV)	$\mathcal{U}^{000}$	$\mathcal{U}^{100}$	$\mathcal{U}^{110}$	$\mathcal{V}^{000}$	$\mathcal{V}^{100}$	$\mathcal{V}^{110}$
$SrVO_3$	3.3	0.66	0.45	16.4	3.9	2.9

Table 6.2: Nearest-neighbor $\mathcal{U}^{100}(\mathcal{V}^{100})$ and next-nearest-neighbor $\mathcal{U}^{110}(\mathcal{V}^{110})$ screened (bare) interaction for $SrVO_3$ in the t_{2g}-t_{2g} model.

dynamical interactions do not exhibit any plasmon pole around 15 eV (or around 5 eV) and is even rather flat in comparison to t_{2g}-t_{2g}. This points out that d-p transitions are at the origin of the plasmonic excitations.

One should add that equivalent results were reported in the literature [Aryasetiawan *et al.* (2006), Miyake and Aryasetiawan(2008)]. Furthermore, a dynamical interaction involving plasmons at 5 eV and 15 eV was recently employed by [Casula *et al.* (2012a)] for analyzing the effects of the dynamical screening in the low-energy spectrum of $SrVO_3$ within an extended DMFT approach.

Off-site interactions

The off-site interactions (see Chapter 5, Eq. 5.14) are given in Tab 6.2 for the t_{2g}-t_{2g} model.
The bare Coulomb interaction $\mathcal{V}^{100}$ between the nearest-neighbor unit cells $\boldsymbol{R}' - \boldsymbol{R} = a\,\vec{i}$ (a is the lattice parameter, see Tab. 7.1), is about $1/4$ of the on-site one, $\mathcal{V}^{000}$. The screening leads to a shorter range effective interaction. Indeed, the nearest-neighbor interaction $\mathcal{U}^{100}$ is about $1/6$ of the on-site interaction.
This is in agreement with the results reported in the literature in which the local states are defined in the MLWF framework [Miyake and Aryasetiawan(2008)].

6.1.3 The "d-dp Hamiltonian"

Localized basis

Within the d-dp model, one makes use of an extended energy window $\mathbb{W} = [-7.5, 5.5]$ eV that contains the oxygen-like p bands and the vanadium-like d bands. The hybridization between e_g and p orbitals justifies to consider also the p Kohn-Sham bands in $\mathbb{W}$ to construct a set of localized functions with d character.

The "leakage" on the oxygen sites- mentioned earlier within the t_{2g}-t_{2g} model- is reduced by orthonormalization within the d-dp model. The orbitals so obtained are thus more atomic-like.

Furthermore, in the hybrid d-dp model, one has to exclude from the RPA polarization the transitions from the occupied d to the empty d states. This is done with the Kohn-Sham indices labeling t_{2g} and e_g bands (Fig. 6.1).

(eV)	F^0	F^2	F^4	F^4/F^2	J	F^0_{bare}	F^2_{bare}	F^4_{bare}	$F^4/F^2\|_{\text{bare}}$	J_{bare}
$SrVO_3$	3.0	6.2	4.9	0.786	0.79	18.6	8.4	5.3	0.629	0.98

Table 6.3: Slater integrals for the d-dp model in $SrVO_3$. On the right part of the table, the Slater integrals correspond to the bare (unscreened) interaction $v = F^0_{\text{bare}}$ and the bare exchange interaction $J_{\text{bare}} = (F^2_{\text{bare}}+F^4_{\text{bare}})/14$, whereas on the left they correspond to the Hubbard interaction $U = F^0$ and Hund's exchange $J = (F^2 + F^4)/14$. These results are respectively deduced from the infinite frequency and static limit of the Hubbard interaction matrix $U_{m_1m_2m_3m_4}(\omega)$ calculated in the spherical symmetry.

Slater integrals

According to Eqs. 5.62 and 5.64, the Hubbard interaction matrix within the d-dp model can be parametrized by a set of Slater integrals $\{F^k\}$. These parameters are deduced from the Hubbard interaction matrix calculated with a localized basis set said "spherical" (see Chapter 5).

The Slater integrals for the screened (static) and the unscreened (bare) cases are given in Tab. 6.3. As discussed in Chapter 5, we can deduce the Hubbard interaction $U = F^0 = 3.0$ eV and Hund's exchange $J = (F^2 + F^4)/14 = 0.79$ eV. U is smaller than the value obtained for the Hubbard-Kanamori parameter $\mathcal{U} = 3.3$ eV within the t_{2g}-t_{2g} model but these two quantities *do not have the same meaning*. Constructing the corresponding interactions but within the d-dp model (see Tab. 6.1 and Chapter 7, Tab. 7.3), leads to $\bar{U}_{mm} = 3.9$ eV. A larger value is expected within d-dp than within t_{2g}-t_{2g} because of the increased orbital localization of the Wannier orbitals within the former (see Chapter 7 for further discussions). This effect is also evidenced with the values of the bare interactions. The bare parameter reads as $v = F^0_{\text{bare}} = 18.6$ eV and Hund's exchange $J_{\text{bare}} = (F^2_{\text{bare}} + F^4_{\text{bare}})/14 = 0.98$ eV. The corresponding interaction between t_{2g} orbitals is $\bar{v}_{mm} = 19.7$ eV (Tab. 7.3), which is notably larger than the value obtained within the t_{2g}-t_{2g} model.

One again observes, on the other hand, that $U = F^0$ strongly lowers with the screening, whereas the exchange interactions- or J- do not change much. The static ratio $F^4/F^2 = 0.786$ significantly deviates from the atomic value (around 0.625) but recovers the atomic value in the infinite frequency limit. The static deviation could be due to anisotropic effects of the screening but requires further investigations. In the next section, we show similar deviations in the cases of iron-based pnictides. The deviation is even larger for these compounds. We attribute this effect to the atomic orbital extension and to the dimensionality.

Accuracy of the Slater parametrization

It is possible to evaluate whether the Slater integrals parametrization is accurate. The parametrization consists in mapping the four-index interaction matrix $U^{(\text{spheric})}_{m_1m_2m_3m_4}$ onto a set of only three numbers. In Chapter 5 (Fig. 5.1), we indicated a method to evaluate this efficiency : it consists in comparing the interactions between t_{2g} orbitals within the d-dp Hamiltonian, $(\bar{U}_{mm}, \bar{J}_m, \bar{U}_{mm'})$, which are deduced from the Slater integrals (from Eq. 5.70 to Eq. 5.72), with the directly calculated ones with cubic symmetry, $(U_{mm}, J_m, U_{mm'})$.

(eV)	U_{mm}	J_m	v_{mm}	J_m^{bare}
directly calculated	4.0	0.57	19.9	0.71
	$\bar{U}_{mm}$	$\bar{J}_m$	$\bar{v}_{mm}$	$\bar{J}_m^{\text{bare}}$
Slater parametrization	3.9	0.60	19.7	0.75
Spherical parametrization	3.9	0.43	19.7	0.54

Table 6.4: Hubbard interactions between the t_{2g} orbitals within the d-dp Hamiltonian for $SrVO_3$: they can be directly calculated with cubic symmetry (first line) or deduced from the Slater integrals (Eqs. 5.70, 5.71 and 5.72) or from the spherical parametrization (assuming in particular that $F^4/F^2 = 0.625$) (third line). The three methods are summarized in Fig. 5.1.

The results are given in Tab. 6.4. All the interaction parameters are correctly reproduced within the Slater integrals which we have calculated (second line of Tab. 6.4). The results of the "spherical parametrization" (Fig. 5.1) are shown for comparison. Using the atomic value for the ratio F^4/F^2 (see Chapter 5, Eqs. 5.73 and 5.74), is not appropriate to deduce the exchange interaction $\bar{J}_m$ between the t_{2g} orbitals, since this approach underestimates this interaction. This is not only due to the choice of the atomic ratio : also $\bar{J}_m^{\text{bare}}$ is underestimated by around 0.2 eV. This can be attributed to the spherical average.

6.2 Iron-based pnictides

The recent discovery of unconventional superconductivity with a T_c up to 55 K in the iron-based pnictides, LaOFeAs [Kamihara *et al.* (2008), Ren *et al.* (2008), Chen *et al.* (2008a), Wen *et al.* (2008), Chen *et al.* (2008b)] and $BaFe_2As_2$ [Rotter *et al.* (2008), Sefat *et al.* (2008), Sharma *et al.* (2010)], and iron-based chalcogenides, α-FeSe [Yeh *et al.* (2008), Hsu *et al.* (2008)], has induced a lot of theoretical and experimental work (see Fig. 6.4 for the crystal structure). The point of the following section is not to describe the amazing properties of such materials but rather to present the cRPA calculations and compare them with the ones obtained within MLWF [Miyake *et al.* (2010), Nakamura *et al.* (2008), Miyake *et al.* (2008)].

A first principles determination of the Hubbard interaction and Hund's exchange is highly desirable for these compounds in order to light on the strength of the correlations (see for instance [Qazilbash *et al.* (2009), Ishida *et al.* (2009), Yin *et al.* (2011)]). For example, LaOFeAs was described either as a strongly correlated system rather close to the Mott transition by [Haule *et al.* (2008), Haule and Kotliar(2009), Yin *et al.* (2011)], as well as a weakly or moderate correlated system by [Anisimov *et al.* (2009b)]. Using LDA+DMFT combined with interaction parameters calculated by cRPA within MLWF, Aichhorn and co-workers have well reproduced the photoemission spectra of LaOFeAs [Aichhorn *et al.* (2009)]. Their findings supported the picture of a moderate correlated metal.

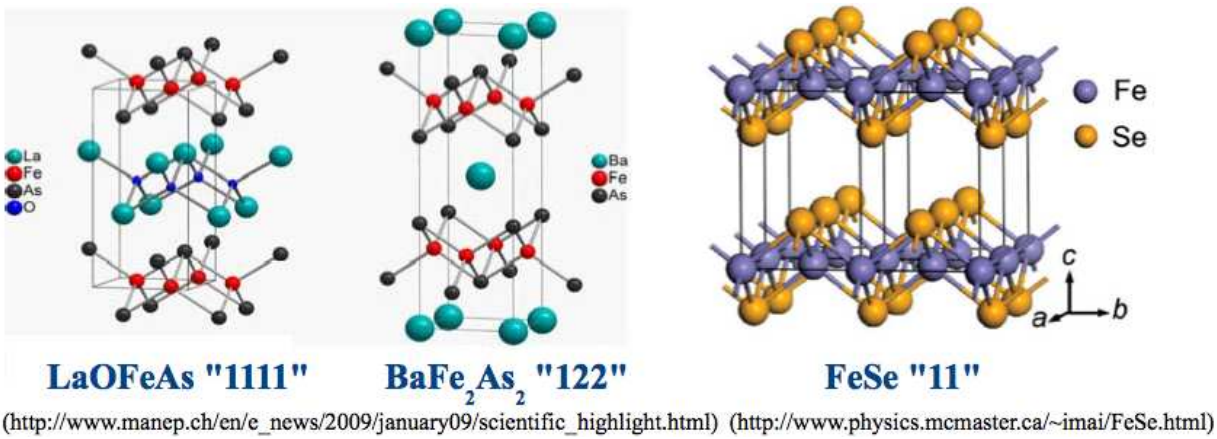

Figure 6.4: Crystal structures of LaOFeAs ("1111"), $BaFe_2As_2$ ("122") pnictides and FeSe ("11") chalcogenide.

In the following, we compute the Hubbard interaction $U = F^0$ and Hund's exchange $J = (F^2 + F^4)/14$ for the *d-dp* model in LaOFeAs, FeSe, $BaFe_2As_2$ and $BaRu_2As_2$. We use as technical parameters 4x4x2 and 4x4x3 $\boldsymbol{k}$ meshes for the integration over the Brillouin zone for LaOFeAs and FeSe, respectively. For $BaFe_2As_2$ and $BaRu_2As_2$, we use a 4x4x4 $\boldsymbol{k}$ mesh.

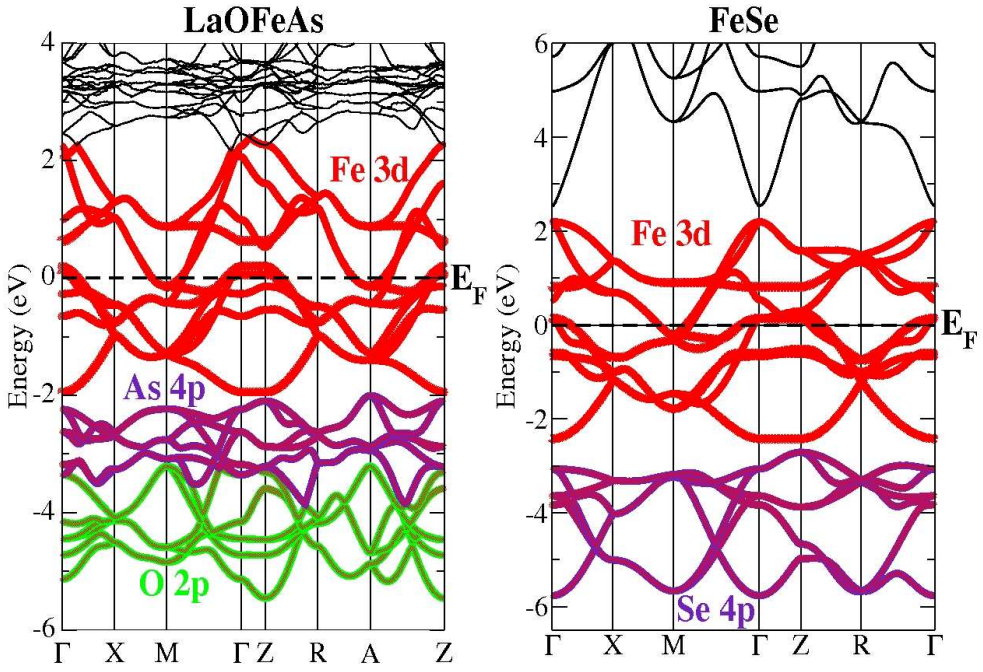

Figure 6.5: (left) DFT-LDA band structure of LaOFeAs in the paramagnetic phase. The iron-d states are highlighted in red, the oxygen-p in purple and the arsenic-p in green. A *fatband* projection on the iron-d atomic orbital (red circles) has been performed in order to show the hybridization between the iron orbitals and the oxygen and arsenic ones. (right) Same but for FeSe. The selenium-p states are in purple.

6.2.1 LaOFeAs

Band structure

The DFT-LDA band structure of LaOFeAs is shown in Fig. 6.5. Lattice parameters, $a = 4.03$ Åand $c = 8.74$ Åare used in agreement with [Miyake *et al.* (2010)].
The band structure exhibits a set of ten Fe d-like bands around the Fermi level with a bandwidth of the order of $D = 4.5$ eV. These bands are surrounded by the p states from the oxygen and the arsenic atoms. An atomic *fatband* projection on the iron-d orbitals indicates that there is a substantial hybridization between d and p states. It is hence reasonable to use an extended energy window $\mathbb{W} = [-5.5, 2.5]$ eV for constructing a set of d-like localized orbitals.
The Slater integrals are then calculated from the Hubbard interaction matrix (Eq. 5.62) within such d-d-p model.

(eV)	U	J	F^2	F^4	F^4/F^2	U	J	v	J_{bare}	$F^4/F^2\|_{\text{bare}}$
LaOFeAs	2.4	0.7	5.84	4.42	0.733	$2.7^{a,b}$	$0.8^{a,b}$	18.9	0.9	0.614
FeSe	3.9	0.9	7.10	5.13	0.723	$4.0^{a,c}$	$0.9^{a,c}$	20.3	1.0	0.621
$BaFe_2As_2$	2.5	0.8	6.14	4.62	0.752	$2.7^{a,d}$		19.3	0.9	0.615
$BaRu_2As_2$	2.3	0.5	4.07	3.32	0.817			12.7	0.7	0.645

[a] [Miyake *et al.* (2010)] [b] [Aichhorn *et al.* (2009)] [c] [Aichhorn *et al.* (2010)]
[d] [Werner *et al.* (2012)]

Table 6.5: Hubbard $U = \text{F}^0$ and Hund's exchange $J = (\text{F}^2 + \text{F}^4)/14$ for the *d-dp* model in pnictides. Our results are in agreement with the ones obtained within the maximally localized Wannier function framework and used in LDA+DMFT. Bare (unscreened) interaction $v = \text{F}^0|_{\text{bare}}$ and bare Hund's exchange $J_{\text{bare}} = (\text{F}^2_{\text{bare}} + \text{F}^4_{\text{bare}})/14$ are also shown. The ratio F^4/F^2 exhibits a significant deviation from the atomic value around 0.625, in contrast to the unscreened ratio $\text{F}^4/\text{F}^2|_{\text{bare}}$.

Slater parametrization

The Slater integrals and the correspinding values for the Hubbard $U = \text{F}^0$ and Hund's exchange $J = (\text{F}^2 + \text{F}^4)/14$, are given in Tab. 6.5. They are in agreement with the parameters obtained within an equivalent *d-dp* model by a "spherical" parametrization (Fig. 5.1) but within MLWF.

Within the Slater parametrization, one observes that the static ratio $\text{F}^4/\text{F}^2 = 0.733$ is deviated from the atomic value, in contrast to the bare ratio. Employing the "spherical" parametrization (for the method, see Fig. 5.1) which relies on the atomic ratio to map the Hubbard interaction matrix calculated with cubic symmetry, leads to another set of Slater integrals, $U^{\text{spheric}} = \text{F}^0_{\text{spheric}} = 2.7$ eV, $J^{\text{spheric}} = (\text{F}^2_{\text{spheric}} + \text{F}^4_{\text{spheric}})/14 = 0.53$ eV ($\text{F}^4/\text{F}^2|_{\text{spheric}} = 0.625$ as imposed). We note that in contrast to the Hubbard U, Hund's exchange is notably underestimated by this method, compared to the Slater parametrization introduced in Chapter 5 (Eq. 5.62).

Since the crystal field symmetry is not cubic in LaOFeAs, the Hubbard-Kanamori relations can not be employed for evaluating the accuracy of the Slater parametrization, as done for $SrVO_3$. We can still compare the reduced interaction matrices $U^{\sigma\sigma'}_{mm'}$ (see Chapter 5, Eqs. 5.78, 5.80 and 5.79) which are deduced from a direct calculation of $U^{(\text{cubic})}_{m_1m_2m_3m_4}$ with cubic symmetry and the ones which are deduced from the *Slater symmetrized* interaction matrix with cubic symmetry (Eq. 5.64). We remind the reader the notations :

$$U^{\sigma\bar{\sigma}}_{mm'} \equiv U^{(\text{cubic})}_{mm'mm'} = \langle\phi_{0m}\phi_{0m'}|W^r(0)|\phi_{0m}\phi_{0m'}\rangle \tag{6.2}$$
$$J_{mm'} \equiv U^{(\text{cubic})}_{mm'm'm} = \langle\phi_{0m}\phi_{0m'}|W^r(0)|\phi_{0m'}\phi_{0m}\rangle \tag{6.3}$$
$$U^{\sigma\sigma}_{mm'} \equiv U^{(\text{cubic})}_{mm'mm'} - J_{mm'}. \tag{6.4}$$

The reduced interaction matrices (in eV) from the direct calculation read as :

$$U^{\sigma\sigma}_{mm'}|_{\text{cRPA}} = \begin{pmatrix} 0 & 1.38 & 1.42 & 2.01 & 2.01 \\ 1.38 & 0 & 2.24 & 1.53 & 1.53 \\ 1.42 & 2.24 & 0 & 1.60 & 1.60 \\ 2.01 & 1.53 & 1.60 & 0 & 1.55 \\ 2.01 & 1.53 & 1.60 & 1.55 & 0 \end{pmatrix} \quad U^{\sigma\bar{\sigma}}_{mm'}|_{\text{cRPA}} = \begin{pmatrix} 3.45 & 2.10 & 2.00 & 2.44 & 2.44 \\ 2.10 & 3.54 & 2.59 & 2.18 & 2.18 \\ 2.00 & 2.59 & 3.09 & 2.07 & 2.07 \\ 2.44 & 2.18 & 2.07 & 3.15 & 2.07 \\ 2.44 & 2.18 & 2.07 & 2.07 & 3.15 \end{pmatrix},$$

where the order of the orbital in these matrices is $d_{z^2}, d_{x^2-y^2}, d_{xy}, d_{xz}, d_{yz}$.

Employing the Slater integrals from Tab. 6.5, one constructs the Slater symmetrized interaction matrix with cubic symmetry :

$$\bar{U}^{\sigma\sigma}_{mm'}|_{\text{Slater}} = \begin{pmatrix} 0 & 1.35 & 1.35 & 1.98 & 1.98 \\ 1.35 & 0 & 2.18 & 1.56 & 1.56 \\ 1.35 & 2.18 & 0 & 1.56 & 1.56 \\ 1.98 & 1.56 & 1.56 & 0 & 1.56 \\ 1.98 & 1.56 & 1.56 & 1.56 & 0 \end{pmatrix} \quad \bar{U}^{\sigma\bar{\sigma}}_{mm'}|_{\text{Slater}} = \begin{pmatrix} 3.24 & 1.98 & 1.98 & 2.40 & 2.40 \\ 1.98 & 3.24 & 2.53 & 2.12 & 2.12 \\ 1.98 & 2.53 & 3.24 & 2.12 & 2.12 \\ 2.40 & 2.12 & 2.12 & 3.24 & 2.12 \\ 2.40 & 2.12 & 2.12 & 2.12 & 3.24 \end{pmatrix}.$$

As we can see, there is no major discrepancy between the reduced interaction matrices. The largest absolute deviation is on the diagonal of $U^{\sigma\bar{\sigma}}_{mm'}$ and yields $\Delta U = 0.3$ eV. The maximum is reached on $d_{x^2-y^2}$ and d_{z^2} orbitals. A similar deviation (around 0.35 eV) was reported by [Aichhorn *et al.* (2009)] with a spherical parametrization within MLWF. The repulsions on $(d_{x^2-y^2}, d_{z^2})$ orbitals are stronger than on the other orbitals due to the As ligand field effects. This is in agreement with the lower spreads of the $(d_{x^2-y^2}, d_{z^2})$ maximally localized Wannier functions as calculated within the d-dp model by [Vildosola *et al.* (2008)]. For further investigations, see [Vaugier *et al.* (2012a)].

Employing the spherical parametrization with our data increases the deviation to 0.54 eV.

$$\bar{U}^{\sigma\sigma}_{mm'}|_{\text{Spheric}} = \begin{pmatrix} 0 & 1.59 & 1.59 & 2.14 & 2.14 \\ 1.59 & 0 & 2.32 & 1.78 & 1.78 \\ 1.59 & 2.32 & 0 & 1.78 & 1.78 \\ 2.14 & 1.78 & 1.78 & 0 & 1.78 \\ 2.14 & 1.78 & 1.78 & 1.78 & 0 \end{pmatrix} \quad \bar{U}^{\sigma\bar{\sigma}}_{mm'}|_{\text{Spheric}} = \begin{pmatrix} 3.00 & 2.06 & 2.06 & 2.43 & 2.43 \\ 2.06 & 3.00 & 2.55 & 2.18 & 2.18 \\ 2.06 & 2.55 & 3.00 & 2.18 & 2.18 \\ 2.43 & 2.18 & 2.18 & 3.00 & 2.18 \\ 2.43 & 2.18 & 2.18 & 2.18 & 3.00 \end{pmatrix}.$$

Dynamical interactions $U_{mm}(\omega)$ can also be calculated on the real-frequency axis (Fig. 6.6). $U_{mm}(\omega)$ is defined here as the diagonal average of the real-part of the interaction matrix elements $U^{(\text{cubic})}_{mmmm}(\omega)$ calculated with cubic symmetry.
In contrast with $SrVO_3$, $U_{mm}(\omega)$ exhibits multiple plasmon poles that we can not reasonably fit with any plasmon frequency of an homogeneous electron gas (Eq. 6.1). In the future, it will be interesting to combine such dynamical Hubbard interaction with a many-body solver like DMFT, as introduced by [Casula *et al.* (2012a), Werner *et al.* (2012)] for $SrVO_3$ and $BaFe_2As_2$.

In LaOFeAs (as well as in FeSe or in fcc Fe, see Fig. 6.13), the screening vanishes above energies of the order of $25 - 30$ eV and the bare Coulomb interaction is recovered above. The interpretation of this common "cut-off" in the screening is not clear yet.

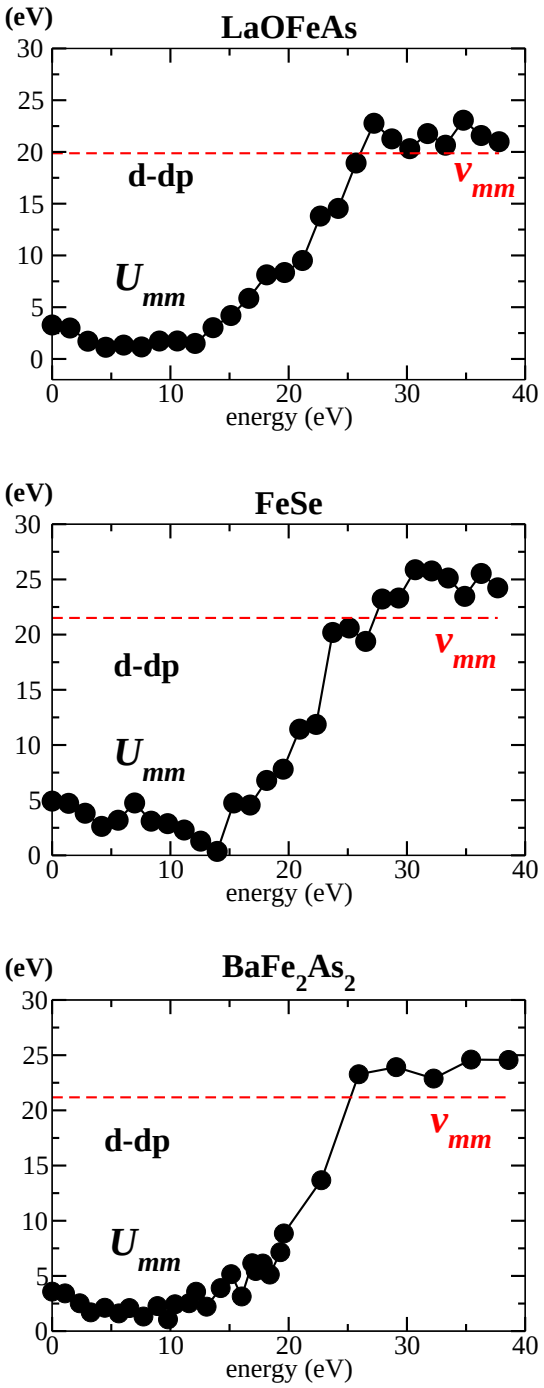

Figure 6.6: Real-part of the dynamical Hubbard interaction $U_{mm}(\omega)$ (black points) for the d-dp model, obtained by averaging over the diagonal interaction matrix elements $U^{(\text{cubic})}_{mmmm}$ calculated with cubic symmetry. The bare interaction is shown in red dashed line. (top panel) LaOFeAs (middle panel) FeSe. (bottom panel) $BaFe_2As_2$. The spectra exhibits multiple plasmon poles in contrast to $SrVO_3$.

6.2.2 FeSe

The paramagnetic DFT-LDA band structure of FeSe is shown in Fig. 6.5 ($a = 3.77$ Å,$c = 5.52$ Å). The bandwidth of the iron d is about $D \approx 4.5$ eV and hence similar to LaOFeAs. This gives an estimation of the kinetic energy. On the other hand, there are fewer p bands that are close to the Fermi level in FeSe than in LaOFeAs. These bands are involved in the screening of the bare Coulomb repulsion on d orbitals. One therefore expects lower screening effects in FeSe.

The results for the Hubbard U and Hund's coupling J are given in Tab. 6.5. The energy window $\mathbb{W} = [-6.5, 2.4]$ eV is employed for constructing d Wannier orbitals within the d-dp model. The numbers are in agreement with the ones obtained within MLWF [Miyake *et al.* (2010), Aichhorn *et al.* (2010)].

The reduced interaction matrices (in eV) with cubic symmetry read as :

$$U^{\sigma\sigma}_{mm'}|_{\text{cRPA}} = \begin{pmatrix} 0 & 2.67 & 2.70 & 3.46 & 3.46 \\ 2.67 & 0 & 3.67 & 2.92 & 2.92 \\ 2.70 & 3.67 & 0 & 2.89 & 2.89 \\ 3.46 & 2.92 & 2.89 & 0 & 2.90 \\ 3.46 & 2.92 & 2.89 & 2.90 & 0 \end{pmatrix} \quad U^{\sigma\bar{\sigma}}_{mm'}|_{\text{cRPA}} = \begin{pmatrix} 5.04 & 3.46 & 3.43 & 3.96 & 3.96 \\ 3.46 & 4.95 & 4.07 & 3.58 & 3.58 \\ 3.43 & 4.07 & 4.81 & 3.55 & 3.55 \\ 3.96 & 3.58 & 3.55 & 4.88 & 3.54 \\ 3.96 & 3.58 & 3.55 & 3.54 & 4.88 \end{pmatrix}.$$

It follows for the *Slater symmetrized* reduced interaction matrices :

$$\bar{U}^{\sigma\sigma}_{mm'}|_{\text{Slater}} = \begin{pmatrix} 0 & 2.63 & 2.63 & 3.41 & 3.41 \\ 2.63 & 0 & 3.67 & 2.89 & 2.89 \\ 2.63 & 3.67 & 0 & 2.89 & 2.89 \\ 3.41 & 2.89 & 2.89 & 0 & 2.89 \\ 3.41 & 2.89 & 2.89 & 2.89 & 0 \end{pmatrix} \quad \bar{U}^{\sigma\bar{\sigma}}_{mm'}|_{\text{Slater}} = \begin{pmatrix} 4.90 & 3.39 & 3.39 & 3.91 & 3.91 \\ 3.39 & 4.90 & 4.08 & 3.56 & 3.56 \\ 3.39 & 4.08 & 4.90 & 3.56 & 3.56 \\ 3.91 & 3.56 & 3.56 & 4.90 & 3.56 \\ 3.91 & 3.56 & 3.56 & 3.56 & 4.90 \end{pmatrix}.$$

The deviation from the directly calculated values is about $\Delta U = 0.14$ eV and much better than in LaOFeAs. FeSe is even the one for which the Slater parametrization is the best among the pnictides considered in this work. This is due to the *more atomic-like* character of the Fe d local orbitals in FeSe. The bare ratio $\text{F}^4/\text{F}^2|_{\text{bare}}$ is also the closest to the empirical atomic value (Tab. 6.5).

The interaction values are notably bigger in FeSe than in LaOFeAs. As shown by [Aichhorn *et al.* (2010)] within a LDA+DMFT calculation with $U = 4.0$ eV and $J = 0.9$ eV and in agreement with photoemission experiments [Yoshida *et al.* (2009), Tamai *et al.* (2010)], FeSe displays a one-particle spectral function that is significantly affected by correlations. Aichhorn and co-workers identified a lower Hubbard band shifted with the strength of U and they demonstrated that the inclusion of the full rotationally-invariant Hund's coupling (spin-flip and pair hopping terms in the Hubbard Hamiltonian, see Eqs. 5.83 and 5.84) is crucial for describing the low-energy properties.

6.2.3 $BaFe_2As_2$ and $BaRu_2As_2$

We finally show the cRPA calculations within the d-dp model for $BaFe_2As_2$ ($a = 3.96$ Å,$c = 13.01$ Å) and $BaRu_2As_2$ ($a = 4.15$ Å,$c = 12.25$ Å). See Fig. 6.4 for an illustration of the crystal structures. Ruthenium (Ru) d-like states have a larger bandwidth $D^{BaRu_2As_2} \approx 6$ eV than iron d, $D^{BaFe_2As_2} \approx 4$ eV. This is attributed to the higher extension of the ruthenium atomic $4d$ orbitals which hence hybridize stronger with arsenic p's.

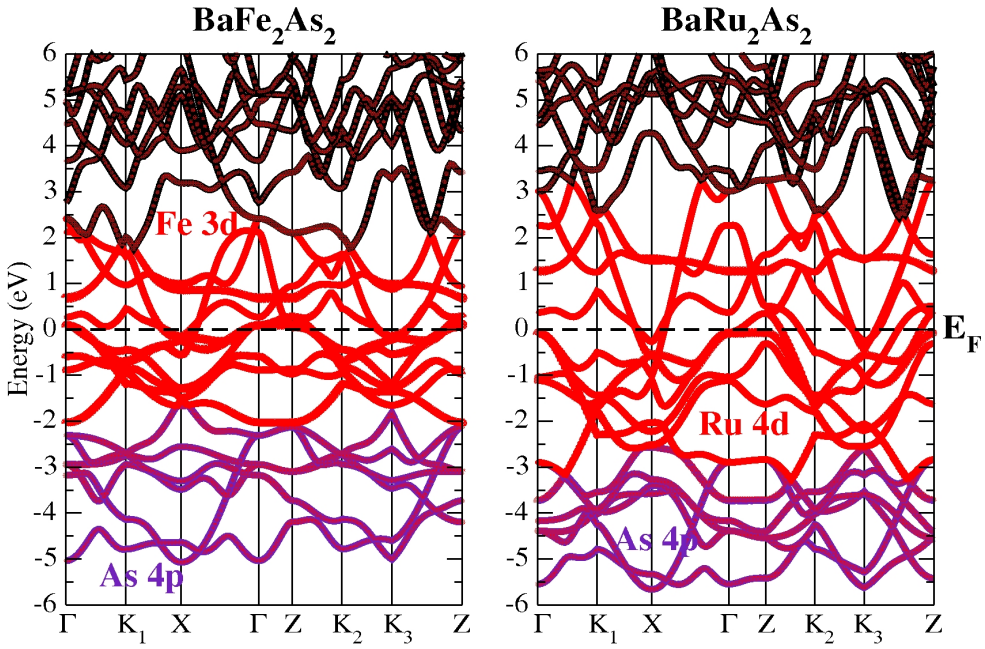

Figure 6.7: DFT-LDA band structure of $BaFe_2As_2$ (left) and $BaRu_2As_2$ (right) in the paramagnetic phase. Iron (ruthenium) d orbitals are in red and arsenic (As) p in purple. An atomic *fatband* projection on the iron (ruthenium) d atomic orbitals (red circles) is also shown.

We get $U = 2.5$ eV and $J = 0.8$ eV (Tab. 6.5) for $BaFe_2As_2$ within the d-dp model with the energy window $\mathbb{W} = [-6.5, 2.7]$ eV. The value for the Hubbard U coincides with the one obtained in MLWF [Werner *et al.* (2012)]. In comparison, for $BaRu_2As_2$, $U = 2.3$ eV and $J = 0.5$ eV ($\mathbb{W} = [-6.5, 2.7]$ eV).

The static Hubbard values are almost the same for $BaFe_2As_2$ and $BaRu_2As_2$ but Hund's exchange is notably smaller in the ruthenium-based compound. The effect of Hund's coupling in pnictides must be crucial but is still unclear [Sawatzky *et al.* (2009), Haule and Kotliar(2009), Aichhorn *et al.* (2010)]. Together with the much larger kinetic energy, this supports the idea that the ruthenium-based pnictides should be less "correlated" than the iron-based ones and correctly described within a wave-like picture such as DFT-LDA. This agrees with the recent angle-resolved photoemission experiments by [Brouet *et al.* (2010)] on $BaFe_2As_2$ and $Ba(Fe_{0.65}Ru_{0.35})_2As_2$.

On the other hand, the bare (unscreened) interaction values agree with the previous statement that the localized ruthenium d orbitals within the d-dp model are more extended than the iron d. This is reasonable if one remembers the atomic d orbital contraction from the bottom to the top of the periodic classification using the Slater rules (see Chapter 7, Tab. 7.4 for example). In Chapter 7, we show that for transition metal oxides, the exchange interaction terms, $\mathcal{J}$, are weakly dependent on screening effects but decrease significantly with an increasing orbital extension. In contrast, the intra-orbital interactions $\mathcal{U}$ are sensitive to both effects. If one applies such statement to the pnictides, this may explain the smaller Hund's coupling in $BaRu_2As_2$ than in $BaFe_2As_2$.

Interestingly, the static ratio $F^4/F^2 = 0.817$ in $BaRu_2As_2$ which is notably deviated from the atomic value. As the atomic value is recovered when the screening disappears (hence for the bare interaction), such effect could be due to an anisotropy in the screening but requires further investigations [Vaugier *et al.* (2012a)]. Such anisotropy would increase from $BaFe_2As_2$ to $BaRu_2As_2$ while the extension of the Wannier orbitals becomes larger. This also suggests that the "spherical parametrization" based on $F^4/F^2 = 0.625$ would not be well justified for these compounds.

To estimate the accuracy of the Slater parametrization, the same method than in LaOFeAs is employed. The reduced interaction matrices (in eV) from the direct calculation with cubic symmetry for $BaFe_2As_2$ read as :

$$U^{\sigma\sigma}_{mm'}|_{\text{cRPA}} = \begin{pmatrix} 0 & 1.49 & 1.46 & 2.10 & 2.11 \\ 1.49 & 0 & 2.34 & 1.65 & 1.66 \\ 1.46 & 2.34 & 0 & 1.60 & 1.61 \\ 2.10 & 1.65 & 1.60 & 0 & 1.69 \\ 2.11 & 1.65 & 1.61 & 1.69 & 0 \end{pmatrix} \quad U^{\sigma\bar{\sigma}}_{mm'}|_{\text{cRPA}} = \begin{pmatrix} 3.66 & 2.19 & 2.13 & 2.55 & 2.56 \\ 2.19 & 3.60 & 2.71 & 2.24 & 2.25 \\ 2.13 & 2.71 & 3.31 & 2.17 & 2.18 \\ 2.55 & 2.24 & 2.17 & 3.26 & 2.14 \\ 2.56 & 2.25 & 2.18 & 2.14 & 3.29 \end{pmatrix},$$

where the order of the orbital in these matrices is $d_{z^2}, d_{x^2-y^2}, d_{xy}, d_{xz}, d_{yz}$.

Employing the Slater integrals from Tab. 6.5, one constructs the Slater symmetrized interaction matrices with cubic symmetry :

$$\bar{U}^{\sigma\sigma}_{mm'}|_{\text{Slater}} = \begin{pmatrix} 0 & 1.40 & 1.40 & 2.06 & 2.06 \\ 1.40 & 0 & 2.28 & 1.62 & 1.62 \\ 1.40 & 2.28 & 0 & 1.62 & 1.62 \\ 2.06 & 1.62 & 1.62 & 0 & 1.62 \\ 2.06 & 1.62 & 1.62 & 1.62 & 0 \end{pmatrix} \quad \bar{U}^{\sigma\bar{\sigma}}_{mm'}|_{\text{Slater}} = \begin{pmatrix} 3.38 & 2.06 & 2.06 & 2.50 & 2.50 \\ 2.06 & 3.38 & 2.64 & 2.20 & 2.20 \\ 2.06 & 2.64 & 3.38 & 2.20 & 2.20 \\ 2.50 & 2.20 & 2.20 & 3.38 & 2.20 \\ 2.50 & 2.20 & 2.20 & 2.20 & 3.38 \end{pmatrix}.$$

The Slater symmetrization leads to a deviation $\Delta U = 0.28$ eV on the diagonal elements of $U^{\sigma\bar{\sigma}}_{mm'}$ and around 0.1 eV on the other off-diagonal elements. The maximum is reached on d_{z^2} orbital pointing towards the interlayer Ba planes. It is bigger than in the other pnictide compounds.

Employing the spherical parametrization of the Hubbard interaction matrix calculated with cubic symmetry, one gets $U^{\text{spheric}} = 2.8$ eV and $J^{\text{spheric}} = 0.55$ eV. Hund's exchange parameter is smaller than the one obtained with the Slater parametrization (Tab. 6.5).

For comparison [Vaugier *et al.* (2012a)], in $BaRu_2As_2$, the deviation within the Slater symmetrization yields $\Delta U = 0.39$ eV and within the spherical parametrization, one gets $U^{\text{spheric}} = 2.5$ eV, $J^{\text{spheric}} = 0.38$ eV and a larger deviation.

The dynamical interactions for $BaFe_2As_2$ within the d-dp model are shown in Fig. 6.6.

6.3 3d transition metals within the projection approach

The projection approach is discussed below for the 3d transition metal (TM) series. The fcc lattice structures are employed for all TM. The lattice parameters used are given in Tab. 6.7. The only adjustable parameter in the method is the energy window $\mathbb{W}$ to construct d localized functions. [2] One relies on the DFT-LDA density of states (Fig. 6.9) in order to set $\mathbb{W}$. The dependence on the choice of $\mathbb{W}$ is shown for paramagnetic nickel.

Here, we focus on the paramagnetic phases of 3d TM. Following the notations in cRPA (see Chapter 4), the so constructed low-energy Hamiltonian is denoted "d-spd" model. Our results (Tab. 6.7 and Fig. 6.11, Fig. 6.12) agree with the ones obtained within MLWF [Miyake *et al.* (2009), Şaşıoğlu *et al.* (2011)], where the authors employed different schemes for treating the entangled bands.

6.3.1 Band structures

As mentioned at the end of Chapter 4, the DFT-LDA band structures exhibiting entangled d and sp bands are serious challenges for the standard cRPA methods. In 3d paramagnetic TM, the 3d orbitals are gradually filled from scandium (Sc) ($4s^2 3d^1$) to copper (Cu) ($4s^1 3d^{10}$) but the d bands are mixed with a dispersive 4s-like band. We give as an example the band structure of nickel (Fig. 6.8) with the atomic "fatband" projection on d orbitals within the energy range $[-10, 10]$ eV (in red circles). The 4s-like band can be identified with the bottom parabola of the band around -10 eV which keeps going up above the Fermi level until much higher energies, together with the 4p-like band. A set of partially filled d-like bands is obtained around the Fermi level on the other hand which can not be labeled with $\boldsymbol{k}$-independent Kohn-Sham indices because of the mixing with sp bands.

The total and the partial d, s and p density of states (DOS) are shown for the 3d paramagnetic TM series in Fig. 6.9. The d character is commonly found in the energy range $[-10, 7]$ eV. This approximately corresponds to the choices made for $\mathbb{W}$ (Tab. 6.7). The results at the end do not depend much on $\mathbb{W}$, as long as the energy window is large enough to construct d localized orbitals within the projection procedure.

One also observes in Fig. 6.9 that the d-like bandwidth, D, decreases from the early to the late TM. This is in agreement with the orbital contraction in atoms within the Slater rules [Cowan(1981)] : the radial distribution of the d atomic wavefunctions decreases with the atomic number in the periodic classification. As a consequence, the electronic hopping between the metallic sites is lowered through the series and the d bandwidth is reduced.

[2] Because of the entanglement of d and sp bands, we do not speak about Wannier functions anymore (see Chapter 5, section 5.3).

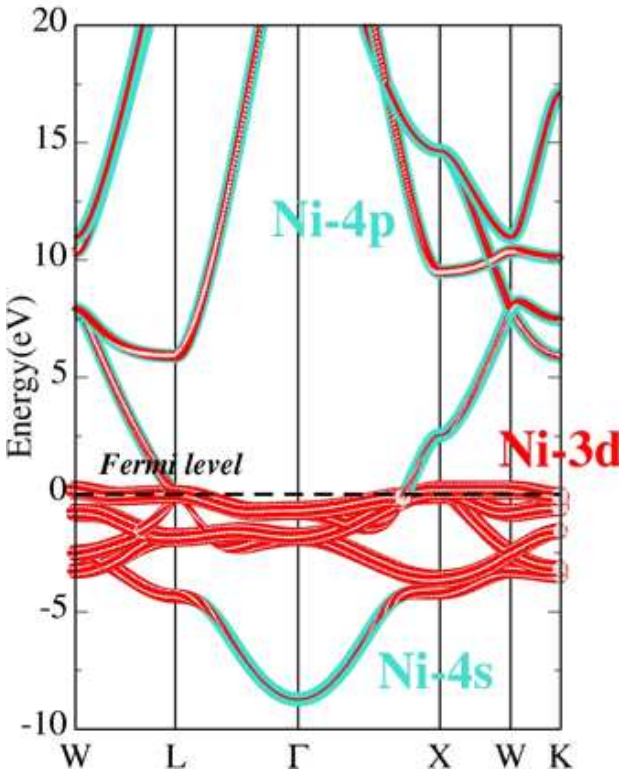

Figure 6.8: DFT-LDA band structure of paramagnetic fcc-Ni with d *fatband* (in red circles) projection. The set of $3d$-like bands (in red) lie around the Fermi level but is entangled with largely dispersive $4s$ and $4p$-like bands (turquoise).

6.3.2 3d series

In contrast to the notations introduced in Chapter 5, U_{mm} refers here to the diagonal average of the Hubbard interaction within the full d manifold (and analogously for W_{mm}, v_{mm}).

We first discuss the cRPA values within the d-spd model for the whole TM series. As technical parameters, a 10x10x10 $\boldsymbol{k}$-mesh for the Brillouin zone integration is employed. The convergence with respect to the number of $\boldsymbol{k}$ vectors is tested on Ni (Fig. 6.10). The fully screened interaction W_{mm} quickly yields a converged value. For the Hubbard interaction U_{mm}, one needs to consider an 8x8x8 $\boldsymbol{k}$-mesh at least . All the values reported in this section were actually obtained with a 10x10x10 $\boldsymbol{k}$-mesh.

The interaction parameters are defined by extending relations Eqs. 5.75 and 5.77 to the whole cubic d manifold : the Hubbard interaction U_{mm} corresponds to the average over the diagonal interaction matrix elements $U^{(\text{cubic})}_{mmmm}$ computed with cubic symmetry. The bare interaction v_{mm} and the fully screened interaction W_{mm} are defined in a similar way. Hund's exchange $J_{mm'}$ corresponds below to the average over the interaction matrix elements $U^{(\text{cubic})}_{mm'm'm,m\neq m'}$ and analogously for $J^{\text{bare}}_{mm'}$ and $J^{\text{screened}}_{mm'}$ but considering respectively the bare interaction matrix $v^{(\text{cubic})}_{mm'm'm,m\neq m'}$ and

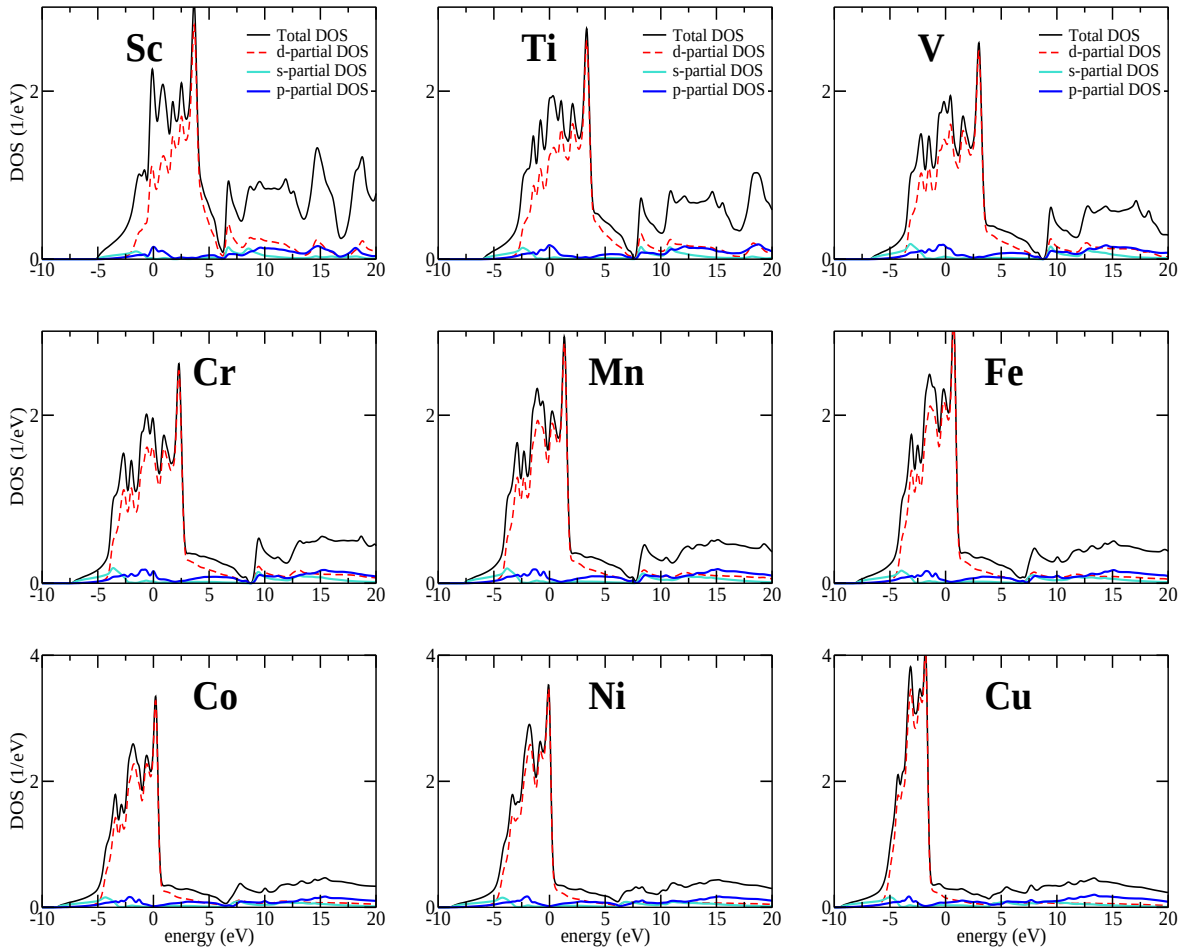

Figure 6.9: DFT-LDA density of states (DOS) for fcc 3d transition metals in the paramagnetic phase. The total DOS is shown in black whereas the d-partial DOS is in red dashed line. 4s and 4p itinerant states are indicated respectively in turquoise and in blue lines.

the fully screened interaction matrix $W^{(\text{cubic})}_{mm'm'm,m\neq m'}$.

Values from the literature

We consider the fcc structure of nickel in order to benchmark our projection approach. We get for the Slater integrals, $U = 2.5$ eV and $J = 1.02$ eV ($F^4/F^2 = 0.730$) within the d-spd model constructed with the energy window $\mathbb{W} = [-10, 15]eV$ (Tab. 6.7). These values are in reasonable agreement with the ones ($U = 3.0$ eV, $J = 0.9$ eV) used by [Lichtenstein *et al.* (2001)] for calculating the finite-temperature magnetism of Ni within LDA+DMFT. In

this work, Lichtenstein and co-workers referred to the Hartree-Fock-Slater atomic calculations[3] by [Bandyopadhyay and Sarma(1989)]. For Fe, they employed $U = 2.3$ eV, $J = 0.9$ eV, thus a bit smaller than the ones obtained within the projection method for the d-spd model (Tab. 6.7).

For comparison, within MLWF in the disentangled cRPA, Miyake and co-workers obtained $U_{mm} = 4.05$ eV with the energy window $\mathbb{W} = [-7, 4]$ eV [Miyake *et al.* (2009)]. Another approach by [Şaşıoğlu *et al.* (2011)] leads to $U_{mm} = 3.95$ eV and $J_{mm'} \approx 0.8$ eV but without mentioning any model. In "soft"-cLDA, Nakamura and co-workers got about $U_{mm'} = 6$ eV [Nakamura *et al.* (2006)], whereas in "hard"-cLDA, Aryasetiawan and co-workers reported about 7 eV [Aryasetiawan *et al.* (2006)].

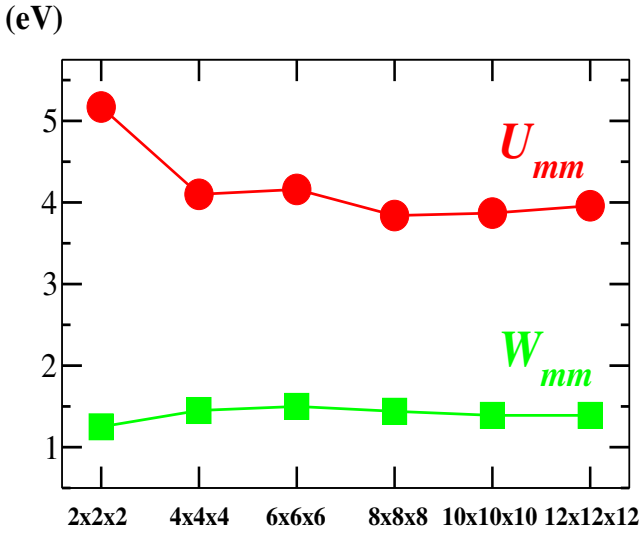

Figure 6.10: Convergence tests of the Hubbard interaction U_{mm} with respect to the number of $\boldsymbol{k}$ vectors used in the Brillouin zone integration. We take the fcc structure of nickel as an example and we use $\mathbb{W} = [-10, 15]$ eV as the energy window for the construction of d localized orbitals. The convergence is reached with the 8x8x8 mesh. It is quicker for the fully screened interaction W_{mm}.

There is also an experimental way of deducing the Hubbard parameters as mentioned in Chapter 4. It consists in combining Auger and X-ray photoemission spectroscopy and then employing a set of Slater integrals for fitting the spectra : in particular, one gets $U = \mathrm{F}^0$ as a fitting parameter. The Slater integrals from the multipole part ($\mathrm{F}^2, \mathrm{F}^4, \ldots$) are taken from atomic calculations. The comparison between such fitting parameters and the values that are computed from first principles, is usually not easy. For nickel, some authors give around 5 eV [Yin *et al.* (1977)], whereas values around 4 eV [de Boer *et al.* (1984)] are also reported. Other estimates from x-ray photoemission data yielded around 2 eV [Hüfner and Wertheim(1973), Herring(1966)]. The

[3]This calculation relies on the Taylor-series expansion of the total energy up to fourth-order in terms of the electron occupancy at various levels.

$\mathbb{W}$ (eV)	v_{mm}	$J^{\text{bare}}_{mm'}$	U_{mm}	$J_{mm'}$	W_{mm}	$J^{\text{screened}}_{mm'}$
$[-10, 3]$	24.4	0.83	3.3	0.69	1.22	0.44
$[-10, 6.5]$	25.2	0.86	3.6	0.72	1.28	0.46
$[-10, 15]$	27.2	0.96	3.9	0.80	1.39	0.51

Table 6.6: Interaction parameters (in eV) with cubic symmetry and depending on the energy window $\mathbb{W}$ employed for constructing the localized orbitals within the projection procedure (see Chapter 3 and 4).

deviations between these experimental results may come from the experimental data and their fit.

Dependence on the energy window $\mathbb{W}$

Throughout this work, we insist on the dependence of the interaction values with the model considered. Within our projection method, the energy window $\mathbb{W}$ to construct d localized orbitals, is the only adjustable parameter. This parameter is required by any downfolding procedure. When extending the energy window $\mathbb{W}$, one expects that the localization of the orbitals increases [Lechermann *et al.* (2006), Aichhorn *et al.* (2009)]. As a consequence, the Coulomb repulsion should also get larger. This trend is reproduced by the results shown in Tab. 6.6 for nickel : the Hubbard interaction yields $U_{mm} = 3.3$ eV within $\mathbb{W} = [-10, 3]$ eV whereas it yields almost 4 eV within $\mathbb{W} = [-10, 15]$ eV.

Bare interaction

The unscreened (bare) on-site Coulomb interaction v_{mm} (Fig. 6.11) monotonically increases with the d electron number, as well as the bare exchange interaction $J^{\text{bare}}_{mm'}$ (Fig. 6.12). This is in agreement with the trends expected from an atomic-like basis according to the Slater rules. We already mentioned that the d atomic wavefunction contracts when the atomic number increases. This gives also confidence in the localized character of the bases constructed to expand the interaction operators.

v_{mm} varies from about 15 eV to almost 30 eV whereas $J^{\text{bare}}_{mm'}$ increases from 0.5 eV to 1 eV. The values are similar to the ones obtained within MLWF by [Şaşıoğlu *et al.* (2011)].

Screened interactions U_{mm} and W_{mm}

The trend for the fully screened on-site interaction W_{mm} (and the corresponding exchange interaction $J^{\text{screened}}_{mm'}$) is rather constant through the series. Copper (Cu) is an exception : W_{mm} (and $J^{\text{screened}}_{mm'}$) notably increase compared to nickel. This will be interpreted later in terms of screening. A qualitatively different trend is reported for U_{mm} (Fig. 6.11 right panel and Tab. 6.7). The Hubbard interaction U_{mm} does not exhibit a monotonic behavior from the early to the late TM but increases from scandium (Sc) to iron (Fe) and then decreases.

	Sc	Ti	V	Cr	Mn	Fe	Co	Ni
a (Å)	4.641	4.133	3.804	3.662	3.651	3.614	3.535	3.520
$\mathbb{W}$	$[-6, 6]$	$[-6, 7.6]$	$[-6, 8.7]$	$[-7, 8.7]$	$[-7, 7.7]$	$[-8, 6]$	$[-8, 6.5]$	$[-10, 6.5]$
U_{mm}	2.6	3.1	3.2	3.4	3.5	5.0	4.5	3.6
$J_{mm'}$	0.38	0.47	0.53	0.58	0.62	0.68	0.71	0.72
$U(=\mathrm{F}^0)$	2.0	2.4	2.3	2.5	2.5	3.9 (2.3)	3.3	2.5 (3.0)
J	0.53	0.66	0.74	0.82	0.87	0.96 (0.9)	0.99	1.02 (0.9)
$\mathrm{F}^4/\mathrm{F}^2$	0.796	0.774	0.765	0.754	0.742	0.716	0.718	0.730

Table 6.7: Lattice parameters used (first row) for the fcc $3d$ transition metals and energy windows $\mathbb{W}$ (in eV) (second row) to construct d localized orbitals. The values for the diagonal averages with cubic symmetry, U_{mm} and $J_{mm'}$, and for the Slater integrals $U = \mathrm{F}^0$ and $J = (\mathrm{F}^2 + \mathrm{F}^4)/14$ (in eV) obtained with the projection method are given. For Fe and Ni, the values (blue parentheses) used by [Lichtenstein *et al.* (2001)] for describing the finite-temperature magnetism are reported in parentheses. For Cu, it does not make sense to calculate Hubbard interactions since the d shell is filled. In Cu, one gets for the fully screened interactions, $W_{mm} = 4.2$ eV and $J^{\text{screened}}_{mm'} = 0.83$ eV using $a = 3.610$ Åand $\mathbb{W} = [-8, 10]$ eV.

Such behavior with a maximum almost in the middle of the series, was already interpreted in cRPA employing the head of LMTO-ASA's as local orbitals, and energy windows for computing the constrained polarization P^d [Aryasetiawan *et al.* (2006)].

In the early TM, the (s to empty d) screening channels are stronger than the (occupied d to non-d) ones, because of the low occupation of the $3d$ orbitals. Aryasetiawan and co-workers did the numerical experiment consisting in keeping only the ($4s$ to empty $3d$) transitions in the polarization. They obtained a partially screened interaction whose behavior was monotonic in contrast to U_{mm}. This is due, first to the ($4s$ to empty $3d$) screening which decreases with the filling of the d shell, and second to the d orbital contraction with the atomic number as evidenced by the increase of v_{mm} through the series.

On the other hand, the strength of the ($3d$ to non-$3d$) screening channels increases with the d orbital filling from the early to the late TM and it competes with the ($4s$ to empty $3d$) channels and with the increased localization induced by the contraction of the d wavefunctions. In Sc, the effects of the ($3d$ to non-$3d$) transitions are weak since the d orbitals only accommodate one electron but these effects should be maximum in nickel (Ni). These transitions in a sense take over the screening from the (s to empty d) channels once the d shell is half-filled. This happens around the middle of the series. Their large contributions explain the lower value of U_{mm} for Ni despite of the stronger orbital localization. In passing, we mention that the antagonism between the orbital localization and the screening is investigated for transition metal oxides in Chapter 7.

A monotonic behavior is observed for W_{mm} (Fig. 6.11 on the left) and $J^{\text{screened}}_{mm'}$. The fact that W_{mm} does not depend on the number of d electrons (except for Cu) can be interpreted in terms of the metallic screening that is induced by the intra-orbital d-d transitions. As discussed earlier in Chapter 5 (Eq. 5.17), such metallic transitions are responsible for the Drude divergence in the dielectric function and induce a long-range screening leading to effective short-range interactions.

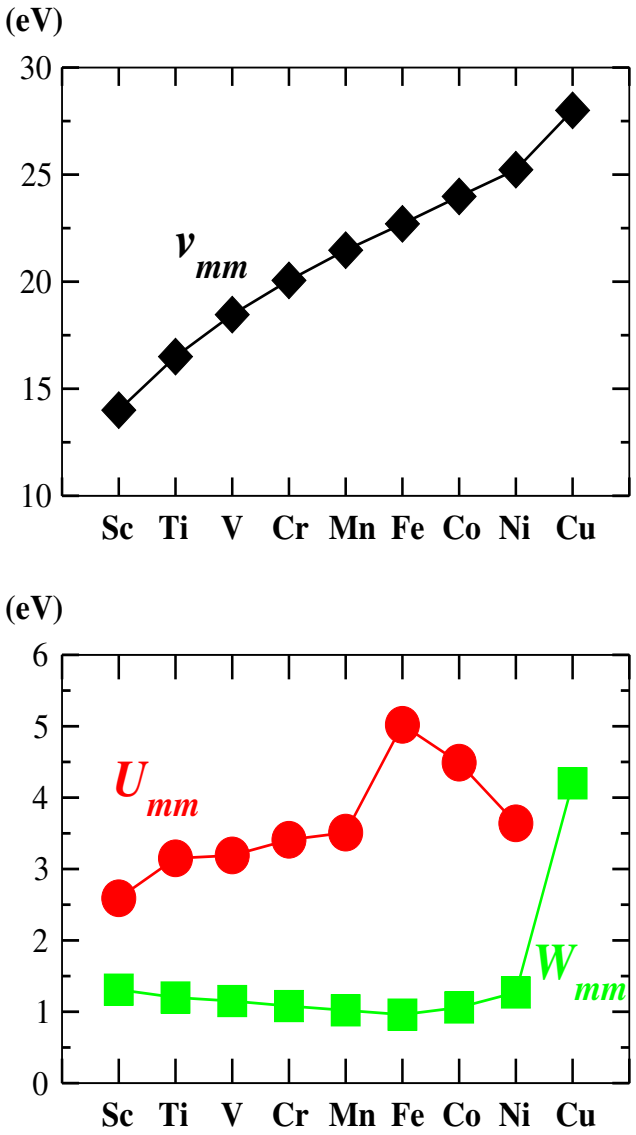

Figure 6.11: (bottom panel) Hubbard interaction U_{mm} (in red circles) for the d-spd model through the 3d (fcc) transition metal series. U_{mm} is obtained by averaging over the diagonal interaction matrix elements $U^{(\text{cubic})}_{mmmm}$ calculated with cubic symmetry with our projection method. The fully screened interaction W_{mm} (in green squares) for the d-spd model of the series is also given for comparison. (top panel) Bare (unscreened) interactions v_{mm} for the d-spd model.

Since the interaction is short-range, W_{mm} is independent of the orbital contraction [Aryasetiawan *et al.* (2006)].

However, the orbital localization effects become notable again when the 3d shell is filled as in copper (Cu). In this case, there are no metallic d-d transitions anymore. Consequently,

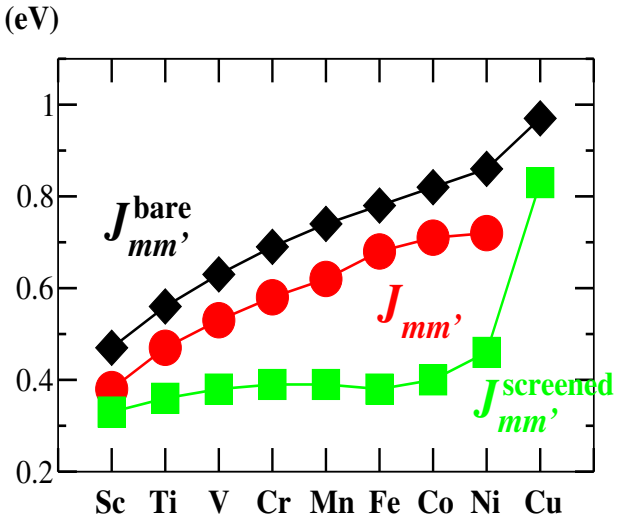

Figure 6.12: Hund's exchange $J_{mm'}$ (in red circles) for the d-spd model through the $3d$ (fcc) transition metal series. $J_{mm'}$ is deduced from the interaction matrix $U^{\text{(cubic)}}_{mm'm'm,m\neq m'}$ calculated with cubic symmetry with our projection method. The bare exchange interaction $J^{\text{bare}}_{mm'}$ (black diamond) and the fully screened exchange interaction $J^{\text{screened}}_{mm'}$ (green squares) are also shown for comparison.

W_{mm} and $J^{\text{screened}}_{mm'}$ strongly increase in this compound. It would be interesting to perform a GW calculation in Cu since the values for W_{mm} seem rather high (for a GW calculation from the literature, see for example [Marini *et al.* (2001)]).
Conceptually, we could construct a Hubbard model for Cu, even if we already know that, since the d shell is filled, the double-counting in LDA+DMFT would cancel out any shift induced by the Hubbard interaction. For Cu, the Hubbard interactions would correspond to the fully screened interactions since there are no d-d transitions as the d shell is filled. This explains that we do not indicate values of U_{mm} or J_{mm} for Cu since they have to equal W_{mm} and $J^{\text{screened}}_{mm'}$ (Fig. 6.11, Fig. 6.12 and Tab. 6.7), respectively.

Analogous trends but with different flavors of cRPA, were reported by [Miyake *et al.* (2009), Şaşıoğlu *et al.* (2011)]. The problem was also addressed in cLDA. In standard cLDA (or "hard"-cLDA), the results for $3d$ TM are about 2 eV larger than in cRPA, especially for the late TM [Aryasetiawan *et al.* (2006)]. A monotonic behavior of U_{mm} is reported within cLDA. The difference with cRPA may come from an artificial cut-off of the hopping terms between the impurity and the rest of the supercell when constraining the d electron number. The strong hybridization between d and sp states should be responsible for it.

As a consequence, one may think that transitions from $3d$ to non-$3d$ orbitals are not properly taken into account in "hard"-cLDA. The fact that the cLDA results are closer to the cRPA ones, but for the early TM, supports this hypothesis. Indeed, for early TM, the ($3d$ to non-$3d$) transitions are negligible because of the low filling of the d shell. It is not the case for the late TM which also corresponds to larger discrepancies between cLDA and cRPA.

Within the recently improved cLDA method formulated in terms of MLWF (or "soft"-

(eV)	Fe (bcc)	Co (fcc)	Ni (fcc)
I	$0.66(U_{mm}+6J_{mm'})/5$	$0.75(U_{mm}+3J_{mm'})/5$	$0.84(U_{mm}+2J_{mm'})/5$
this work	1.20	0.99	0.85
From [Şaşıoğlu *et al.* (2011)]	0.98	1.08	1.04

Table 6.8: Stoner parameters I with the renormalization calculated by [Stollhoff *et al.* (1990)] as functions of U_{mm} and $J_{mm'}$ for the late 3d TM. U_{mm} and $J_{mm'}$ are determined within the projection method of cRPA. In the case of Fe (bcc), we assume that U_{mm} and $J_{mm'}$ can be approximated by the values obtained with the fcc structure.

cLDA), the values agree better with cRPA but the trend still qualitatively differs [Nakamura *et al.* (2006)] : an analogous increase of U_{mm} is obtained from scandium (Sc) to vanadium (V), followed by a plateau-like behavior between chromium (Cr) and iron (Fe), but a strong increase is obtained at the end of the series.

Hund's exchange $J_{mm'}$

In contrast to U_{mm}, a monotonic behavior is observed for Hund's exchange (Fig. 6.12) : $J_{mm'}$ increases with the atomic number in an equivalent way than $J^{\text{bare}}_{mm'}$. This is in agreement with the statement that the exchange interactions do not depend on the screening as much as U_{mm} and are more sensitive to the orbital localization. Similar conclusions will be established for transition metal oxides in Chapter 7.

Paramagnetic instability

According to the values of U_{mm} (Fig. 6.11), one notes that, even if the effective Coulomb interaction is larger in the late TM than in the early TM, it remains smaller than the kinetic energy approximated by the DFT-LDA bandwidth (Fig. 6.9). Qualitatively, with the Stoner criterion $I\rho(\epsilon_F) > 1$ where I is the Stoner parameter, one can expect that in the late TM, the increase of the interactions is in favor of a paramagnetic instability leading to an itinerant ferromagnetism. Employing a formulation of I that was established by [Stollhoff *et al.* (1990)] with Hartree-Fock calculations in order to take into account the renormalization due to the correlations (around 60%), one can test the Stoner criterion for Fe (bcc), Co (fcc) and Ni (fcc) with U_{mm} and $J_{mm'}$ calculated by cRPA (Tab. 6.8). The values of I are in reasonable agreement with the ones obtained by [Şaşıoğlu *et al.* (2011)].

6.3.3 Dynamical interactions

The energy-dependence of the Hubbard interaction $U_{mm}(\omega)$ and Hund's exchange $J_{mm'}(\omega)$ within the d-spd model ($\mathbb{W} = [-10, 15]$ eV) is shown in Fig. 6.13. The real-part of $U_{mm}(\omega)$ on

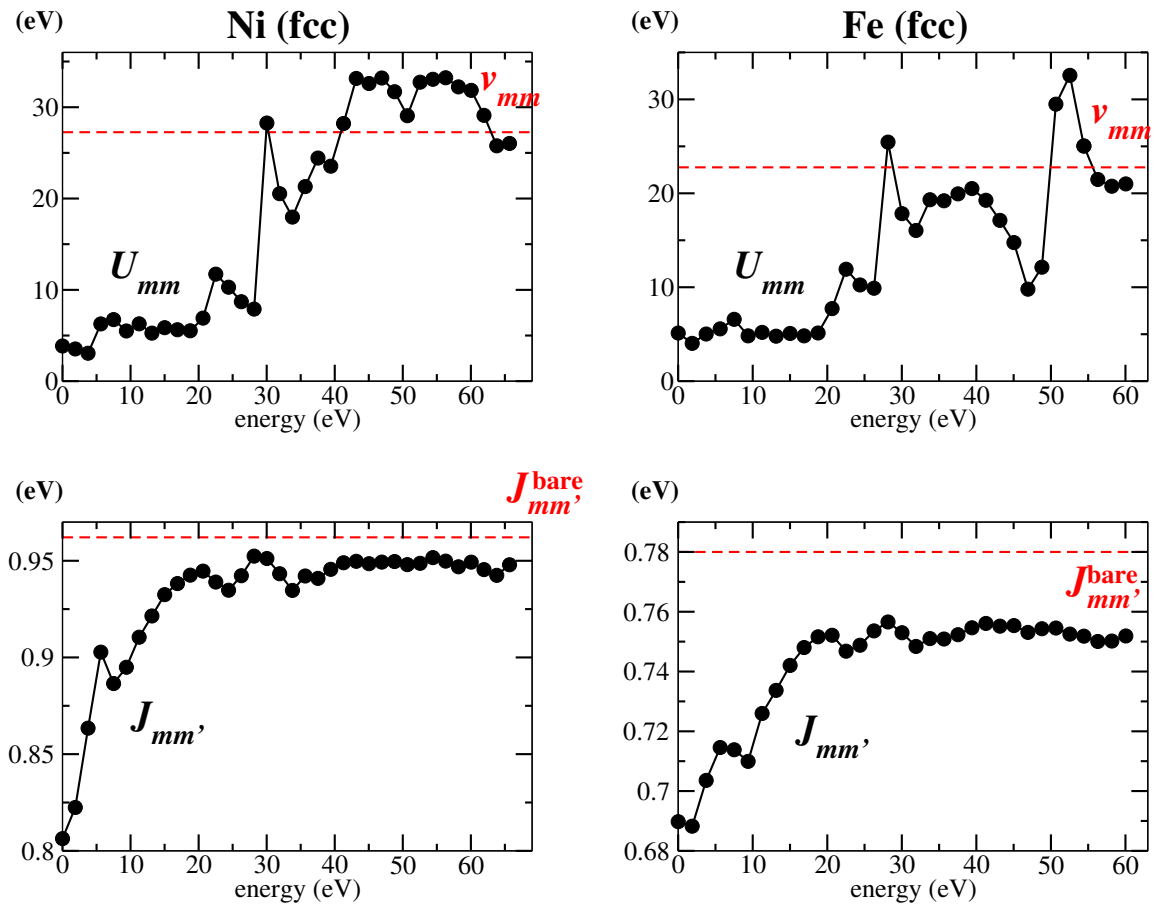

Figure 6.13: Real-part of the Hubbard interaction $U_{mm}(\omega)$ (top panel) and Hund's exchange $J_{mm'}(\omega)$ (bottom panel) on the real-frequency axis for Ni (fcc) (left) and Fe (fcc) (right). U_{mm} and $J_{mm'}$ tend to the unscreened values, respectively v_{mm} and $J^{\text{bare}}_{mm'}$. The interaction matrices were calculated within the projection method in cRPA.

the real-frequency axis is obtained by averaging over the interaction matrix elements $U^{(\text{cubic})}_{mmmm}(\omega)$ and similarly for the real-part of $J_{mm'}(\omega)$ but averaging over $U^{(\text{cubic})}_{mm'm'm,m\neq m'}(\omega)$.

The plasmon poles observed in $U_{mm}(\omega)$ can not be fitted with the plasmon frequency (Eq. 6.1) of an homogeneous electron gas. The plasmonic excitations are effective in an energy window of the order of 30 eV. This seems a common feature for the iron-based materials (see also iron-based pnictides, Fig. 6.6). The dynamical Hund's coupling, on the other hand, does not exhibit such plasmon poles.

6.4 Conclusions

In order to benchmark our cRPA implementation, we evaluated the Coulomb interactions in $SrVO_3$ and in the pnictide compounds, LaOFeAs, FeSe, $BaFe_2As_2$ and $BaRu_2As_2$.

The localized bases employed for spanning the correlated subspace, are constructed by promoting projected atomic orbitals within a given energy window to Wannier-like orbitals (see Chapter 4). The degree of localization of such bases depends on the bands included in the energy window.
Our results are in agreement with the ones reported in the literature for similar models, in which the local states were defined as the head of the LMTO-ASA's or within the maximally localized Wannier function framework.

We presented a parametrization of the four-index interaction matrix that relies on the calculation of an optimal set of Slater integrals $\{F^k\}$ without constraining the ratio F^4/F^2 to the atomic value (see Chapter 5 and Appendix B). The so constructed Slater parametrization is more accurate than the one based on the spherical average of the four-index matrix interaction supplemented by the atomic ratio for F^4/F^2 (see Chapter 5, Fig. 5.1).

In the $3d$ transition metal series, we applied the projection method introduced in Chapter 5 consisting in projecting the total polarization onto the d correlated subspace in order to calculate the d-restricted polarization P^d.
The results are in reasonable agreement with the ones obtained with other first principles approaches for calculating P^d [Miyake *et al.* (2009), Şaşıoğlu *et al.* (2011)] and with values commonly employed in LDA+DMFT [Lichtenstein *et al.* (2001)].

We finally showed the dynamical Hubbard interaction for $SrVO_3$, for the considered pnictides and for $3d$ transition metals (Ni, Fe) using the projection approach. The on-site interactions display plasmonic excitations whose interpretation in terms of charge density is still an open issue. The combination of such plasmonic structures with solvers like LDA+DMFT is currently receiving high attention and applications are in development.

Chapter 7

Transition Metal Oxides: Screening vs. Localization Trends

The cRPA calculations for the cubic crystal structures of transition metal oxides $SrMO_3$ (M = V, Cr, Mn, Nb, Mo, Tc) and Sr_2MO_4 (M = Mo, Tc, Ru, Rh) employing the t_{2g}-t_{2g} and d-dp models, are presented below. The trends for the Hubbard interactions and Hund's exchanges are discussed for both families. These results can be found in [Vaugier et al. (2012b)].

7.1 $SrMO_3$ (M = V, Cr, Mn, Nb, Mo, Tc)

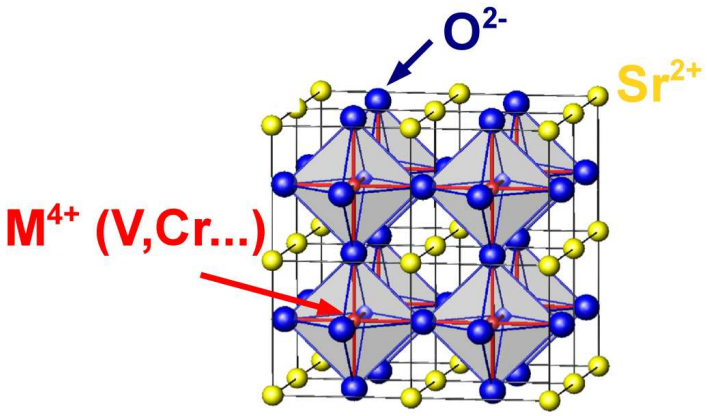

Figure 7.1: Schematic structure of a cubic perovskite structure (from [Pavarini *et al.* (2005)]). The metal element (in red) is surrounded by an octahedron of oxygen ligands (in blue). Strontium atoms are in yellow. Due to the electronegativity of the oxygen atoms, the metal has a 4^+ oxidation state.

In the following, we consider the perovskite oxides of early $3d$ and $4d$ transition metals. Cubic modified crystal structures are employed. A schematic picture of the cubic perovskite

	a (Å)	$\mathbb{W}_{dp}$	$\mathbb{W}_{t_{2g}}$
$SrVO_3$	3.842	$[-7.5, 5.5]$	$[-1.8, 1.8]$
$SrCrO_3$	3.820	$[-7.5, 4.7]$	$[-1.7, 1.0]$
$SrMnO_3$	3.805	$[-7.5, 4.2]$	$[-1.7, 1.0]$
$SrNbO_3$	3.997		$[-3.0, 2.8]$
$SrMoO_3$	3.976		$[-3.0, 2.0]$
$SrTcO_3$	3.950		$[-2.6, 1.3]$

Table 7.1: Lattice parameters used for cubic perovskites $SrMO_3$ and energy windows $\mathbb{W}$ (in eV) for the d-dp and the t_{2g}-t_{2g} models. d and t_{2g} Wannier-like functions are constructed out of the Kohn-Sham states included in $\mathbb{W}$. Because of the entanglement of the e_g states with Sr-like d states, the d-dp model is not considered for $4d$ $SrMO_3$.

structure is given in Fig. 7.1. The lattice parameters used are given in Tab. 7.1. The DFT-LDA calculations are performed in the paramagnetic phase.

In such materials, the direct hopping between the metallic sites is rather weak. The electronic hopping between the metallic sites has to occur mainly via the hybridization with the oxygen atoms that surround the metal. Denoting t_{pd} such hopping amplitude and Δ_{pd} the charge transfer energy between the oxygen p and metallic d states, the effective d-d hopping integral can be approximated to $t_{dd}^{\text{eff}} \approx \frac{t_{pd}^2}{\Delta_{pd}}$ (in the limit of large charge transfer energies). This gives an estimation of the expected bandwidth for the d states $D \approx t_{dd}^{\text{eff}}$: the smaller the d-p hybridization, the smaller the d bandwidth and the stronger the localization of the d states. Inversely, when the charge transfer energy decreases, the bandwidth increases, as well as the kinetic energy of the d electrons. Charge transfer energy, bandwidth and on-site Coulomb interaction U_{dd} are the three common key energy-scales that are invoked in the description of the electronic struggling between localization and itineracy in transition metal oxides. This in particular leads to the Zaanen-Sawatzky-Allen classification for oxides which distinguishes Mott insulators from charge-transfer insulators and metals [Zaanen *et al.* (1985)].

7.1.1 Band structures

$SrVO_3$

Cubic perovskite $SrVO_3$ is an undistorted paramagnetic metal which has been well characterized by experiments like optics, thermodynamical measurements, transport or angle-resolved and angle-integrated photoemission spectroscopies (for optical and x-ray absorption spectroscopies, see e.g. [Mossanek *et al.* (2009)] and references therein). The bonding with the oxygen atoms leads to the d^1 nominal valence for V^{4+}. $SrVO_3$ is often compared to $CaVO_3$ which is also metallic but exhibits a $GdFeO_3$-like distortion [Yoshida *et al.* (2010), Sekiyama *et al.* (2004), Eguchi *et al.* (2006)]. For a review, see [Imada *et al.* (1998)].

Photoemission spectra by [Yoshida *et al.* (2010),Fujimori *et al.* (1992),Yoshida *et al.* (2005)] show a lower Hubbard band with about 1.3 eV binding energy and a quasiparticle peak characterized by the renormalization factor $Z \approx 0.6$. An upper Hubbard band was discussed by inverse photoemission at about $2.5 - 3$ eV [Morikawa *et al.* (1995)].

The DFT-LDA band structure of $SrVO_3$ (Fig. 7.2 and also Chapter 4, Fig. 4.6 for details on the notations) corresponds to a metallic state because of the partial filling of the bands. As already indicated in Chapter 4, the t_{2g} bands are filled with one electron and clearly emerge around the Fermi level. They are weakly hybridized with the oxygen p's since (d_{xy}, d_{xz}, d_{yz}) orbitals do not point toward the ligands, in contrast to the e_g's. $(d_{3z^2-r^2}, d_{x^2-y^2})$ orbitals indeed form bonding and anti-bonding states with the oxygen p's (see also the partial density of states Fig. 7.2).

However, the DFT-LDA picture does not quantitatively agree with experiments: the t_{2g} band is much broader than the experimental quasiparticle peak and DFT-LDA does not reproduce the two Hubbard satellites that are seen in the photoemission spectra. LDA+U methods also fail and the GW approximation only reduces the t_{2g} bandwidth by about 30% [Imada and Miyake(2010)].

A major breakthrough in the description of $SrVO_3$ has emerged with the LDA+DMFT combination, which correctly reproduces the incoherent Hubbard peaks as well as the coherent quasiparticle excitations. Such calculations were carried out within the LMTO-ASA framework as well as within the (L)APW+lo framework, employing Hubbard interaction parameters calculated by cLDA [Sekiyama *et al.* (2004)] or cRPA [Aichhorn *et al.* (2009)]. A discussion on the values of these parameters from these different methods is given in Chapter 6 (see Tab. 6.1).

One has to say that the static cRPA values are usually smaller compared to the ones needed in LDA+DMFT to reproduce the experimental quasiparticle renormalization [Aichhorn *et al.* (2009), Lechermann *et al.* (2006)]. Aichhorn and co-workers employed the Hubbard-Kanamori interactions $\mathcal{U} = 4$ eV, $\mathcal{J} = 0.65$ eV within the t_{2g}-t_{2g} model and onsite intra-orbital interactions $U_{mm} = 6$ eV, $J_m = 0.65$ eV within the hybrid d-dp model (for a discussion on the model notations, see Chapter 4, Fig. 4.6). With these values, both models equivalently describe the electronic features in agreement with photoemission experiments. This ensures in particular that the t_{2g}-t_{2g} model is appropriate for $SrVO_3$. Recently, extended DMFT calculations using the *dynamical* Hubbard interaction $\mathcal{U}(\omega)$ determined from cRPA (see Chapter 4, Fig. 4.9), demonstrated that the dynamical screening makes the system more correlated [Casula *et al.* (2012a), Casula *et al.* (2012b)].

As mentioned earlier in Chapter 4 with the introduction of the limitations of the cRPA method, the accuracy of the Hubbard interactions is related to the one of the screening as described within DFT-LDA. The polarizability of the electronic system is due to the formation of electron-hole pairs in a wide range of energy. The contribution of the oxygen-p states in the polarization of the t_{2g}-t_{2g} and d-dp models will be investigated in the following. A recent comparison with photoemission spectra indicates that the position of the oxygen-p states is actually not so poorly approximated by DFT-LDA [A. Fujimori, (private communications)]. This gives additional motivation for cRPA methods.

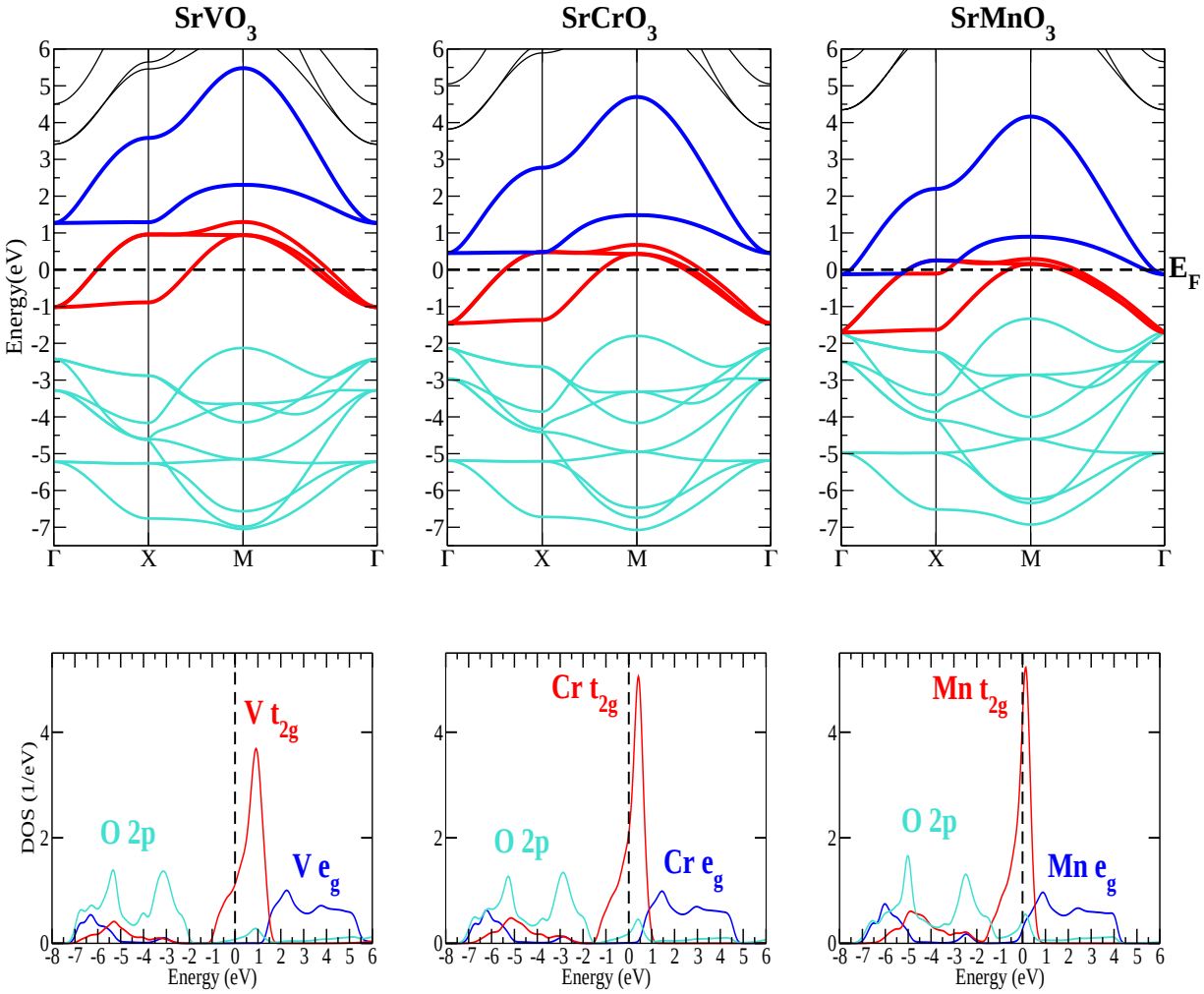

Figure 7.2: DFT-LDA eigenstates (top) and partial density of states (bottom) of $SrMO_3$ (M = V, Cr, Mn from left to right) in the paramagnetic phase. The t_{2g} states are highlighted in red, the e_g's in blue and the oxygen p's in turquoise.

$SrCrO_3$

$SrCrO_3$ compounds have not been studied a lot because of the difficulties of their synthesis. Early works on single crystals of cubic perovskite structure [Chamberland(1967)] show a metallic behavior with a Pauli paramagnetic law. This is in disagreement with a recent study on polycrystals that reports transport, thermal conductivity and magnetic susceptibility exhibiting a non-magnetic insulating state [Zhou *et al.* (2006)]. $SrCrO_3$ crystals have been recently reinvestigated within x-ray diffraction studies [Ortega-San-Martin *et al.* (2007)]. The common belief found in the literature – supported by density functional calculations – is that a structural transition from a non-magnetic orbitally-degenerate cubic to a distorted tetragonal- maybe antiferromagnetic-structure with orbital ordering could appear below 70 K [Ortega-San-Martin *et al.* (2007), Lee and Pickett(2009), Qian *et al.* (2011)].

LDA+U calculations, with U ranging from 0 eV to 8 eV and $J = 1$ eV, were carried out for both the cubic and the tetragonal phases assuming an antiferromagnetic order [Lee and Pickett(2009)]. According to these calculations, only the tetragonal phase exhibits an orbital ordering under the condition that U is chosen larger than 4 eV whereas both phases are still metallic. Following [Qian *et al.* (2011)], a so large value of U would stabilize an antiferromagnetic configuration in the tetragonal structure but is not the one observed experimentally.

$SrMnO_3$

At room temperature, $SrMnO_3$ is found either in a cubic, or in an hexagonal phase. A structural transition from the four-layers hexagonal to an orthorhombic phase is described below 350K [Daoud-Aladine *et al.* (2007)]. The cubic phase can be quenched and stabilized in a metastable state down to lower temperatures [Takeda and Ohara(1974), Søndenå *et al.* (2006), Chmaissem *et al.* (2001)]. Both hexagonal and cubic phases are deeply insulating with a band gap that is larger for the hexagonal phase [Søndenå *et al.* (2006)]. The Néel temperature is reported around 260K with a G-type antiferromagnetic order emerging below [Takeda and Ohara(1974)].

According to x-ray photoemission and absorption [Saitoh *et al.* (1995), Bocquet *et al.* (1996), Kang *et al.* (2008)], the spectroscopic properties of $SrMnO_3$ are rather involved. Indeed, the O-p states are strongly entangled with the lower Hubbard band of t_{2g} character, and the conduction band has been proposed to be of e_g character [Saitoh *et al.* (1995)]. These facts strongly question the validity of a pure t_{2g} model for the description of the low-energy spectra. We nevertheless present both, a t_{2g} and d-dp model, for the sake of comparison with work done in the literature and assessing trends along the perovskite series.

Very recently, LDA+DMFT calculations reproducing the experimental magnetic moments, were carried out employing Hubbard-Kanamori interactions $\mathcal{U} = 3.5$ eV, $\mathcal{U}' = 2.3$ eV and $\mathcal{J} = 0.6$ eV within a three-orbital model comprising the t_{2g} states only, as the e_g's were shown to be inactive for the magnetic moments [Mravlje *et al.* (2012)]. These parameters were chosen in order to fit the low energy part of the photoemission spectrum from [Kang *et al.* (2008)]. The metal-insulator transition from the paramagnetic metallic phase was observed for interactions larger than $\mathcal{U}_c = 1.2$ eV for $\mathcal{J} = 0.6$ eV.

$SrNbO_3$

$SrNbO_3$ is usually found as a non-stoechiometric perovskite oxide [Hannerz *et al.* (1999)]. With doping in Sr_xNbO_3 with $x > 0.80$, a cubic perovskite phase was observed with a poor paramagnetic metallic behavior at temperatures below 300K [Isawa *et al.* (1993)].

$SrMoO_3$

$SrMoO_3$ is, in contrast, an excellent paramagnetic metal. It is even the $4d$ transition metal oxide that displays the highest electrical conductivity [Nagai *et al.* (2005)]. With two electrons on the t_{2g} shell, it is an electronic analogue of $SrRuO_3$ that has two holes on the t_{2g} but also larger correlation strength [de' Medici *et al.* (2011)]. The Van Hove singularity found in the density of states of $SrRuO_3$ makes this system more correlated [Mravlje *et al.* (2011)].

$SrTcO_3$

Because of the radioactivity of technetium, this compound has been less studied, and only structural and magnetic properties are known. A huge Néel temperature of 1023 K – accompanied by a G-type antiferromagnetic ordering with the magnetic moment $2.1\mu_B$ below T_N – has been recently discovered [Rodriguez *et al.* (2011)]. In particular, this high T_N is larger than in the $3d$ analogue $SrMnO_3$. The large T_N in $SrTcO_3$ was first interpreted within density functional calculations [Rodriguez *et al.* (2011), Franchini *et al.* (2011), Middey *et al.* (2011)], e.g. in terms of the larger covalency of the Tc-O bonding compared to Mn-O [Rodriguez *et al.* (2011)]. Recently, another scenario has been put forward for interpreting the difference of magnitude in T_N between $SrTcO_3$ and $SrMnO_3$, based on the proximity of $SrTcO_3$ to the Mott transition in the presence of large Hund's exchange at half-filling [Mravlje *et al.* (2012)]. These LDA+DMFT calculations for the t_{2g} subspace were successful in catching the experimental magnetic moments of $SrTcO_3$ with Hubbard-Kanamori interactions, $\mathcal{U} = 2.3$ eV, $\mathcal{U}' = 1.7$ eV and $\mathcal{J} = 0.3$ eV [Mravlje *et al.* (2012)]. The metal-insulator critical value was estimated, $\mathcal{U}_c = 2.4$ eV for $\mathcal{J} = 0.3$ eV.

In the following, we first consider $SrMO_3$ (M=V, Cr, Mn) compounds and the Hubbard parameters U and Hund's exchanges J are deduced from the Slater integrals within the d-dp model. The calculations of the bare interaction parameter v and fully screened one W, as well as the corresponding exchange interaction parameters, are also shown. One can then calculate the interactions between the t_{2g} orbitals within the Hubbard-Kanamori relations (see Chapter 5). We show that the values for the bare (unscreened) interactions increase with the atomic number in agreement with atomic expectations. The rather constant trend in the series for the partially screened interactions U_{mm}, and the decrease for W_{mm} (fully screened interactions), are interpreted in terms of the increasing screening from the the Kohn-Sham bands close to the Fermi level.

(eV)	F^0	F^2	F^4	F^4/F^2	J	F^0_{bare}	F^2_{bare}	F^4_{bare}	$F^4/F^2\|_{\text{bare}}$	J_{bare}
V	3.2	6.6	5.3	0.795	0.85	19.5	9.0	5.8	0.652	1.06
Cr	2.9	6.7	5.2	0.781	0.85	20.1	9.1	5.7	0.628	1.06
Mn	2.8	7.0	5.4	0.774	0.89	21.2	9.6	6.0	0.625	1.11

Table 7.2: (d-dp model) Static (screened) and bare (unscreened) Slater integrals for the d-dp model of $SrMO_3$ (M=V, Cr, Mn). It follows that Hubbard $U = F^0$ and $J = (F^2 + F^4)/14$. In the unscreened case, $v = F^0_{\text{bare}}$ and $J_{\text{bare}} = (F^2_{\text{bare}} + F^4_{\text{bare}})/14$. The screened ratio F^4/F^2 is deviated from the empirical atomic value 0.625. The bare ratio $F^4/F^2|_{\text{bare}}$ is close to 0.625.

7.1.2 Hubbard parameters within the d-dp Hamiltonian

Localized orbitals

As described earlier in Chapter 6, an extended energy window $\mathbb{W}$ is employed for constructing d Wannier localized orbitals. Such energy window includes Kohn-Sham bands with both d and oxygen p characters. Because of the orthonormalization within $\mathbb{W}$, the downfolded d local orbitals are atomic-like. The various energy windows $\mathbb{W}$ used for $SrMO_3$ (M=V, Cr, Mn) are indicated in Tab. 7.1.

Hubbard parameters

We have computed the Slater integrals corresponding to the (bare) unscreened and to the (partially) screened interaction cases (Tab. 7.2). It results for the bare interaction parameter that $v = F^0|_{\text{bare}}$ and for the Hubbard interaction, $U = F^0$. On the other hand, the bare exchange interaction reads as $J_{\text{bare}} = (F^2_{\text{bare}} + F^4_{\text{bare}})/14$ and Hund's exchange $J = (F^2 + F^4)/14$. These quantities are the fitting parameters employed for constructing the matrix interaction with the symmetry of the crystal field. For example, one can extract the onsite interactions within the t_{2g} subspace (Eqs. 5.70, 5.71 and 5.72, see Chapter 5 and Appendix B) :

$$\bar{U}_{mm}(\bar{v}_{mm}) = F^0_{(\text{bare})} + \frac{4}{49}F^2_{(\text{bare})} + \frac{4}{49}F^4_{(\text{bare})} \tag{7.1}$$

$$\bar{U}_{mm'}(\bar{v}_{mm'}) = F^0_{(\text{bare})} - \frac{2}{49}F^2_{(\text{bare})} - \frac{4}{441}F^4_{(\text{bare})} \tag{7.2}$$

$$\bar{J}_m(\bar{J}^{\text{bare}}_m) = \frac{3}{49}F^2_{(\text{bare})} + \frac{20}{441}F^4_{(\text{bare})}. \tag{7.3}$$

The values for $SrMO_3$ are summarized in Tab. 7.3 and plotted in Fig. 7.3. Analogously but with the Slater integrals computed within RPA, the fully screened interaction $\bar{W}_m$ and the corresponding exchange interaction $\bar{J}^{\text{screened}}_m$ between the t_{2g} orbitals, are deduced.

As introduced in Eqs. 7.1, 7.2 and 7.3, the intra-t_{2g} interactions $(\bar{U}_{mm}, \bar{U}_{mm'}, \bar{J}_m)$ which are deduced from the Slater integrals, correspond to the Coulomb interactions between the t_{2g} orbitals with cubic symmetry. Within the d-dp model, they allow for a visualization of the t_{2g}

(eV)	$\bar{U}_{mm}$	$\bar{U}_{mm'}$	$\bar{J}_m$	$\bar{v}_{mm}$	$\bar{v}_{mm'}$	$\bar{J}_m^{\text{bare}}$	$\bar{W}_{mm}$	$\bar{W}_{mm'}$	$\bar{J}_m^{\text{screened}}$
V	4.1	2.8	0.65	20.7	19.1	0.81	1.4	0.4	0.50
Cr	3.9	2.6	0.65	21.4	19.7	0.82	1.0	0.1	0.43
Mn	3.8	2.4	0.68	22.5	20.8	0.86	0.9	0.1	0.37

Table 7.3: (d-dp model) Static (screened) ($\bar{U}_{mm}, \bar{U}_{mm'}, \bar{J}_m$) and bare (unscreened) ($\bar{v}_{mm}, \bar{v}_{mm'}, \bar{J}_m^{\text{bare}}$) interactions between t_{2g} orbitals in the d-dp Hamiltonian for $SrMO_3$ (M=(V, Cr, Mn)). Fully screened interactions ($\bar{W}_{mm}, \bar{W}_{mm'}, \bar{J}_m^{\text{screened}}$) are also given for comparison. Such parameters are deduced from the Slater integrals (from Eq. 7.1 to Eq. 7.3).

subspace of the interaction matrix. The results are given in Tab. 7.3. These parameters reproduce the same trend as their analogues, the Hubbard U and Hund's exchange J.

As indicated for $SrVO_3$ in Chapter 6, it is possible to evaluate the accuracy of the Slater parametrization : the values from Tab. 7.3 can be compared to the ones from a direct calculation of the interactions with cubic symmetry (following the method shown in Fig. 5.1). For further details, see Chapter 6. The orbitally-resolved Hubbard interaction matrices are given at the end of the section. For $SrVO_3$, the direct calculation gives for the intra-t_{2g} interaction $U_{mm} = 4.0$ eV and $J_m = 0.60$ eV, hence in reasonable agreement with the values calculated from the Slater integrals in Tab. 7.3. *For the $SrMO_3$ series below, we will hence refer either to U_{mm}, J_m or $\bar{U}_{mm}, \bar{J}_m$.*

Through the $3d$ series, the interaction parameters v and J_{bare} clearly increase with the atomic number in agreement with atomic expectations - and equivalently, $\bar{v}_{mm}$ and $\bar{J}_m^{\text{bare}}$ (Fig. 7.3). This increase is related to the increasing localization of the localized d orbitals within the d-dp low-energy Hamiltonian from the left to the right of the periodic classification. A similar trend is reproduced for the hydrogenoid systems within the Slater rules. One can compute the average radial distribution (in bohr units) $\langle r \rangle^{4+} = [3n^{*2} - l(l+1)]/2Z^*$ for 4^+ transition metal atomic d-wavefunctions [1], where n^*, Z^* are the effective principal quantum number and the effective nuclear charge respectively, which are deduced from the Slater rules [Cowan(1981)]. The results for $3d$ (and also $4d$ and $5d$ for comparison) are given in Tab. 7.4. Since the atomic d radial distribution decreases from V^{4+} to Mn^{4+}, the d atomic-like wavefunctions are more and more localized around the nuclei. This agrees with the trend displayed by the bare interaction v : the less extended the orbitals, the higher the Coulomb repulsion. This also confirms that the so constructed localized basis within the d-dp model mimics an atomic-like basis.

One has to comment now about the trends for the Hubbard and fully screened interactions from $SrVO_3$ to $SrMnO_3$ (Fig. 7.3). U_{mm} and W_{mm} differentiate from the bare interaction v_{mm} because of the screening that arises from the electronic polarizability and lowers the Coulomb repulsion. W_{mm} decreases with the atomic number as a consequence of the screening which increases with the atomic number. The evaluation of the ratio W_{mm}/v_{mm} quantifies the increase of the screening from V to Mn compounds : the smaller this ratio and the stronger the screening.

[1] In the perovskites $SrMO_3$ and Sr_2MO_4, the transition metal M has 4^+ oxidation state.

(bohr)	**V**	**Cr**	**Mn**		
$\langle r \rangle_{3d}^{4+}$	2.10	1.86	1.66		
	Nb	**Mo**	**Tc**	**Ru**	**Rh**
$\langle r \rangle_{4d}^{4+}$	3.50	3.10	2.78	2.52	2.30
					Ir
$\langle r \rangle_{5d}^{4+}$					2.76

Table 7.4: Average radial distribution (in bohr units) for $3d$ orbitals with 4^+ oxidation state, calculated with the Slater rules. Analogous quantities for $4d$ and $5d$ (iridium) orbitals are given for comparison. One observes the contraction of the d atomic wavefunction since $\langle r \rangle_d^{4+}$ decreases from the left to the right and from the bottom to the top of the periodic classification. This induces an increased electronic localization on the d atomic orbitals from the left to the right and from the bottom to the top.

One gets $7.1/100$ in $SrVO_3$, $4.6/100$ in $SrCrO_3$ and $4/100$ in $SrMnO_3$.

Screening has therefore an impact into the effective Coulomb interaction but in the *opposite direction* than the orbital localization. The latter makes the repulsion stronger whereas the former makes it lower. The clue for understanding the trends in Fig. 7.3 hence relies on the interpretation of the screening evolution from $SrVO_3$ to $SrMnO_3$.

At the RPA level, the electronic screening is induced by the creation of single particle-hole excitations and their strength varies with the inverse of the energy difference between occupied and empty states. In the cRPA method, the analysis of the DFT-LDA band structure allows for a characterization of the screening.

The paramagnetic DFT-LDA band structures and the density of states for the perovskite structures $SrMO_3$ are shown in Fig. 7.2. The charge transfer energy between the oxygen p and the d states decreases from $SrVO_3$ to $SrMnO_3$: the p states go up toward the t_{2g}'s. Furthermore, the e_g's come closer to the t_{2g}'s. As a consequence, one expects stronger d-d and p-d polarization effects in $SrMnO_3$ than in $SrVO_3$.

The d-d and p-d screening channels are pieces of the multiple screening channels that lead to the reduction of the Coulomb repulsion from the bare interaction (v_{mm}) to the fully screened one (W_{mm}). For example, in $SrVO_3$, $v_{mm} = 20.7$ eV and $W_{mm} = 1.4$ eV. As already pointed out by [Aryasetiawan *et al.* (2006)], the screening channels effects are not additive, but their contribution to the total polarizability can be estimated by evaluating partially screened interactions. The Hubbard parameter $U = \mathrm{F}^0$ as well as the intra-t_{2g} repulsion U_{mm} are such examples of partially screened interactions.

In the calculation of U_{mm}, transitions from and to the d states are excluded from the total polarization by construction of cRPA. The values of U_{mm} are thus bigger than W_{mm} since the screening was partly constrained. The evaluation of the quantity U_{mm}/v_{mm} and the comparison with W_{mm}/v_{mm}, quantify the weight of the d-d transitions in the total polarization. For example in $SrVO_3$, U_{mm}/v_{mm} equals $19.8/100$ whereas W_{mm}/v_{mm} equals $6.7/100$. In $SrCrO_3$, $U_{mm}/v_{mm} = 18.2/100$ and $W_{mm}/v_{mm} = 4.6/100$, while in $SrMnO_3$, $U_{mm}/v_{mm} = 16.9/100$ and $W_{mm}/v_{mm} = 4.0/100$. According to these values, we conclude that the screening *without*

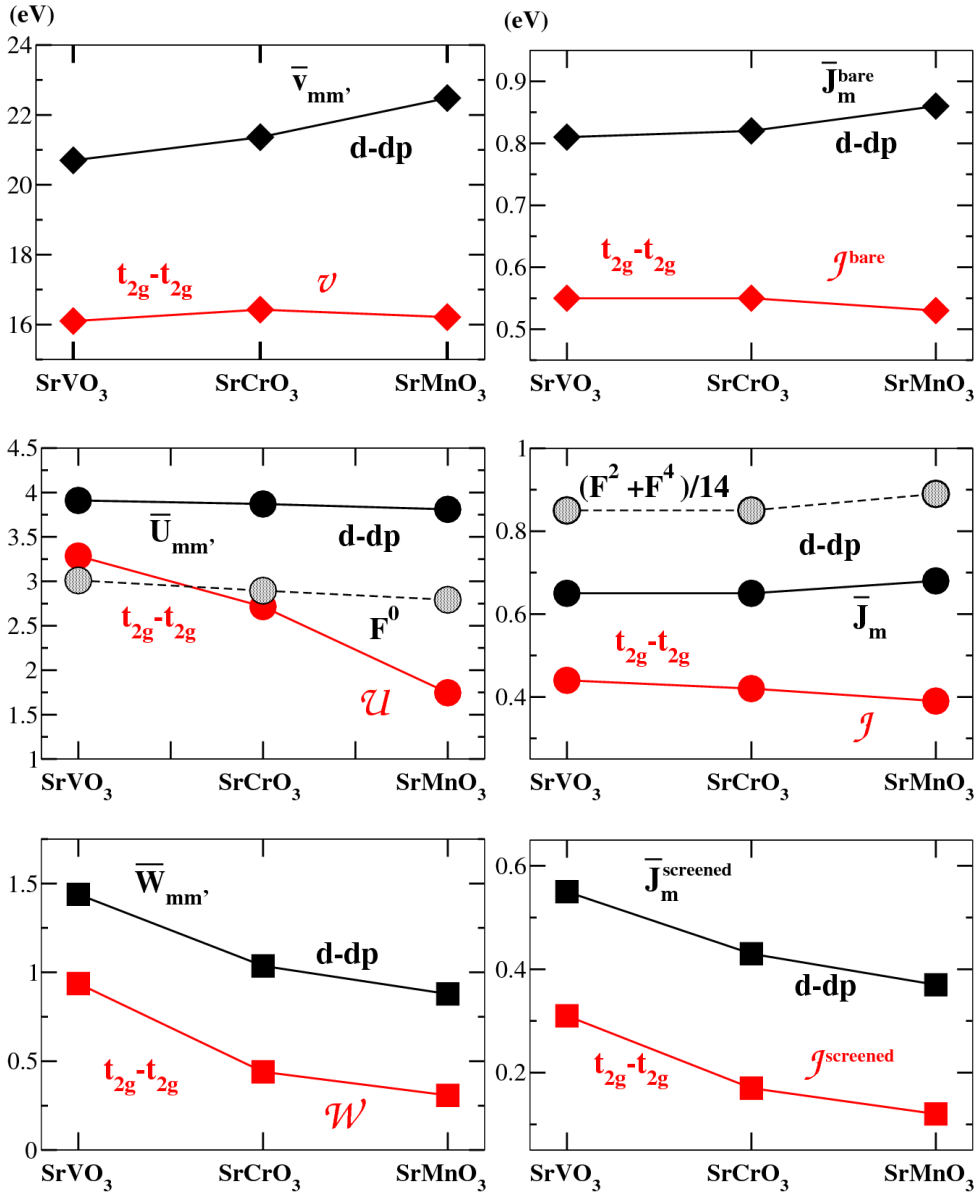

Figure 7.3: Middle panel: On-site Hubbard interaction $\bar{U}_{mm}$ (left) and exchange interaction $\bar{J}_{mm}$ (right) between t_{2g} orbitals within the d-dp (black curve) low-energy Hamiltonians for $3d$ $SrMO_3$, compared to the on-site $\mathcal{U}$ and $\mathcal{J}$ within t_{2g}-t_{2g} (red curve). In dashed line with open circles, the Hubbard parameter $U = F^0$ and Hund's exchange $J = (F^2 + F^4)/14$ are shown. Top panel: Same but for the bare interactions between t_{2g} orbitals. Bottom panel: Same but for the fully screened interactions between t_{2g} orbitals.

the d-d screening channels, increases slower than the total screening [2].

[2] We remind the reader that the lower U_{mm}/v_{mm}, the stronger the screening.

The interactions U_{mm} thus correspond to an intermediate case between v_{mm} and W_{mm}, where the partial screening counterbalances the effects due to the orbital localization. This makes the trend for U_{mm} rather "flat" in comparison to W_{mm} and v_{mm}.

The values of U_{mm}, on the other hand, indicate how strong the contribution of the dd screening channels is to the total polarizability. These channels are however only partly responsible for the screening that reduces v_{mm}. The role of the p-d screening channels can be also evaluated. These channels seem relevant according to the position of the Kohn-Sham p states. By computing the partially screened interaction after the elimination of all transitions within the energy window $\mathbb{W}$ (mainly p-d and d-d transitions), one gets 11 eV in $SrVO_3$, 10.8 eV for $SrCrO_3$ and 10.7 eV for $SrMnO_3$. It is about the half of v_{mm}. The lower-energy screening channels (dd, pd, ...) thus contribute to about the half of the total screening. As empirically expected, the higher-energies transitions notably participate to the total polarizability leading to the strong reduction of the bare Coulomb repulsion.

Hund's exchange J is deduced from the Slater integrals F^2 and F^4 (Tab. 7.2). J goes from about 0.8 eV to $J_{\text{bare}} \approx 1.0$ eV in $SrMO_3$. The exchange interactions between t_{2g} orbitals, J_m, are smaller than J (about $0.6 - 0.7$ eV) and agree with the values usually employed in the Hubbard models for such oxides.

We also evaluate the fully screened exchange interaction J_m^{screened} when taking into account the total polarization (Tab. 7.3).J_m^{screened} slightly decreases from V to Mn compounds whereas it is the opposite for unscreened exchanges J_m^{bare}. This can be related to the screening. Cutting off only transitions from and to the d bands leads to J_m which is still increasing with the atomic number: on the difference to U_{mm}, J_m hence reproduces an atomic-like trend. The dependence on the screening is much weaker for exchange interactions [Antonides *et al.* (1977), van der Marel(1985)]. This justifies that the partially screened exchange interactions J_m vary in a similar way than J_m^{bare}.

Orbitally-resolved Hubbard interaction matrices

We give below the reduced interaction matrices (Eqs. 5.78, 5.79 and 5.80) within the d-dp Hamiltonian (see Tab. 7.1 for the choice of the energy windows used to construct the d Wannier orbitals) and calculated with cubic symmetry. In the following, the ordering of the orbitals in these matrices is $d_{z^2}, d_{x^2-y^2}, d_{xy}, d_{xz}, d_{yz}$. The values are given in eV.

$SrVO_3$

$$U^{\sigma\bar{\sigma}}_{mm'} = \begin{pmatrix} 4.43 & 2.88 & 2.73 & 3.19 & 3.19 \\ 2.88 & 4.43 & 3.35 & 2.88 & 2.88 \\ 2.73 & 3.35 & 3.97 & 2.75 & 2.75 \\ 3.19 & 2.88 & 2.75 & 3.97 & 2.75 \\ 3.19 & 2.88 & 2.75 & 2.75 & 3.97 \end{pmatrix}, U^{\sigma\sigma}_{mm'} = \begin{pmatrix} 0 & 2.10 & 2.01 & 2.70 & 2.70 \\ 2.10 & 0 & 2.94 & 2.24 & 2.24 \\ 2.01 & 2.94 & 0 & 2.15 & 2.15 \\ 2.70 & 2.24 & 2.15 & 0 & 2.15 \\ 2.70 & 2.24 & 2.15 & 2.15 & 0 \end{pmatrix}.$$

$SrCrO_3$

$$U^{\sigma\bar{\sigma}}_{mm'} = \begin{pmatrix} 3.84 & 2.39 & 2.40 & 2.87 & 2.87 \\ 2.39 & 3.84 & 3.02 & 2.56 & 2.56 \\ 2.40 & 3.02 & 3.89 & 2.59 & 2.59 \\ 2.87 & 2.56 & 2.59 & 3.89 & 2.59 \\ 2.87 & 2.56 & 2.59 & 2.59 & 3.89 \end{pmatrix}, U^{\sigma\sigma}_{mm'} = \begin{pmatrix} 0 & 1.66 & 1.67 & 2.38 & 2.38 \\ 1.66 & 0 & 2.61 & 1.91 & 1.91 \\ 1.67 & 2.61 & 0 & 1.94 & 1.94 \\ 2.38 & 1.91 & 1.94 & 0 & 1.94 \\ 2.38 & 1.91 & 1.94 & 1.94 & 0 \end{pmatrix}.$$

$SrMnO_3$

$$U^{\sigma\bar{\sigma}}_{mm'} = \begin{pmatrix} 3.62 & 2.17 & 2.25 & 2.74 & 2.74 \\ 2.17 & 3.62 & 2.90 & 2.41 & 2.41 \\ 2.25 & 2.90 & 3.90 & 2.52 & 2.51 \\ 2.74 & 2.41 & 2.52 & 3.91 & 2.52 \\ 2.74 & 2.41 & 2.51 & 2.52 & 3.90 \end{pmatrix}, U^{\sigma\sigma}_{mm'} = \begin{pmatrix} 0 & 1.44 & 1.49 & 2.22 & 2.22 \\ 1.44 & 0 & 2.47 & 1.73 & 1.73 \\ 1.49 & 2.47 & 0 & 1.81 & 1.81 \\ 2.22 & 1.73 & 1.81 & 0 & 1.81 \\ 2.22 & 1.73 & 1.81 & 1.81 & 0 \end{pmatrix}.$$

We now switch to the t_{2g}-t_{2g} model which was already introduced for $SrVO_3$ in Chapter 6. One advantage of such reduced model is the smaller number of correlated orbitals that have to be solved within a many-body approach. If the model is appropriate, then the physical results at the end (e.g. spectral densities, transport properties) do not depend on the model considered, whereas interaction parameters do.
Within the t_{2g}-t_{2g} model, it is not possible to compute the Slater integrals by Eq. 5.62. We calculate the Hubbard-Kanamori fitting parameters $\mathcal{U}, \mathcal{J}$ directly from the reduced interaction matrices with cubic symmetry $U^{(cubic)}_{mm'mm'}$ and $U^{(cubic)}_{mm'm'm,m\neq m'}$, respectively (from Eq. 5.75 to Eq. 5.77). Since the so constructed basis is far away from an atomic-like basis and because of the screening, the results are deviated from the atomic expectations: $\mathcal{U}$ significantly decreases with the atomic number. Values for $\mathcal{J}$ are much smaller than the ones within the d-dp model, showing that Hund's exchange depends on the orbital extension.

7.1.3 Hubbard parameters within the t_{2g}-t_{2g} Hamiltonian

Localized orbitals

Within the t_{2g}-t_{2g} Hamiltonian, the t_{2g}-projected local orbitals within the energy window $\mathbb{W}_{t_{2g}}$ (Tab. 7.1) lead to "extended" t_{2g} Wannier orbitals. The charge transfer energy and the hybridization between the t_{2g} and the oxygen ligand p bands, are responsible for the finite weight of the t_{2g} Wannier functions on the oxygen atomic sites. The tail and hence the extension of the so constructed local orbitals, increases when the pd charge transfer energy becomes smaller, as happens for the $3d$ $SrMO_3$ series.

Looking at the DFT-LDA band structure and the partial density of states (Fig. 7.2), the charge transfer energy p-t_{2g} decreases from $SrVO_3$ to $SrMnO_3$ as already pointed out in the previous section. This is not an artifact of DFT-LDA: the evolution of the p-d charge transfer energy in

(eV)	V	Cr	Mn	Nb	Mo	Tc
$\mathcal{U}$	3.2	2.7	1.8	3.0	3.0	2.9
$\mathcal{J}$	0.44	0.42	0.39	0.29	0.31	0.31
$\mathcal{V}$	16.1	16.4	16.2	10.7	11.6	11.8
$\mathcal{J}_{\text{bare}}$	0.55	0.55	0.53	0.38	0.40	0.39
$\mathcal{W}$	0.9	0.4	0.3	0.9	0.5	0.4
$\mathcal{J}_{\text{screened}}$	0.30	0.17	0.12	0.24	0.19	0.16
$\mathcal{U}/\mathcal{V} \times 100$	19.8	16.4	11.1	28	25.8	24.6
$\mathcal{W}/\mathcal{V} \times 100$	5.6	2.4	1.8	8.4	4.3	3.4

Table 7.5: Hubbard-Kanamori $\mathcal{U}$, bare $\mathcal{V}$ and fully screened $\mathcal{W}$ interactions and corresponding exchange interactions, $\mathcal{J}$, $\mathcal{J}_{\text{bare}}$ and $\mathcal{J}_{\text{screened}}$ between t_{2g} orbitals within the t_{2g}-t_{2g} downfolded Hamiltonian for the early $3d$ series $SrMO_3$ (M= V, Cr, Mn) and $4d$ (M= Nb, Mo, Tc). The inter-orbital interactions $\mathcal{U}'$ coincide with $\mathcal{U} - 2\mathcal{J}$.

perovskite oxides was known for a long time [Torrance *et al.* (1991), Imada *et al.* (1998)] and was evidenced in optics experiments [Lee *et al.* (2003)].

The t_{2g} local orbitals are hence more extended in $SrMnO_3$ than in $SrVO_3$, in contrast to the atomic orbitals. It implies that i) the unscreened interaction $\mathcal{V}$ within the t_{2g}-t_{2g} model does not increase with the atomic number as v_{mm} in the previous d-dp model (Fig. 7.3 and Tab. 7.2) and ii) the values of $\mathcal{V}$ are smaller than the values of v_{mm} within d-dp.

Hubbard parameters

The Hubbard-Kanamori values employed in the t_{2g}-restricted Hubbard Hamiltonian (Eq. 5.86) are given in Tab. 7.5 and shown in Fig. 7.3: compared to the d-dp model [3], the decrease of $\mathcal{U}$ is much more pronounced. $\mathcal{U}$ significantly lessens from $SrVO_3$ to $SrMnO_3$.

This is induced by the screening which gets larger with the atomic number. In particular, the p-t_{2g} and the t_{2g}-e_g screening channels contribute more and more to the screening from $SrVO_3$ to $SrMnO_3$, because the p and e_g Kohn-Sham bands come closer and closer to the Fermi level. Quantitatively, one compares the ratios $\mathcal{U}/\mathcal{V}$: it is indeed about twice larger in $SrVO_3$ than in $SrMnO_3$. Considering all screening channels (hence looking at $\mathcal{W}$) does not change our interpretation : the screening through the $3d$ series induces a strong reduction of $\mathcal{W}$.

We insist on the fact that the lower-energy screening channels such as d-p or t_{2g}-t_{2g}, are not enough to fully reduce the bare interaction $\mathcal{V}$ to $\mathcal{W}$. In $SrVO_3$, for example, removing the t_{2g}-t_{2g} transitions makes $\mathcal{W}/\mathcal{V}$ varying from $5.5/100$ to $\mathcal{U}/\mathcal{V} = 20.3/100$. The screening channels at higher energies – or polarizabilities at higher energies – also contribute to the total polarizability.

The exchange interactions within the t_{2g}-t_{2g} Hamiltonian for $SrMO_3$ are given in Tab. 7.5. In contrast to d-dp, $\mathcal{J}$ and $\mathcal{J}_{\text{bare}}$ slightly decrease with the number of d electrons. On the other

[3] We remind the reader that in the d-dp model, all d-d transitions are removed.

hand, there is a significant reduction in $\mathcal{J}_{\text{screened}}$ through the series, which can be attributed to the screening induced by the t_{2g}-t_{2g} transitions.

The exchange interactions thus depend on the extension of the localized orbitals. This dependence is also evidenced by the smaller values obtained within t_{2g}-t_{2g} than within the d-dp Hamiltonian.

7.1.4 Comparison between 3d and 4d perovskites

Band structures

The DFT-LDA band structures for 4d perovskites are shown in Fig. 7.4. The evolution of the Kohn-Sham bands from Nb to Tc is globally equivalent to the one for the isoelectronic and isostructural 3d oxides, but the trends are less pronounced in 4d: the p-d charge transfer energy decreases slower in the 4d series as well as the crystal field effect that splits t_{2g} and e_g. One therefore expects smaller screening effects in $SrTcO_3$ than in $SrMnO_3$.

Due to the entanglement of the e_g's with the strontium states, it is not appropriate to construct a d-dp model with a cRPA scheme that is based on band indices or energy windows for constraining the polarization. Only t_{2g}-t_{2g} Hamiltonians are thus considered below for 4d $SrMO_3$.

Localized orbitals

The atomic-like character of the localized orbitals with t_{2g} character is evidenced by the atomic-like behavior of the bare interaction $\mathcal{V}$ in the 4d series (Fig. 7.3) : $\mathcal{V}$ becomes larger with the atomic number, as in 3d oxides but within the d-dp model. The local basis constructed with t_{2g} degrees of freedom is atomic-like for 4d TMO in contrast to the one for 3d. The difference in 4d comes from the larger charge transfer energy between t_{2g} and the oxygen ligand p states, leading to smaller "leakages" on the oxygen sites.

However, the extension of the t_{2g} orbitals in 4d TMO is larger than in 3d since the bare interactions $\mathcal{V}$ are significantly smaller (Tab. 7.5). This makes sense in an atomic-like basis where the 4d atomic wavefunction extension is much larger than the one for 3d (Tab. 7.4).

In the following, the Hubbard-Kanamori interaction $\mathcal{U}$ and Hund's exchange $\mathcal{J}$ are calculated for a further use in the t_{2g}-restricted Hubbard Hamiltonian (Eq. 5.86). We expect similar trends for these interactions in 4d within t_{2g}-t_{2g} models than in 3d within d-dp models.

Hubbard parameters

In a similar way than in 3d, one has to study the screening in order to interpret the values of $\mathcal{U}$ (Tab. 7.5). Since the pd charge transfer energy as well as the t_{2g}-e_g splitting energy decrease slower, the p-d and the t_{2g}-e_g screening channels are not as effective as in the 3d analogues. This is quantitatively highlighted by the comparison of the ratios $\mathcal{U}/\mathcal{V}$ (Tab. 7.5). First, these

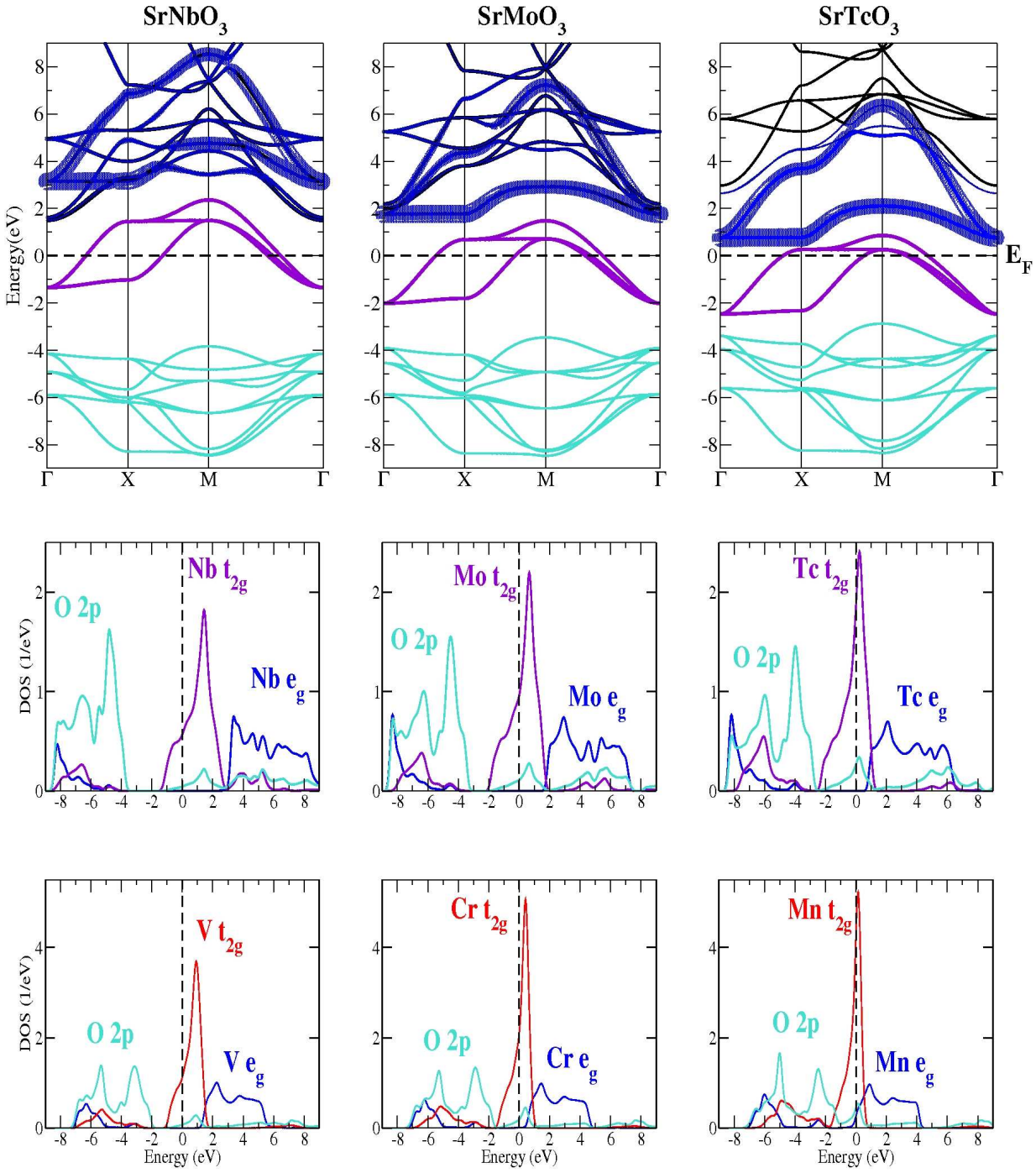

Figure 7.4: DFT-LDA paramagnetic eigenstates (top) and partial density of states (middle) of $SrMO_3$ (M = Nb, Mo, Tc from left to right). $4d$ t_{2g} states are highlighted in purple, $4d$ e_g in blue and oxygen $2p$ in turquoise. For comparison, the density of states of the $3d$ isoelectronic and isostructural analogues (bottom) are also shown. It is clear that the LDA p-d charge transfer energy is bigger in $4d$ than in $3d$ perovskites.

quantities are always bigger in $4d$ than in $3d$ and second, the decrease of $\mathcal{U}/\mathcal{V}$ through the $4d$ series is much slower.

Consequently, $\mathcal{U}$ in $4d$ is almost constant with the d electron number (as U_{mm} within the d-dp model for $3d$ TMO), whereas $\mathcal{U}$ in $3d$ significantly lessens until becoming smaller in $SrMnO_3$ than in $SrTcO_3$ (Fig. 7.5). This is an effect of the screening which has stronger impact in the $3d$ *extended* local basis than in the $4d$ *atomic-like*. The values for the ratios $\mathcal{W}/\mathcal{V}$ (Tab. 7.5) also agree with a smaller electronic polarizability in $4d$ than in $3d$ TMO since they are larger in $4d$ than in $3d$.

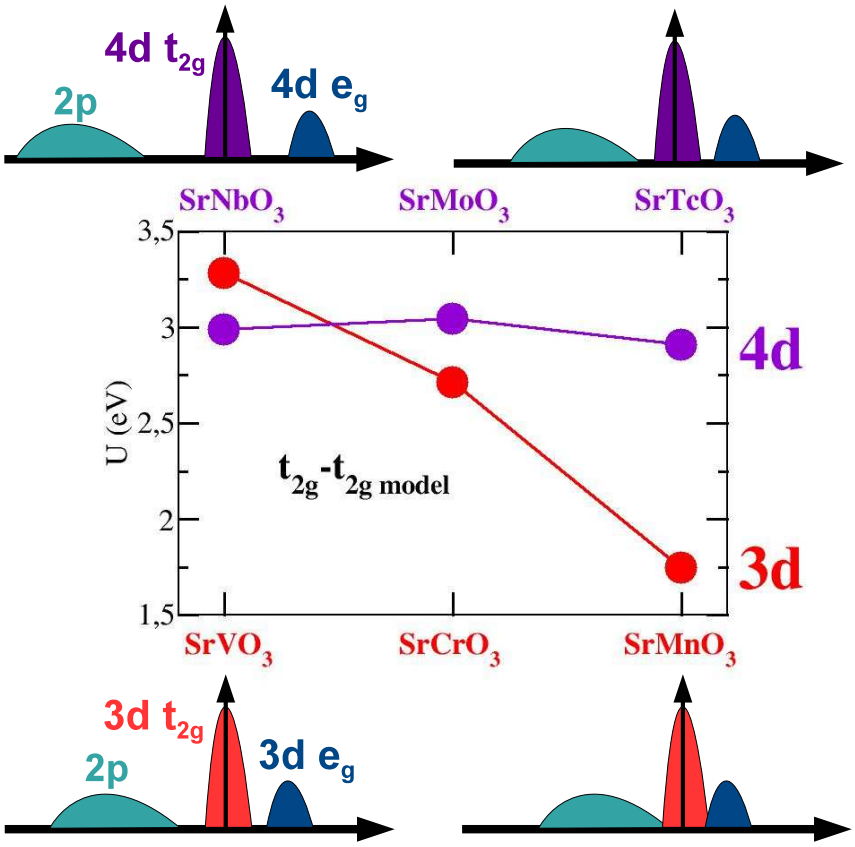

Figure 7.5: Hubbard-Kanamori interactions $\mathcal{U}$ between t_{2g} orbitals within the t_{2g}-t_{2g} model : $3d$ (in red) and $4d$ (in purple) perovskites $SrMO_3$. The schematic DFT-LDA density of states are shown in order to highlight the evolution of the pd charge transfer energy and the t_{2g}-e_g splitting energy. Comparing $SrMnO_3$ to $SrTcO_3$, the screening becomes strong enough in $SrMnO_3$ such that $\mathcal{U}$ is smaller than in $SrTcO_3$.

The exchange interactions in $4d$ TMO behave in a similar way than in $3d$ (Tab. 7.5) but $\mathcal{J}_{\text{bare}}$, $\mathcal{J}$ and $\mathcal{J}_{\text{screened}}$ decrease slower with the d electron number.

The atomic-like character of the localized basis and the weaker screening effects in $4d$ $SrMO_3$ explain the slower decrease of the exchange interactions.
Furthermore, the exchange interactions in $4d$ TMO are smaller by about 0.1 eV than in $3d$. This

is attributed to the higher extension of the $4d$ orbitals, which was also responsible for the smaller bare interactions $\mathcal{V}$.

7.1.5 $SrMnO_3$

Hubbard $\mathcal{U} = 1.8$ eV within the t_{2g}-t_{2g} model seems surprisingly small for cubic $SrMnO_3$ in particular compared to $SrVO_3$ ($\mathcal{U} = 3.2$ eV) and $SrTcO_3$ ($\mathcal{U} = 2.9$ eV). The proximity of the d and p states around the Fermi level in $SrMnO_3$ makes difficult the cRPA scheme employing Kohn-Sham $\boldsymbol{k}$-independent indices for calculating the constrained polarization P^r. This causes a small uncertainty for determining $\mathcal{U}$. Indeed, employing the same energy window $[-1.7, 0.9]$ eV than $\mathbb{W}$ (Tab. 7.1) for cutting off the t_{2g}-t_{2g} transitions leads to $\mathcal{U} = 2.3$ eV and $\mathcal{J} = 0.41$ eV. Hund's exchange, on the other hand, does not really change.

The small magnitude of $\mathcal{U}$ was interpreted in the previous section in terms of the screening (especially the p-d and t_{2g}-e_g screening channels) so approximated by the DFT-LDA Kohn-Sham states. As already discussed, the calculation within the d-dp model leads to larger results : $U = \mathrm{F}^0 = 2.8$ eV and $\bar{U}_{mm} = 3.8$ eV between the t_{2g} orbitals, but these values are still smaller than the ones expected in the literature. Indeed, $SrMnO_3$ was described within configuration-interaction approaches employing $\mathrm{F}^0 \approx 8$ eV and a charge transfer energy around 2 eV in order to fit the $2p$ core-level XPS spectra [Bocquet *et al.* (1992), Saitoh *et al.* (1995)].

As shown recently in $SrVO_3$ by considering the dynamical screening in the Hubbard model [Casula *et al.* (2012a), Werner *et al.* (2012), Casula *et al.* (2012b)], one knows that the dynamical structure of the Hubbard interactions increases the strength of the correlations and hence leads to a more "correlated" system. The aspect of the Hubbard interaction in $SrMnO_3$ within the d-dp Hamiltonian (Fig. 7.6) is rather close to the one of $SrVO_3$. Consequently, one expects similar renormalization effects in $SrMnO_3$ than in $SrVO_3$ from an extended DMFT calculation with $U(\omega)$.

For $SrMnO_3$, one observes a strong plasmon pole around 13 eV and hence at a smaller energy than in $SrVO_3$ (around 15 eV). This does not fit with the plasmon frequency formula established for the homogeneous electron gas (Eq. 6.1), since the number of d electrons is larger in $SrMnO_3$ and the volume is smaller (see Tab. 7.1).

On the other hand, it would be interesting to investigate the effects in the screening of the rearrangement of the electronic structure due to the correlations. An overestimated screening in DFT-LDA would result into underestimated Coulomb interactions. This could be corrected for by a self-consistent "LDA+cRPA+DMFT" scheme employing an update of the polarization as described in Chapter 4 (see Fig. 4.7). A preliminary attempt to deal with a more realistic screening can be done by evaluating the constrained polarization P^r within Green's functions shifted by $(+) - \Delta$ for transitions involving (un)occupied Mn-t_{2g} states. This mimicks the contribution of the t_{2g} states in the constrained polarization that would be calculated within the Hubbard-I approximation.

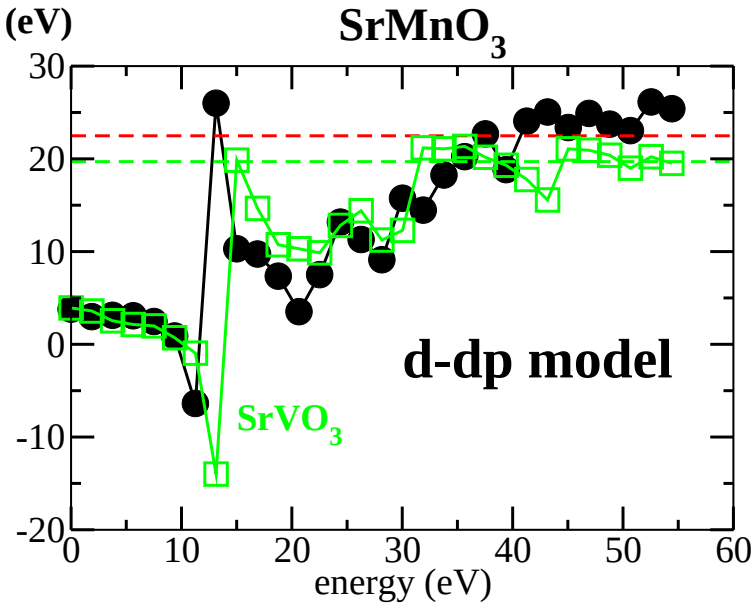

Figure 7.6: Real-part of the dynamical Hubbard interaction $U_{mm}(\omega)$ for the d-dp Hamiltonian in $SrMnO_3$ (black). The bare interaction is shown in red dashed line. The real-part of $U_{mm}(\omega)$ within the d-dp Hamiltonian of $SrVO_3$ (green) and the corresponding bare interaction (green dashed line) are shown for comparison. The main plasmon pole in $SrMnO_3$ is obtained around 13 eV. This is smaller than in $SrVO_3$ whereas the number of d electrons in $SrMnO_3$ is larger and the volume of the unit cell is smaller.

With $\Delta = 2$ eV, we obtain $\mathcal{U} = 3.4$ eV and $\mathcal{J} = 0.45$ eV within the t_{2g}-t_{2g} Hamiltonian. [4] The values are hence notably increased compared to the ones from standard cRPA. This promising approach requires further investigations.

However, $\mathcal{U}$ as small as it is calculated by standard cRPA within the t_{2g}-t_{2g} Hamiltonian does not yield wrong physical picture because of the value of Hund's exchange $\mathcal{J} = 0.39$ eV. The ratio $\mathcal{J}/\mathcal{U} = 0.22$ is rather high. In $SrMnO_3$, the t_{2g} manifold is half-filled. It is known that in this case, Hund's coupling promotes a Mott insulating state and tends to increase the Mott gap (see e.g. [de' Medici *et al.* (2011)]).

In the following, we show the LDA+DMFT calculation for the t_{2g}-t_{2g} model with the cRPA interaction parameters $\mathcal{U} = 1.8$ eV and $\mathcal{J} = 0.4$ eV, in order to demonstrate that the correct physical picture is obtained. Indeed, with these values, $SrMnO_3$ results into a Mott insulating state with a gap of about 2.2 eV. In PES experiments, the lower Hubbard band is embedded with oxygen p states around 2 eV [Kang et al. (2008)].
We then consider the hexagonal crystal structure of $SrMnO_3$ as described by [Daoud-Aladine et al. (2007)]. It is satisfying that the cRPA results do not depend much on the crystal structure.

[4] We mention that the e_g states have been shifted by 0.5 eV above the Fermi level in this scheme. The metallicity arising from the e_g's (see Fig. 7.2) is an artefact of LDA.

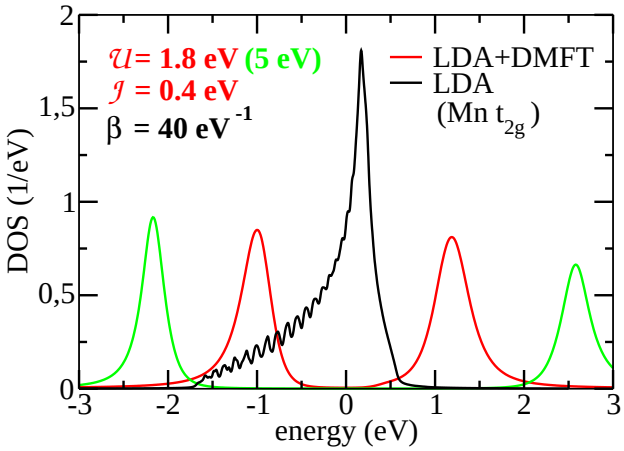

Figure 7.7: (top) LDA density of states (in black) and LDA+DMFT spectral density (in red) for the t_{2g} orbitals in cubic $SrMnO_3$. One employed $\mathcal{U} = 1.8$ eV and $\mathcal{J} = 0.4$ eV as obtained by cRPA within the t_{2g}-t_{2g} Hamiltonian. We also calculate (in green) the LDA+DMFT spectral density using same J but $\mathcal{U} = 5$ eV in order to approximatively fit the lower Hubbard band from PES [Kang *et al.* (2008)].

LDA+DMFT calculation for the t_{2g}-t_{2g} Hamiltonian

As discussed earlier, a set of local orbitals with t_{2g} character is constructed out of Kohn-Sham bands within the energy window $\mathbb{W} = [-1.7, 0.9]$ eV. The basis is employed for expanding the interaction Hubbard Hamiltonian (Eq. 5.86). The Hubbard-Kanamori parameters are calculated within cRPA : $\mathcal{U} = 1.8$ eV, $\mathcal{J} = 0.4$ eV and $\mathcal{U}' = \mathcal{U} - 2\mathcal{J} = 1$ eV. The reduced interaction matrices with cubic symmetry read as ($\mathcal{U} - 3\mathcal{J} = 0.6$ eV) :

$$U^{\sigma\sigma}_{mm'} = \begin{pmatrix} 0 & 0.6 & 0.6 \\ 0.6 & 0 & 0.6 \\ 0.6 & 0.6 & 0 \end{pmatrix} U^{\sigma\bar{\sigma}}_{mm'} = \begin{pmatrix} 1.8 & 1.0 & 1.0 \\ 1.0 & 1.8 & 1.0 \\ 1.0 & 1.0 & 1.8 \end{pmatrix}.$$

The non-density-density terms are neglected in the Hubbard Hamiltonian. Only density-density Hubbard Hamiltonian is then solved by DMFT. The quantum impurity solver chosen is the CTQMC algorithm as implemented in [Aichhorn *et al.* (2009)] (see Chapter 3). We employ $\beta = 40$ eV^{-1} in the *"one-shot"* version of LDA+DMFT (Fig. 7.7).

Within the t_{2g}-restricted Hubbard Hamiltonian from cRPA, the Mott insulating state is caught by LDA+DMFT. The gap obtained yields around 2.2 eV. The lower Hubbard band is located around -1 eV. This is smaller than in PES experiments [Kang *et al.* (2008)], which report the lower Hubbard band at about -2 eV. Larger values of $\mathcal{U}$ for the same value of $\mathcal{J}$ make the lower Hubbard band going down to lower energies (Fig. 7.7).

The influences of structural distortions

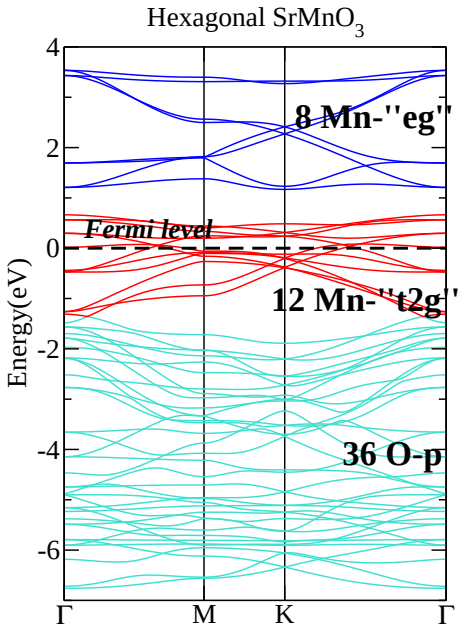

Figure 7.8: DFT-LDA band structure of the four-layers hexagonal unit cell of $SrMnO_3$ in the paramagnetic phase. Lattice parameters $a = 5.461\text{A}^\circ, c = 9.093\text{A}^\circ$ are taken from [Daoud-Aladine *et al.* (2007)].

At room temperature, $SrMnO_3$ is more often found in the four-layers hexagonal structure ($P63/mmc$) with $a = 5.461$ Å, $c = 9.093$ Å [Daoud-Aladine *et al.* (2007)]. The DFT-LDA band structure is shown in Fig. 7.8 : similarly than in the cubic structure, DFT-LDA leads to a metallic phase whereas $SrMnO_3$ is an insulator.

The four-times larger unit cell leads to a backfolding of bands in the first Brillouin zone. A set of t_{2g}-like bands (Fig. 7.8) can be identified with the twelve bands around the Fermi level and a set of e_g-like bands with the eight ones above. A d-dp model is constructed rather than a t_{2g} one. This allows for a direct comparison of the Slater integrals (Eq. 5.62) calculated within the d-dp model built for the cubic crystal structure (Tab. 7.6).

U as well as v are slightly bigger in the hexagonal phase than in the cubic one. This is an effect of the Wannier orbital localization rather than a screening effect since also the bare interaction v is enhanced. Hund's exchange J does not change much between the two crystal structures.

(eV)	F^0	F^2	F^4	F^4/F^2	J	F^0_{bare}	F^2_{bare}	F^4_{bare}	$F^4/F^2\|_{\text{bare}}$	J_{bare}
cubic	2.8	7.0	5.4	0.774	0.9	21.2	9.6	6.0	0.625	1.1
hexagonal	3.1	7.2	5.6	0.777	0.9	21.9	9.9	6.2	0.621	1.1

Table 7.6: Screened and bare Slater integrals for the d-dp model in cubic and hexagonal $SrMnO_3$. Values of F^0 are slightly larger in the hexagonal crystal structure whereas Hund's couplings $J = (F^2 + F^4)/14$ are identical.

7.2 Sr_2MO_4 (M = Mo, Tc, Ru, Rh)

7.2.1 Band structures

The layered perovskite oxides Sr_2MO_4, where M^{4+} is a $3d$ transition metal, have been extensively studied because of their fascinating properties, e.g. cuprates exhibit high-Tc superconductivity, manganites and nickelates display spin, charge and orbital stripes (for a review, see [Imada *et al.* (1998)]). Many of these properties are believed to arise from the quasi-two-dimensionality of the electronic states close to the Fermi level and induced by the presence of inter-layer planes. These planes behave as charge reservoirs (Fig. 7.9) and their number, until a certain limit, even seems to induce a higher critical temperature for superconductivity in cuprates.

The series of $4d$ transition metal layered perovskite oxides, on the other hand, have not received as much attention as $3d$, although they are also intriguing materials. For example, they can display unconventional superconductivity as it was discovered in Sr_2RuO_4 ($T_c \leq 2$K) [Mackenzie and Maeno(2003)]. The lattice parameters used in the electronic structure calculations for the paramagnetic phase are given in Table 7.7.

Sr_2MoO_4

This compound exhibits a metallic behavior over a wide range of temperature between 80 mK and 300 K, with a resistivity increasing between 2 and 10 mΩ.cm [Ikeda *et al.* (2000)]. It is usually investigated under the possibility that it could exhibit analogous electronic properties than Sr_2RuO_4, although a superconducting state has not been reported down to 25 mK.

Sr_2TcO_4

Due to the radioactivity of technetium elements, only structural properties are known for Sr_2TcO_4. An undistorted layered perovskite structure is considered below.

Sr_2RuO_4

The resistivity of this compound obeys a T^2 law below 30 K, evidencing a Fermi liquid behavior. A strong anisotropy of the transport properties – due to its layered structure – was re-

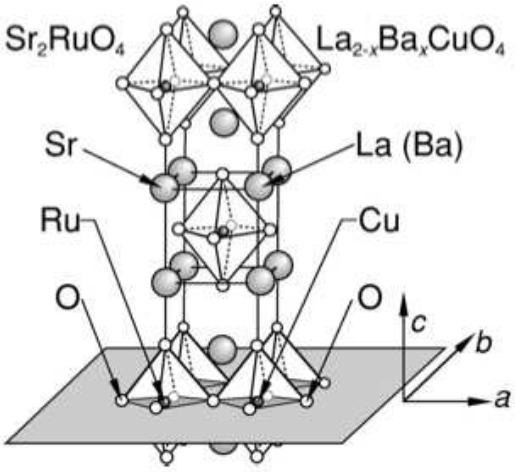

Figure 7.9: Schematic crystal structure of Sr_2RuO_4 in analogy with the cuprate compound $La_{2-x}Ba_xCuO_4$ (from [Mackenzie and Maeno(2003)]). The ruthenium atoms are surrounded by octahedra RuO_6 of oxygen atoms as in $SrMO_3$ but planes of strontium atoms are inserted between the planes of octahedra.

ported [Hussey *et al.* (1998)]. A large mass enhancement and a low coherence scale have been determined experimentally. Sr_2RuO_4 also exhibits an unconventional superconductivity below 2 K [Mackenzie and Maeno(2003)].
The three-sheet Fermi surface determined experimentally is reasonably well described by DFT-LDA calculations, but the enhancement and the anisotropy in the mass are missed. The largest mass enhancement surprisingly appears for the widest d_{xy} band as determined by quantum oscillations experiments [Mackenzie and Maeno(2003)]. Several LDA+DMFT calculations have been carried out to reproduce the low-energy properties of the photoemission spectra [Mravlje *et al.* (2011), Liebsch and Lichtenstein(2000), Anisimov *et al.* (2002), Pchelkina *et al.* (2007)]. In [Mravlje *et al.* (2011)], the authors employed a t_{2g}-t_{2g}-like model : they constructed (d_{xy}, d_{xz}, d_{yz}) Wannier functions out of Kohn-Sham bands with the energy window $\mathbb{W} = [-3, 1]$ eV and they applied cRPA within MLWF by removing the t_{2g}-t_{2g} transitions from the total polarization. They got orbitally-resolved Hubbard interaction matrix elements, $U_{\text{dxy}} = 2.5$ eV, $U_{\text{dxz/dyz}} = 2.2$ eV, and used as Hubbard-Kanamori parameters, $\mathcal{U} = 2.3$ eV and $\mathcal{J} = 0.4$ eV in the t_{2g}-like Hubbard Hamiltonian (Eq. 5.86).

Sr_2RhO_4

The symmetry is lowered from the K_2NiF_4 class by 11° rotation around the c-axis of the RhO_6 octahedra [Huang *et al.* (1994)]. It is a paramagnetic metal down to 36 mK [Moon *et al.* (2006)]. Spin-orbit coupling (SOC) was found to be relevant in addition to electronic correlations [Tamai *et al.* (2008), Haverkort *et al.* (2008), Liu *et al.* (2008)]. LDA+DMFT calculations with SOC have

	a (Å)	c (Å)	$\mathbb{W}_{dp}$	$\mathbb{W}_{t_{2g}}$
Sr_2MoO_4	3.917	12.859	$[-10, 8.5]$	$[-2.0, 2.0]$
Sr_2TcO_4	3.902	12.720	$[-10, 7.5]$	$[-2.6, 1.3]$
Sr_2RuO_4	3.863	12.724	$[-10, 6.9]$	$[-3.0, 1.0]$
Sr_2RhO_4	3.854	12.880	$[-10, 6.0]$	$[-3.3, 0.5]$

Table 7.7: Lattice parameters used for the layered Sr_2MO_4 perovskites and energy windows $\mathbb{W}$ (in eV) for the d-dp and t_{2g}-t_{2g} models.

been recently performed for the distorted structure and compared to the isoelectronic but Mott insulating Sr_2IrO_4 [Martins *et al.* (2011)]. In particular, it was shown how the interplay of SOC, correlations and structural distortions leads to a suppress of the effective orbital degeneracy, leaving only two orbitals at the Fermi level. In the following, for computational reasons, the undistorted crystal structure of Sr_2RhO_4 is considered. The distorted band structure will be discussed in Chapter 8 in comparison with Sr_2IrO_4.

The DFT-LDA band structures for the paramagnetic phases are shown in Fig. 7.10. Bands with (d_{xy},d_{xz},d_{yz}) orbital character emerge around the Fermi level, whereas the ($d_{3z^2-r^2}$,$d_{x^2-y^2}$) orbital character is found above and the oxygen p's lie below. The band with d_{xy} character leads to a quasi-two dimensional Fermi surface whereas the degenerate bands with (d_{xz},d_{yz}) character give rise to a quasi-one dimensional Fermi surface. In Sr_2MoO_4 and Sr_2TcO_4, the e_g states are entangled with the strontium-like d's but come closer to the t_{2g}'s when the $4d$ electron number increases. On the other hand, the pd charge transfer energy decreases with this number, since the p's go up toward the Fermi level. This decrease makes larger the screening from the p channels, in an analogous way to in the early transition metal oxide series.

7.2.2 Hubbard parameters within the d-dp Hamiltonian

Orbital localization

The localized orbitals with d character within the d-dp model are constructed out of Kohn-Sham bands within an extended energy window $\mathbb{W}$ (Tab. 7.7) that includes the d's as well as the oxygen p eigenstates.

The Slater integrals are given in Tab. 7.8. The value of the ratio $F^4/F^2|_{\text{bare}}$ is close to the one calculated for $4d$ atoms [Haverkort(2005)]. A significant deviation is obtained for the screened ratio of the Slater integrals, which is even stronger than the one in the $3d$ $SrMO_3$ series. This seems natural, given the anisotropy of the structure and the screening which increases with the orbital extension.

A cubic approximation can be used for deducing a set of interactions between (d_{xy},d_{xz},d_{yz}) local orbitals from the Slater integrals (Eqs. 5.70, 5.71 and 5.72). The values are shown in Tab. 7.9 and can be compared to the matrix elements calculated directly (Tab. 7.10). The latter are

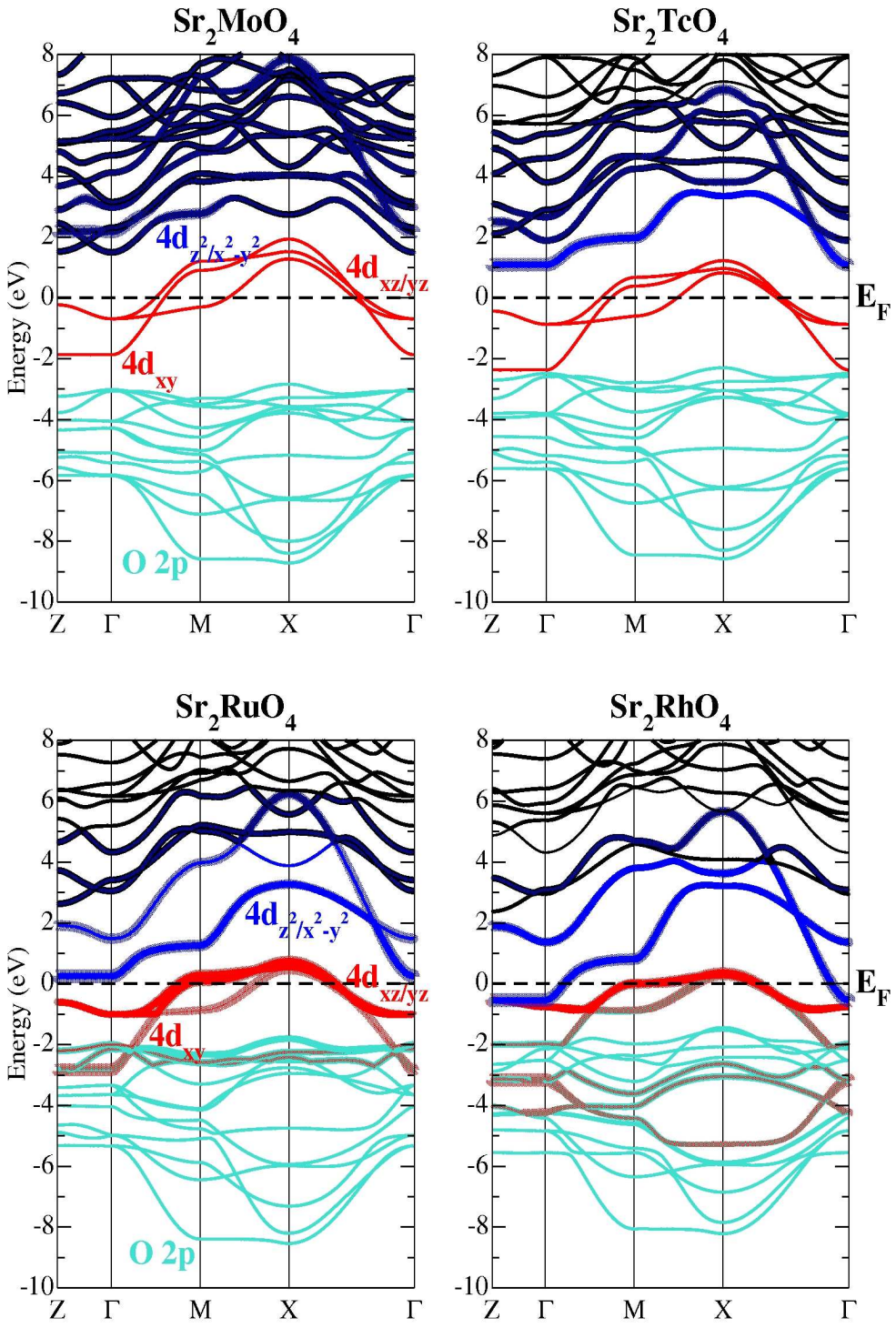

Figure 7.10: DFT-LDA paramagnetic band structures for layered perovskite oxides Sr_2MO_4. (top panel): From left to right: M = Mo, Tc. (bottom panel): From left to right: M = Ru, Rh.

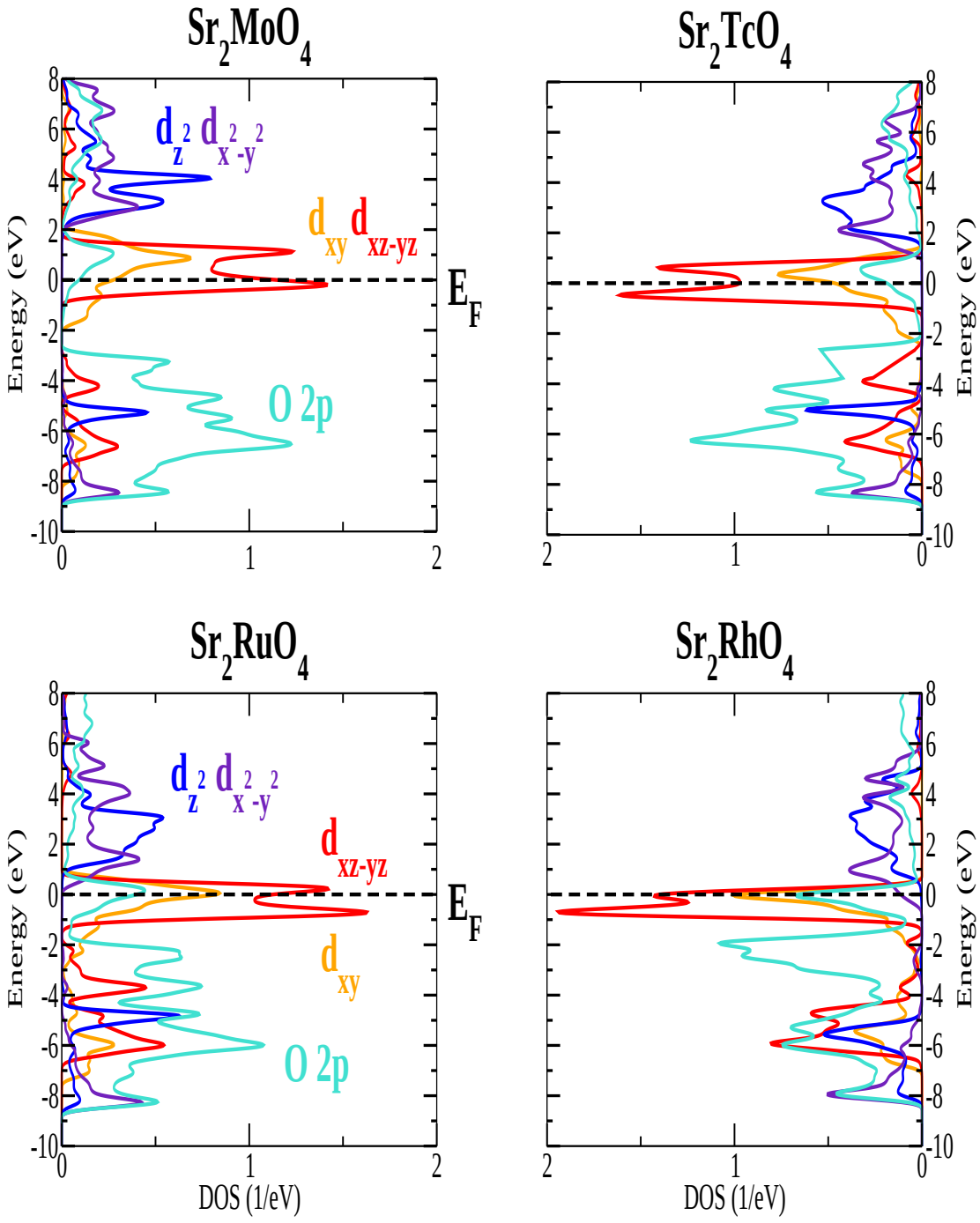

Figure 7.11: DFT-LDA paramagnetic density of states for layered perovskite oxides Sr_2MO_4. (top panel): From left to right: M = Mo, Tc. (bottom panel): From left to right: M = Ru, Rh.

(eV)	F^0	F^2	F^4	F^4/F^2	J	F^0_{bare}	F^2_{bare}	F^4_{bare}	$F^4/F^2\|_{\text{bare}}$	J_{bare}
Mo	3.26	5.05	4.36	0.862	0.67	14.50	7.19	4.92	0.684	0.86
Tc	3.19	5.30	4.51	0.850	0.70	15.25	7.53	5.07	0.673	0.90
Ru	3.23	5.64	4.73	0.838	0.74	15.97	7.87	5.26	0.669	0.94
Rh	3.44	6.04	4.95	0.820	0.78	16.77	8.24	5.46	0.663	0.98

Table 7.8: (d-dp model) Static (screened) and bare (unscreened) Slater integrals for the d-dp Hamiltonian in $4d$ Sr_2MO_4. It follows that the Hubbard parameter $U = F^0$ and Hund's exchange $J = (F^2 + F^4)/14$. On the other hand, the bare interaction parameter reads as $v = F^0_{\text{bare}}$ and bare exchange as $J_{\text{bare}} = (F^2_{\text{bare}} + F^4_{\text{bare}})/14$. The screened ratio F^4/F^2 is strongly deviated from the atomic value but at large frequency $F^4/F^2|_{\text{bare}}$ corresponds to the empirical value reported for $4d$ hydrogenoid atoms.

(eV)	$\bar{U}_{mm}$	$\bar{U}_{mm'}$	$\bar{J}_m$	$\bar{v}_{mm}$	$\bar{v}_{mm'}$	$\bar{J}^{\text{bare}}_m$
Mo	4.0	3.0	0.50	15.5	14.1	0.66
Tc	4.0	2.9	0.53	16.3	14.9	0.69
Ru	4.1	2.9	0.56	17.0	15.6	0.72
Rh	4.3	3.1	0.59	17.9	16.4	0.75

Table 7.9: (d-dp model) Screened ($\bar{U}_{mm}, \bar{U}_{mm'}, \bar{J}_m$) and bare (unscreened) interactions between t_{2g} orbitals within the d-dp Hamiltonian for Sr_2MO_4.

anisotropic within the plane of the TM and oxygen octahedra. The Slater parametrization is more accurate for the late materials, Sr_2TcO_4 and Sr_2RhO_4, for which the spherical approximation of the $4d$ orbital is better due to the smaller hybridization with the ligands.

The bare on-site and exchange interactions increase with the number of the $4d$ electrons (Fig. 7.12), suggesting a rather atomic-like behavior of the $4d$ Wannier orbitals within the d-dp Hamiltonian. This agrees with the atomic expectations based on the Slater rules, *ie* a higher localization due to the contraction of the atomic $4d$ wavefunction from the left to the right of the periodic classification.

Hubbard U and Hund's exchange J

In the d-dp model, the dd transitions are removed from the screening in order to obtain the Hubbard interaction matrices (Tabs. 7.8 and 7.9). As the bare interaction, the on-site Hubbard interaction gets larger with the $4d$ electron number (Fig. 7.12). This is rationalized by the fact that the screening only slightly increases from Sr_2MoO_4 to Sr_2RhO_4 as indicated by the small decrease of the ratio U_{mm}/v_{mm} (Tab. 7.10), from $25.8/100$ to $24.8/100$. The increase of the screening is thus not able to counterbalance the effects due to the stronger orbital localization.

The Hund's exchange interaction (Fig. 7.12) also reproduces the atomic trend, increasing with the atomic number.

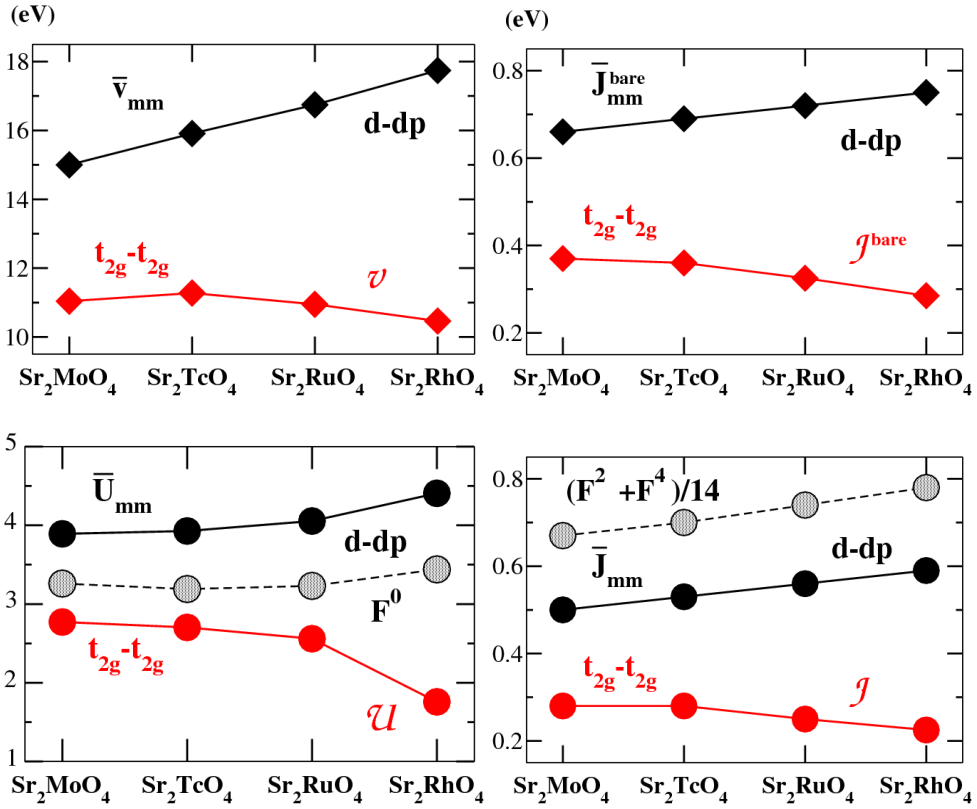

Figure 7.12: Bottom panel: On-site interaction $\bar{U}_{mm}$ (left) and exchange interaction $\bar{J}_m$ (right) between t_{2g} orbitals within the d-dp (black curve) model for Sr_2MO_4 and on-site interactions $\mathcal{U}$ (left) and $\mathcal{J}$ (right) but within t_{2g}-t_{2g} (red curve). In dashed line with open circles, the Hubbard parameter $U = F^0$ and Hund's exchange $J = (F^2 + F^4)/14$ are shown. Top panel: Same but for the bare interactions between the t_{2g} orbitals.

Interestingly, the screened ratio F^4/F^2 (Tab. 7.8) is strongly deviated from the atomic value, whereas the unscreened ratio $F^4/F^2|_{\text{bare}}$ recovers the atomic value. It may be an anisotropic effect coming from the screening that needs to be more investigated. However, this does not lead to strong anisotropies in the orbitally-resolved Hubbard interaction matrices $U^{(\text{cubic})}_{mm'mm'}$ or $J_{mm'} = U^{(\text{cubic})}_{mm'm'm,m\neq m'}$ (see Chapter 5, from Eq. 5.78 to Eq. 5.80). By calculating the interaction matrix elements directly with cubic symmetry, one has access to the orbitally-resolved interactions (see the end of the section for the orbitally-resolved Hubbard interaction matrices). Within the d-dp Hamiltonian, a small anisotropy between U_{dxy} and $U_{\text{dxz/yz}}$ is observed but the same anisotropy is found for the bare interaction. The anisotropy is larger for Sr_2MoO_4 than for Sr_2RhO_4 in agreement with the deviation of F^4/F^2 which is bigger in Sr_2MoO_4. On the other hand, the exchange interaction within the d-dp Hamiltonian does not exhibit any anisotropy.

The deviation from the atomic value of the static ratio F^4/F^2 is stronger in the $4d$ layered perovskite oxides, Sr_2MO_4, than in the $3d$ oxides, $SrMO_3$ (Tab. 7.2) and is comparable to the

one reported for the pnictide compound $BaRu_2As_2$ (Tab. 6.5). The deviation was smaller in $BaFe_2As_2$. It seems to be due to the higher extension of the $4d$ atomic-like orbitals compared to $3d$.
The pnictide compounds and the layered perovskites are quasi-two-dimensional systems. The dimensionality could participate to an anisotropy. The question of the impact of dimensionality in screening is an interesting question (see for example [van den Brink and Sawatzky(2000)]) and investigations for surfaces are currently in development.

Accuracy of the Slater parametrization

By comparing the interaction matrix elements directly calculated with cubic symmetry (U_{mm}, J_m) and the Slater average interactions $(\bar{U}_{mm}, \bar{J}_m)$ (see Chapter 5, Fig. 5.1) deduced from the Slater integrals, the accuracy of the Slater integrals parametrization can be probed. Similar method was already applied for $SrVO_3$ in Chapter 6.

Considering e.g. Sr_2MoO_4, we get for the t_{2g} on-site interaction $U_{mm} = 3.8$ eV, in well agreement with $\bar{U}_{mm} = 4.0$ eV deduced from the Slater integrals (Tab. 7.8). For the exchange interaction between the t_{2g} orbitals, $J_m = 0.48$ eV while $\bar{J}_m = 0.5$ eV.

Orbitally-resolved Hubbard interaction matrices

The reduced interaction matrices within the d-dp Hamiltonian (Tab. 7.7) and calculated with cubic symmetry, are given below for the layered perovskites. The ordering of the orbitals in these matrices is $d_{z^2}, d_{x^2-y^2}, d_{xy}, d_{xz}, d_{yz}$. The values are given in eV.

Sr_2MoO_4

$$U^{\sigma\bar{\sigma}}_{mm'} = \begin{pmatrix} 4.20 & 3.04 & 2.90 & 3.22 & 3.22 \\ 3.04 & 4.35 & 3.43 & 3.06 & 3.05 \\ 2.90 & 3.43 & 3.97 & 2.93 & 2.92 \\ 3.22 & 3.06 & 2.93 & 3.86 & 2.89 \\ 3.22 & 3.05 & 2.92 & 2.89 & 3.84 \end{pmatrix}, U^{\sigma\sigma}_{mm'} = \begin{pmatrix} 0 & 2.48 & 2.38 & 2.83 & 2.83 \\ 2.48 & 0 & 3.10 & 2.56 & 2.55 \\ 2.38 & 3.10 & 0 & 2.44 & 2.44 \\ 2.83 & 2.56 & 2.44 & 0 & 2.41 \\ 2.83 & 2.55 & 2.44 & 2.41 & 0 \end{pmatrix}.$$

Sr_2TcO_4

$$U^{\sigma\bar{\sigma}}_{mm'} = \begin{pmatrix} 4.06 & 2.88 & 2.81 & 3.13 & 3.13 \\ 2.88 & 4.23 & 3.38 & 2.96 & 2.96 \\ 2.81 & 3.38 & 4.04 & 2.90 & 2.90 \\ 3.13 & 2.96 & 2.90 & 3.86 & 2.84 \\ 3.13 & 2.96 & 2.90 & 2.84 & 3.86 \end{pmatrix}, U^{\sigma\sigma}_{mm'} = \begin{pmatrix} 0 & 2.29 & 2.25 & 2.72 & 2.72 \\ 2.29 & 0 & 3.04 & 2.44 & 2.44 \\ 2.25 & 3.04 & 0 & 2.38 & 2.38 \\ 2.72 & 2.44 & 2.38 & 0 & 2.33 \\ 2.72 & 2.44 & 2.38 & 2.33 & 0 \end{pmatrix}.$$

	t_{2g}-t_{2g}				d-dp		
(eV)	$\mathcal{U}$	$\mathcal{U}'$	$\mathcal{J}$	$\mathcal{U}/\mathcal{V}$	U_{mm}	J_m	U_{mm}/v_{mm}
Mo	2.77	2.15	0.28	24.8	3.8	0.48	25.3
Tc	2.70	2.07	0.28	24.3	3.9	0.52	24.5
Ru	2.56	1.94	0.26	23.2	4.0	0.55	23.9
Rh	1.76	1.18	0.23	16.6	4.4	0.61	24.8

Table 7.10: Hubbard-Kanamori parameters $\mathcal{U}$,$\mathcal{U}'$,$\mathcal{J}$ for the t_{2g}-t_{2g} model and average interactions between the t_{2g} orbitals within d-dp in Sr_2MO_4. The ratios $\mathcal{U}/\mathcal{V}$ in t_{2g}-t_{2g} and U_{mm}/v_{mm} in d-dp have been multiplied by a factor 100.

Sr_2RuO_4

$$U^{\sigma\bar{\sigma}}_{mm'} = \begin{pmatrix} 4.06 & 2.83 & 2.78 & 3.17 & 3.18 \\ 2.83 & 4.22 & 3.37 & 2.98 & 2.99 \\ 2.78 & 3.37 & 4.07 & 2.94 & 2.95 \\ 3.17 & 2.98 & 2.94 & 4.02 & 2.93 \\ 3.18 & 2.99 & 2.95 & 2.93 & 4.05 \end{pmatrix}, U^{\sigma\sigma}_{mm'} = \begin{pmatrix} 0 & 2.22 & 2.19 & 2.73 & 2.74 \\ 2.22 & 0 & 3.01 & 2.42 & 2.44 \\ 2.19 & 3.01 & 0 & 2.39 & 2.39 \\ 2.73 & 2.42 & 2.39 & 0 & 2.38 \\ 2.74 & 2.44 & 2.39 & 2.38 & 0 \end{pmatrix}.$$

Sr_2RhO_4

$$U^{\sigma\bar{\sigma}}_{mm'} = \begin{pmatrix} 4.18 & 2.93 & 2.95 & 3.37 & 3.38 \\ 2.93 & 4.34 & 3.55 & 3.15 & 3.16 \\ 2.95 & 3.55 & 4.37 & 3.18 & 3.19 \\ 3.37 & 3.15 & 3.18 & 4.39 & 3.20 \\ 3.38 & 3.16 & 3.19 & 3.20 & 4.44 \end{pmatrix}, U^{\sigma\sigma}_{mm'} = \begin{pmatrix} 0 & 2.29 & 2.31 & 2.92 & 2.94 \\ 2.29 & 0 & 3.17 & 2.56 & 2.58 \\ 2.31 & 3.17 & 0 & 2.57 & 2.58 \\ 2.92 & 2.56 & 2.57 & 0 & 2.59 \\ 2.94 & 2.58 & 2.58 & 2.59 & 0 \end{pmatrix}.$$

7.2.3 Hubbard parameters within the t_{2g}-t_{2g} Hamiltonian

Alternatively, one can construct the low-energy Hamiltonian that only includes the (d_{xy},d_{xz},d_{yz}) degrees of freedom. The energy windows $\mathbb{W}_{t_{2g}}$ are given in Tab. 7.7.

Since the pd charge transfer energy decreases throughout the series, the tail on the oxygen atomic sites of the downfolded local orbitals gets larger from Sr_2MoO_4 to Sr_2RhO_4. Consequently, the orbital localization decreases with the $4d$ electron number, in contrast to the atomic d wavefunctions. The trends for the bare interactions thus deviate from the atomic ones, which were previously reported for the d-dp model (Fig. 7.12 and Tab. 7.10).

The orbitally-resolved interactions (see [Vaugier *et al.* (2012b)]) calculated within the t_{2g}-t_{2g} Hamiltonian are more anisotropic than their analogues within the d-dp Hamiltonian. This is another signature of the less spherical character of the downfolded orbitals within t_{2g}-t_{2g}. The largest interactions are interestingly obtained on the d_{xy} local orbital, for both the screened and bare cases.

(eV)	$SrMoO_3$	Sr_2MoO_4	$SrTcO_3$	Sr_2TcO_4
$\mathcal{U}$	3.0	2.7	2.9	2.7
$\mathcal{J}$	0.31	0.28	0.31	0.28
$\mathcal{V}$	11.6	11.0	11.8	11.2
$\mathcal{J}_{\text{bare}}$	0.40	0.37	0.39	0.36

Table 7.11: (t_{2g}-t_{2g} model) Hubbard-Kanamori interactions between t_{2g} orbitals in the t_{2g}-t_{2g} Hamiltonian for $SrMO_3$ compared to layered Sr_2MO_4 perovskite.

The on-site t_{2g} interaction $\mathcal{U}$ and Hund's exchange $\mathcal{J}$ exhibit trends that are similar to $\mathcal{V}$ and $\mathcal{J}_{\text{bare}}$ (Fig. 7.12). The decrease from Sr_2MoO_4 to Sr_2RhO_4 is even more pronounced. This is due to the screening which strongly and non-linearly increases between Sr_2RuO_4 and Sr_2RhO_4. Indeed, the ratio $\mathcal{U}/\mathcal{V}$ within the t_{2g}-t_{2g} model (Tab. 7.10) is divided by almost a factor two through the series, whereas the ratio U_{mm}/v_{mm} is slowly decreasing within the d-dp model.

The difference in the screening between the two low-energy Hamiltonians comes from the transitions between t_{2g} and e_g Kohn-Sham eigenstates, which are removed from the total polarization in the d-dp model. These transitions – by causing a notable increase of the screening between Sr_2RuO_4 and Sr_2RhO_4 – are responsible for the smaller effective interactions in the latter. Within DFT-LDA (Fig. 7.10), the e_g's come closer to the Fermi level in the late Sr_2MO_4 perovskites. The e_g bands are even partially filled in Sr_2RhO_4 leading to a metallic screening that contributes to lower the effective interactions. This is an artefact of the undistorted crystal structure of Sr_2RhO_4 and is not the case for the realistic distorted structure [Martins *et al.* (2011)].

Comparison between $SrMO_3$ and Sr_2MoO_4

One finally observes that the values for the Hubbard-Kanamori interactions $\mathcal{U}$ and $\mathcal{J}$ within the t_{2g}-t_{2g} Hamiltonian are very close for Mo and Tc elements in $SrMO_3$ and Sr_2MO_4 compounds (Tab. 7.11).

7.3 Conclusions

We investigated the effective Coulomb interactions in $SrMO_3$ (M = V, Cr, Mn, Nb, Mo, Tc) and in Sr_2MO_4 (M = Mo, Tc, Ru, Rh) series depending on the low-energy Hamiltonian constructed (t_{2g}-t_{2g} and d-dp). It illustrates the role of the one-body Hamiltonian in the values of the downfolded interacting Hamiltonian, as stressed in Chapter 4 (Fig. 4.3).

Furthermore, within Wannier orbitals spanning the t_{2g} correlated subspace within t_{2g}-t_{2g} Hamiltonians, screening can lead to trends for the Hubbard interaction and Hund's exchange that are in contrast to generally spread ideas. Atomic-like behaviors are recovered when using atomic-like Wannier orbitals within d-dp Hamiltonians.

The Hubbard on-site interactions notably vary with the screening, in contrast to the exchange interactions. The on-site and the exchange interactions are sensitive to the extension of the localized orbitals.

Chapter 8

Towards a Truly First Principles Approach

In this chapter, we present LDA+cRPA+DMFT studies for two layered perovskites Sr_2RhO_4 and Sr_2IrO_4, and for the rare-earth compound CeSF. We performed the cRPA calculations which were combined with LDA+DMFT by C. Martins and M. Aichhorn for the layered oxides [Martins et al. (2011)], and by L. Pourovskii, J. Tomczak et al. for CeSF [Tomczak et al. (2012)].

8.1 Sr_2RhO_4 vs. Sr_2IrO_4

In this section, we discuss the interplay of Coulomb interactions with spin-orbit coupling (SOC) and lattice distortions for Sr_2RhO_4 and Sr_2IrO_4 materials in their paramagnetic phases. These materials are isoelectronic and isostructural analogues. However, they exhibit very different electronic properties. Despite of an odd number of electrons in the d manifold, Sr_2IrO_4 displays an insulating behavior at all temperatures with an optical gap of about 0.26 eV at room temperature [Moon *et al.* (2009)]. On the other hand, Sr_2RhO_4 is a paramagnetic metal down to 36 mK [Moon *et al.* (2006)].

Spin-orbit interactions are expected to be relevant for both compounds but stronger in $5d$ Sr_2IrO_4. Recently, SOC was shown to be necessary for describing the Mott insulating state of Sr_2IrO_4 in the canted-antiferromagnetic phase below 240 K [Kim *et al.* (2008),Kim *et al.* (2009)]. This phase has, indeed, triggered much experimental (e.g. XAS, ARPES, optics, transport measurements) and theoretical work. The importance of the SOC, in particular, was highlighted as an effect that has to be taken into account when fitting the XAS spectra by multiplet theories [Kim *et al.* (2009)]. Kim and co-workers even speak about a *"novel $J_{eff} = 1/2$ Mott state"* induced by SOC in Sr_2IrO_4.

It is at first glance surprising that a $5d$ system is strongly correlated and even a Mott insulator. Coulomb interactions are usually believed to be more efficient in the $3d$ compounds, due to the more localized character of $3d$ orbitals.
The question of SOC was also addressed in Sr_2RhO_4 by [Haverkort *et al.* (2008),Liu *et al.* (2008)] :

DFT-LDA calculations augmented by Coulomb interactions within the LDA+U method, reproduce the Fermi surface only if SO interactions are considered. One inadequacy of such method comes from the assumption of an antiferromagnetic ordering in Sr_2RhO_4 whereas the material is known to be non-magnetic.

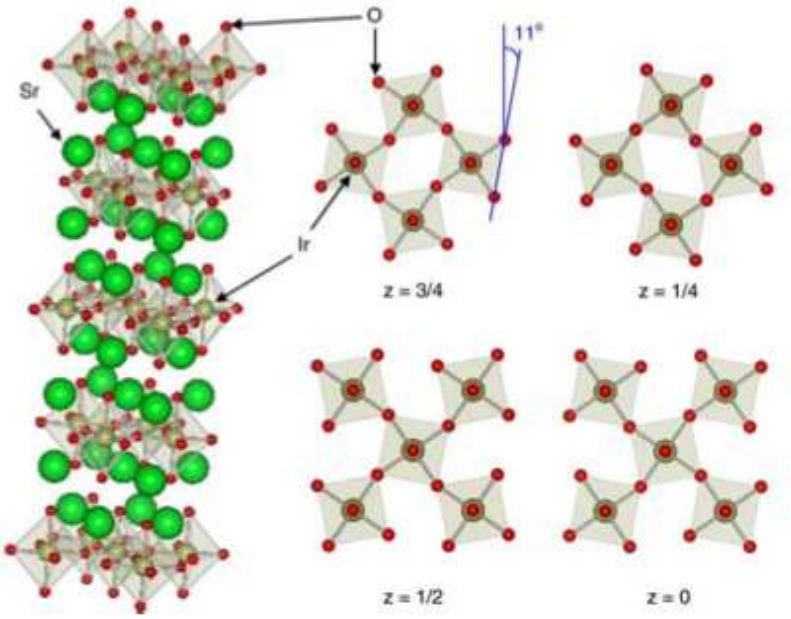

Figure 8.1: Conventional unit cell of Sr_2IrO_4 [Klein and Terasaki(2008)]. Iridium atoms (golden spheres) are surrounded by six oxygen atoms (red). IrO_6 octahedra are alternatively rotated clockwise and anticlockwise by about $11°$. Inter-layer planes are made of strontium atoms (in green). Sr_2RhO_4 has a similar crystal structure.

We present below the cRPA calculations for Sr_2IrO_4 and Sr_2RhO_4 as our contributions in the collaboration with C. Martins and M. Aichhorn. For computational reasons, we employed the undistorted DFT-LDA band structure without SOC. The (t_{2g} to one e_g) transitions are excluded from the total polarization in the range of the hybridization gap (see Fig. 8.2) in order to mimic the effects of the distortions. The Coulomb interactions obtained by cRPA in the t_{2g}-t_{2g} model are then used in LDA+DMFT as implemented by [Aichhorn *et al.* (2009)] and extended by [Martins *et al.* (in preparation)]. This leads to an entirely first principles scenario for the paramagnetic insulating state of Sr_2IrO_4 and for the paramagnetic metallic state of Sr_2RhO_4 [Martins *et al.* (2011)].

8.1.1 Band structures : interplay of spin-orbit coupling and distortions

Sr_2IrO_4 is a $5d$ transition metal oxide with a tetragonal crystal structure ($I4_1/acd$ space group) whose symmetry is lowered from the K_2NiF_4-type (common to Sr_2RuO_4 and Sr_2MoO_4, see chapter 7) [Huang *et al.* (1994)]. The corner-shared octahedra IrO_6 are not well-aligned in the iridium layers anymore but are alternatively rotated clockwise and anticlockwise around the $\boldsymbol{c}$-axis by about $11°$ (Fig. 8.1). The lattice parameters of the resulting superstructure are $a = \sqrt{2}a_t = 5.497\text{A}°$ and $c = 2c_t = 25.798\text{A}°$, where a_t, c_t correspond to the lattice parameters of the K_2NiF_4-type unit-cell (see Chapter 7, Tab. 7.7). The superstructure contains now four formula units.

Sr_2IrO_4 and Sr_2RhO_4 are isoelectronic and isostructural materials that both accommodate five electrons in their respective d manifold. However, their electronic properties are very different as mentioned earlier. For an exhaustive review on Sr_2IrO_4, see [Martins(2010)].
According to the DFT-LDA calculations (Fig. 8.2) in the paramagnetic phases, both compounds are metallic within the undistorted structure without SOC as well as within the distorted one with SOC. One therefore needs to go beyond DFT-LDA in order to get the correct insulating spectrum in Sr_2IrO_4 and in order to reproduce better the Fermi surface in Sr_2RhO_4. This motivates the LDA+DMFT approach that takes the SOC into account and solves the low-energy Hamiltonian obtained from cRPA.

Undistorted band structure

Within the undistorted K_2NiF_4 unit cell without SOC, the DFT-LDA band structures for Sr_2IrO_4 and Sr_2RhO_4 appear rather similar (Fig. 8.2). In the tetragonal symmetry, the t_{2g}-like orbitals (d_{xy},d_{xz},d_{yz}) almost equally accommodate five electrons. The d bandwidth is large, around 8.5 eV in Sr_2RhO_4 and 10 eV in Sr_2IrO_4. Oxygen p states (in turquoise) are found below and hybridize with t_{2g}-like states.

As expected in $4d$ oxides, the bandwidth in Sr_2RhO_4 is smaller than in $5d$ as well as the pd charge transfer energy Δ_{pd}. This is due to the weaker hybridization between Rh-$4d$ and oxygen-p orbitals induced by the smaller $4d$ orbital extension.
We already mentioned in Chapter 7 that the charge transfer Δ_{pd} energy increases from the $3d$ to $4d$ transition metal oxides (see also [Lee *et al.* (2003), Imada *et al.* (1998)]). Here, Δ_{pd} is about 1 eV larger in Sr_2IrO_4.

With distortions

The structural distortions lead to the four-times larger unit cell as indicated in the introduction and therefore to four-folded bands. This explains the set of twelve bands found around the Fermi level.
In both compounds, a d_{xy}-$d_{x^2-y^2}$ hybridization gap opens between the t_{2g} (in red) and e_g bands (in blue) : it equals about 0.9 eV in Sr_2IrO_4 and 0.6 eV in Sr_2RhO_4. The d_{xy} band is almost filled

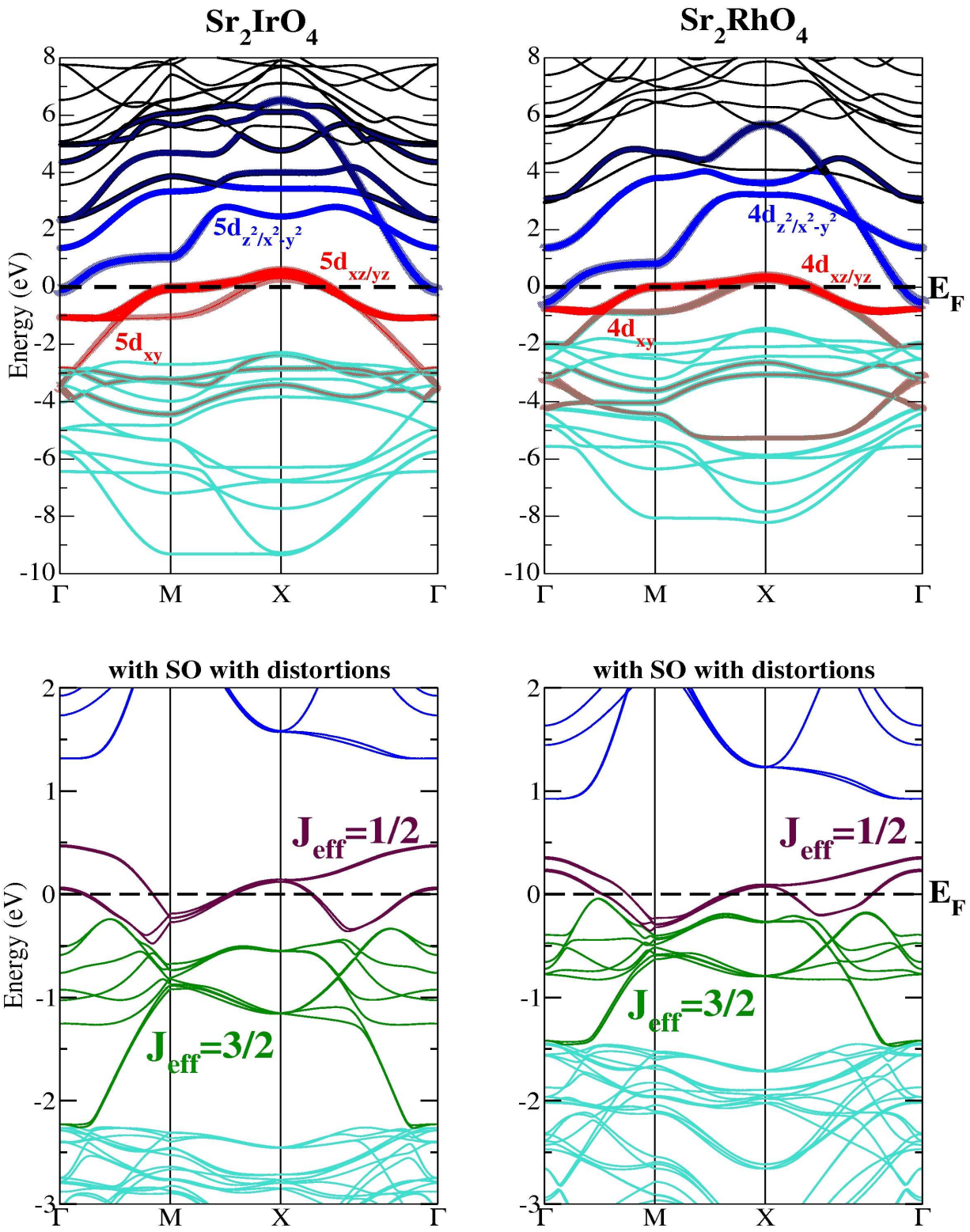

Figure 8.2: DFT-LDA paramagnetic band structure of Sr_2IrO_4 (left) and Sr_2RhO_4 (right). (top) The calculation was done for the undistorted crystal structure without spin-orbit interactions. The t_{2g} bands in the tetragonal symmetry (in red) lie on the Fermi level. The e_g bands (in blue) are found above and oxygen p (in turquoise) below. (bottom) The structural distortions and the spin-orbit coupling have been taken into account, leading respectively to a reduction of the bandwidth and a lift of the degeneracies at the Fermi level. Sr_2IrO_4 can be mapped into an almost $j_{eff} = 1/2$ single-band Hubbard model, whereas it gives a quarter-filled two-band model for Sr_2RhO_4.

in the distorted phase. The orbital polarization is thus enhanced with respect to the undistorted case.

On the other hand, the distortions induce a reduction of the bandwidth. This makes the system effectively more correlated since the kinetic energy is lowered. This is a well-known effect for materials like 1T-TaS_2 or $TaSe_2$ where a bandwidth-controlled Mott transition can be monitored by charge-density-wave distortions [Perfetti *et al.* (2003)]. As a consequence in Sr_2IrO_4 and Sr_2RhO_4, the critical value for the Mott transition is reduced with respect to the undistorted case [Martins *et al.* (2011)].

With Spin-Orbit

The introduction of SOC [1] modifies the degeneracy of the bands around the Fermi level (Fig. 8.2). The large SOC in Sr_2IrO_4 ($\zeta_{SO} = 0.4$ eV) and, to a lesser extent in Sr_2RhO_4 ($\zeta_{SO} = 0.161$ eV), splits the t_{2g} states into a quartet of states, commonly labeled $j_{eff} = 3/2$, and a higher lying doublet $j_{eff} = 1/2$. Furthermore, each state is twice degenerate in pseudospins ($\pm m_j$) since the $I4_1/acd$ space group includes the spatial inversion [Sugano *et al.* (1970)]. j_{eff} states can be related to the cubic t_{2g} states by the following transformations :

$$\begin{cases} |J_{eff} = \frac{1}{2}, m_j = \pm\frac{1}{2}\rangle = \frac{1}{\sqrt{3}}\Big(|d_{yz}, \mp\rangle \pm i|d_{xz}, \mp\rangle\Big) \pm \frac{1}{\sqrt{3}}|d_{xy}, \pm\rangle \\ |J_{eff} = \frac{3}{2}, m_j = \pm\frac{1}{2}\rangle = \frac{1}{\sqrt{6}}\Big(\mp|d_{yz}, \mp\rangle - i|d_{xz}, \mp\rangle\Big) + \sqrt{\frac{2}{3}}|d_{xy}, \pm\rangle \\ |J_{eff} = \frac{3}{2}, m_j = \pm\frac{3}{2}\rangle = \mp\frac{1}{\sqrt{2}}|d_{yz}, \pm\rangle - \frac{i}{\sqrt{2}}|d_{xz}, \pm\rangle, \end{cases} \tag{8.1}$$

where $\pm$ stands for the up ($\uparrow$) and down ($\downarrow$) spin of t_{2g} orbitals.

Due to a larger spin-orbit splitting, the four $j_{eff} = 3/2$ states are almost filled in Sr_2IrO_4 ($n_{3/2,|1/2|} = 1.98$ and $n_{3/2,|3/2|} = 1.84$) and the $j_{eff} = 1/2$ state slightly exceeds half-filling ($n_{1/2,|1/2|} = 1.16$). In Sr_2RhO_4, the effective splitting between $j_{eff} = 1/2$ and $j_{eff} = 3/2$ states is smaller : only the $j_{eff} = (3/2, |1/2|)$ orbital is filled whereas $j_{eff} = 1/2$ and $j_{eff} = (3/2, |3/2|)$ have similar filling.

Structural distortions and SOC thus lead to different effective models for Sr_2IrO_4 and Sr_2RhO_4 : almost half-filled single band for the former and quarter-filled two-band for the latter. As well-known for multi-orbital Hubbard models, this will have consequences on the Mott transition : the critical interaction for the formation of the Mott insulating state increases with the degeneracy [Georges *et al.* (2004)].

Wannier orbitals

Wannier t_{2g} orbitals for a further use in the t_{2g}-t_{2g} model, are constructed out of the Kohn-Sham bands within a given energy window $\mathbb{W}$ (Tab. 7.7). We follow the projection procedure as already

[1] Spin-Orbit interactions in the electronic structure code WIEN2K are treated with a second variational method using scalar relativistic orbitals as basis functions.

U(eV)	Sr_2RhO_4			Sr_2IrO_4		
	d_{xy}	d_{xz}	d_{yz}	d_{xy}	d_{xz}	d_{yz}
d_{xy}	1.81	1.18	1.18	2.23	1.53	1.53
d_{xz}	1.18	1.75	1.19	1.53	2.02	1.49
d_{yz}	1.18	1.19	1.75	1.53	1.49	2.02

Table 8.1: Orbitally-resolved Hubbard interaction matrix for the t_{2g}-t_{2g} model in the undistorted phases of Sr_2RhO_4 and Sr_2IrO_4. Exchange interaction matrix $J_{mm'}$ does not exhibit any anisotropy and yields about $\mathcal{J} = 0.23$ eV in both Sr_2RhO_4 and Sr_2IrO_4.

explained in Chapter 3 and Chapter 4. Same energy windows are chosen for the undistorted and distorted phases[2] : $\mathbb{W} = [-3.6, 0.6]$ eV and $[-3.3, 0.5]$ eV (with respect to the Fermi level) for Sr_2IrO_4 and Sr_2RhO_4, respectively. The Wannier j_{eff} orbitals are then obtained by applying the transformation relations (Eq. 8.1).

The four bands that cross the Fermi level in Sr_2IrO_4 are not purely formed by the $j_{eff} = 1/2$ orbitals, but there is a slight mixture of the $j_{eff} = 1/2$ and $(j_{eff} = 3/2, m_j = |3/2|)$ characters, especially at the Γ point (Fig. 8.3). It is similar in Sr_2RhO_4 but the mixture is stronger. We hence have to redefine the j_{eff} spin-orbital characters by diagonalizing the density matrix of the local problem.

8.1.2 cRPA calculations within the t_{2g}-t_{2g} model

Undistorted phase

Considering the t_{2g}-t_{2g} model for Sr_2IrO_4 and Sr_2RhO_4 seems reasonable, especially for describing the distorted phases. Indeed, due to the structural distortions, the e_g Kohn-Sham bands are pushed far away from the Fermi level and SOC does not mix e_g with t_{2g}. The e_g states are thus expected to stay empty.

By employing Kohn-Sham indices to exclude the transitions from and to the t_{2g}-like Kohn-Sham bands from the total polarization, one calculates the reduced orbitally-resolved interaction matrix $U^{(\text{cubic})}_{mm'mm'}$ (denoted $U_{mm'}$ in the following) and $U^{(\text{cubic})}_{mm'm'm,m\neq m'}$ within cRPA in the t_{2g} Wannier basis introduced in the previous section. The results for undistorted Sr_2RhO_4 and Sr_2IrO_4 are given in Tab. 8.1. They are in reasonable agreement with the ones from [Arita *et al.* (2012)] : in this recent work, the authors constructed a t_{2g}-like Wannier basis within a maximally localized Wannier function framework and employed the RPA polarization from time-dependent DFT in their version of cRPA. They got for undistorted Sr_2IrO_4 : $U_{d_{xy}} = 2.35$ eV and $U_{d_{xz}/d_{yz}} = 2.21$ eV, and $\mathcal{J} = 0.16$ eV.

[2] In [Martins *et al.* (2011)], we actually chose slightly smaller energy windows for the distorted phase : $\mathbb{W} = [-3.0, 0.5]$ eV in Sr_2IrO_4 and $\mathbb{W} = [-2.67, 0.37]$ eV in Sr_2RhO_4. Selecting the same energy windows as for the undistorted phase has negligible consequences on the total charge.

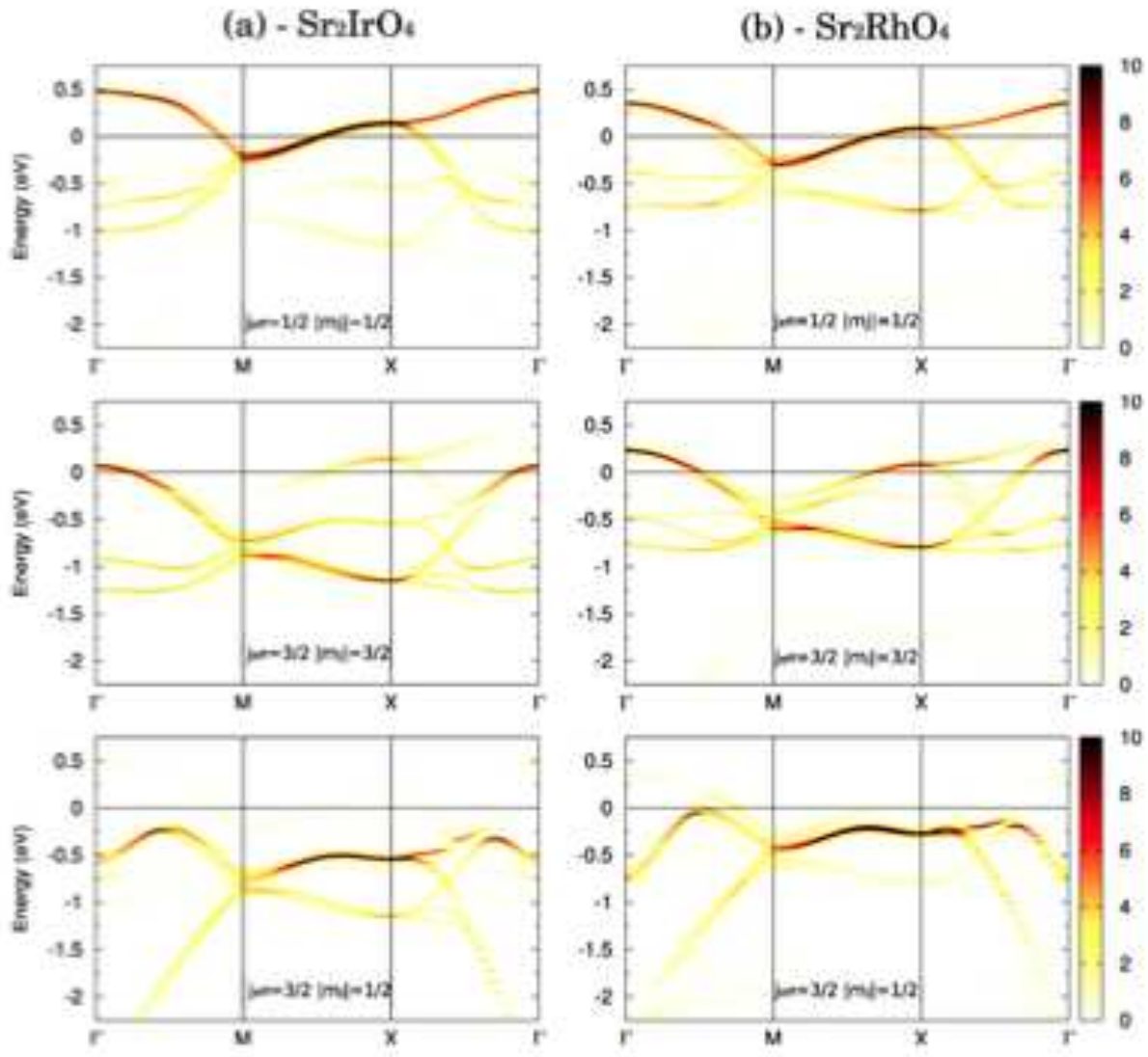

Figure 8.3: Spin-orbital j_{eff} character of the Wannier orbitals for Sr_2IrO_4 (left) and Sr_2RhO_4 (right) in DFT-LDA, projected on the $j_{eff} = 1/2$ (top), $j_{eff} = 3/2\,|m_j| = 3/2$ (middle) and $j_{eff} = 3/2\,|m_j| = 1/2$ (bottom) spin-orbitals. For the four bands crossing the Fermi level in Sr_2IrO_4, there is a slight overlap of $j_{eff} = 1/2$ and $j_{eff} = 3/2\,|m_j| = 3/2$, especially at Γ. The mixture is stronger in Sr_2RhO_4.

(eV)	$\mathcal{U}$	$\mathcal{V}$	$\mathcal{U}/\mathcal{V} \times 100$	$\mathcal{J}$	$\mathcal{J}_{\text{bare}}$
Rh	1.7	10.4	16.6	0.23	0.28
Ir	2.1	9.9	21.2	0.23	0.28

Table 8.2: Hubbard-Kanamori interaction $\mathcal{U}$ and exchange interaction $\mathcal{J}$ for the t_{2g}-t_{2g} model in the undistorted phases of Sr_2RhO_4 and Sr_2IrO_4. The bare on-site $\mathcal{V}$ and exchange $\mathcal{J}_{\text{bare}}$ interactions are given.

Applying a cubic approximation, the Hubbard interaction matrix can be parametrized by a set of pseudo Hubbard-Kanamori parameters $(\mathcal{U}, \mathcal{U}', \mathcal{J})$, as if the symmetry was perfectly cubic (Tab. 8.2). $\mathcal{U}$ ($\mathcal{J}$) is the average over the Hubbard interaction matrix elements $U^{(\text{cubic})}_{mmmm}$ ($U^{(\text{cubic})}_{mm'm'm,m\neq m'}$) and $\mathcal{U}'$ is assumed to be equal to $\mathcal{U} - 2\mathcal{J}$.

Regarding the bare interaction $\mathcal{V}$, a smaller value is obtained for Sr_2IrO_4 than for Sr_2RhO_4 (Tab. 8.2). This is expected from the evolution through the rows of the periodic classification for the d atomic wavefunction following the Slater rules. The average orbital extension for a $5d$ atomic wavefunction is, indeed, larger than for $4d$ (Tab. 7.4). This also agrees with the interpretations established in Chapter 7, when comparing $3d$ to $4d$ transition metal oxides (see Fig. 7.3 for example).

Interestingly, the trend reported for $\mathcal{V}$ is inverted for $\mathcal{U}$ (Tab. 8.2). The effective intra-orbital interactions within the t_{2g}-t_{2g} model are larger in Sr_2IrO_4 than in Sr_2RhO_4. This relies on the screening which competes with the orbital localization effects. As already pointed out (see chapter 7), t_{2g} Wannier orbitals are extended within t_{2g}-t_{2g} models. The smaller the pd charge transfer energy, the larger the "leakage" on the ligand atomic sites. On the other hand, the screening gets larger when the pd charge transfer energy decreases. It may even happen that the screening becomes strong enough to invert the atomic trend reported for the unscreened interaction $\mathcal{V}$. This was the case in $SrMnO_3$ and its counterpart $SrTcO_3$: $\mathcal{U}$ in $SrMnO_3$ is smaller than in its $4d$ isoelectronic analogue $SrTcO_3$ whereas $\mathcal{V}$ is larger (see Tab. 7.5). Things are similar here : we already mentioned that the pd charge transfer energy is larger by about 1 eV in Sr_2IrO_4 than in Sr_2RhO_4 (Fig. 8.2). Furthermore, the ratio $\mathcal{U}/\mathcal{V}$ is significantly larger in Sr_2IrO_4 (Tab. 8.2). It thus confirms that the static screening has weaker effects in Sr_2IrO_4 than in Sr_2RhO_4.

One can finally experience the following, which consists in shifting by 1 eV all the oxygen p Kohn-Sham bands in Sr_2RhO_4. The motivation is to mimic the position of the oxygen screening bands of Sr_2IrO_4. An increased value for the Hubbard interaction $\mathcal{U} = 1.9$ eV and same Hund's exchange $\mathcal{J} = 0.23$ eV, are obtained. The increase agrees with our interpretations.

Mimicking the distorted phase

Due to the computational cost, the undistorted phases without SO are employed for calculating the Coulomb interactions within cRPA. In a simplified way, one can mimic the distorted phase by shifting in the undistorted band structure, the e_g band that crosses the Fermi level. Indeed, the structural distortions push this band upward the Fermi level by about 1.45 eV in both Sr_2RhO_4

U(eV)	Sr_2RhO_4			Sr_2IrO_4		
	d_{xy}	d_{xz}	d_{yz}	d_{xy}	d_{xz}	d_{yz}
d_{xy}	2.47	1.82	1.82	2.74	2.03	2.03
d_{xz}	1.82	2.38	1.82	2.03	2.52	1.99
d_{yz}	1.82	1.82	2.38	2.03	1.99	2.52

Table 8.3: Orbitally-resolved Hubbard interaction matrix for the t_{2g}-t_{2g} model in Sr_2RhO_4 and Sr_2IrO_4. The distorted phase has been mimicked by shifting the e_g band of the undistorted phase by 1.45 eV. This shift corresponds to the hybridization gap d_{xy}-$d_{x^2-y^2}$ that is opened by the structural distortions. Exchange interaction matrix $J_{mm',m\neq m'}$ does not exhibit any anisotropy and still yields about $\mathcal{J} = 0.23$ eV in both Sr_2RhO_4 and Sr_2IrO_4.

(eV)	$\mathcal{U}$	$\mathcal{J}$	$\mathcal{U}'$
Rh	2.4	0.23	1.82
Ir	2.6	0.23	2.01

Table 8.4: Hubbard-Kanamori parameters ($\mathcal{U}$,$\mathcal{U}'$ and $\mathcal{J}$) calculated for the t_{2g}-t_{2g} model in the mimicked distorted phases of Sr_2RhO_4 and Sr_2IrO_4. As established earlier for the t_{2g}-t_{2g} model by employing a cubic approximation, $\mathcal{U}$ is the average over the Hubbard interaction matrix elements $\{U^{(\text{cubic})}_{mm}\}$ whereas $\mathcal{U}'$ is the average over the inter-orbital interactions $\{U^{(\text{cubic})}_{m\neq m'}\}$ (Eq. 5.77 and Tab. 8.3). The exchange interaction $\mathcal{J}$ is deduced from the average over the interaction matrix elements $U^{(\text{cubic})}_{mm'm'm,m\neq m'}$. We can reasonably assume that $\mathcal{U}' \approx \mathcal{U} - 2\mathcal{J}$ ($= 1.94$ eV in Sr_2RhO_4 and 2.16 eV in Sr_2IrO_4 considering $U^{(\text{cubic})}_{mm'mm',m\neq m'}$), as if the symmetry was perfectly cubic.

and Sr_2IrO_4. The t_{2g} bands are also notably rearranged by the interplay of distortions and SOC, but the polarization due to the t_{2g}-t_{2g} transitions is removed from the screening within the t_{2g}-t_{2g} model. On the other hand, oxygen-p bands are shifted by about 0.5 eV upward the Fermi level. This will have consequences for the screening but is *not* mimicked in our calculations.

The results for the orbitally-resolved interaction matrix $U_{mm'}$ are given in Tab. 8.3. One can still reasonably make a cubic approximation in order to parametrize this matrix with a set of pseudo Hubbard-Kanamori parameters ($\mathcal{U}$,$\mathcal{U}'$ and $\mathcal{J}$) (Tab. 8.4). It results for the exchange interaction that $\mathcal{J} = 0.23$ eV for both Sr_2RhO_4 and Sr_2IrO_4.

The deviation between the diagonal elements $\{U_{mm}\}$ and their average, $\mathcal{U}$, yields about 5% in Sr_2IrO_4. The dispersion is even smaller for the nondiagonal elements $\{U_{m\neq m'}\}$. Furthermore, assuming that $\mathcal{U}' = \mathcal{U} - 2\mathcal{J}$ introduces an overestimation of $\mathcal{U}'$ by about 7%, compared to the directly estimated value.
All the deviations coming from the cubic parametrization are smaller than 10%. This gives confidence in the cubic approximation.

We stress out that the Hubbard-Kanamori on-site interactions $\mathcal{U}$ are still smaller in Sr_2RhO_4 than in Sr_2IrO_4. As explained earlier, this is due to the weaker hybridization effects between Rh-4d and oxygen-p states which leave the latter about 1 eV higher in energy in the undistorted and distorted phases of Sr_2RhO_4 than in Sr_2IrO_4. The induced screening is hence larger in Sr_2RhO_4 than in Sr_2IrO_4. In the distorted phase, the oxygen-p bands come actually closer to the

Fermi level by about 0.5 eV in both compounds. This is not taken into account in the mimicked distorted phase. Consequently, one may expect that the values from Tab. 8.3 and Tab. 8.4, are slightly overestimated, especially for Sr_2RhO_4.
Furthermore, one observes that the values of $\mathcal{U}$ are larger by about $0.5 - 0.7$ eV in the mimicked distorted phase than in the undistorted one. This agrees with the previous interpretations about the screening strength. Shifting the position of the e_g band has lowered the strength of the t_{2g}-e_g screening channel.

Transformation 8.1 could then be used for constructing the interaction Hubbard Hamiltonian in the j_{eff} spin-orbital basis previously introduced.
Within an alternative parametrization, a set of pseudo Slater integrals $(\tilde{F}^0, \tilde{F}^2, \tilde{F}^4)$ is deduced by inverting the Hubbard-Kanamori relations (see Chapter5, from Eq. 5.70 to Eq. 5.72). The ratio $r = \tilde{F}^4/\tilde{F}^2 = 0.63$ is set to the atomic value :

$$\tilde{F}^0 = \mathcal{U} - \frac{4(1+r)441}{49(27+20r)}\mathcal{J} \tag{8.2}$$

$$\tilde{F}^2 = \frac{441}{27+20r}\mathcal{J} \tag{8.3}$$

$$\tilde{F}^4 = r\tilde{F}^2. \tag{8.4}$$

This leads to the effective Hubbard parameter $\tilde{U} = \tilde{F}^0$ and Hund's exchange $\tilde{J} = (\tilde{F}^2 + \tilde{F}^4)/14$. The values for $\tilde{U}$ and $\tilde{J}$ are found stable when increasing the ratio r from 0.63 to 0.9. One then merely constructs the Hubbard interaction matrix in the j_{eff} spin-orbital basis by employing Eq. 5.64 (see Chapter 5).

8.1.3 Application : Reduced effective spin-orbital degeneracy and spin-orbital ordering

The results from the LDA+DMFT scenario on top of cRPA, in collaboration with C. Martins and M. Aichhorn [Martins *et al.* (2011)], are summarized below. Moderate Coulomb interactions induce a Mott insulating state in the paramagnetic phase of Sr_2IrO_4 due to the interplay of distortions and large spin-orbit coupling (SOC). In Sr_2RhO_4, smaller SOC and smaller Coulomb interactions lead to a less dramatic reduction of the spin-orbital fluctuations and results into a paramagnetic metal in agreement with experiments.

LDA+DMFT calculations - including the spin-orbit interactions - have been performed at $\beta = 40$ eV^{-1}. The strong-coupling CTQMC algorithm was employed for solving the quantum impurity problem in DMFT (see Chapter 3). Only density-density terms for the interacting Hubbard Hamiltonian were considered.

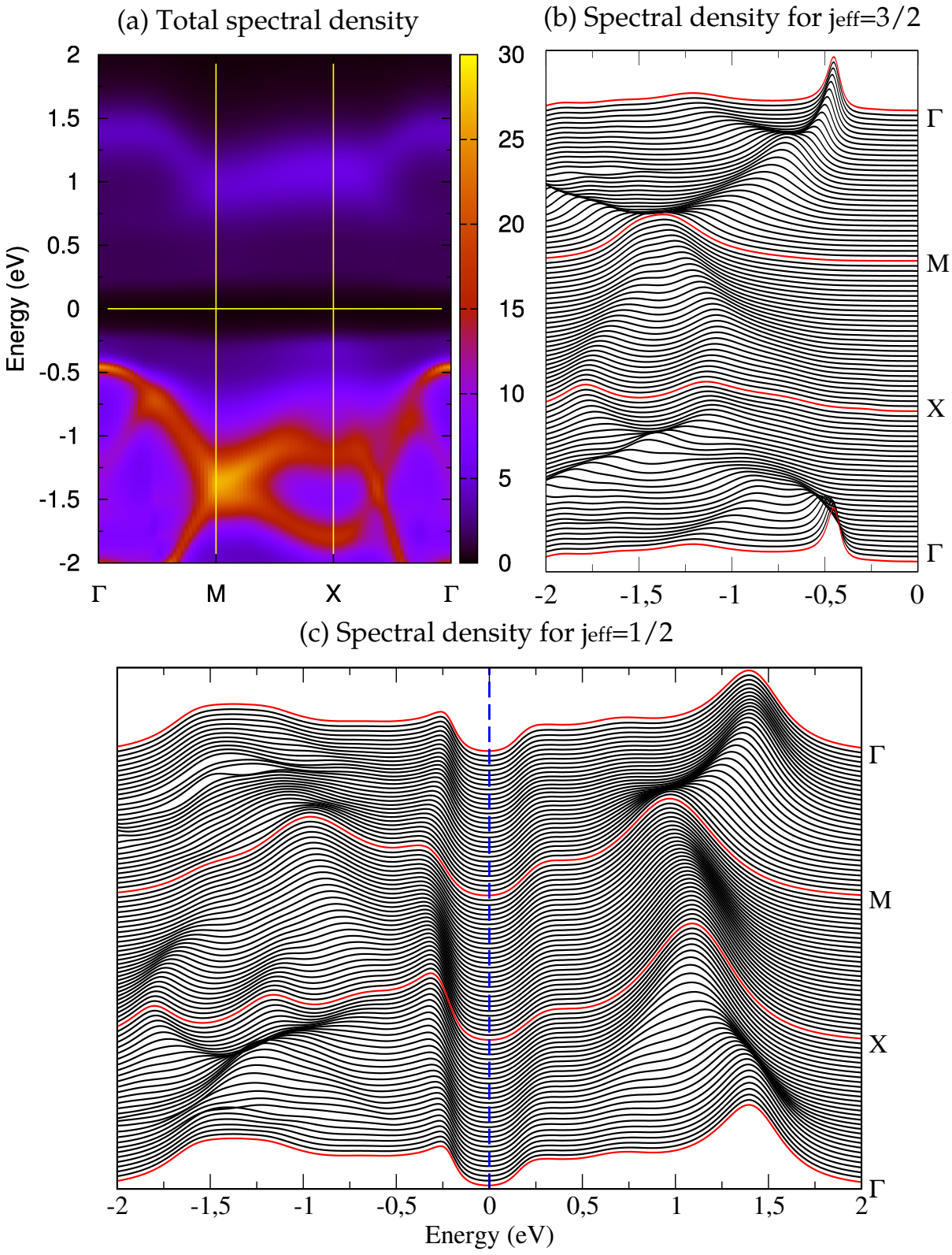

Figure 8.4: Momentum-resolved spectral function of the paramagnetic phase of Sr_2IrO_4 from LDA+DMFT at $T = 300$ K. We get a Mott insulating state with a gap which agrees with the optical gap at ambient temperature (about 0.26 eV). Panel (a) is the total spectral density and panel (b) and (c) show the orbitally-resolved spectral densities $j_{eff} = 3/2$ and $j_{eff} = 1/2$, respectively. Red lines are guides for the eyes. The $j_{eff} = 1/2$ lower Hubbard band is found at about -0.5 eV in agreement with the ARPES results from [Kim *et al.* (2008)].

Sr_2IrO_4

The interacting part of the Hubbard Hamiltonian expanded into the Wannier j_{eff} basis is calculated within cRPA for the mimicked distorted phase. We get $\tilde{U} = \tilde{F}^0 = 2.2$ eV and $\tilde{J} = 0.3$ eV using the Slater parametrization introduced in the previous section (from Eq. 8.2 to Eq. 8.4).

In the Wannier spin-orbital j_{eff} basis, the reduced interaction matrices (in eV) read as

$$U_{jj'}^{m_j\bar{m}_j}|_{\text{Slater}} = \begin{pmatrix} 2.24 & 1.98 & 1.89 \\ 1.98 & 2.38 & 2.03 \\ 1.89 & 2.03 & 2.31 \end{pmatrix} \; U_{jj'}^{m_j m_j}|_{\text{Slater}} = \begin{pmatrix} 0 & 2.08 & 2.21 \\ 2.08 & 0 & 1.93 \\ 2.21 & 1.93 & 0 \end{pmatrix}.$$

The order of the spin-orbitals in these matrices is $j_{eff} = 1/2, j_{eff} = 3/2\,|m_j| = 1/2, j_{eff} = 3/2\,|m_j| = 3/2$. The pseudospin m_j can be seen as a spin degree of freedom and $\bar{m}_j$ as the opposite pseudospin. For comparison, Arita and co-workers get a smaller $U_{1/2\,1/2}^{1/2\,-1/2} = 1.96$ eV [Arita *et al.* (2012)]. This may explain why they do not catch the insulating Mott phase within LDA+DMFT. Indeed, the critical on-site interaction for such half-filled single-band system is found between 2.1 and 2.2 eV. Sr_2IrO_4 therefore lies on the verge of the Mott insulator transition. The role of the structural distortions and SOC is crucial : the distortions lead to larger on-site interactions and SOC to an effective single-band model.

Such moderate interactions are hence enough to induce a Mott insulating state in the half-filled one-orbital Hubbard model. The Mott gap yields the size of the optical gap measured at room temperature (about 0.26 eV) [Moon *et al.* (2009)]. Despite the fact that the ARPES measurements by [Kim *et al.* (2008)] have been achieved in the antiferromagnetic phase, the total spectral functions (Fig. 8.4) agree with the experimental energy distribution curves. From the orbitally-resolved spectral functions, one can locate the lower $j_{eff} = 1/2$ Hubbard band at about -0.5 eV, in agreement with ARPES results.

On the other hand, the spin-orbital polarization is enhanced compared to DFT-LDA. The Wannier orbital $j_{eff} = 1/2$ is now exactly half-filled and the upper Hubbard band is of $j_{eff} = 1/2$-type only.
Sr_2IrO_4 thus exhibits a "spin-orbital" order with neither orbital nor magnetic order.

Sr_2RhO_4

In Sr_2RhO_4, $\mathcal{U} = 1.94$ eV and $\mathcal{J} = 0.23$ eV were cjosen for the pseudo Hubbard-Kanamori interactions. This corresponds to a kind of counterbalanced on-site interaction value between the undistorted and the mimicked distorted phase calculated within cRPA. Indeed, for computational reasons, the cRPA calculations were carried out with the undistorted phase but using a shift of 1.45 eV of the e_g band at the Fermi level. The position of the oxygen-p bands is not mimicked although they come closer to the Fermi level in the real distorted band structure (Fig. 8.2). We know from previous studies (see Chapter 7) that these bands notably contribute to the screening. Therefore, the results given in Tab. 8.4 must be overestimated, especially in Sr_2RhO_4, since the p

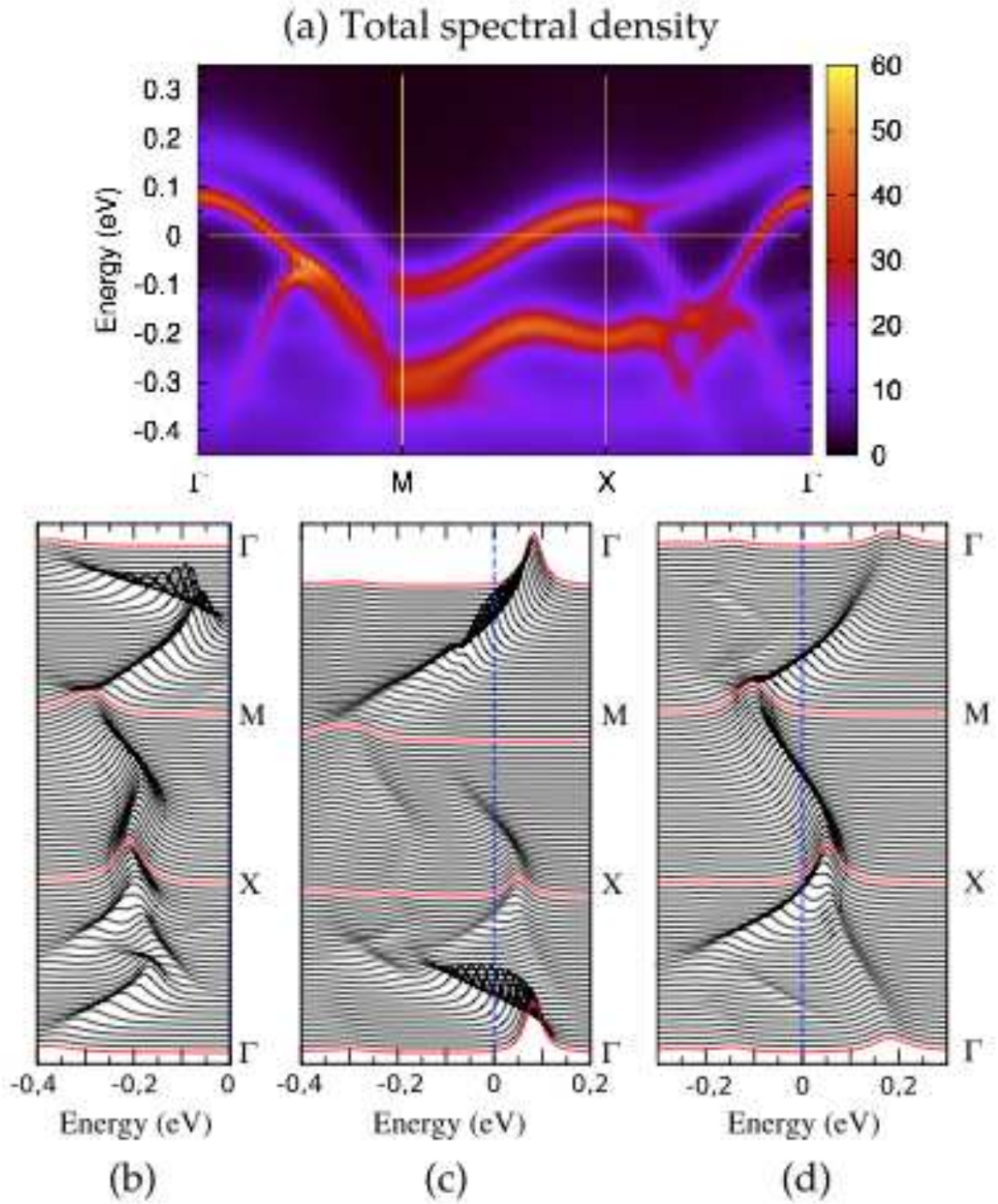

Figure 8.5: Momentum-resolved spectral function of Sr_2RhO_4 (a) from LDA+DMFT at $T = 300$ K. This corresponds to a paramagnetic metal. Bottom panels display the orbitally-resolved spectral densities $j_{eff} = 3/2\ |m_j| = 1/2$ (b), $j_{eff} = 3/2\ |m_j| = 3/2$ (c) and $j_{eff} = 1/2$ (d). Red lines are guides for the eyes.

bands locate about 1 eV higher in energy than in Sr_2IrO_4 and the effects of the screening channels are not linear [Aryasetiawan *et al.* (2006)].

With $\mathcal{U} = 1.94$ eV and $\mathcal{J} = 0.23$ eV, one gets from the Slater parametrization, $\tilde{U} = \tilde{F}^0 = 1.6$ eV for the Hubbard parameter and $\tilde{J} = 0.3$ eV for Hund's exchange (Eqs. 8.2, 8.3 and 8.4). The reduced Hubbard interaction matrices (in eV) in the spin-orbital Wannier basis then read as

$$U_{jj'}^{m_j\bar{m}_j}|_{\text{Slater}} = \begin{pmatrix} 1.67 & 1.31 & 1.27 \\ 1.31 & 1.85 & 1.45 \\ 1.27 & 1.45 & 1.71 \end{pmatrix} U_{jj'}^{m_j m_j}|_{\text{Slater}} = \begin{pmatrix} 0 & 1.48 & 1.66 \\ 1.48 & 0 & 1.29 \\ 1.66 & 1.29 & 0 \end{pmatrix}.$$

The order of the spin-orbitals is the same than previously : $j_{eff} = 1/2, j_{eff} = 3/2\,|m_j| = 1/2, j_{eff} = 3/2\,|m_j| = 3/2$.

Sr_2RhO_4 results into a paramagnetic metal with a partial spin-orbital polarization. Indeed, because of the smaller SOC, the system is mapped onto a quarter-filled two-band Hubbard model and the Coulomb interactions obtained by cRPA are not strong enough to induce a Mott insulating state with this degeneracy. The LDA+DMFT calculations (Fig. 8.5) are in agreement with energy distribution curves obtained by ARPES at 10 K [Baumberger *et al.* (2006)].

Sr_2RhO_4 also appears rather close to the Mott insulator transition. The critical interaction is found around $\tilde{U}_c = 1.8 - 2.0$ eV with $\tilde{J} = 0.3$ eV. This corresponds to $\mathcal{U}_c = 2.1$ eV and $\mathcal{J}_c = 0.23$ eV. A cRPA calculation for the realistic distorted phase is therefore desirable and currently in development.

8.1.4 Conclusions

The electronic properties of the isoelectronic and isostructural analogues Sr_2IrO_4 and Sr_2RhO_4 were analyzed within the *ab initio* LDA+DMFT approach on top of the cRPA interaction Hamiltonian. Distortions as well as spin-orbit coupling were taken into account and play a crucial role in the electronic nature of Sr_2IrO_4 and Sr_2RhO_4.

A $j_{eff} = 1/2$ Mott insulating phase is caught in the paramagnetic phase of Sr_2IrO_4. The calculated spectrum agrees with angle-resolved photoemission and optical measurements. In Sr_2RhO_4, lower effective Coulomb interactions due to screening and lower spin-orbit coupling lead to a paramagnetic metal whose characteristics at the Fermi level are in reasonable agreement with angle-resolved photoemission experiments.

8.2 Cerium Fluorosulfide (CeSF) pigments

This last section is devoted to the cRPA calculations of the Hubbard U and Hund's exchange J for the rare-earth compounds CeSF. The first principles description of materials containing lanthanide or actinide elements is usually regarded as a very challenging task, due to the presence of highly localized f states mixed with itinerant ones. The treatment of such localized states require to go beyond DFT-LDA. Several attempts have been proposed in the literature in order to reproduce, for example, the non-monotonic evolution of the band gap along the lanthanide sesquioxide or sesquisulfide series [Golubkov *et al.* (1995), Prokofiev *et al.* (1996)]. Such evolution relies on the position of the occupied f states relatively to the p and d surrounding bands. Recent GW calculations on top of LDA+U [Jiang *et al.* (2009)] were able to qualitatively reproduce the experimental trends. Full self-consistent LDA+DMFT calculations based on the Hubbard-I approximation [Pourovskii *et al.* (2007)] were also carried out. In both approaches, the Hubbard U and Hund's exchange J are treated as adjustable parameters.

The present work is a contribution to the LDA+DMFT calculations performed by L. Pourovskii, J. Tomczak *et al.* [Tomczak *et al.* (2012)]. The optical properties of the promising CeSF pigments can be characterized using LDA+DMFT as implemented by [Tomczak(2007)]. Understanding the origin of the optical properties and the color of such materials in relation with their electronic structure is a major challenge in the perspective of designing new pigments.

8.2.1 A brief review

The investigation of new pigments able to absorb ultra-violet (UV) radiation but without employing toxic heavy metals (like cadmium or mercury) has received much attention for several decades [Jansen and Letschert(2000)]. In practice, one wants to make use of UV absorbers in order to prevent the deterioration of biological tissue or other materials. Compounds made of rare-earth elements like sesquisulfides Ln_2S_4 or ALn_2S_4 (A = Ca, Sr) have demonstrated to be very promising : they are semi-conductors with a color ranging from red to yellow [Maestro and Huguenin(1995), Pauwels(2003)]. In the literature, the intense red color in Ce_2S_3 is attributed to the $4f$-$5d$ intra-atomic transitions and therefore crucially relies on the position of the cerium $4f$ bands relatively to the valence $3p$ and the conduction $5d$ bands. The question whether lanthanide fluorosulfides LnSF (Ln = La, Ce, Sm, etc...) are also good pigments, was recently addressed by [Demourgues *et al.* (2001b), Macaudière and Demourgues(2002)] : such materials could indeed have important applications because of their better chemical and thermal stability, attributed to the environment induced by the fluorine (F) elements. [3]

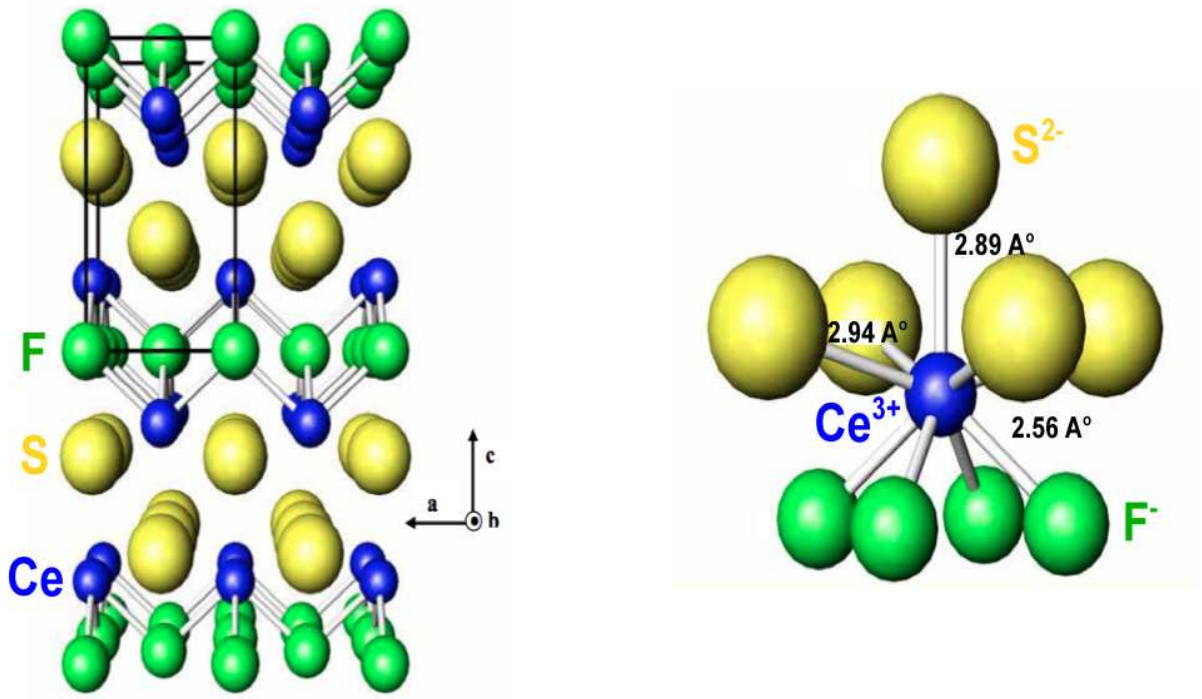

Figure 8.6: CeSF crystal structure ($P4/nmm$). Cerium atoms are in blue whereas sulfur atoms are in yellow and fluorine atoms in green (from [Pauwels(2003)]).

Crystal structure

Rare-earth fluorosulfides have been characterized by X-ray diffraction [Demourgues *et al.* (2001a), Schleid and Grossholz(2001)]. They adopt the PbFCl-type structure with $P4/nmm$ space group representation (Fig. 8.6). The rare-earth is at the center of a distorted square antiprism with four F atoms in one base and four S atoms in the other. A fifth Ln-S bond smaller than the other ones, appears parallel to the c-axis. Lattice parameters $a = 3.992\text{A}^\circ, c = 6.947\text{A}^\circ$ [Demourgues *et al.* (2001a)] will be used for the calculation of the band structure in CeSF.

CeSF : a good pigment

One can characterize the optical properties of a pigment - a specific semi-conductor - by its absorption edge, its refractive index and its extinction coefficient.

The absorption edge is extracted from the diffuse reflectance spectra and corresponds to the maximum of the second derivative of the absorption curve. For CeSF, Demourgues and co-workers give $\lambda_c = 597$ nm. This is enough for explaining the red color of the material

[3]Due to the high electronegativity of fluorine in the Ln-F bonding, there is by compensation an enhancement of the Ln-S bonding with respect to sesquisulfides.

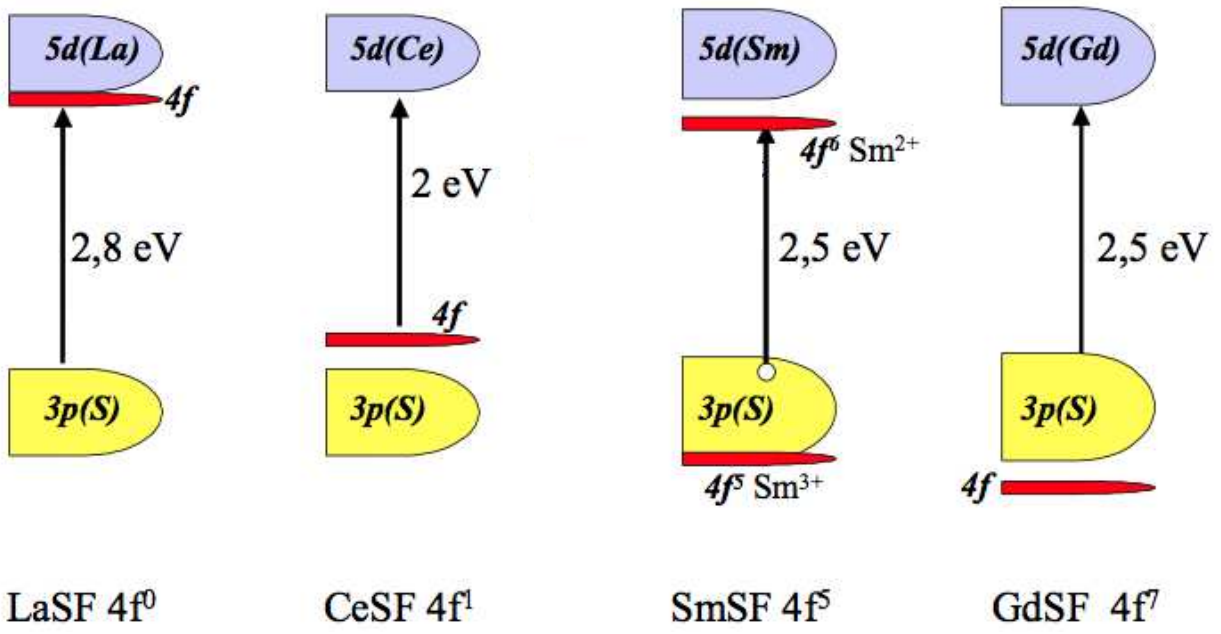

Figure 8.7: Interpretation from XPS of the mechanisms involved in the chromatic evolution along the early lanthanid fluorosulfide series (from [Pauwels(2003)]). In CeSF, the color is empirically attributed to the intra-atomic f to d transitions as shown in this figure. However, this does not agree with the positions of the f bands calculated with LDA+DMFT (see Fig. 8.11). Our interpretation of the color is based on the $3p$ to $4f$ transitions.

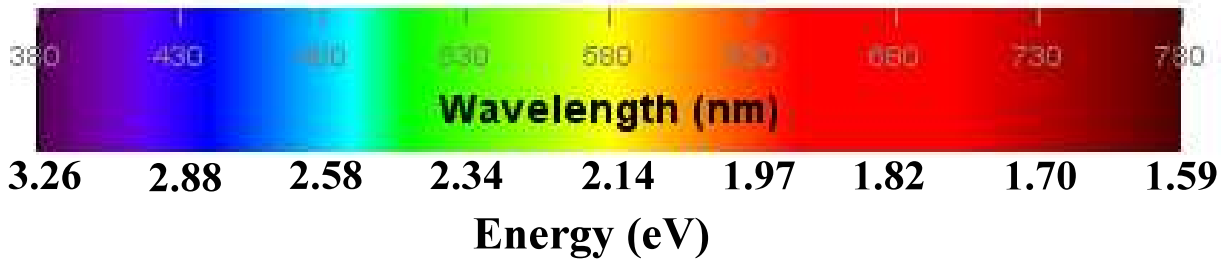

Figure 8.8: Color vs. wavelength diagram in the visible range.

(see Fig. 8.8 for the color vs. wavelength correspondance) [Demourgues *et al.* (2001b)]. For comparison, $\lambda_c = 443$ nm in LaSF and $\lambda_c = 490$ nm in SmSF. Nevertheless, these compounds are rather yellow, in contrast to the wavelength value (see Fig. 8.8). How sharp is the absorption spectrum around the absorption edge, determines the purity of the color. In CeSF, there is a steep absorption edge which justifies the sharp red color of the material.

The chromatic evolution (yellow-red-yellow) through the early lanthanide fluorosulfide series has to originate from different mechanisms, as reported in Fig. 8.7. The position of the rare-earth $4f$ band is mainly responsible for this : since there are no occupied f states in LaSF, the most probable optical transitions around 2.8 eV arise from the top of the $3p$ valence band to

the bottom of the rare-earth $5d$ conduction band. SmSF, on the other hand, is usually described as a charge-transfer insulator with an optical transition from $3p$ to $4f$ bands.

In CeSF, one expects the partially-filled f bands to be split in Hubbard bands. The p-d gap is hence reduced. [4] The optical transitions will depend on the position of the occupied and unoccupied f bands relatively to $3p$ and $5d$ bands. In [Goubin *et al.* (2004), Pauwels(2003)] (their results are shown in Fig. 8.7), the authors employed X-ray photoelectron spectroscopy (XPS) and electron energy-loss spectroscopy (EELS) for interpreting the gap around 2 eV in terms of the intra-atomic transitions from the lower Hubbard $4f$ bands to $5d$ bands. This is not in agreement with the positions of $4f$ multiplets calculated by LDA+DMFT and employing the cRPA interaction Hamiltonian (see below, Fig. 8.11).
In passing, we mention that the evolution of the conduction and valence bandwidths also play a role in the optical properties.

The refractive index n and the extinction coefficient κ are determined experimentally from the loss function $\mathrm{Im}(-1/\epsilon)$ that is deduced from EELS spectra. This was done for LaSF and CeSF compounds [Goubin *et al.* (2004)]. ϵ corresponds to the dielectric function of the material. The extinction coefficient κ characterizes the strength of the color due to the light absorption capacity of the material whereas the refractive index n has an impact on the light scattering power and thus explains the color opacity. In the visible range, both n and κ decrease from LaSF to CeSF. This can be interpreted by the weak radial distribution and the low electronic concentration of $4f$ states involved in the optical transitions [Goubin *et al.* (2004)].

From these studies, CeSF compounds appear appropriate for pigment applications whereas LaSF could be used as UV-blockers under the form of extra-fine particles in order to reduce the light scattering.

8.2.2 Band structure

As the starting point of cRPA, one first computes the Kohn-Sham band structure for CeSF (Fig. 8.9). We use as lattice parameters $a = 3.992\text{A}^\circ, c = 6.947\text{A}^\circ$ following [Demourgues *et al.* (2001a)].

As mentioned in the introduction, systems with f electrons are poorly described by DFT-LDA. First, the band structure of CeSF corresponds to a metal with narrow $4f$ bands at the Fermi level, instead of a semi-conductor. Second, the valence band consists in sulfur-like $3p$ bands and the conduction band in cerium-like $5d$ bands but the distance between the $3p$ and $5d$ bands is underestimated by DFT-LDA.

This distance was also underestimated in LaSF : the DFT-LDA spectrum correctly reproduces the semi-conductor nature of LaSF but the resulting p-d gap is about 2.0 eV. This is clearly too small compared to the experimental gap of 2.8 eV [Goubin *et al.* (2004), Pauwels(2003)]. In CeSF, the DFT-LDA p-d gap is even smaller than in LaSF whereas it should be comparable. In Fig. 8.10, we show the GW density of states for the paramagnetic phase of CeSF compared to

[4] This is very similar to cerium sesquioxides Ce_2O_3.

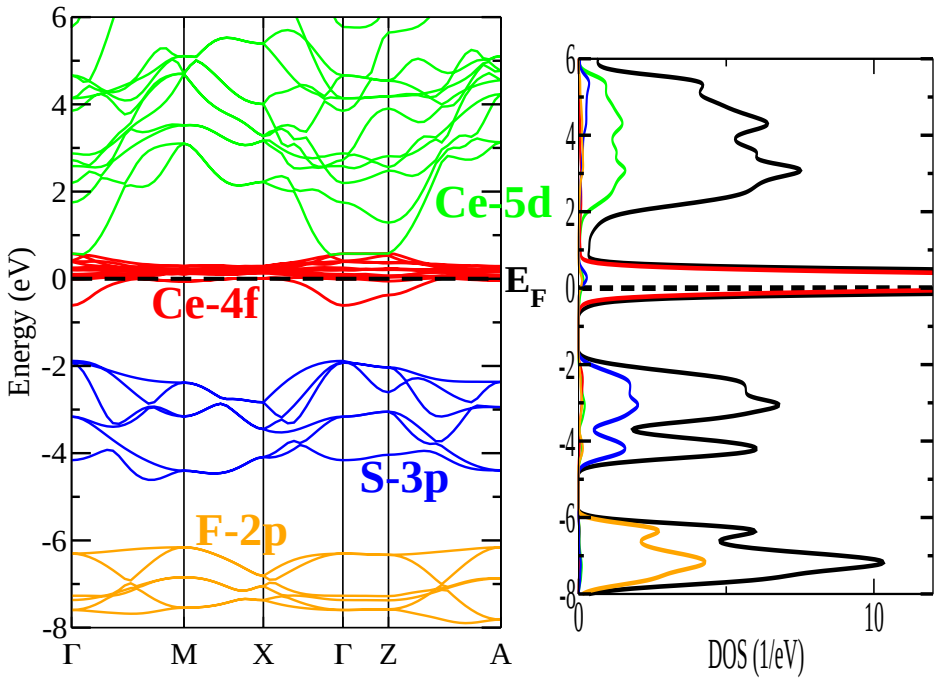

Figure 8.9: (left) DFT-LDA paramagnetic band structure of CeSF. (right) Total density of states (in black) and partial density of states. Cerium-4f character is highlighted in red, cerium-5d in green, sulfur-3p in blue and fluorine-2p in orange. The DFT-LDA spectrum corresponds to a metal with narrow f bands at the Fermi level. Furthermore, the gap between 3p and 5d is underestimated.

DFT-LDA. As explained in Chapter 2, the GW approximation does not open a gap in a strongly correlated material using Kohn-Sham eigenstates as initial guesses. The pd gap, however, is partially corrected for by the upward shift of the d bands by about 1 eV. On the other hand, the sulfur-like p bands do not shift as much. This encourages the scissor-like correction of the pd gap in the LDA+DMFT calculations shown in Fig. 8.11 and detailed later.

8.2.3 The "f-f Hamiltonian"

Adapting the cRPA method for CeSF pigments, projected 4f Wannier orbitals centered on the cerium atoms are constructed out of the Kohn-Sham states within the energy window $\mathbb{W} = [-1, 0.6]$ eV. All transitions from and to the f-like bands within $\mathbb{W}$ are then excluded from the total polarization to compute the constrained polarization P^r at the RPA level.

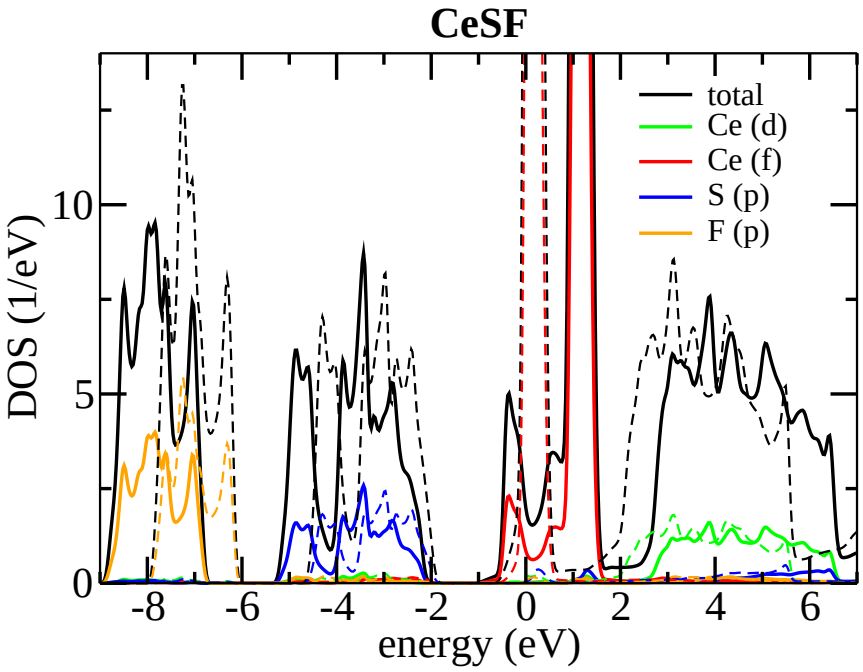

Figure 8.10: GW density of states calculated in the paramagnetic phase of CeSF. DFT-LDA density of states is shown in dashed lines for comparison.

cRPA results

In Tab. 8.5, we give the cRPA results under the form of four Slater integrals for both the screened and bare interactions. The Hubbard U interaction reads as $U = \mathrm{F}^0 = 4.8$ eV and Hund's exchange $J(\mathrm{F}^2, \mathrm{F}^4, \mathrm{F}^6) = 0.70$ eV, following Eq. 5.69.

As already reported for screened interactions in $4d$ layered perovskite and in pnictide compounds, one observes a deviation of the Slater integrals ratio $\mathrm{F}^4/\mathrm{F}^2$ and $\mathrm{F}^6/\mathrm{F}^2$ from the atomic values. The agreement with the atomic values is better for the bare (unscreened) interactions. We remind the reader (Eq. 5.60) that in the atom, $\mathrm{F}^4/\mathrm{F}^2 \approx 0.67$ and $\mathrm{F}^4/\mathrm{F}^2 \approx 0.49$. The deviation for the screened interactions might come from screening anisotropies (see also Chapter 7 for the layered perovskites and Chapter 6 for the pnictides).

Comparison with cLDA

Using "hard"-cLDA (see Chapter 4), the Hubbard on-site interaction between f orbitals within the head of the LMTO-ASA framework as local orbitals, yields $U = 4.6$ eV and Hund's exchange $J = 0.43$ eV. Whereas the on-site interactions from cLDA and cRPA are rather similar, one observes a significant difference for the exchange interactions.

	(eV)	F^0	F^2	F^4	F^6	F^4/F^2	F^6/F^2	J
CeSF	bare	21.9	10.01	6.20	4.59	0.619	0.458	0.81
	screened	4.8	7.86	5.85	4.54	0.745	0.578	0.70
Ce_2O_3	bare	21.5	9.75	6.18	4.59	0.634	0.470	0.80
	screened	5.3	7.58	5.84	4.48	0.771	0.591	0.69

Table 8.5: Slater integrals for the f-f model in CeSF and in Ce_2O_3. The first line (bare) corresponds to the bare interaction v whereas the second line to the screened Hubbard U interaction.

J from cRPA is actually similar to the value obtained by extrapolation in Dieke's diagram so established for lanthanide (Ln) elements [Dieke(1968)]. It also agrees with the values reported for Ln^{3+} impurities in LaF_3 experimental spectra fitted by (F^2, F^4, F^6) Slater integrals [Carnall *et al.* (1989)].

It is usually believed that the multipole part of the Coulomb interaction leading to J is weakly dependent on the crystal structure. The comparison with isoelectronic cerium (Ce^{3+}) sesquioxide Ce_2O_3 confirms this point, since the values for J are very close (Tab. 8.5).

For these reasons, LDA+DMFT calculations were preferently combined with the cRPA values rather than the cLDA ones. Furthermore, as recently highlighted by [de' Medici *et al.* (2011)], J can play a significant role in the estimation of the Mott gap. This again points out the importance of calculating effective Coulomb interactions from first principles within a reliable and consistent way.

Comparison with Ce_2O_3

Several times, we have compared CeSF to its isoelectronic analogue Ce_2O_3. Both materials are indeed quite similar since their physical properties rely on the relative position of the $4f$ Hubbard bands relatively to the valence and conduction bands. Cerium sesquioxide compounds have already received an intense attention and are not the topic of the work here. Only for comparison with CeSF, we add in Tab. 8.5 the cRPA calculation for Ce_2O_3 using the f-f model which is equivalent to the one employed for CeSF.

We stress that the exchange interactions for CeSF ($J = 0.70$ eV) and Ce_2O_3 ($J = 0.69$ eV) are very close. This confirms the previous statement that J does not depend much on the crystal structure.

For further comparison, we deduce for Ce_2O_3 an effective interaction $U_{\text{eff}} = U - J = 0.34$ Ry, which is in reasonable agreement with $U_{\text{eff}} = 0.4$ Ry employed in GW@LDA+U calculations by [Jiang *et al.* (2009)].

In the following, we show the spectra calculated by LDA+DMFT within the LMTO-ASA framework and using Coulomb interactions on f shells from cRPA [Tomczak et al. (2012)]. The self-consistency over the charge density was performed in LDA+DMFT but the self-consistency over the polarization for cRPA was not implemented.

8.2.4 Application : the *ab initio* k-resolved spectral function

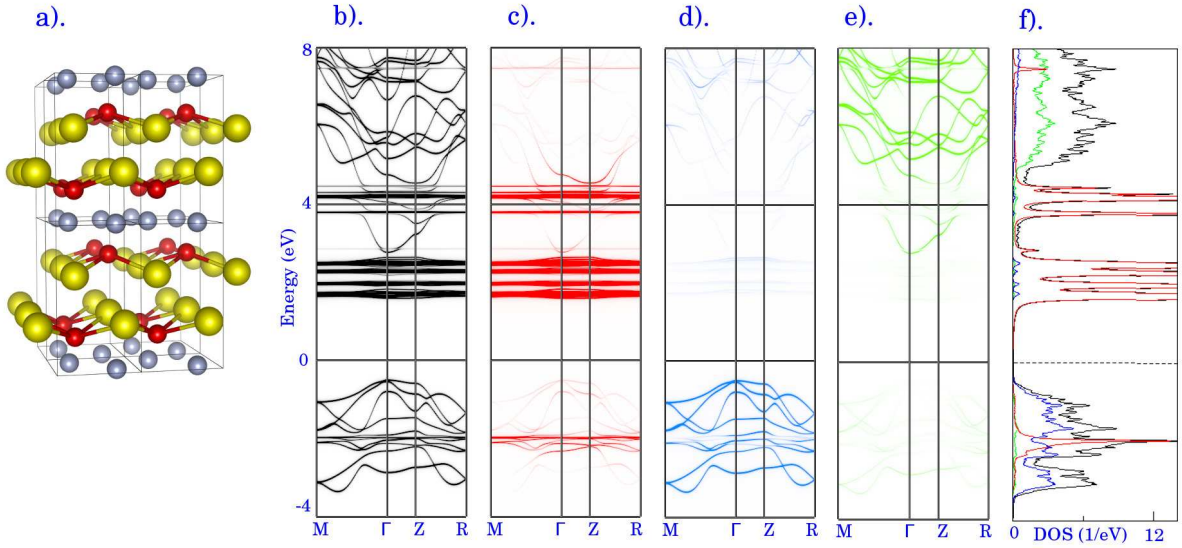

Figure 8.11: (a) The CeSF crystal structure. The red, yellow and gray balls represent Ce, S and F, respectively. (b-e) The total (b), partial Ce $4f$ (c), S $3p$ (d) and Ce $5d$ (e) LDA+DMFT $\boldsymbol{k}$-resolved spectral functions. (f) The total (black curve) as well as partial Ce $4f$ (red curve), S $3p$(blue curve) and Ce $5d$ (green curve) integrated spectral functions (see [Tomczak *et al.* (2012)] for more details).

The LDA+DMFT scheme used by [Tomczak *et al.* (2012)] was implemented within the LMTO-ASA framework. The Hubbard-I approximation was employed as a quantum impurity solver. The full self- consistency over the charge density was also performed (see Chapter 3). Spin-orbit coupling has been taken into account through the second variation method.
The local Coulomb interaction parameters $U = 4.8$ eV and $J = 0.70$ eV on Ce $4f$ shell were determined by cRPA employing the paramagnetic DFT-LDA band structure of CeSF without spin-orbit coupling for computational reasons (Tab. 8.5).

As mentioned earlier, the local density approximation leads to a rather expected significant underestimation of the semiconducting gap between S $3p$ and lanthanide $5d$ bands in the rare-earth fluorosulfides. In LaSF, the error yields about 0.8 eV. The LDA+DMFT approach employed in [Tomczak *et al.* (2012)], does not contain corrections for this LDA error, which is due to long-range correlations in the semi-conducting bands. As shown in Fig. 8.10, the GW approximation in CeSF increases the pd gap by inducing a shift for $5d$ bands and not for $3p$ ones. An *ad hoc* scissor-like correction term can hence be used for circumventing this LDA error in CeSF : in the one-electron Hamiltonian, a constant upward shift for $5d$ states of 2.5 eV is added in order to correct for the ~ 0.8 eV band gap underestimation in LaSF.

The LDA+DMFT $\boldsymbol{k}$-resolved spectrum is shown in Fig. 8.11. The red curve indicates the multiplet structure of the $4f$ states.

According to this calculation, one attributes the 2.8 eV optical gap in CeSF to the inter-atomic $3p$-$4f$ transitions. Further analyzes of the optical properties of CeSF so calculated within LDA+DMFT and supporting this interpretation are given in [Tomczak *et al.* (2012)].

8.2.5 Conclusions

The LDA+DMFT approach, where the f-restricted Hubbard Hamiltonian was constructed within cRPA and solved by DMFT within the Hubbard-I approximation, is able to catch the insulating state of CeSF compounds. A scissor-like correction in agreement with GW calculations, was employed for correcting for the LDA underestimate of the p-d gap.

In contrast to previous studies by [Goubin *et al.* (2004), Pauwels(2003)], the optical gap around 2 eV leading to the red color of CeSF, is attributed to the inter-atomic $3p$-$4f$ transitions. The calculations of the optical properties based on LDA+DMFT are reported in [Tomczak *et al.* (2012)].

Part IV

Conclusions

Conclusions and outlook

The goal of the present thesis was the determination of Coulomb interactions in correlated solids from first principles. To achieve this, we have implemented the constrained-random phase approximation (cRPA) method starting from an Hamiltonian taken from density functional theory, implemented within the linearized augmented plane wave framework (Fig. 4.5). The method gives access to the matrix elements of the Hubbard interaction matrix in a localized basis set of a downfolded lattice Hamiltonian. The strength of the Coulomb interactions is parametrized by the Hubbard U and Hund's exchange J, which are crucial for the description of correlated electron systems within interacting lattice Hamiltonians. Furthermore, the full energy-dependence of these parameters is calculated, which enables one to consider the effects of dynamical screening.

Several definitions of U exist in the literature, which may lead to confusion. In this thesis, we stress that values for these parameters must always be reported together with the model it is used with. U first introduced in the single-orbital Hubbard-Kanamori-Gutzwiller model, as the Coulomb energy cost for placing two electrons at the same atomic site *in a localized orbital*, is also employed as a fitting parameter for experimental spectra. On the other hand, several schemes have been proposed for the first principles evaluation of U.
We argue that the confusion can be explained by the following statement : U *itself* is not a physical observable, whereas U *and the model considered*, become well defined. Consequently, addressing values for Coulomb interactions but without the indication of the model, does not have any meaning.
In spectroscopy experiments, for materials with strongly localized electrons, multiplet structures may lead to an unambiguous determination of U (see for example the photoemission spectrum of CuO in Chapter 4, Fig. 4.2). In this case, one could argue that U itself is a physical observable, which can be measured experimentally. However, this is actually biased by the fact that a natural localized basis has emerged in this system. A majority of correlated materials, because of e.g. hybridization effects or spin-orbit coupling, do not display a spectrum that leads to *such a natural choice* of a localized basis. Therefore, such a choice (in other words, a model) has to be done and we get back to the previous statement that only U *together with the model considered* are well defined.
Even if values for U differ from one model to another, *results for physical observables are the same at the end*, under the condition that the model is appropriate.

We have investigated this point for several materials and we have systematically indicated the low-energy model constructed.

To benchmark our approach, $SrVO_3$ perovskite and iron-based pnictides were considered. The results agree with the ones reported in the literature. A calculation of Slater integrals was also introduced in order to parametrize efficiently the effective four-index Coulomb matrix without referring to the Slater integrals atomic ratio F^4/F^2.

Since both U and J depend on the model considered for a given compound, so do their trends for a family of these compounds. When employing extended Wannier functions in the $3d$ perovskite family $SrMO_3$ (M=V, Cr, Mn), effective Coulomb interactions decrease with the d occupation number as a consequence of the increasing screening (Fig. 7.3). This is in contrast with generally spread ideas but can be rationalized by the increasing charge transfer energy with the oxygen ligands through the series. However, atomic-like behavior is recovered when employing more localized Wannier functions.
Compared to their isoelectronic and isostructural analogues, $4d$ transition metal oxides $SrMO_3$ (M=Nb, Mo, Tc) exhibit weaker screening effects within an extended Wannier basis. This surprisingly leads to an effective larger on-site repulsion on $4d$ shells than on $3d$ (Fig. 7.5). However, atomic-like trends are recovered when employing a more atomic-like Wannier basis and the repulsion becomes larger on $3d$ shells as commonly expected from physical intuition.
Similar conclusions were established for the effective Coulomb interactions in the layered perovskites Sr_2MO_4 (M=Mo, Tc, Ru, Rh) (Fig. 7.12).

Within this framework, we stressed out that an *ab initio* Hamiltonian of multi-orbital Hubbard type is defined. The Hamiltonian can then be solved by any appropriate many-body method. In Chapter 8 of this thesis, an *ab initio* LDA+cRPA+DMFT approach was employed. This scheme consisted in determining the interaction parameters within the cRPA and combining it with LDA+DMFT in a fully consistent way.
It was applied to the layered perovskite Sr_2IrO_4 and Sr_2RhO_4, which both exhibit significant spin-orbit coupling and distortions but different electronic properties. This study was done in collaboration with C. Martins *et al.* [Martins *et al.* (2011)] who did the LDA+DMFT calculations. At room temperature, Sr_2IrO_4 is a paramagnetic Mott insulator, whereas Sr_2RhO_4 is a paramagnetic metal. Such different behavior can be related to the larger spin-orbit coupling and the weaker static screening in Sr_2IrO_4, leading to an effective *single-band* model where the effective Coulomb interaction is larger than the critical value (Fig. 8.4). On the other hand, Sr_2RhO_4 is mapped onto a quarter-filled *two-band* Hubbard model with a smaller effective interaction. This leaves Sr_2RhO_4 metallic even if it is on the verge of the metal-insulator transition (Fig. 8.5).
As a last application, we have described the electronic structure of the rare-earth fluorosulfide CeSF compounds for which we calculated the effective Coulomb interactions. This project was done in collaboration with L. Pourovskii, J. Tomczak *et al.* [Tomczak *et al.* (2012)] who did the LDA+DMFT calculations within the Hubbard-I approximation. Systems including partially filled f shells are challenging systems for first principles methods. The *ab initio* spectrum (Fig. 8.11) indicates that, in contrast to previous beliefs, the inter-atomic $3p$-$4f$ transitions are at the origin of the red color of the pigment.

Several extensions can be addressed into the future. A first logical one is technical. It would be interesting to carry out calculations on larger systems, displaying distortions for instance. Another important technical improvement would be the implementation of the spin-orbit coupling.

Indeed, the interplays of spin-orbit coupling and electronic Coulomb interactions are relevant in many materials, as shown in Sr_2IrO_4 and Sr_2RhO_4 for example.

A reliable approach for materials including entangled correlated and itinerant states, is also desirable. A majority of correlated materials indeed exhibit an electronic structure with localized states overlapping with itinerant ones (Fig. 4.8). This makes the standard cRPA method rather inappropriate. We have introduced a projection method based on the *projection of the polarization onto the correlated subspace* defined by a set of target bands. The calculations performed on the $3d$ transition metal series are promising and encourage further investigations. Applications for materials like cerium, cuprates and iron-based pnictides are currently in development. The questions regarding which physical models are appropriate, are particularly relevant.

The combination of the energy-dependent Hubbard $U(\omega)$ with many-body solvers like LDA+DMFT, also represents a great challenge for the future. Methods in this direction have been recently proposed. The results show that the dynamical structure of U with plasmonic excitations (Fig. 4.9) has consequences on the spectral properties of $SrVO_3$ [Casula *et al.* (2012a)] and $BaFe_2As_2$ compounds [Werner *et al.* (2012), Casula *et al.* (2012b)].

We finish with the project of developing of a truly first principles LDA+DMFT scheme with an *update of the polarization* within cRPA (Fig. 4.7). This would allow for a better description of the screening in strongly correlated materials like Mott insulators and can be seen as an approximation to the GW+DMFT method.

Alternatively to DMFT, a combination with diagrammatic Monte-Carlo approaches [Kozik *et al.* (2011)] to go beyond the GW approximation, is currently in development.

Acknowledgments

Part V

Postliminaries

Summaries of the articles

Implementation of cRPA and application to oxides

1. U and J in Transition Metal Oxides (2012) (arXiv: 1206.3533, PRB in press)

Hubbard U and Hund's Exchange J in Transition Metal Oxides: Screening vs. Localization Trends from Constrained Random Phase Approximation

Loïg Vaugier,[1,2,*] Hong Jiang,[3,†] and Silke Biermann[1,2,‡]

[1] *Centre de Physique Théorique, Ecole Polytechnique, CNRS UMR 7644, 91128 Palaiseau, France*
[2] *Japan Science and Technology Agency, CREST, Kawaguchi 332-0012, Japan*
[3] *Beijing National Laboratory for Molecular Sciences, State Key Laboratory of Rare Earth Material Chemistry and Application, Institute of Theoretical and Computational Chemistry, College of Chemistry and Molecular Engineering, Peking University, 100871 Beijing, China*

(Dated: today)

In this work, we address the question of calculating the local effective Coulomb interaction matrix in materials with strong electronic Coulomb interactions from first principles. To this purpose, we implement the constrained random phase approximation (cRPA) into a density functional code within the linearized augmented plane wave (LAPW) framework.

We apply our approach to the $3d$ and $4d$ early transition metal oxides $SrMO_3$ (M=V, Cr, Mn) and (M=Nb, Mo, Tc) in their paramagnetic phases. For these systems, we explicitly assess the differences between two physically motivated low-energy Hamiltonians: The first is the three-orbital model comprising the t_{2g} states only, that is often used for early transition metal oxides. The second choice is a model where both, metal d- and oxygen p-states are retained in the construction of Wannier functions, but the Hubbard interactions are applied to the d-states only ("d-dp Hamiltonian"). Interestingly, since – for a given compound – both U and J depend on the choice of the model, so do their trends within a family of these compounds. In the $3d$ perovskite series $SrMO_3$ the effective Coulomb interactions in the t_{2g} Hamiltonian decrease along the series, due to the more efficient screening. The inverse – generally expected – trend, increasing interactions with increasing atomic number, is however recovered within the more localized "d-dp Hamiltonian". Similar conclusions are established in the layered $4d$ perovskites series Sr_2MO_4 (M=Mo, Tc, Ru, Rh). Compared to their isoelectronic and isostructural $3d$ analogues, the $4d$ 113 perovskite oxides $SrMO_3$ (M=Nb, Mo, Tc) exhibit weaker screening effects. Interestingly, this leads to an effectively larger U on $4d$ shells than on $3d$ when a t_{2g} model is constructed.

PACS numbers: 71.27.+a,71.10.Fd,71.15.Ap,71.45.Gm

Applications of cRPA to various systems

2. Reduced Effective Spin-Orbital Degeneracy and Spin-Orbital Ordering in Paramagnetic Transition Metal Oxides: Sr_2IrO_4 vs. Sr_2RhO_4 (2011)

PRL **107,** 266404 (2011) PHYSICAL REVIEW LETTERS week ending 23 DECEMBER 2011

Reduced Effective Spin-Orbital Degeneracy and Spin-Orbital Ordering in Paramagnetic Transition-Metal Oxides: Sr_2IrO_4 versus Sr_2RhO_4

Cyril Martins,[1,2] Markus Aichhorn,[3,1] Loïg Vaugier,[1] and Silke Biermann[1,2]
[1]*Centre de Physique Théorique, Ecole Polytechnique, CNRS, 91128 Palaiseau Cedex, France*
[2]*Japan Science and Technology Agency, CREST, Kawaguchi 332-0012, Japan*
[3]*Institute of Theoretical and Computational Physics, TU Graz, Petersgasse 16, Graz, Austria*
(Received 5 July 2011; revised manuscript received 31 October 2011; published 22 December 2011)

We discuss the notions of spin-orbital polarization and ordering in paramagnetic materials, and address their consequences in transition-metal oxides. Extending the combined density functional and dynamical mean field theory scheme to the case of materials with large spin-orbit interactions, we investigate the electronic excitations of the paramagnetic phases of Sr_2IrO_4 and Sr_2RhO_4. We show that the interplay of spin-orbit interactions, structural distortions and Coulomb interactions suppresses spin-orbital fluctuations. As a result, the room temperature phase of Sr_2IrO_4 is a paramagnetic spin-orbitally ordered Mott insulator. In Sr_2RhO_4, the effective spin-orbital degeneracy is reduced, but the material remains metallic, due to both, smaller spin-orbit and smaller Coulomb interactions. The corresponding spectra are in excellent agreement with photoemission data. Finally, we make predictions for the spectra of paramagnetic Sr_2IrO_4.

DOI: 10.1103/PhysRevLett.107.266404 PACS numbers: 71.27.+a, 71.15.−m, 75.25.Dk, 75.70.Tj

3. What about U on surfaces? (2012) (accepted in Journal of Physics: Condensed Matter)

What about U on Surfaces? – Extended Hubbard Models for Adatom Systems from First Principles

Philipp Hansmann[1], Loïg Vaugier[1], Hong Jiang[2], and Silke Biermann[1,3]

[1]Centre de Physique Théorique, Ecole Polytechnique, CNRS-UMR7644, 91128 Palaiseau, France
[2]Beijing National Laboratory for Molecular Sciences, College of Chemistry and Molecular Engineering, Peking University, 100871 Beijing, China
[3]Japan Science and Technology Agency, CREST, Kawaguchi 332-0012, Japan

E-mail: philipp.hansmann@cpht.polytechnique.fr

Abstract. Electronic correlations together with dimensional constraints lead to some of the most fascinating properties known in condensed matter physics. As possible candidates where these conditions are realized, semiconductor (111) surfaces and adatom systems on surfaces have been under investigation for quite some time. However, state-of-the-art theoretical studies on these materials that include many body effects beyond the band picture are rare. First principles estimates of inter-electronic Coulomb interactions for the correlated states are missing entirely, and usually these interactions are treated as adjustable parameters. In the present work, we report on calculations of the interaction parameters for the group IV surface-adatom systems in the α-phase series of Si(111):C, Si, Sn, Pb. For all systems investigated, inter-electronic Coulomb interactions are indeed large compared to the kinetic energy of the states in question. Moreover, our study reveals that intersite interactions cannot be disregarded. We explicitly construct an extended Hubbard model for the series of group IV surface-adatom systems on silicon, which can be used for further many-body calculations.

4. Low-energy Models for Correlated Materials: Bandwidth Renormalization from Coulombic Screening (2012) (arXiv: 1204.4900, Phys. Rev. Lett. in press)

Low-energy models for correlated materials: bandwidth renormalization from Coulombic screening

M. Casula,[1] Ph. Werner,[2] L. Vaugier,[3,4] F. Aryasetiawan,[5] A. Millis,[6] and S. Biermann[3,4]

[1]*CNRS and Institut de Minéralogie et de Physique des Milieux condensés, Université Pierre et Marie Curie, case 115, 4 place Jussieu, 75252, Paris cedex 05, France*
[2]*Department of Physics, University of Fribourg, 1700 Fribourg, Switzerland*
[3]*Centre de Physique Théorique, Ecole Polytechnique, CNRS-UMR7644, 91128 Palaiseau, France*
[4]*Japan Science and Technology Agency, CREST, Kawaguchi 332-0012, Japan*
[5]*Department of Physics, Mathematical Physics, Lund University, Sölvegatan 14A, 22362 Lund, Sweden*
[6]*Department of Physics, Columbia University, 538 West, 120th Street, New York, NY 10027, USA*

We provide a prescription for constructing Hamiltonians representing the low energy physics of correlated electron materials with dynamically screened Coulomb interactions. The key feature is a renormalization of the hopping and hybridization parameters by the processes that lead to the dynamical screening. The renormalization is shown to be non-negligible for various classes of correlated electron materials. The bandwidth reduction effect is necessary for connecting models to materials behavior and for making quantitative predictions for low-energy properties of solids.

PACS numbers: 71.27.+a,71.30.+h,71.10.Fd

5. How Good is the Slater Parametrization in Iron-based Pnictides and Chalcogenides? (to be submitted to Phys. Rev. B)

How good is the Slater parametrization in iron-based pnictides and chalcogenides ?

L. Vaugier,[1] H. Jiang,[2] and S. Biermann[1]

[1]*Centre de physique théorique, Ecole Polytechnique, 91128 Palaiseau, France**
[2]*College of Chemistry, Peking University, Beijing 100871, China*

(Dated: today)

In this paper, the strength of the on-site and nearest-neighbor electronic correlations in iron-based pnictides (LaOFeAs, $BaFe_2As_2$) and chalcogenides (FeSe) is calculated from first principles within the constrained random phase approximation (cRPA). The local interaction matrices so calculated are dedicated to Hubbard models that retain both Fe d and As p (and O p in oxypnictides) degrees of freedom but counting for a Coulomb energy cost only on Fe d orbitals. We then discuss a parametrization of the interaction matrices that is based on Slater integrals. Within the assumption that the d localized orbitals of the downfolded Hamiltonian still have a spherical symmetry as in an isolated atom, we stress that one can calculate a set of optimal parameters for fitting the local interaction matrices. In particular, no approximation of the ratios of the Slater integrals is required in such approach. The accuracy of the approach hence relies on how close to atomic sphericity are the downfolded Fe-d local orbitals. Such sphericity can be broken at different levels for several reasons investigated below, such as screening or hybridization. We show that anisotropies increase with the ligands (from chalcogenides to pnictides) but also with the interlayer planes, whose contribution to screening is examined. A comparison between $BaFe_2As_2$ and $BaRu_2As_2$ is introduced in order to light on the effects of isovalent substitutions in the electronic structure and correlations.

6. Colors from First Principles: Heavy-Metal vs. Rare-Earth Pigments (2012) (submitted to Nature Materials Letters)

Colors from First-Principles: Heavy-Metal *vs.* Rare-Earth Pigments

J. M. Tomczak,[1] L. V. Pourovskii,[2] L. Vaugier,[2] S. Biermann,[2] and A. Georges[2,3,4]

[1]*Department of Physics and Astronomy, Rutgers University, Piscataway, NJ 08854, USA*
[2]*Centre de Physique Théorique, Ecole Polytechnique, CNRS, 91128 Palaiseau, France.*
[3]*Collège de France, 11 place Marcelin Berthelot, 75005 Paris, France*
[4]*DPMC-MaNEP, Université de Genève, 24 quai Ernest Ansermet, CH-1211 Genève, Suisse*

PACS numbers:

Many inorganic pigments contain heavy metals hazardous to health and the environment [1]. Much attention has been devoted to non-toxic alternatives [2] based on rare-earth elements [3, 4]. The computation of colours from first principles is a challenge to electronic structure methods however, especially for materials with localized *f*-orbitals. Here, starting from atomic positions only, we compute the actual colour of the red pigment cerium fluorosulfide CeSF, as well as of mercury sulfide HgS (classic 'vermilion'). Our methodology employs many-body theories [5–8] to compute the optical absorption, combined with an intermediate length-scale modelization [9] to assess how colouration depends on film thickness, pigment concentration and granularity. We introduce a quantitative criterion for the performance of a pigment. While for HgS this criterion is satisfied due to large transition matrix elements between wide bands, CeSF presents an alternative paradigm: the bright red color is shown to stem from the combined effect of the quasi two-dimensionality and the localized nature of 4*f* states. Our work demonstrates the power of modern computational methods, with implications for the theoretical design of materials with specific optical properties.

Light propagating inside a heterogeneous solid experiences (i) absorption, and (ii) scattering. The light that is not absorbed is diffusely reflected and is responsible for the perceived colour. The visual appearance of a material is hence determined by *selective absorption of light* and sufficient *(back)scattering*. For a material to be e.g. a luminous red pigment, two criteria must thus be satisfied. First, its absorption edge should be located at the appropriate energy (~ 2.1 eV) so that the red component of the visible spectrum is not absorbed. Second, the absorption edge should be sharp, so that most other photons within the visible range (green, blue) are absorbed.

The computation of these effects from first principles is faced with three fundamental difficulties. First, in view of the sensitivity of the human eye, the optical gap must be obtained with a precision of at least 100 meV. Conventional electronic structure methods yield a well-documented underestimation of the gap of conventional semiconductors [10]. Second, the quasi-localized 4f states, which play a crucial role in optical properties of rare-earth based pigments, are poorly described by standard density-functional theory or even GW approaches. Thirdly, a realistic assessment of the colouration of a pigment must take into account scattering properties depending on concentration, granularity and film thickness. *Ab initio* simulations so far have not ventured beyond calculating the optical conductivity of infinite bulk samples (see however Ref. [11] for organic molecules). In this article we address all these issues and develop a general methodology for the prediction of the colour of narrow-band materials.

Extension to a new GW_Γ scheme

7. Electronic Structure of Materials with Shallow Semi-Core States: Vertex Corrections from Constrained GW Approximation (2012) (to be submitted to Phys. Rev. Lett.)

Electronic structure of materials with shallow semi-core states: vertex corrections from constrained GW approximation

Hong Jiang,[1] Loïg Vaugier,[2] Takashi Miyake,[3] Ferdi Aryasetiawan,[3] Samuel Oliveira-Costa,[2] and Silke Biermann[2,4]

[1]*Beijing National Laboratory for Molecular Sciences, College of Chemistry and Molecular Engineering, Peking University, 100871 Beijing, China*
[2]*Centre de Physique Théorique, Ecole Polytechnique, CNRS, 91128 Palaiseau Cedex, France*
[3]*1Research Institute for Computational Sciences, National Institute of Advanced Industrial Science and Technology, Tsukuba, Ibaraki 305-8568, Japan*
[4]*Japan Science and Technology Agency, CREST, Kawaguchi, 332-0012, Japan*

The accurate description of electronic band structures of systems with shallow semi-core states is a notoriously difficult task. In this letter, we propose an approach that takes into account the localized nature of these states in a vertex corrected *GW* approximation. Our approach builds on the success of the constrained random phase approximation scheme for the calculation of local Coulomb interactions for models of correlated electrons: it constructs a vertex that suppresses spurious self-interaction effects for the localized states, while sticking to the *screened* Hartree-Fock concept that is at the heart of the *GW* method for the delocalized states. We find excellent agreement with experimental spectra for a series of IIB-VI and III-V semiconductors including GaAs, GaN, CdS, CdSe to ZnSe, ZnS, and ZnO. While our approach yields good agreement with experiment in terms of the band gap, even more importantly, in all of the above compounds the position of the shallow semi-core states is correctly described.

Previous works on quantum impurity models

8. Comment on "Zero-field Kondo Splitting and Quantum-Critical Transition in Double Quantum Dots" (2007) in collaboration with A. A. Aligia and A. M. Lobos

Comment on "Zero-field Kondo Splitting and Quantum-Critical Transition in Double Quantum Dots"

In a recent Letter [1], a system containing a noninteracting and a Kondo quantum dot (QD) has been studied. Interesting effects are observed in the spectral density of the Kondo QD $A_{11}(\omega)$ due to the nonconstant density of states $\rho_2(\omega)$ to which the Kondo QD interacts. For a side-dot configuration, if the width Δ_2 of $\rho_2(\omega)$ is sufficiently smaller than the Kondo temperature T_K, the Kondo peak is split in two. This splitting was found also in a similar model for quantum mirages [2]. In Ref. [1] the splitting is interpreted as due to a decrease in $A_{11}(\epsilon_F)$, where ϵ_F is the Fermi energy, to satisfy the Friedel sum rule (FSR). An alternative interpretation, based on interference between noninteracting resonances is in principle unjustified for a highly correlated system. Here we show that the first interpretation is not correct and provide a justification for the second.

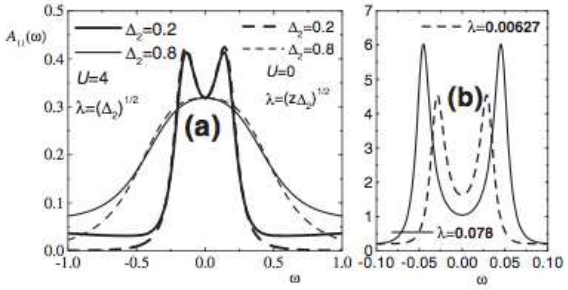

FIG. 1. (a) Full lines: $A_{11}(\omega)$ for $U = 4$ and two values of $\lambda = \sqrt{\Delta_2}$. Dashed lines: $zA_{11}(\omega)$ for $U = 0$ and $\lambda = \sqrt{z\Delta_2}$. (b) $A_{11}(\omega)$ for the parameters of Fig. 2 (b)–(c) of Ref. [1]

We have calculated $\Sigma_{dd}(\omega)$ using perturbation theory to order U^2 [2,4]. The approximation satisfies Fermi liquid relations $\mathrm{Im}\Sigma_{dd}(\omega) = 0$ and we have verified numerically that the integral in Eq. (1) vanishes. The resulting $A_{11}(\omega)$ is

9. Spectral Density of an Interacting Dot Coupled Indirectly to Conducting Leads (2007)

PHYSICAL REVIEW B 76, 165112 (2007)

Spectral density of an interacting dot coupled indirectly to conducting leads

L. Vaugier, A. A. Aligia, and A. M. Lobos
Centro Atómico Bariloche and Instituto Balseiro, Comisión Nacional de Energía Atómica, 8400 Bariloche, Argentina
(Received 28 May 2007; revised manuscript received 23 August 2007; published 10 October 2007)

We study the spectral density of electrons $\rho_{d\sigma}(\omega)$ in an interacting quantum dot (QD) with a hybridization λ to a noninteracting QD, which, in turn, is coupled to a noninteracting conduction band. The system corresponds to an impurity Anderson model in which the conduction band has a Lorentzian density of states of width Δ_2. We solved the model using perturbation theory in the Coulomb repulsion U (PTU) up to second order and a slave-boson mean-field approximation (SBMFA). The PTU works surprisingly well near the exactly solvable limit $\Delta_2 \to 0$. For fixed U and large enough λ or small enough Δ_2, the Kondo peak in $\rho_{d\sigma}(\omega)$ splits into two peaks. This splitting can be understood in terms of weakly interacting quasiparticles. Before the splitting takes place, the universal properties of the model in the Kondo regime are lost. Using the SBMFA, simple analytical expressions for the occurrence of split peaks are obtained. For small or moderate Δ_2, the side bands of $\rho_{d\sigma}(\omega)$ have the form of narrow resonances that were missed in previous studies using the numerical renormalization group. This technique also has shortcomings for properly describing the split Kondo peaks. As the temperature is increased, the intensity of the split Kondo peaks decreases, but it is not completely suppressed at high temperatures.

DOI: 10.1103/PhysRevB.76.165112 PACS number(s): 72.15.Qm, 73.23.−b, 73.63.Kv

Part VI

Appendices

Appendix A

Projected Wannier functions within the (L)APW+lo framework

A.1 Augmented plane waves

In this thesis, the Kohn-Sham wave functions $|\psi_{\boldsymbol{k}\nu}\rangle$ are expanded into augmented plane waves ((L)APW+lo) as implemented in the electronic structure code WIEN2K [Blaha *et al.* (2001)]. Such a basis set is adapted for the shape of the nuclear potential, which varies smoothly in the interstitial region between the atoms and is atomic-like near the atomic nuclei. The crystal is hence divided into non-overlapping muffin-tin spheres (S^{α}_{MT}) centered at the atomic sites α and interstitial regions (IPW) in between (Fig. 2.1).

The original augmented plane waves (APW) basis set was energy-dependent, since the radial solutions of the Scrödinger equation expanding a Kohn-Sham eigenstate inside S^{α}_{MT} had to be evaluated at the corresponding eigenenergy. Linearized versions of APW have hence been introduced, in order to avoid such complication.

Linearized augmented plane waves (LAPW)

In the linearized augmented plane wave (LAPW) method [Andersen(1975), Singh(1994)], the plane wave is augmented with muffin-tin spheres by a combination of radial solutions, evaluated at chosen linearization energies E_{1l}, and their energy derivatives. The linearized augmented plane wave functions $\phi^{\boldsymbol{k}}_{\boldsymbol{G}}(\boldsymbol{r})$ then reads as

$$\phi^{\boldsymbol{k}}_{\boldsymbol{G}}(\boldsymbol{r}) = \begin{cases} \frac{1}{\sqrt{\Omega}} e^{i(\boldsymbol{k}+\boldsymbol{G})\cdot\boldsymbol{r}} & \text{if } \boldsymbol{r} \in \text{IPW} \\ \sum_{lm}[A^{\alpha,\boldsymbol{k}+\boldsymbol{G}}_{lm} u^{\alpha,\sigma}_{l}(r, E^{\alpha}_{1l}) + B^{\alpha,\boldsymbol{k}+\boldsymbol{G}}_{lm} \dot{u}^{\alpha,\sigma}_{l}(r, E^{\alpha}_{1l})]Y_{lm}(\theta,\phi) & \text{if } \boldsymbol{r} \in S^{\alpha}_{MT}, \end{cases} \tag{A.1}$$

where $\boldsymbol{G}$ are reciprocal lattice vectors and A_{lm}, B_{lm} are determined from the requirement for $\phi^{\boldsymbol{k}}_{\boldsymbol{G}}(\boldsymbol{r})$ to be continuous at the sphere boundaries.

Local orbitals (LO) for semicore states in LAPW

Local orbitals (LO) can be introduced for semicore states, for which a single set of reference energies E_{1l} is inappropriate. A second set of reference energies E_{2l} is hence employed. They are denoted with capital letters (LO) as in the following and are defined only in the muffin-tin spheres (thus zero in the interstitial regions) :

$$\phi^{LO}_{lm,\alpha}(\boldsymbol{r}) \quad = \quad [A^{\alpha,LO}_{lm} u^{\alpha,\sigma}_l(r, E^\alpha_{1l}) + B^{\alpha,LO}_{lm} \dot{u}^{\alpha,\sigma}_l(r, E^\alpha_{1l}) + C^{\alpha,LO}_{lm} u^{\alpha,\sigma}_l(r, E^\alpha_{2l})] Y_{lm}(\theta, \phi), \tag{A.2}$$

where A_{lm}, B_{lm}, C_{lm} coefficients are determined by requiring the local orbital and its radial derivative to be zero at the sphere boundaries.

Compared to the energy-dependent APW, a larger number of LAPW's in the basis set is usually required to attain the same accuracy [Singh(1994)]. This gives motivation to another linearization method called APW+lo, as introduced by [Sjöstedt *et al.* (2000)].

Augmented plane waves within local orbitals (APW+lo)

The APW+lo basis set is based on the evaluation of the augmented plane waves but at a fixed energy E_{1l} :

$$\phi^{\boldsymbol{k}}_{\boldsymbol{G}}(\boldsymbol{r}) = \begin{cases} \frac{1}{\sqrt{\Omega}} \mathrm{e}^{i(\boldsymbol{k}+\boldsymbol{G})\cdot\boldsymbol{r}} & \text{if } \boldsymbol{r} \in \text{IPW} \\ \sum_{lm} A^{\alpha,\boldsymbol{k}+\boldsymbol{G}}_{lm} u^{\alpha,\sigma}_l(r, E^\alpha_{1l}) Y_{lm}(\theta, \phi) & \text{if } \boldsymbol{r} \in S^\alpha_{MT}, \end{cases} \tag{A.3}$$

where the coefficient A_{lm} is set as previously in LAPW, in such a way that $\phi^{\boldsymbol{k}}_{\boldsymbol{G}}(\boldsymbol{r})$ are continuous at the sphere boundaries. The fixed-energy APW's (Eq. A.3) are supplemented for the physically important orbitals (with $l \leq 3$) by a set of local orbitals (lo) that are defined only in the muffin-tin spheres (thus zero in the interstitial regions) :

$$\phi^{lo}_{lm,\alpha}(\boldsymbol{r}) \quad = \quad [A^{\alpha,lo}_{lm} u^{\alpha,\sigma}_l(r, E^\alpha_{1l}) + B^{\alpha,lo}_{lm} \dot{u}^{\alpha,\sigma}_l(r, E^\alpha_{1l})] Y_{lm}(\theta, \phi), \tag{A.4}$$

where A_{lm}, B_{lm} coefficients are chosen in such a way that the local orbital as well as its slope, are zero at the sphere boundaries [Sjöstedt *et al.* (2000)].

Local orbitals (LO) for semicore states in APW+lo

In a similar way than in LAPW, one can employ additional local orbitals $\phi^{LO}_{lm,\alpha}$ to account for the semi-core states. The expression is the same than Eq. A.2 but the coefficient B_{lm} is set to zero.

General expansion of the Kohn-Sham states

Generally, in the full-potential augmented plane-wave method, the LAPW, APW+lo and LO types of orbitals can be used simultaneously. This leads to the general expansion for the Kohn-Sham eigenstates $\psi^{\sigma}_{\boldsymbol{k}\nu}(\boldsymbol{r})$, as given in Chapter 2 (Eq. 2.12)

$$\psi^{\sigma}_{\boldsymbol{k}\nu}(\boldsymbol{r}) = \frac{1}{\sqrt{\Omega}} \sum_{\boldsymbol{G}}^{N_{\mathrm{PW}}} c^{\nu\sigma}_{\boldsymbol{G}}(\boldsymbol{k}) \mathrm{e}^{i(\boldsymbol{k}+\boldsymbol{G})\cdot\boldsymbol{r}} \quad \text{if } \boldsymbol{r} \in \mathrm{IPW} \tag{A.5}$$

$$\begin{aligned} = & \sum_{\boldsymbol{G}}^{N_{\mathrm{PW}}} c^{\nu\sigma}_{\boldsymbol{G}}(\boldsymbol{k}) \sum_{lm} A^{\alpha,\boldsymbol{k}+\boldsymbol{G}}_{lm} u^{\alpha,\sigma}_{l}(r, E^{\alpha}_{1l}) Y_{lm}(\theta,\phi) \quad \text{if } \boldsymbol{r} \in S^{\alpha}_{MT} \\ & + \sum_{n_{\mathrm{lo}}=1}^{N_{\mathrm{lo}}} c^{\nu,\sigma}_{\mathrm{lo}} [A^{\alpha,\mathrm{lo}}_{lm} u^{\alpha,\sigma}_{l}(r, E^{\alpha}_{1l}) + B^{\alpha,\mathrm{lo}}_{lm} \dot{u}^{\alpha,\sigma}_{l}(r, E^{\alpha}_{1l})] Y_{lm}(\theta,\phi) \\ & + \sum_{n_{\mathrm{LO}}=1}^{N_{\mathrm{LO}}} c^{\nu,\sigma}_{\mathrm{LO}} [A^{\alpha,\mathrm{LO}}_{lm} u^{\alpha,\sigma}_{l}(r, E^{\alpha}_{1l}) + C^{\alpha,\mathrm{LO}}_{lm} u^{\alpha,\sigma}_{l}(r, E^{\alpha}_{2l})] Y_{lm}(\theta,\phi), \end{aligned} \tag{A.6}$$

where $N_{\mathrm{PW}}, n_{\mathrm{lo}}, n_{\mathrm{LO}}$ are the total number of plane waves in the interstitial region, the number of local orbitals (lo) for Eq. A.4 and the number of local orbitals (LO) for semicore states, respectively.

A.2 Wannier functions

Projected Wannier-like functions have been recently implemented in the (L)APW+lo framework by [Aichhorn *et al.* (2009)]. It is an important step in the LDA+DMFT implementation. An exhaustive presentation of such localized basis functions is also given in [Martins(2010)].

Projected Wannier functions

In Chapter 3, we already explained the basics of the projection procedure for the construction of Wannier functions. We started from a set of local atomic-like orbitals $|\chi^{\alpha\sigma}_{\boldsymbol{k}m}\rangle$ which can be expanded over the full Bloch basis set (Eq. 3.15).[1] After the truncation of this expansion for the states within a given energy window $\mathbb{W}$, we get a set of orbitals $|\tilde{\chi}^{\alpha\sigma}_{\boldsymbol{k}m}\rangle$ (Eq. 3.16). We denote as $\tilde{P}^{\alpha\sigma}_{m\nu}(\boldsymbol{k})$ the matrix elements of the projection operator for this subset :

$$\tilde{P}^{\alpha,\sigma}_{m\nu}(\boldsymbol{k}) = \langle \tilde{\chi}^{\alpha\sigma}_{\boldsymbol{k}m} | \psi^{\sigma}_{\boldsymbol{k}\nu} \rangle, \quad \nu \in \mathbb{W}. \tag{A.7}$$

In general, the transformation above is not-unitary and hence the matrices $\tilde{P}^{\alpha,\sigma}$ are non-square matrices. The last step of the construction is the orthonormalization of this set of orbitals. The

[1] For the simplicity of the notations, we identify in the following the Bloch basis set with the Kohn-Sham one.

resulting orthonormal orbitals $|\phi^{\alpha\sigma}_{\boldsymbol{k}m}\rangle$ are promoted to Wannier functions :

$$|\phi^{\alpha\sigma}_{\boldsymbol{k}m}\rangle = \sum_{\alpha',m'} S^{\alpha,\alpha'}_{m,m'}|\tilde{\chi}^{\alpha'}_{\boldsymbol{k}m'}\rangle, \tag{A.8}$$

where $S^{\alpha,\alpha'}_{m,m'} = \left[O(\boldsymbol{k},\sigma)^{-1/2}\right]^{\alpha,\alpha'}_{m,m'}$ and $O^{\alpha,\alpha'}_{m,m'}(\boldsymbol{k},\sigma) = \langle\tilde{\chi}^{\alpha,\sigma}_{\boldsymbol{k}m}|\tilde{\chi}^{\alpha',\sigma}_{\boldsymbol{k}m'}\rangle$ are the overlap matrix elements. Introducing the projectors in the formula leads to :

$$O^{\alpha,\alpha'}_{m,m'}(\boldsymbol{k},\sigma) = \sum_{\nu\in\mathbb{W}} \tilde{P}^{\alpha,\sigma}_{m\nu}(\boldsymbol{k})[\tilde{P}^{\alpha',\sigma}_{m'\nu}(\boldsymbol{k})]^* \tag{A.9}$$

and for the projectors that we have used throughout this thesis (Eq. 3.17)

$$P^{\alpha,\sigma}_{m\nu}(\boldsymbol{k}) = \sum_{\alpha',m'} \left[O(\boldsymbol{k},\sigma)^{-1/2}\right]^{\alpha,\alpha'}_{m,m'} \tilde{P}^{\alpha',\sigma}_{m'\nu}(\boldsymbol{k}). \tag{A.10}$$

In the (L)APW+lo framework

The solutions of the Schrödinger equation within the muffin-tin spheres, $|u^{\alpha,\sigma}_l(r,E_{1l})Y_{lm}(\theta,\phi)\rangle$, at the linearization energy E_{1l}, are chosen for representing the "initial" correlated orbitals $|\chi^{\alpha,\sigma}_m\rangle$. Within the relations between the radial solutions and their energy derivatives

$$\langle u^{\alpha,\sigma}_l(E_{1l})Y_{lm}|u^{\alpha,\sigma}_{l'}(E_{1l})Y_{l'm'}\rangle = \delta_{ll'}\delta_{mm'} \tag{A.11}$$
$$\langle u^{\alpha,\sigma}_l(E_{1l})Y_{lm}|\dot{u}^{\alpha,\sigma}_{l'}(E_{1l})Y_{l'm'}\rangle = 0 \tag{A.12}$$
$$\langle u^{\alpha,\sigma}_l(E_{1l})Y_{lm}|u^{\alpha,\sigma}_{l'}(E_{2l})Y_{l'm'}\rangle = \tilde{O}^{\alpha,\sigma}_{lm,l'm'} \neq 0 \tag{A.13}$$

it follows for $\tilde{P}^{\alpha,\sigma}_{m\nu}$

$$\tilde{P}^{\alpha,\sigma}_{m\nu} = \langle u^{\alpha,\sigma}_l(E_{1l})Y_{lm}|\psi^{\sigma}_{\boldsymbol{k}\nu}\rangle = A^{\nu,\alpha}_{lm}(\boldsymbol{k},\sigma) + \sum_{n_{LO}}^{N_{LO}} C^{\nu,\alpha}_{lm,LO}(\boldsymbol{k},\sigma). \tag{A.14}$$

In this expression, A_{lm} coefficients read as

$$A^{\nu,\alpha}_{lm}(\boldsymbol{k},\sigma) = \sum_{\boldsymbol{G}}^{N_{\text{PW}}} c^{\nu,\sigma}_{\boldsymbol{G}}(\boldsymbol{k})A^{\alpha,\boldsymbol{k}+\boldsymbol{G}}_{lm} + \sum_{n_{lo}}^{N_{lo}} c^{\nu,\sigma}_{lo}A^{\alpha,lo}_{lm} + \sum_{n_{LO}}^{N_{LO}} c^{\nu,\sigma}_{LO}A^{\alpha,LO}_{lm} \tag{A.15}$$

and

$$C^{\nu,\alpha}_{lm,LO}(\boldsymbol{k},\sigma) = c^{\nu,\sigma}_{LO}C^{\alpha,LO}_{lm}\tilde{O}^{\alpha,\sigma}_{lm,l'm'}. \tag{A.16}$$

We finally orthonormalize the orbitals $|\tilde{\chi}^{\alpha}_{\boldsymbol{k}m}\rangle$ and we deduce the projectors $P^{\alpha,\sigma}_{m\nu}(\boldsymbol{k})$ that were also employed in the cRPA implementation.

Appendix B

Slater integrals

B.1 Slater integrals in a cubic crystal field

If d-electrons in crystals are relatively localized around the nuclei, it is reasonable to assume that the t_{2g} and e_g wavefunctions have pure d-character and are thus linear combination of the spherical harmonics $\phi_{dm}(\boldsymbol{r}) = R_d(r)Y_{dm}(\theta,\phi)$ (Tab. B.1).

Let us call $\bar{v}_{mm}^{t_{2g}}$ the following intra-t_{2g} atomic Coulomb repulsion (thus without any screening effect) :

$$\begin{aligned}\bar{v}_{mm}^{t_{2g}} &= \int d^3\boldsymbol{r}_1 d^3\boldsymbol{r}_2 (i/\sqrt{2})(\phi^*_{d2}(\boldsymbol{r}_1) - \phi^*_{d-2}(\boldsymbol{r}_1))(i/\sqrt{2})(\phi^*_{d2}(\boldsymbol{r}_2) - \phi^*_{d-2}(\boldsymbol{r}_2)) \\ &\times \frac{1}{r_{12}}(-i/\sqrt{2})(\phi_{d2}(\boldsymbol{r}_1) - \phi_{d-2}(\boldsymbol{r}_1))(-i/\sqrt{2})(\phi_{d2}(\boldsymbol{r}_2) - \phi_{d-2}(\boldsymbol{r}_2)) \qquad \text{(B.1)}\end{aligned}$$

If we adopt same conventions than in [Sugano *et al.* (1970)], we can write the above expression as :

$$\begin{aligned}\bar{v}_{mm}^{t_{2g}} &= \frac{1}{4}\Big[\langle 22||22\rangle + \langle -2-2||-2-2\rangle + \langle 2-2||2-2\rangle \\ &+\langle -22||-22\rangle + \langle 2-2||-22\rangle + \langle -22||2-2\rangle\Big], \qquad \text{(B.2)}\end{aligned}$$

where

$$\langle m_1 m_2||m_1' m_2'\rangle \equiv \int d^3\boldsymbol{r}_1 d^3\boldsymbol{r}_2 \phi^*_{dm_1}(\boldsymbol{r}_1)\phi^*_{dm_2}(\boldsymbol{r}_2)\frac{1}{r_{12}}\phi_{dm_1'}(\boldsymbol{r}_1)\phi_{dm_2'}(\boldsymbol{r}_2), \qquad \text{(B.3)}$$

t_{2g}	$\zeta = d_{yz} = (i/\sqrt{2})(\phi_1 + \phi_{-1})$	$\eta = d_{xz} = (-1/\sqrt{2})(\phi_1 - \phi_{-1})$	$\xi = d_{xy} = (-i/\sqrt{2})(\phi_2 - \phi_{-2})$
e_g	$u = d_{3z^2-r^2} = \phi_0$	$v = d_{x^2-y^2} = (\phi_2 + \phi_{-2})/\sqrt{2}$	

Table B.1: t_{2g} and e_g states as linear combination of the spherical harmonics ϕ_{dm} in a cubic crystal field, assuming that the d-electrons are well localized around the nuclei [Sugano *et al.* (1970)].

which are non-zero if $m_1 + m_2 = m_1' + m_2'$.

Expanding $1/r_{12}$ into Legendre polynomials, one can show that [Sugano *et al.* (1970)]

$$1/|\boldsymbol{r}_1 - \boldsymbol{r}_2| = \sum_{k=0}^{\infty} \frac{4\pi}{2k+1} \frac{r_<^k}{r_>^{k+1}} \sum_{q=-k}^{k} Y_{kq}(\theta_1, \phi_1) Y_{kq}^*(\theta_2, \phi_2), \tag{B.4}$$

and it follows (within d orbitals) :

$$\langle m_1 m_2 || m_1' m_2' \rangle = \delta(m_1 + m_2, m_1' + m_2')(-1)^{m_1 - m_1'} \sum_k c^k(m_1, m_1') c^k(m_2, m_2') \mathrm{F}_{\mathrm{bare}}^k, \tag{B.5}$$

where we have introduced the Slater integrals $\mathrm{F}_{\mathrm{bare}}^k$ as follows (see Eq. 5.57)

$$\mathrm{F}_{\mathrm{bare}}^k = \int_0^\infty r_1^2 dr_1 \int_0^\infty r_2^2 dr_2 \frac{r_<^k}{r_>^{k+1}} R(r_1)^2 R(r_2)^2. \tag{B.6}$$

$r_<(r_>)$ is the lesser (greater) of r_1 and r_2.

On the other hand, $c^k(m, m')$ are well-known numbers that are listed in [Sugano *et al.* (1970)] (p.11) due to specific selection rules due to spherical harmonics:

$$c^k(m, m') = \sqrt{\frac{4\pi}{2k+1}} \int d\theta \sin\theta d\phi Y_{l,m}^*(\theta, \phi) Y_{k,m-m'}(\theta, \phi) Y_{l',m'}(\theta, \phi). \tag{B.7}$$

In particular, we have :

$$\begin{aligned}
\langle 22||22\rangle &= \langle -2-2||-2-2\rangle = \langle 2-2||2-2\rangle = \langle -22||-22\rangle \\
&= \mathrm{F}_{\mathrm{bare}}^0 + \frac{4}{49}\mathrm{F}_{\mathrm{bare}}^2 + \frac{1}{441}\mathrm{F}_{\mathrm{bare}}^4 && \text{(B.8)} \\
\langle 2-2||-22\rangle &= \langle -22||2-2\rangle = \frac{70}{441}\mathrm{F}_{\mathrm{bare}}^4 && \text{(B.9)} \\
\langle 00||00\rangle &= \mathrm{F}_{\mathrm{bare}}^0 + \frac{4}{49}\mathrm{F}_{\mathrm{bare}}^2 + \frac{4}{49}\mathrm{F}_{\mathrm{bare}}^4 && \text{(B.10)} \\
\langle 11||11\rangle &= \langle -1-1||-1-1\rangle = \langle 1-1||1-1\rangle = \langle -11||-11\rangle \\
&= \mathrm{F}_{\mathrm{bare}}^0 + \frac{1}{49}\mathrm{F}_{\mathrm{bare}}^2 + \frac{16}{441}\mathrm{F}_{\mathrm{bare}}^4 && \text{(B.11)} \\
\langle 1-1||-11\rangle &= \langle -11||1-1\rangle = \frac{6}{49}\mathrm{F}_{\mathrm{bare}}^2 + \frac{4}{10}\mathrm{F}_{\mathrm{bare}}^4. && \text{(B.12)}
\end{aligned}$$

This leads to the following density-density interaction matrices for the atom in terms of the Slater integrals [1] [2]

$$\bar{v}_{mm'}^{\sigma\bar{\sigma}}|_{\mathrm{Slater}} = \begin{pmatrix}
\langle -2-2||-2-2\rangle & . & . & . & . \\
\langle -2-1||-2-1\rangle & \langle -1-1||-1-1\rangle & . & . & . \\
\langle -20||-20\rangle & \langle -10||-10\rangle & \langle 00||00\rangle & . & . \\
\langle -21||-21\rangle & \langle -11||-11\rangle & \langle 0-1||0-1\rangle & \langle 11||11\rangle & . \\
\langle -22||-22\rangle & \langle -12||-12\rangle & \langle 02||02\rangle & \langle 12||12\rangle & \langle 22||22\rangle
\end{pmatrix},$$

[1] In solids, these matrices would be the bare reduced interaction matrices with spherical symmetry.

[2] As the matrices are symmetric, only the half is shown.

$$\bar{J}^{\text{bare}}_{mm'}|_{\text{Slater}} = \begin{pmatrix} 0 & . & . & . & . \\ \langle -2-1||-1-2\rangle & 0 & . & . & . \\ \langle -20||0-2\rangle & \langle -10||0-1\rangle & 0 & . & . \\ \langle -21||1-2\rangle & \langle -11||1-1\rangle & \langle 0-1||-10\rangle & 0 & . \\ \langle -22||2-2\rangle & \langle -12||2-1\rangle & \langle 02||20\rangle & \langle 12||21\rangle & 0 \end{pmatrix},$$

$$\bar{v}^{\sigma\sigma}_{mm'}|_{\text{Slater}} = (1-\delta_{mm'})(\bar{v}^{\sigma\bar{\sigma}}_{mm'}|_{\text{Slater}} - \bar{J}^{\text{bare}}_{mm'}|_{\text{Slater}})$$

In Chapter 5, we called F^k_{bare} such Slater integrals, since the screening has not been taken into account. In the next section, we show that Slater integrals F^k can also be constructed in a similar manner but for the screened Coulomb repulsion $U_{m_1m_2m_3m_4}$.

Atomic interactions between t_{2g} orbitals

Coming back to Eq. B.2, one can derive an expression for the atomic intra-orbital Coulomb repulsion $\bar{v}^{t_{2g}}_{mm}$ (equivalent to the bare t_{2g} interaction $\bar{v}_{mm}$, see Eq. 5.70) :

$$\bar{v}^{t_{2g}}_{mm} = \text{F}^0_{\text{bare}} + \frac{4}{49}\text{F}^2_{\text{bare}} + \frac{4}{49}\text{F}^4_{\text{bare}}. \tag{B.13}$$

Following the same method but for other combinations of spherical harmonics, we deduce expressions for the bare exchange interactions $\bar{v}_{mm'}$ and $\bar{J}^{\text{bare}}_m$:

$$\bar{v}^{t_{2g}}_{mm'} = \text{F}^0_{\text{bare}} - \frac{2}{49}\text{F}^2_{\text{bare}} - \frac{4}{441}\text{F}^4_{\text{bare}} \tag{B.14}$$

$$\bar{J}^{\text{bare}}_{t_{2g}} = \frac{3}{49}\text{F}^2_{\text{bare}} + \frac{20}{441}\text{F}^4_{\text{bare}} \tag{B.15}$$

One verifies that in the cubic crystal field, $\bar{v}^{t_{2g}}_{mm'} = \bar{v}^{t_{2g}}_{mm} - 2\bar{J}^{\text{bare}}_{t_{2g}}$.

Atomic interactions between e_g orbitals

In a similar way than previously, one deduces the atomic interactions, but for the e_g orbitals :

$$\bar{v}^{e_g}_{mm} = \bar{v}^{t_{2g}}_{mm} \tag{B.16}$$

$$\bar{v}^{e_g}_{mm'} = \text{F}^0_{\text{bare}} - \frac{4}{49}\text{F}^2_{\text{bare}} + \frac{6}{441}\text{F}^4_{\text{bare}} \tag{B.17}$$

$$\bar{J}^{\text{bare}}_{e_g} = \frac{4}{49}\text{F}^2_{\text{bare}} + \frac{15}{441}\text{F}^4_{\text{bare}} \tag{B.18}$$

The relation $\bar{v}^{e_g}_{mm'} = \bar{v}^{e_g}_{mm} - 2\bar{J}^{\text{bare}}_{e_g}$ still holds within the e_g subspace.
We can also derive the interaction parameters between t_{2g} and e_g orbitals (see Tab. B.1 for

(ζ, η, ξ, u, v) notations) :

$$\bar{v}_{mm'}(\zeta u) = \bar{v}_{mm'}(\xi u) = \bar{v}_{mm'}(\eta u) = \mathrm{F}^0_{\text{bare}} - \frac{4}{49}\mathrm{F}^2_{\text{bare}} + \frac{6}{441}\mathrm{F}^4_{\text{bare}} \quad \text{(B.19)}$$

$$\bar{v}_{mm'}(\zeta v) = \bar{v}_{mm'}(\xi v) = \bar{v}_{mm'}(\eta v) = \mathrm{F}^0_{\text{bare}} + \frac{4}{49}\mathrm{F}^2_{\text{bare}} - \frac{34}{441}\mathrm{F}^4_{\text{bare}} \quad \text{(B.20)}$$

$$\bar{J}^{\text{bare}}(\zeta u) = \bar{J}^{\text{bare}}(\xi u) = \bar{J}^{\text{bare}}(\eta u) = \frac{4}{49}\mathrm{F}^2_{\text{bare}} + \frac{15}{441}\mathrm{F}^4_{\text{bare}} \quad \text{(B.21)}$$

$$\bar{J}^{\text{bare}}(\zeta v) = \bar{J}^{\text{bare}}(\xi v) = \bar{J}^{\text{bare}}(\eta v) = \frac{35}{441}\mathrm{F}^4_{\text{bare}} \quad \text{(B.22)}$$

All these interaction terms can be extended to the case where the screening reduces the bare interaction to an effective screened interaction. In that case, one needs to introduce a set of Slater integrals F^k (see next section). Equivalent relations then hold, but for the Hubbard interactions $\bar{U}_{mm}, \bar{U}_{mm'}$ and $\bar{J}_m$.

Other conventions : Slater-Condon and Racah parameters

Other conventions are sometimes introduced in the literature. Slater-Condon parameters $(\mathrm{F}_0^{(\text{bare})}, \mathrm{F}_2^{(\text{bare})}, \mathrm{F}_4^{(\text{bare})})$ are defined as :

$$\mathrm{F}_0 = \mathrm{F}^0 \quad \text{(B.23)}$$

$$\mathrm{F}_2 = \frac{1}{49}\mathrm{F}^2 \quad \text{(B.24)}$$

$$\mathrm{F}_4 = \frac{1}{441}\mathrm{F}^4. \quad \text{(B.25)}$$

On the other hand, one can also use the Racah parameters $(A^{(\text{bare})}, B^{(\text{bare})}, C^{(\text{bare})})$:

$$A = \mathrm{F}^0 - \frac{49}{441}\mathrm{F}^4 \quad \text{(B.26)}$$

$$B = \frac{1}{49}\mathrm{F}^2 - \frac{5}{441}\mathrm{F}^4 \quad \text{(B.27)}$$

$$C = \frac{35}{441}\mathrm{F}^4. \quad \text{(B.28)}$$

B.2 How to calculate Slater integrals from $U_{m_1m_2m_3m_4}$?

In this paragraph, we indicate how to calculate an optimal set of Slater integrals that are adapted to the screened Coulomb interaction matrix $U^{\text{spheric}}_{m_1m_2m_3m_4}$. For the definition of "spheric", see Chapter 5. We leave the definition of Hubbard U and Hund's exchange J for the next section.

$U^{\textbf{spheric}}_{m_1m_2m_3m_4}(\mathbf{F}^k)$

We assume that the Coulomb interaction matrix within solids in the spherical symmetry can be approximated by a finite set of Slater integrals $\mathrm{F}^k, 0 \leq k \leq 2l$, where l is the orbital number. The following relation is obtained by the extension of the definition of Slater integrals from the atomic to the solid case :

$$U^{\text{spheric}}_{m_1m_2m_3m_4} = \sum_{k=0}^{2l} \alpha_k(m_1, m_2, m_3, m_4)\mathrm{F}^k, \tag{B.29}$$

whereas α_k are known as the the Racah-Wigner coefficients, which are entirely determined by a combination of spherical harmonics $Y_{lm}(\theta, \phi)$

$$\alpha_k(m_1, m_2, m_3, m_4) = \frac{4\pi}{2k+1} \sum_{q=-k}^{k} \langle Y_{lm_1}|Y_{kq}Y_{lm_3}\rangle\langle Y_{lm_2}Y_{kq}|Y_{lm_4}\rangle. \tag{B.30}$$

$\langle Y_{l_1m_1}|Y_{l_2m_2}Y_{l_3m_3}\rangle$ notation correspond to the Gaunt coefficients.

In the following, we calculate specific Slater integrals within solids but the angular part is approximated to the atomic one $\alpha_k(m_1, m_2, m_3, m_4)$.

Notations

We need to introduce notations for *Racah-Wigner 3j-symbols* $\begin{bmatrix} l & k & l \\ -m_1 & q & m_3 \end{bmatrix}$ and *Wigner 3j-symbols* $\begin{pmatrix} l & k & l \\ -m_1 & q & m_3 \end{pmatrix}$. They are related by a phase factor

$$\begin{bmatrix} l & k & l \\ -m_1 & q & m_3 \end{bmatrix} = (-1)^{l-k-m_1} \begin{pmatrix} l & k & l \\ -m_1 & q & m_3 \end{pmatrix}. \tag{B.31}$$

Non-zero values of Wigner 3j-symbols are constrained by the following selection rule :

$$\begin{pmatrix} l & k & l \\ -m_1 & q & m_3 \end{pmatrix} \neq 0 \qquad \text{if} \quad -m_1 + q + m_3 = 0. \tag{B.32}$$

The Gaunt coefficients can then be expressed in terms of the Racah-Wigner 3j-symbols such as [3]

$$< Y_{lm_1}|Y_{kq}Y_{lm_3} > = (2l+1)\sqrt{\frac{2k+1}{4\pi}} \begin{bmatrix} l & k & l \\ 0 & 0 & 0 \end{bmatrix} \begin{bmatrix} l & k & l \\ -m_1 & q & m_3 \end{bmatrix} \tag{B.33}$$

[3] We remind the reader that $Y^*_{kq} = (-1)^q Y_{k,-q}$.

It follows for Eq. B.29 once the Gaunt coefficients have been replaced by the above relation (Eq. B.33) :

$$U^{\text{spheric}}_{m_1m_2m_3m_4} = (2l+1)^2 \sum_{k=0}^{2l} \mathrm{F}^k \begin{bmatrix} l & k & l \\ 0 & 0 & 0 \end{bmatrix}^2 \sum_{q=-k}^{k} (-1)^q \begin{bmatrix} l & k & l \\ -m_1 & q & m_3 \end{bmatrix} \begin{bmatrix} l & k & l \\ -m_2 & -q & m_4 \end{bmatrix} \tag{B.34}$$

$$= (2l+1)^2 \sum_{k=0}^{2l} \mathrm{F}^k \begin{pmatrix} l & k & l \\ 0 & 0 & 0 \end{pmatrix}^2 \sum_{q=-k}^{k} (-1)^{m_1+m_2+q} \begin{pmatrix} l & k & l \\ -m_1 & q & m_3 \end{pmatrix} \begin{pmatrix} l & k & l \\ -m_2 & -q & m_4 \end{pmatrix} \tag{B.35}$$

$\mathbf{F}^k(U^{\text{spheric}}_{m_1m_2m_3m_4})$

We first remind the reader the result (Eq. 5.62) we want to demonstrate in this section :

$$F^k(\omega) = \mathcal{C}_{l,k} \sum_{m_1,m_2,m_3,m_4} (-1)^{m_1+m_4} U^{\text{spheric}}_{m_1m_2m_3m_4}(\omega) \begin{pmatrix} l & k & l \\ -m_1 & m_1-m_3 & m_3 \end{pmatrix} \begin{pmatrix} l & k & l \\ -m_2 & m_2-m_4 & m_4 \end{pmatrix}, \tag{B.36}$$

where the coefficients $\mathcal{C}_{l,k}$ read as

$$\mathcal{C}_{l,k} = \frac{2k+1}{(2l+1)^2 \begin{pmatrix} l & k & l \\ 0 & 0 & 0 \end{pmatrix}^2}. \tag{B.37}$$

By inverting the Eq. B.35, one can have access to the Slater integrals as function of the Coulomb matrix elements, which we have calculated in the spherical representation. The role of these Slater integrals is to parametrize the whole Coulomb matrix. They are employed in a second time for constructing the Coulomb interaction matrix, but with appropriate symmetry for the low-energy solver (see Eq. 5.64). Furthermore, since the Coulomb matrix elements depend on the frequency (see Chapter 4), it follows that the Slater integrals are also frequency-dependent. In the future, this will be useful for taking into account the dynamical screening in the solution of the extended Hubbard model.

Demonstration

Let us start from the following auxiliary quantity $\mathcal{F}^{\text{aux}}$

$$\mathcal{F}^{\text{aux}} = \sum_{m_1,m_2,m_3,m_4} < Y_{lm_1} | Y_{k,q_{13}} Y_{lm_3} > U^{\text{spheric}}_{m_1m_2m_3m_4} < Y_{lm_2} Y_{k,q_{24}} | Y_{lm_4} > \tag{B.38}$$

$$= (2l+1)^2 \frac{2k+1}{4\pi} \begin{bmatrix} l & k & l \\ 0 & 0 & 0 \end{bmatrix}^2 \sum_{m_1,m_2,m_3,m_4} \begin{bmatrix} l & k & l \\ -m_1 & q_{13} & m_3 \end{bmatrix} (-1)^{q_{24}} \begin{bmatrix} l & k & l \\ -m_2 & -q_{24} & m_4 \end{bmatrix} U^{\text{spheric}}_{m_1m_2m_3m_4},$$

which consists in summing the Coulomb matrix elements in the spherical symmetry with the Gaunt coefficients which are employed in Eq. B.30.

Referring to the relation between $U^{\text{spheric}}_{m_1m_2m_3m_4}$ and the Slater integrals (Eq. B.29), it follows for the intermediate quantity I,

$$I = \sum_{m_1,m_2,m_3,m_4} \begin{bmatrix} l & k & l \\ -m_1 & q_{13} & m_3 \end{bmatrix} (-1)^{q_{24}} \begin{bmatrix} l & k & l \\ -m_2 & -q_{24} & m_4 \end{bmatrix} U^{\text{spheric}}_{m_1m_2m_3m_4} \tag{B.39}$$

$$= (2l+1)^2 \sum_{m_1,m_2,m_3,m_4} (-1)^{q_{24}} \begin{bmatrix} l & k & l \\ -m_1 & q_{13} & m_3 \end{bmatrix} \begin{bmatrix} l & k & l \\ -m_2 & -q_{24} & m_4 \end{bmatrix}$$

$$\times \sum_{k'} \mathrm{F}^{k'} \begin{bmatrix} l & k' & l \\ 0 & 0 & 0 \end{bmatrix}^2 \sum_{q=-k'}^{k'} (-1)^q \begin{bmatrix} l & k' & l \\ -m_1 & q & m_3 \end{bmatrix} \begin{bmatrix} l & k' & l \\ -m_2 & -q & m_4 \end{bmatrix}$$

$$= (2l+1)^2 \sum_{k'} \mathrm{F}^{k'} \begin{bmatrix} l & k' & l \\ 0 & 0 & 0 \end{bmatrix}^2 \sum_{q=-k'}^{k'} (-1)^q \tag{B.40}$$

$$\times \sum_{m_1,m_2,m_3,m_4} \begin{bmatrix} l & k & l \\ -m_1 & q_{13} & m_3 \end{bmatrix} \begin{bmatrix} l & k' & l \\ -m_1 & q & m_3 \end{bmatrix} (-1)^{q_{24}} \begin{bmatrix} l & k & l \\ -m_2 & -q_{24} & m_4 \end{bmatrix} \begin{bmatrix} l & k' & l \\ -m_2 & -q & m_4 \end{bmatrix}$$

Orthogonality relations

We replace the Racah-Wigner 3j-symbols by the corresponding Wigner 3j-symbols (Eq. B.31) and it follows for I :

$$\sum_{m_1,m_3} \begin{bmatrix} l & k & l \\ -m_1 & q_{13} & m_3 \end{bmatrix} \begin{bmatrix} l & k' & l \\ -m_1 & q & m_3 \end{bmatrix} = (-1)^{k+k'} \sum_{m_1,m_3} \begin{pmatrix} l & k & l \\ -m_1 & q_{13} & m_3 \end{pmatrix} \begin{pmatrix} l & k' & l \\ -m_1 & q & m_3 \end{pmatrix}$$

By employing the following orthogonality-like relations [Slater(1960)] :

$$(2j+1) \sum_{m_1,m_2} \begin{pmatrix} j_1 & j_2 & j \\ m_1 & m_2 & m \end{pmatrix} \begin{pmatrix} j_1 & j_2 & j' \\ m_1 & m_2 & m' \end{pmatrix} = \delta_{jj'}\delta_{mm'}$$

the expression for I simplifies :

$$\sum_{m_1,m_3} \begin{bmatrix} l & k & l \\ -m_1 & q_{13} & m_3 \end{bmatrix} \begin{bmatrix} l & k' & l \\ -m_1 & q & m_3 \end{bmatrix} = (-1)^{k+k'} \frac{1}{2k+1} \delta_{k,k'}\delta_{q,q_{13}}$$

$$\sum_{m_2,m_4} (-1)^{q_{24}} \begin{bmatrix} l & k & l \\ -m_2 & -q_{24} & m_4 \end{bmatrix} \begin{bmatrix} l & k' & l \\ -m_2 & -q & m_4 \end{bmatrix} = (-1)^{q+k+k'} \frac{1}{2k+1} \delta_{k,k'}\delta_{q,q_{24}}$$

and hence one gets for I :

$$\begin{aligned} I &= (2l+1)^2 \sum_{k'} \mathrm{F}^{k'} \begin{bmatrix} l & k' & l \\ 0 & 0 & 0 \end{bmatrix}^2 \sum_{q=-k'}^{k'} (-1)^q \sum_{m_1,m_2,m_3,m_4} (-1)^q \frac{1}{(2k+1)^2} \delta_{k,k'} \delta_{q,q_{13}} \delta_{q,q_{24}} \\ &= (2l+1)^2 \mathrm{F}^k \begin{bmatrix} l & k & l \\ 0 & 0 & 0 \end{bmatrix}^2 \frac{1}{(2k+1)^2} \sum_{m_1,m_2} \sum_{q=-k}^{k} \delta_{q,m_1-m_3} \delta_{m_1-m_3,m_2-m_4} \\ &= (2l+1)^2 \mathrm{F}^k \begin{bmatrix} l & k & l \\ 0 & 0 & 0 \end{bmatrix}^2 \frac{1}{(2k+1)^2} (2k+1), \end{aligned} \tag{B.41}$$

where we used $q_{13} = m_1 - m_3$ and $q_{24} = m_2 - m_4$ from the property of the non-zero Wigner 3j-symbols (Eq. B.32). Only inequivalent combinations of (m_1, m_2, m_3, m_4) orbital numbers for each k have to be retained in this summation. The number of these combinations is set to $(2k+1)$.

It follows for the auxiliary quantity $\mathcal{F}^{\text{aux}}$:

$$\mathcal{F}^{\text{aux}} = \frac{2k+1}{4\pi} \mathcal{N}_{l,k} \, \mathrm{F}^k, \tag{B.42}$$

where $\mathcal{N}_{l,k}$ is defined as :

$$\mathcal{N}_{l,k} = \frac{(2l+1)^4 \begin{bmatrix} l & k & l \\ 0 & 0 & 0 \end{bmatrix}^4}{2k+1}. \tag{B.43}$$

Final expression

We finally deduce for the Slater integrals

$$\mathrm{F}^k = \frac{4\pi}{2k+1} \frac{1}{\mathcal{N}_{l,k}} \mathcal{F}^{\text{aux}} \tag{B.44}$$

$$= \frac{4\pi}{2k+1} \frac{1}{\mathcal{N}_{l,k}} \sum_{m_1,m_2,m_3,m_4} < Y_{lm_1} | Y_{k,m_1-m_3} Y_{lm_3} > U^{\text{spheric}}_{m_1 m_2 m_3 m_4} < Y_{lm_2} Y_{k,m_2-m_4} | Y_{lm_4} >, \tag{B.45}$$

This relation is analogous to the one given in [Kutepov *et al.* (2010)].
Employing the Wigner 3j-symbols, we get the expression B.36 given at the beginning :

$$F^k(\omega) = \mathcal{C}_{l,k} \sum_{m_1,m_2,m_3,m_4} (-1)^{m_1+m_4} U^{\text{spheric}}_{m_1 m_2 m_3 m_4}(\omega) \begin{pmatrix} l & k & l \\ -m_1 & m_1 - m_3 & m_3 \end{pmatrix} \begin{pmatrix} l & k & l \\ -m_2 & m_2 - m_4 & m_4 \end{pmatrix}, \tag{B.46}$$

where the coefficients $\mathcal{C}_{l,k}$ read as

$$\mathcal{C}_{l,k} = \frac{2k+1}{(2l+1)^2 \begin{pmatrix} l & k & l \\ 0 & 0 & 0 \end{pmatrix}^2}. \tag{B.47}$$

How good is the parametrization?

In order to have an idea of how good the parametrization of a four-index matrix is within the Slater integrals, one can calculate an updated Coulomb interaction matrix but starting from the Slater integrals :

$$\bar{U}^{(\text{Slater})}_{m_1m_2m_3m_4}(\omega) = \sum_{k=0}^{2l} \alpha_k(m_1,m_2,m_3,m_4)\mathrm{F}^k(\omega). \tag{B.48}$$

In particular, one can compare the on-site interactions $\bar{U}_{mm}$ and exchange interactions $\bar{J}_m$ to the directly calculated ones (see Fig. 5.1). In Chapter 6, the results are in well agreement for $SrVO_3$. The parametrization for pnictides is also discussed in Chapter 6.

Some numbers

We remind the reader that the quantities $\begin{pmatrix} l & k & l \\ 0 & 0 & 0 \end{pmatrix}$ are well defined by :

$$\begin{pmatrix} l & k & l \\ 0 & 0 & 0 \end{pmatrix} = (-1)^g \sqrt{\frac{[(2g-2l)!]^2(2g-2k)!}{(2g+1)!}} \frac{g!}{[(g-l)!]^2(g-k)!} \quad \text{if } 2l+k=2g \quad (0 \text{ otherwise}) \tag{B.49}$$

This leads in particular to :

- for $k=0$, we get $g=l$ and then

$$\begin{pmatrix} l & 0 & l \\ 0 & 0 & 0 \end{pmatrix} = (-1)^l \sqrt{\frac{1}{2l+1}} \tag{B.50}$$

  It follows that

$$\mathcal{N}_{l,0} = (2l+1)^2 \tag{B.51}$$

$$\mathcal{C}_{l,0} = \frac{1}{2l+1}. \tag{B.52}$$

- Considering $l=2, k=2$,

$$\mathcal{N}_{l=2,k=2} = (2l+1)^3 \begin{pmatrix} l & l & l \\ 0 & 0 & 0 \end{pmatrix}^4. \tag{B.53}$$

  Since $\begin{pmatrix} 2 & 2 & 2 \\ 0 & 0 & 0 \end{pmatrix} = -\sqrt{\frac{8}{7!}} \cdot 6$, one deduces

$$\mathcal{N}_{2,2} = 5^3(\frac{8}{7!})^2 6^4 = 5(\frac{5\cdot 8\cdot 6\cdot 6}{7!})^2 = 5(\frac{2}{7})^2 \sim 0.408$$

- Considering $l = 2, k = 4$,

$$\mathcal{N}_{l=2,k=4} = \frac{(2l+1)^4}{9} \begin{pmatrix} 2 & 4 & 2 \\ 0 & 0 & 0 \end{pmatrix}^4. \tag{B.54}$$

Since $\begin{pmatrix} 2 & 4 & 2 \\ 0 & 0 & 0 \end{pmatrix} = \frac{(4!)^2}{\sqrt{9!}} \frac{1}{4}$, one deduces

$$\mathcal{N}_{l=2,k=4} = \frac{5^4}{9}(\frac{(4!)^2}{4 \cdot \sqrt{9!}})^4 = (\frac{5 \cdot 4! \cdot 3!}{3})^2 (\frac{5 \cdot 4! \cdot 3!}{9!})^2 = (\frac{5 \cdot 4! \cdot 3!}{3})^2 (\frac{1}{9 \cdot 8 \cdot 7})^2 = (\frac{10}{21})^2 \sim 0.226$$

B.3 Hubbard U and Hund's coupling J

Following [Anisimov *et al.* (1993)], one can define from the Slater integrals the Hubbard U and Hund's exchange J for a model that includes all the d (or f) orbitals. All the following relations can be adapted to the definition of v and J_{bare} but starting from $(\mathrm{F}^0_{\text{bare}}, \mathrm{F}^2_{\text{bare}}, \mathrm{F}^4_{\text{bare}})$.

Hubbard U

The Hubbard U parameter is defined as the average over all possible pairs (m, m') such as :

$$U \equiv \frac{1}{(2l+1)^2} \sum_{mm'} \sum_{k=0}^{2l} \alpha_k(m, m', m, m') \mathrm{F}^k, \tag{B.55}$$

where α_k are some particular Racah-Wigner coefficients which we have defined in a more general way in Eq. B.30 :

$$\alpha_k(m, m', m, m') = \frac{4\pi}{2k+1} \sum_{q=-k}^{k} \langle Y_{lm} | Y_{kq} Y_{lm} \rangle \langle Y_{lm'} Y_{kq} | Y_{lm'} \rangle, \tag{B.56}$$

and $\langle Y_{lm} | Y_{kq} Y_{lm} \rangle$ are integrals over products of three spherical harmonics Y_{lm}. Replacing the Gaunt coefficients by the corresponding Racah-Wigner 3j-symbols (Eq. B.33), it follows :

$$\begin{aligned} U &= \frac{1}{(2l+1)^2} \sum_k \mathrm{F}^k \frac{4\pi}{2k+1} \sum_{mm'} \sum_{q=-k}^{k} (-1)^q (2l+1)^2 \frac{2k+1}{4\pi} \begin{bmatrix} l & k & l \\ 0 & 0 & 0 \end{bmatrix}^2 \begin{bmatrix} l & k & l \\ -m & q & m \end{bmatrix} \begin{bmatrix} l & k & l \\ -m' & -q & m' \end{bmatrix} \\ &= \sum_k \mathrm{F}^k \sum_{mm'} \sum_{q=-k}^{k} (-1)^q \begin{pmatrix} l & k & l \\ 0 & 0 & 0 \end{pmatrix}^2 (-1)^m \begin{pmatrix} l & k & l \\ -m & q & m \end{pmatrix} (-1)^{m'} \begin{pmatrix} l & k & l \\ -m' & -q & m' \end{pmatrix} \\ &= \sum_k \mathrm{F}^k \begin{pmatrix} l & k & l \\ 0 & 0 & 0 \end{pmatrix}^2 \sum_{m=-l}^{l} (-1)^m \begin{pmatrix} l & k & l \\ -m & 0 & m \end{pmatrix} \sum_{m'=-l}^{l} (-1)^{m'} \begin{pmatrix} l & k & l \\ -m' & 0 & m' \end{pmatrix}. \end{aligned} \tag{B.57}$$

We employed for the last equation, the condition B.32 $m-m+q=0$ and hence $q=0$. Invoking the following property of the Wigner 3j-symbols :

$$\sum_{m=-l}^{l}(-1)^m \begin{pmatrix} l & k & l \\ -m & 0 & m \end{pmatrix} = -\sqrt{\frac{2l+1}{2k+1}}\delta_{k0}, \tag{B.58}$$

it follows for U :

$$\begin{aligned} U &= \sum_k \mathrm{F}^k \begin{pmatrix} l & k & l \\ 0 & 0 & 0 \end{pmatrix}^2 \frac{2l+1}{2k+1}\delta_{k0} \\ &= \mathrm{F}^0 \end{aligned} \tag{B.59}$$

since $\begin{pmatrix} l & 0 & l \\ 0 & 0 & 0 \end{pmatrix}^2 = \frac{1}{2l+1}$ (Eq. B.50).

Hund's exchange J

Hund's exchange J is defined as :

$$J \equiv \frac{1}{2l(2l+1)} \sum_{m\neq m'} \sum_k \alpha_k(m,m',m',m)\mathrm{F}^k \tag{B.60}$$

$$= \frac{1}{2l(2l+1)} \sum_{m\neq m'} \sum_k \mathrm{F}^k \frac{4\pi}{2k+1} \sum_{q=-k}^{k} |\langle Y_{lm}|Y_{kq}Y_{lm'}\rangle|^2 \tag{B.61}$$

$$= \frac{2l+1}{2l}\sum_k \mathrm{F}^k \begin{pmatrix} l & k & l \\ 0 & 0 & 0 \end{pmatrix}^2 \sum_{q=-k}^{k} \sum_{m\neq m'} (-1)^{m+m'} \begin{pmatrix} l & k & l \\ -m & q & m' \end{pmatrix} \begin{pmatrix} l & k & l \\ -m' & -q & m \end{pmatrix} \tag{B.62}$$

According to the condition B.32, it follows that only $q=m-m'$ terms lead to non-zero Wigner 3j-symbols. F^0 only contributes via $k=q=0$ but $q=0\neq m-m'$ since $m\neq m'$. Therefore, J does not depend on F^0. For $k\neq 0$, one can still employ the orthogonality-like relation (Eq. B.41) and hence :

$$J = \frac{2l+1}{2l}\sum_{k\neq 0} \mathrm{F}^k \begin{pmatrix} l & k & l \\ 0 & 0 & 0 \end{pmatrix}^2 \tag{B.63}$$

It follows for d electrons that :

$$\begin{aligned} J &= \frac{2l+1}{2l}\mathrm{F}^2 \begin{pmatrix} 2 & 2 & 2 \\ 0 & 0 & 0 \end{pmatrix}^2 + \frac{2l+1}{2l}\mathrm{F}^4 \begin{pmatrix} 2 & 4 & 2 \\ 0 & 0 & 0 \end{pmatrix}^2 \\ &= \frac{5}{4}\frac{8\cdot 36}{7!}\mathrm{F}^2 + \frac{5}{4}\frac{(4!)^4}{16\cdot 9!}\mathrm{F}^4 \\ &= \frac{\mathrm{F}^2+\mathrm{F}^4}{14} \end{aligned} \tag{B.64}$$

And analogously for f electrons, one gets :

$$J = \frac{2l+1}{2l}\mathrm{F}^2 \begin{pmatrix} 3 & 2 & 3 \\ 0 & 0 & 0 \end{pmatrix}^2 + \frac{2l+1}{2l}\mathrm{F}^4 \begin{pmatrix} 3 & 4 & 3 \\ 0 & 0 & 0 \end{pmatrix}^2 + \frac{2l+1}{2l}\mathrm{F}^6 \begin{pmatrix} 3 & 6 & 3 \\ 0 & 0 & 0 \end{pmatrix}^2 \tag{B.65}$$

Employing the relation B.49, one can calculate values for $\begin{pmatrix} 3 & k & 3 \\ 0 & 0 & 0 \end{pmatrix}$:

$$\begin{pmatrix} 3 & 2 & 3 \\ 0 & 0 & 0 \end{pmatrix} \approx 0.19518$$
$$\begin{pmatrix} 3 & 4 & 3 \\ 0 & 0 & 0 \end{pmatrix} \approx -0.16116$$
$$\begin{pmatrix} 3 & 6 & 3 \\ 0 & 0 & 0 \end{pmatrix} \approx 0.18248$$

and one verifies that

$$J = \frac{286\mathrm{F}^2 + 195\mathrm{F}^4 + 250\mathrm{F}^6}{6435}. \tag{B.66}$$

Appendix C

Expansions of the symmetrized dielectric functions at the Γ point

In this appendix, we indicate how to calculate the symmetrized dielectric function in the product mixed basis used in our implementation. The method has been used in Chapter 5, at the end of Section 5.1.5 (Eq. 5.40 and below). For additional details, see also [Jiang et al. (2012), Li(2008)].

C.1 Plane wave expansion : head, wings, body

The bare Coulomb potential is diagonal in the plane wave basis :

$$v_{\boldsymbol{GG'}} = \delta_{\boldsymbol{GG'}} \frac{4\pi}{|\boldsymbol{q}+\boldsymbol{G}|^2} \tag{C.1}$$

$$v^{\frac{1}{2}}_{\boldsymbol{GG'}} = \delta_{\boldsymbol{GG'}} \frac{\sqrt{4\pi}}{|\boldsymbol{q}+\boldsymbol{G}|} \tag{C.2}$$

The symmetrized dielectric function then reads :

$$\varepsilon_{GG'}(\boldsymbol{q},\omega) = \delta_{\boldsymbol{GG'}} - \frac{4\pi}{|\boldsymbol{q}+\boldsymbol{G}||\boldsymbol{q}+\boldsymbol{G'}|} P_{\boldsymbol{GG'}}(\boldsymbol{q},\omega), \tag{C.3}$$

where the polarization $P_{\boldsymbol{GG'}}$ is defined by :

$$P_{\boldsymbol{GG'}}(\boldsymbol{q},\omega) = \frac{1}{\mathcal{N}} \sum_{\boldsymbol{k}} \sum_{nn'} M^{\boldsymbol{G}}_{nn'}(\boldsymbol{k},\boldsymbol{q}) F_{nn'\boldsymbol{k}}(\boldsymbol{q},\omega) [M^{\boldsymbol{G'}}_{nn'}(\boldsymbol{k},\boldsymbol{q})]^*. \tag{C.4}$$

$F_{nn'\boldsymbol{k}}(\boldsymbol{q},\omega)$ was introduced in Eq. 5.24 and $M^{\boldsymbol{G}}_{nn'}(\boldsymbol{k},\boldsymbol{q})$ reads :

$$M^{\boldsymbol{G}}_{nn'}(\boldsymbol{k},\boldsymbol{q}) = \int_\Omega \frac{1}{\Omega^{1/2}} \mathrm{e}^{-i(\boldsymbol{q}+\boldsymbol{G})\cdot\boldsymbol{r}} \psi_{\boldsymbol{k}n}(\boldsymbol{r}) \psi^*_{\boldsymbol{k}-\boldsymbol{q},n'}(\boldsymbol{r}). \tag{C.5}$$

$M_{nn'}^{\boldsymbol{G}=0}(\boldsymbol{k}, \boldsymbol{q} \to 0)$

Using $\boldsymbol{k}\cdot\boldsymbol{p}$ perturbation theory and taking into account the Bloch character of the eigenfunctions $\psi_{\boldsymbol{k}n}(\boldsymbol{r})$ [Ambrosch-Draxl and Sofo(2004)], one can write :

$$\psi_{\boldsymbol{k}n}(\boldsymbol{r}) = \mathrm{e}^{i\boldsymbol{k}\cdot\boldsymbol{r}} u_{\boldsymbol{k}n}(\boldsymbol{r}) \tag{C.6}$$

$$u_{\boldsymbol{k}+\boldsymbol{q},n}(\boldsymbol{r}) = u_{\boldsymbol{k}n}(\boldsymbol{r}) - \sum_{n'\neq n} \frac{\boldsymbol{p}_{n'n\boldsymbol{k}}\cdot\boldsymbol{q}}{\epsilon_{\boldsymbol{k}n'} - \epsilon_{\boldsymbol{k}n}} u_{\boldsymbol{k}n}(\boldsymbol{r}) \tag{C.7}$$

$$\epsilon_{\boldsymbol{k}+\boldsymbol{q},n} = \epsilon_{\boldsymbol{k}n} + \boldsymbol{p}_{nn'\boldsymbol{k}}\cdot\boldsymbol{q}, \tag{C.8}$$

where the momentum matrix elements $\boldsymbol{p}_{nn'\boldsymbol{k}}$ are defined such as :

$$p_{nn'\boldsymbol{k}} \equiv \langle\psi_{\boldsymbol{k}n}|\boldsymbol{p}|\psi_{\boldsymbol{k}n'}\rangle. \tag{C.9}$$

It follows for the quantities $M_{nn'}^{\boldsymbol{G}=0}(\boldsymbol{k}, \boldsymbol{q} \to 0)$:

$$\begin{aligned} M_{nn'}^{\boldsymbol{G}=0}(\boldsymbol{k}, \boldsymbol{q} \to 0) &= \frac{1}{\Omega^{1/2}} \int_\Omega d\boldsymbol{r} \left[u_{\boldsymbol{k}n'}(\boldsymbol{r}) + \sum_{n''\neq n'} \frac{\boldsymbol{p}_{n''n'\boldsymbol{k}}\cdot\boldsymbol{q}}{\epsilon_{\boldsymbol{k}n''} - \epsilon_{\boldsymbol{k}n'}} u^*_{\boldsymbol{k}n''}(\boldsymbol{r}) \right] u_{\boldsymbol{k}n}(\boldsymbol{r}) \\ &= \frac{1}{\Omega^{1/2}} \left[\delta_{nn'} + (1-\delta_{nn'}) \frac{\boldsymbol{p}^*_{nn'\boldsymbol{k}}\cdot\boldsymbol{q}}{\epsilon_{\boldsymbol{k}n} - \epsilon_{\boldsymbol{k}n'}} \right]. \end{aligned} \tag{C.10}$$

The head : $P_{\boldsymbol{G}=0,\boldsymbol{G}'=0}(\boldsymbol{q} \to 0, \omega)$

Inserting Eq. C.10 into Eq. C.4, it follows :

$$\begin{aligned} P_{\boldsymbol{G}=0,\boldsymbol{G}'=0}(\boldsymbol{q} \to 0, \omega) &= \frac{1}{\mathcal{N}} \sum_{\boldsymbol{k}} \sum_{nn'} M_{nn'}^{\boldsymbol{G}=0}(\boldsymbol{k}, \boldsymbol{q} \to 0) F_{nn'\boldsymbol{k}}(\boldsymbol{q} \to 0, \omega) [M_{nn'}^{\boldsymbol{G}'=0}(\boldsymbol{k}, \boldsymbol{q} \to 0)]^* \\ &= \frac{1}{\mathcal{N}\Omega} \sum_{\boldsymbol{k}} \sum_{nn'} \left[\delta_{nn'} + (1-\delta_{nn'}) \left| \frac{\boldsymbol{p}_{nn'\boldsymbol{k}}\cdot\boldsymbol{q}}{\epsilon_{\boldsymbol{k}n} - \epsilon_{\boldsymbol{k}n'}} \right|^2 \right] F_{nn'\boldsymbol{k}}(\boldsymbol{q} \to 0, \omega) \\ &= \frac{1}{\mathcal{N}\Omega} \sum_{\boldsymbol{k}} \left[\sum_n F_{nn\boldsymbol{k}}(\boldsymbol{q} \to 0, \omega) + \sum_{n'\neq n} \left| \frac{\boldsymbol{p}_{nn'\boldsymbol{k}}\cdot\boldsymbol{q}}{\epsilon_{\boldsymbol{k}n} - \epsilon_{\boldsymbol{k}n'}} \right|^2 F_{nn'\boldsymbol{k}}(\boldsymbol{q} \to 0, \omega) \right]. \end{aligned} \tag{C.11}$$

Limit of $F_{nn\boldsymbol{k}}(\boldsymbol{q} \to 0)$

At zero-temperature ($\Delta \equiv -\boldsymbol{p}_{nn\boldsymbol{k}}\cdot\boldsymbol{q}$ and $f(\epsilon_{n\boldsymbol{k}})(1-f(\epsilon_{n\boldsymbol{k}})) = 0$), it follows that :

$$\begin{aligned} F_{nnk}(\boldsymbol{q} \to 0) &= f(\epsilon_{n\boldsymbol{k}})(1 - f(\epsilon_{n\boldsymbol{k}}) - f'(\epsilon_{n\boldsymbol{k}})\Delta) \left[\frac{1}{\omega - \Delta + i\eta} - \frac{1}{\omega + \Delta - i\eta} \right] \\ &= -\theta(\epsilon_F - \epsilon_{nk}) \delta(\epsilon_F - \epsilon_{nk}) \frac{2\Delta^2}{\omega^2} \\ &= -\frac{1}{2} \delta(\epsilon_F - \epsilon_{nk}) \frac{2\Delta^2}{\omega^2} \\ &= -\delta(\epsilon_F - \epsilon_{nk}) \frac{|p_{nnk}\cdot q|^2}{\omega^2} \end{aligned} \tag{C.12}$$

It follows for the polarization $P_{\boldsymbol{G}=0,\boldsymbol{G}'=0}(\boldsymbol{q}\rightarrow 0,\omega)$:

$$P_{00}(\boldsymbol{q}\rightarrow 0,\omega) = \frac{1}{\mathcal{N}\Omega}\Big[\sum_{n} -\delta(\epsilon_f-\epsilon_{\boldsymbol{k}n})\frac{|p_{nnk}\cdot q|^2}{\omega^2}+\sum_{n'\neq n} F_{nn'\boldsymbol{k}}(0,\omega)\Big|\frac{\boldsymbol{p}_{nn'\boldsymbol{k}}\cdot\boldsymbol{q}}{\epsilon_{\boldsymbol{k}n}-\epsilon_{\boldsymbol{k}n'}}\Big|^2\Big]. \tag{C.13}$$

The wings : $P_{\boldsymbol{G}=0,\boldsymbol{G}'\neq 0}(\boldsymbol{q}\rightarrow 0,\omega)$

Employing the $\boldsymbol{k}\cdot\boldsymbol{p}$ perturbation method introduced previously, one deduces for the polarization $P_{\boldsymbol{G}=0,\boldsymbol{G}'\neq 0}(\boldsymbol{q}\rightarrow 0,\omega)$:

$$\begin{aligned} P_{\boldsymbol{G}=0,\boldsymbol{G}'\neq 0}(\boldsymbol{q}\rightarrow 0,\omega) &= \frac{1}{\mathcal{N}\Omega^{1/2}}\sum_{\boldsymbol{k}}\sum_{n,n'}\Big(\delta_{nn'}+(1-\delta_{nn'})\frac{p^*_{nn'\boldsymbol{k}}\cdot\boldsymbol{q}}{\epsilon_{\boldsymbol{k}n}-\epsilon_{\boldsymbol{k}n'}}\Big)[M^{\boldsymbol{G}'}_{nn'}(\boldsymbol{k},0)]^* F_{nn'\boldsymbol{k}}(\boldsymbol{q}\rightarrow 0,\omega) \\ &= \frac{1}{\mathcal{N}\Omega^{1/2}}\sum_{\boldsymbol{k}}\sum_{n\neq n'} F_{nn'\boldsymbol{k}}(0,\omega)\frac{p^*_{nn'\boldsymbol{k}}\cdot\boldsymbol{q}}{\epsilon_{\boldsymbol{k}n}-\epsilon_{\boldsymbol{k}n'}}[M^{\boldsymbol{G}'}_{nn'}(\boldsymbol{k},0)]^*, \end{aligned} \tag{C.14}$$

since the intra-band term ($n'=n$) goes to zero as $\boldsymbol{q}^2$ whereas the inter-band one goes to zero as $\boldsymbol{q}$.

The body : $P_{\boldsymbol{G}\neq 0,\boldsymbol{G}'\neq 0}(\boldsymbol{q}\rightarrow 0,\omega)$

The expression for the body part is straightforward :

$$\begin{aligned} P_{\boldsymbol{G}\neq 0,\boldsymbol{G}'\neq 0}(\boldsymbol{q}\rightarrow 0,\omega) &= \frac{1}{\mathcal{N}}\sum_{\boldsymbol{k}}\Big[\sum_{n} M^{\boldsymbol{G}}_{nn}(\boldsymbol{k},0)(-\delta(\epsilon_F-\epsilon_{nk})\frac{|p_{nnk}\cdot q|^2}{\omega^2})[M^{\boldsymbol{G}'}_{nn}(\boldsymbol{k},0)]^* \\ &\quad +\sum_{n\neq n'} M^{\boldsymbol{G}}_{nn}(\boldsymbol{k},0)F_{nn'\boldsymbol{k}}(0,\omega)[M^{\boldsymbol{G}'}_{nn}(\boldsymbol{k},0)]^*\Big]. \end{aligned} \tag{C.15}$$

C.2 Mixed basis expansion

In the mixed basis, the divergences at $\boldsymbol{q}=0$ are not necessarily located in particular matrix elements of the bare Coulomb potential and the bare Coulomb potential is not diagonal any more. It is useful to introduce the transformation matrices $\mathcal{W}^i_{\boldsymbol{G}}$ from the plane wave $\{\chi^{\boldsymbol{q}=0}_{\boldsymbol{G}}\}$ to

the product mixed basis $\{\chi_i^{\boldsymbol{q}=0}\}$:

$$\varepsilon_{ij}(\boldsymbol{q}\to 0,\omega) = \sum_{\boldsymbol{G},\boldsymbol{G}'} \mathcal{W}^i_{\boldsymbol{G}}\varepsilon_{\boldsymbol{G}\boldsymbol{G}'}(\boldsymbol{q}\to 0,\omega)[\mathcal{W}^j_{\boldsymbol{G}'}]^* \tag{C.16}$$

$$\begin{aligned} v_{ij}^{1/2}(\boldsymbol{q}\to 0) &= \sqrt{4\pi}\sum_{\boldsymbol{G},\boldsymbol{G}'}\frac{\mathcal{W}^i_{\boldsymbol{G}}[\mathcal{W}^j_{\boldsymbol{G}'}]^*}{|\boldsymbol{q}+\boldsymbol{G}|} \\ &= \frac{\sqrt{4\pi}}{q}\mathcal{W}^i_0[\mathcal{W}^j_0]^* + \sum_{\boldsymbol{G}\neq 0}\frac{\sqrt{4\pi}}{|\boldsymbol{G}|}\mathcal{W}^i_{\boldsymbol{G}}[\mathcal{W}^j_{\boldsymbol{G}'}]^* \\ &= \frac{\sqrt{4\pi}}{q}\mathcal{W}^i_0[\mathcal{W}^j_0]^* + \sum_{\boldsymbol{G}}\tilde{v}^{1/2}_{\boldsymbol{G}}\mathcal{W}^i_{\boldsymbol{G}}[\mathcal{W}^j_{\boldsymbol{G}'}]^*, \end{aligned} \tag{C.17}$$

where $\mathcal{W}^i_{\boldsymbol{G}} \equiv \langle\chi_i^{\boldsymbol{q}=0}|\chi_{\boldsymbol{G}}^{\boldsymbol{q}=0}\rangle$ and $\tilde{v}_{\boldsymbol{G}\neq 0} = 4\pi/\boldsymbol{G}^2$ is the regularized Coulomb matrix ($\tilde{v}_{\boldsymbol{G}=0}=0$). It follows for the symmetrized dielectric function in the product mixed basis (see Chapter 5, Eq. 5.40) :

$$\begin{aligned} \varepsilon_{ij}(\boldsymbol{q}\to 0,\omega) &= \mathcal{W}^i_0\varepsilon_{0,0}(\boldsymbol{q}\to 0,\omega)[\mathcal{W}^j_0]^* \\ &\quad + \sum_{\boldsymbol{G}\neq 0}\left[\mathcal{W}^i_{\boldsymbol{G}}\varepsilon_{\boldsymbol{G},0}(\boldsymbol{q}\to 0,\omega)[\mathcal{W}^j_0]^* + \mathcal{W}^i_0\varepsilon_{0,\boldsymbol{G}}(\boldsymbol{q}\to 0,\omega)[\mathcal{W}^j_{\boldsymbol{G}}]^*\right] \\ &\quad + \sum_{\boldsymbol{G},\boldsymbol{G}'\neq 0}\mathcal{W}^i_{\boldsymbol{G}}\varepsilon_{\boldsymbol{G},\boldsymbol{G}'}(\boldsymbol{q}\to 0,\omega)[\mathcal{W}^j_{\boldsymbol{G}'}]^* \\ &\equiv \varepsilon^H_{ij}(\omega) + \varepsilon^{W_1}_{ij}(\omega) + \varepsilon^{W_2}_{ij}(\omega) + \varepsilon^B_{ij}(\omega). \end{aligned} \tag{C.18}$$

Head

By definition of the head in the plane wave basis, we get :

$$\varepsilon^H_{ij}(\omega) = \mathcal{W}^i_0[1-4\pi P^H(\omega)][\mathcal{W}^j_0]^* \tag{C.19}$$

Wings

Similarly, one gets for the wings :

$$\begin{aligned} \varepsilon^{W_2}_{ij}(\omega) &= \mathcal{W}^i_0\left(\frac{-4\pi}{\Omega^{1/2}}\right)\frac{1}{\mathcal{N}}\sum_{\boldsymbol{k}}\sum_{n\neq n'}F_{nn'\boldsymbol{k}}(0,\omega)\frac{\boldsymbol{p}^*_{nn'\boldsymbol{k}}\cdot\boldsymbol{q}}{\epsilon_{\boldsymbol{k}n}-\epsilon_{\boldsymbol{k}n'}}\sum_{\boldsymbol{G}\neq 0}\frac{[M^{\boldsymbol{G}}_{nn'}(\boldsymbol{k},0)]^*}{|\boldsymbol{G}|}[\mathcal{W}^j_{\boldsymbol{G}}]^* \\ &= \mathcal{W}^i_0\left(-\sqrt{\frac{4\pi}{\Omega}}\right)\frac{1}{\mathcal{N}}\sum_{\boldsymbol{k}}\sum_{n\neq n'}F_{nn'\boldsymbol{k}}(0,\omega)\frac{\boldsymbol{p}^*_{nn'\boldsymbol{k}}\cdot\boldsymbol{q}}{\epsilon_{\boldsymbol{k}n}-\epsilon_{\boldsymbol{k}n'}}\sum_{\boldsymbol{G}}\left[\tilde{v}^{1/2}_{\boldsymbol{G}}M^{\boldsymbol{G}}_{nn'}(\boldsymbol{k},0)\mathcal{W}^j_{\boldsymbol{G}}\right]^* \end{aligned} \tag{C.20}$$

and analogously for $\varepsilon^{W_1}_{ij}(\omega)$.

Body

It follows for the body part :

$$\begin{aligned}\varepsilon^B_{ij}(\omega) &= \sum_{\boldsymbol{G}\boldsymbol{G}'\neq 0} \mathcal{W}^i_{\boldsymbol{G}}\varepsilon_{\boldsymbol{G}\boldsymbol{G}'}(0,\omega)[\mathcal{W}^j_{\boldsymbol{G}'}]^* \\ &= \sum_{\boldsymbol{G}\boldsymbol{G}'\neq 0} \mathcal{W}^i_{\boldsymbol{G}}\Big[\delta_{\boldsymbol{G},\boldsymbol{G}'} - \frac{4\pi}{|\boldsymbol{G}||\boldsymbol{G}'|}P_{\boldsymbol{G}\boldsymbol{G}'}(0,\omega)\Big][\mathcal{W}^j_{\boldsymbol{G}'}]^*. \end{aligned} \tag{C.21}$$

C.3 Bare Coulomb matrix eigenvectors

As introduced in the first section of Chapter 5, it is practical to employ the eigenvectors of the bare Coulomb potential constructed from the original mixed basis detailed previously. In the following, the indices (i,j) will refer to the original mixed basis, whereas (μ,ν) to the mixed basis composed by the bare Coulomb matrix eigenvectors.

One can expand the bare Coulomb potential into the original mixed basis as follows :

$$\begin{aligned} v_{ij}(\boldsymbol{q}\to 0) &= \langle\chi^0_i|v|\chi^0_j\rangle \\ &= \sum_{\boldsymbol{G}\boldsymbol{G}'} \mathcal{W}^i_{\boldsymbol{G}} v_{\boldsymbol{G}\boldsymbol{G}'}(\boldsymbol{q}\to 0)[\mathcal{W}^j_{\boldsymbol{G}'}]^* \\ &= \frac{v^s_{ij}}{\boldsymbol{q}^2} + \tilde{v}_{ij}, \end{aligned} \tag{C.22}$$

where $v^s_{ij} \equiv 4\pi\mathcal{W}^i_0[\mathcal{W}^j_0]^*$ and $\tilde{v}_{ij} \equiv \sum_{\boldsymbol{G}} \mathcal{W}^i_{\boldsymbol{G}}\tilde{v}_{\boldsymbol{G}}[\mathcal{W}^j_{\boldsymbol{G}}]^*$.
By diagonalizing the regular part of the Coulomb interaction $\tilde{v}$ at $\boldsymbol{q}\to 0$ (which equals v for all $\boldsymbol{q}\neq 0$), the eigenvectors $\{\chi^{\boldsymbol{q}}_\mu(\boldsymbol{r})\}$ read

$$\chi^{\boldsymbol{q}}_\mu(\boldsymbol{r}) = \sum_i \mathcal{T}^{\boldsymbol{q}}_{\mu i}\chi^{\boldsymbol{q}}_i(\boldsymbol{r}), \tag{C.23}$$

and generate a product mixed basis that is equivalent to the plane waves basis and almost as accurate as the original product mixed basis.
Rigorously, the matrix $\{v^s_{ij}\}$ is not diagonal in the $\{\chi^{\boldsymbol{q}}_\mu\}$ basis :

$$\begin{aligned} v^s_{\mu\nu} &= \langle\chi^0_\mu|v^s|\chi^0_\nu\rangle & \text{(C.24)}\\ &= \sum_{ij}\langle\chi^0_\mu|\chi^0_i\rangle\langle\chi^0_i|v^s|\chi^0_j\rangle\langle\chi^0_j|\chi^0_\nu\rangle \\ &= \sum_{ij}[\mathcal{T}^0_{i\mu}]^* v^s_{ij}\mathcal{T}^0_{j\nu}, & \text{(C.25)} \end{aligned}$$

and hence in the $\{\chi^{\boldsymbol{q}}_\mu\}$ basis, the representation of v reads :

$$v_{\mu\nu}(\boldsymbol{q}\to 0) = \frac{v^s_{\mu\nu}}{\boldsymbol{q}^2} + \tilde{v}_\mu\delta_{\mu,\nu}. \tag{C.26}$$

In the implementation, we assume that v^s is diagonal in the new mixed basis such as $v^s_{\mu\nu} = 4\pi\delta_{\mu 0}\delta_{\nu 0}$. Since :

$$\begin{aligned} v^s_{\mu\nu} &= 4\pi \sum_{ij} [\mathcal{T}^0_{i\mu}]^* \mathcal{W}^i_0 [\mathcal{W}^j_0]^* \mathcal{T}^0_{j\nu} \\ &= 4\pi \sum_{i} [\mathcal{T}^0_{i\mu}]^* \mathcal{W}^i_0 \sum_{j} [\mathcal{W}^j_0]^* \mathcal{T}^0_{j\nu}, \end{aligned} \tag{C.27}$$

the approximation implies :

$$\sum_i [\mathcal{T}^0_{i\mu}]^* \mathcal{W}^i_0 = \langle \chi^0_\mu | \chi^0_{\boldsymbol{G}=0} \rangle = \delta_{\mu 0}. \tag{C.28}$$

This is a reasonable constraint. Using the transformation matrices from the original mixed basis to the new one which contains the eigenvectors of the bare interaction, it follows the following relations given in Chapter 5 (from Eq. 5.41 to Eq. 5.45) (the indices (i, j) now correspond to the new product mixed basis previously denoted (μ, ν)) :

$$\varepsilon_{ij}(\boldsymbol{q} \to 0, \omega) = \varepsilon^H_{ij}(\omega) + \varepsilon^W_{ij}(\omega) + \varepsilon^B_{ij}(\omega), \tag{C.29}$$

where ($\tilde{\delta_{ij}} \equiv 1 - \delta_{ij}$) :

$$\varepsilon^H_{ij}(\omega) = \delta_{i0}\delta_{j0}\Bigg\{1 - \frac{4\pi}{\Omega\mathcal{N}} \lim_{\boldsymbol{q}\to 0} \sum_{\boldsymbol{k}} \Bigg(\sum_n \frac{-\delta(\epsilon_{n\boldsymbol{k}} - \epsilon_F)}{\omega^2} |\boldsymbol{p}_{nn\boldsymbol{k}} \cdot \boldsymbol{q}|^2 \tag{C.30}$$

$$+ \sum_{n \neq n'} F_{nn'\boldsymbol{k}}(0, \omega) |\frac{\boldsymbol{p}_{nn'k} \cdot \boldsymbol{q}}{\epsilon_{n\boldsymbol{k}} - \epsilon_{n'\boldsymbol{k}}}|^2 \Bigg) \Bigg\} \tag{C.31}$$

$$\varepsilon^{W_1}_{ij}(\omega) = -\tilde{\delta}_{i0}\delta_{j0} \sqrt{\frac{4\pi}{\Omega}} \frac{1}{\mathcal{N}} \lim_{\boldsymbol{q}\to 0} \sum_{\boldsymbol{k}} \sum_{n \neq n'} F_{nn'\boldsymbol{k}}(0, \omega) \frac{\boldsymbol{p}_{nn'\boldsymbol{k}} \cdot \boldsymbol{q}}{\epsilon_{n\boldsymbol{k}} - \epsilon_{n'\boldsymbol{k}}} \tilde{v}_i^{\frac{1}{2}} M^i_{nn'}(\boldsymbol{k}, 0) \tag{C.32}$$

$$\varepsilon^{W_2}_{ij}(\omega) = -\delta_{i0}\tilde{\delta}_{j0} \sqrt{\frac{4\pi}{\Omega}} \frac{1}{\mathcal{N}} \lim_{\boldsymbol{q}\to 0} \sum_{\boldsymbol{k}} \sum_{n \neq n'} F_{nn'\boldsymbol{k}}(0, \omega) \frac{\boldsymbol{p}_{nn'\boldsymbol{k}} \cdot \boldsymbol{q}}{\epsilon_{n\boldsymbol{k}} - \epsilon_{n'\boldsymbol{k}}} [\tilde{v}_j^{\frac{1}{2}} M^j_{nn'}(\boldsymbol{k}, 0)]^* \tag{C.33}$$

$$\varepsilon^B_{ij}(\omega) = \tilde{\delta}_{i0}\tilde{\delta}_{j0} \Bigg(\delta_{ij} - \frac{1}{\mathcal{N}} \sum_{\boldsymbol{k}} \sum_{n \neq n'} F_{nn'\boldsymbol{k}}(0, \omega) \tilde{v}_i^{\frac{1}{2}} M^i_{nn'}(\boldsymbol{k}, 0) [\tilde{v}_j^{\frac{1}{2}} M^j_{nn'}(\boldsymbol{k}, 0)]^* \Bigg). \tag{C.34}$$

Appendix D

The Γ point treatment in the Brillouin-Zone summation

In this appendix, a method for an efficient Brillouin-zone integration is given. It has been used in Chapter 5, at the end of Section 5.1.5 (Eq. 5.50). For further details, see also [Jiang et al. (2012), Li(2008)].

We consider the Brillouin-zone integration of a function that diverges at the Γ point ($\boldsymbol{q} = 0$) :

$$\begin{aligned} I &= \frac{1}{\mathcal{N}} \sum_{\boldsymbol{q}} \mathcal{F}(\boldsymbol{q}) \\ &= \frac{\Omega}{2\pi^3} \int d^3\boldsymbol{q} \mathcal{F}(\boldsymbol{q}). \end{aligned} \tag{D.1}$$

In the $\boldsymbol{q} \to 0$ limit, we can divide the function $\mathcal{F}$ into a singular part and a regular one called $\tilde{\mathcal{F}}$:

$$\mathcal{F}(\boldsymbol{q}) = \frac{\mathcal{F}^{s2}}{\boldsymbol{q}^2} + \frac{\mathcal{F}^{s1}}{\boldsymbol{q}} + \tilde{\mathcal{F}}(\boldsymbol{q}). \tag{D.2}$$

The singularity at Γ is integrable but a direct numerical integration will converge very slowly. Following [Massidda *et al.* (1993)], we introduce two auxiliary functions :

$$F_1(\boldsymbol{q}) = \sum_{\boldsymbol{G}} \frac{\mathrm{e}^{-\alpha|\boldsymbol{q}+\boldsymbol{G}|}}{|\boldsymbol{q}+\boldsymbol{G}|} \tag{D.3}$$

$$F_2(\boldsymbol{q}) = \sum_{\boldsymbol{G}} \frac{\mathrm{e}^{-\alpha|\boldsymbol{q}+\boldsymbol{G}|^2}}{|\boldsymbol{q}+\boldsymbol{G}|^2}, \tag{D.4}$$

which show similar singularities since :

$$F_1(\boldsymbol{q} \to 0) = \frac{1}{\boldsymbol{q}} + \tilde{F}_1(\boldsymbol{q}) \tag{D.5}$$

$$F_2(\boldsymbol{q} \to 0) = \frac{1}{\boldsymbol{q}^2} + \tilde{F}_2(\boldsymbol{q}). \tag{D.6}$$

In this last expression, $\tilde{F}_{1,2}$ are the regularized parts of $F_{1,2}$, obtained by avoiding $\boldsymbol{G} = 0$ in the summation.

We can then write the integration over $\boldsymbol{q}$ as follows :

$$\begin{aligned} I &= \frac{1}{\mathcal{N}}\sum_{\boldsymbol{q}}[\mathcal{F}(\boldsymbol{q}) - \mathcal{F}^{s1}F_1(\boldsymbol{q}) - \mathcal{F}^{s2}F_2(\boldsymbol{q})] + \frac{1}{\mathcal{N}}\mathcal{F}^{s1}\sum_{\boldsymbol{q}}F_1(\boldsymbol{q}) + \frac{1}{\mathcal{N}}\mathcal{F}^{s2}\sum_{\boldsymbol{q}}F_2(\boldsymbol{q}) \\ &= \frac{1}{\mathcal{N}}\sum_{\boldsymbol{q}}[\mathcal{F}(\boldsymbol{q}) - \mathcal{F}^{s1}\tilde{F}_1(\boldsymbol{q}) - \mathcal{F}^{s2}\tilde{F}_2(\boldsymbol{q})] + \mathcal{F}^{s1}I_{s1} + \mathcal{F}^{s2}I_{s2} \\ &= \frac{1}{\mathcal{N}}\sum_{\boldsymbol{q}}\tilde{\mathcal{F}}(\boldsymbol{q}) + \mathcal{F}^{s1}\Big[I_{s1} - \frac{1}{\mathcal{N}}\sum_{\boldsymbol{q}}\tilde{F}_1(\boldsymbol{q})\Big] + \mathcal{F}^{s2}\Big[I_{s2} - \frac{1}{\mathcal{N}}\sum_{\boldsymbol{q}}\tilde{F}_2(\boldsymbol{q})\Big] \\ &= \frac{1}{\mathcal{N}}\sum_{\boldsymbol{q}}\tilde{\mathcal{F}}(\boldsymbol{q}) + C_{s1}\mathcal{F}^{s1} + C_{s2}\mathcal{F}^{s2}, \end{aligned} \tag{D.7}$$

where

$$I_{s1} \equiv \frac{1}{\mathcal{N}}\sum_{\boldsymbol{q}}F_1(\boldsymbol{q}) = \frac{\Omega}{(2\pi)^2\alpha} \tag{D.8}$$

$$I_{s2} \equiv \frac{1}{\mathcal{N}}\sum_{\boldsymbol{q}}F_2(\boldsymbol{q}) = \frac{\Omega}{(2\pi)^2}\sqrt{\pi}\alpha, \tag{D.9}$$

and α is a parameter that equals $(\frac{\Omega}{6\pi^2})^{\frac{1}{3}}$. It follows for the $C_{s1,2}$ coefficients :

$$C_{s1} = I_{s1} - \frac{1}{\mathcal{N}}\sum_{\boldsymbol{q}}\tilde{F}_1(\boldsymbol{q}) \tag{D.10}$$

$$C_{s2} = I_{s2} - \frac{1}{\mathcal{N}}\sum_{\boldsymbol{q}}\tilde{F}_2(\boldsymbol{q}) \tag{D.11}$$

Bibliography

[Aichhorn *et al.* (2010)] M. Aichhorn, S. Biermann, T. Miyake, A. Georges, and M. Imada. *Theoretical evidence for strong correlations and incoherent metallic state in FeSe*. *Phys. Rev. B* **82** (2010)(6): 064504. 6, 41, 55, 56, 112, 115, 116

[Aichhorn *et al.* (2011)] M. Aichhorn, L. Pourovskii, and A. Georges. *Importance of electronic correlations for structural and magnetic properties of the iron pnictide superconductor LaFeAsO*. *Phys. Rev. B* **84** (2011): 054529. 41

[Aichhorn *et al.* (2009)] M. Aichhorn, L. Pourovskii, V. Vildosola, M. Ferrero, O. Parcollet, T. Miyake, A. Georges, and S. Biermann. *Dynamical mean-field theory within an augmented plane-wave framework: Assessing electronic correlations in the iron pnictide LaFeAsO*. *Phys. Rev. B* **80** (2009)(8): 085101. 37, 41, 55, 56, 69, 77, 86, 110, 112, 113, 123, 133, 149, 164, 207

[Aligia *et al.* (1995)] A. A. Aligia, L. Arrachea, and E. R. Gagliano. *Phase diagram of an extended Hubbard model with correlated hopping at half filling*. *Phys. Rev. B* **51** (1995): 13774. 32

[Ambrosch-Draxl and Sofo(2004)] C. Ambrosch-Draxl and J. O. Sofo. *Linear optical properties of solids within the full-potential linearized augmented planewaves method*. *Unpublished* (2004). 79, 222

[Andersen(1975)] O. K. Andersen. *Linear methods in band theory*. *Phys. Rev. B* **12** (1975)(8): 3060. 19, 37, 205

[Andersen and Saha-Dasgupta(2000)] O. K. Andersen and T. Saha-Dasgupta. *Muffin-tin orbitals of arbitrary order*. *Phys. Rev. B* **62** (2000)(24): R16219. 19, 37

[Anderson(1961)] P. W. Anderson. *Localized Magnetic States in Metals*. *Phys. Rev.* **124** (1961)(1): 41. 29

[Anisimov *et al.* (2009a)] V. Anisimov, D. Korotin, M. A. Korotin, A. V. Kozhevnikov, J. Kuneš, A. O. Shorikov, S. L. Skornyakov, and S. V. Streltsov. *Coulomb repulsion and correlation strength in LaFeAsO from density functional and dynamical mean-field theories*. *J. Phys. Condens. Matter* **21** (2009a)(7): 075602. 64

[Anisimov *et al.* (1997a)] V. I. Anisimov, F. Aryasetiawan, and A. I. Lichtenstein. *First-principles calculations of the electronic structure and spectra of strongly correlated systems: the LDA+U method*. *J. Phys. Condens. Matter* **9** (1997a)(4): 767. 27, 35, 36, 40, 64, 82, 83, 84, 86

[Anisimov and Gunnarsson(1991)] V. I. Anisimov and O. Gunnarsson. *Density-functional calculation of effective Coulomb interactions in metals*. *Phys. Rev. B* **43** (1991)(10): 7570. 63, 64, 65

[Anisimov *et al.* (2005)] V. I. Anisimov, D. E. Kondakov, A. V. Kozhevnikov, I. A. Nekrasov, Z. V. Pchelkina, J. W. Allen, S.-K. Mo, H.-D. Kim, P. Metcalf, S. Suga, A. Sekiyama, G. Keller, I. Leonov, X. Ren, and D. Vollhardt. *Full orbital calculation scheme for materials with strongly correlated electrons*. *Phys. Rev. B* **71** (2005)(12): 125119. 37

[Anisimov *et al.* (2009b)] V. I. Anisimov, D. Korotin, M. Korotin, A. V. Kozhevnikov, J. Kunes, S. A. O., S. L. Skornyakov, and S. V. Streltsov. *Coulomb repulsion and correlation strength in LaFeAsO from density functional and dynamical mean-field theories*. *J. Phys. Condens. Matter* **21** (2009b): 075602. 110

[Anisimov *et al.* (2002)] V. I. Anisimov, I. A. Nekrasov, D. E. Kondakov, T. M. Rice, and M. Sigrist. *Orbital-selective Mott-insulator transition in* $Ca_{2-x}Sr_xRuO_4$. *Eur. Phys. Lett.* **25** (2002): 191. 152

[Anisimov *et al.* (1997b)] V. I. Anisimov, A. Poteryaev, M. Korotin, A. Anokhin, and G. Kotliar. *First-principles calculations of the electronic structure and spectra of strongly correlated systems : dynamical mean-field theory*. *J. Phys. Condens. Matter* **9** (1997b): 943. 35, 36, 41

[Anisimov *et al.* (1993)] V. I. Anisimov, I. V. Solovyev, M. A. Korotin, M. T. Czyżyk, and G. A. Sawatzky. *Density-functional theory and NiO photoemission spectra*. *Phys. Rev. B* **48** (1993)(23): 16929. 40, 84, 218

[Anisimov *et al.* (1991)] V. I. Anisimov, J. Zaanen, and O. K. Andersen. *Band theory and Mott insulators: Hubbard U instead of Stoner I*. *Phys. Rev. B* **44** (1991)(3): 943. 35, 40, 64, 65

[Antonides *et al.* (1977)] E. Antonides, E. C. Janse, and G. A. Sawatzky. *LMM Auger spectra of Cu, Zn, Ga, and Ge. I. Transition probabilities, term splittings, and effective Coulomb interaction*. *Phys. Rev. B* **15** (1977)(4): 1669. 46, 63, 105, 141

[Arita *et al.* (2012)] R. Arita, J. Kuneš, A. V. Kozhevnikov, A. G. Eguiluz, and M. Imada. *Ab initio Studies on the Interplay between Spin-Orbit Interaction and Coulomb Correlation in* Sr_2IrO_4 *and* Ba_2IrO_4. *Phys. Rev. Lett.* **108** (2012): 086403. 168, 174

[Aryasetiawan(2000)] F. Aryasetiawan. *Strong Coulomb correlations in electronic structure calculations : beyond the local density approximation*. Editor : V. I. Anisimov, Gordon and Breach Science Publishers, Amsterdam, The Netherlands (2000). 23, 25, 27

[Aryasetiawan and Gunnarsson(1998)] F. Aryasetiawan and O. Gunnarsson. *The GW Method*. *Rep. Prog. Phys.* **61** (1998)(8): 237. 5, 24, 25, 27, 52, 70, 75

[Aryasetiawan *et al.* (2004)] F. Aryasetiawan, M. Imada, A. Georges, G. Kotliar, S. Biermann, and A. I. Lichtenstein. *Frequency-dependent local interactions and low-energy effective models from electronic structure calculations*. *Phys. Rev. B* **70** (2004)(19): 195104. 41, 49, 51, 55

[Aryasetiawan *et al.* (2006)] F. Aryasetiawan, K. Karlsson, O. Jepsen, and U. Schönberger. *Calculations of Hubbard U from first-principles*. *Phys. Rev. B* **74** (2006)(12): 125106. 55, 60, 64, 65, 102, 103, 104, 107, 122, 124, 125, 126, 139, 176

[Aryasetiawan *et al.* (2009)] F. Aryasetiawan, J. M. Tomczak, T. Miyake, and R. Sakuma. *Downfolded Self-Energy of Many-Electron Systems*. *Phys. Rev. Lett.* **102** (2009)(17): 176402. 49

[Auerbach(1994)] A. Auerbach. *Interacting Electrons and Quantum Magnetism*. Springer Verlag (1994). 7, 8

[Bandyopadhyay and Sarma(1989)] T. Bandyopadhyay and D. D. Sarma. *Calculation of Coulomb interaction strengths for 3d transition metals and actinides*. *Phys. Rev. B* **39** (1989): 3517. 122

[Baumberger *et al.* (2006)] F. Baumberger, N. J. C. Ingle, W. Meevasana, K. M. Shen, D. H. Lu, R. S. Perry, A. P. Mackenzie, Z. Hussain, D. J. Singh, and Z.-X. Shen. *Fermi Surface and Quasiparticle Excitations of Sr_2RhO_4*. *Phys. Rev. Lett.* **96** (2006): 246402. 176

[Biermann(2006)] S. Biermann. *"LDA+DMFT" - a Tool for Investigating the Electronic Structure of Materials with Strong Electronic Coulomb Correlations*. *Encyclopedia of materials : Science and Technology* (2006). 28, 37, 41

[Biermann *et al.* (2003)] S. Biermann, F. Aryasetiawan, and A. Georges. *First-Principles Approach to the Electronic Structure of Strongly Correlated Systems: Combining the GW Approximation and Dynamical Mean-Field Theory*. *Phys. Rev. Lett.* **90** (2003)(8): 086402. 25, 28, 57, 58, 93

[Biroli and Kotliar(2002)] G. Biroli and G. Kotliar. *Cluster methods for strongly correlated electron systems*. *Phys. Rev. B* **65** (2002)(15): 155112. 30

[Blaha *et al.* (2001)] P. Blaha, K. Schwarz, G. Madsen, D. Kvasnicka, and J. Luitz. *Wien2k, An Augmented Plane Wave+Local Orbitals Program for Calculating Crystal Properties*. Tech. Universität Wien, Austria (2001). 19, 41, 47, 68, 69, 205

[Bocquet *et al.* (1996)] A. E. Bocquet, T. Mizokawa, K. Morikawa, A. Fujimori, S. R. Barman, K. Maiti, D. D. Sarma, Y. Tokura, and M. Onoda. *Electronic structure of early 3d-transition-metal oxides by analysis of the 2p core-level photoemission spectra*. *Phys. Rev. B* **53** (1996)(3): 1161. 63, 135

[Bocquet *et al.* (1992)] A. E. Bocquet, T. Mizokawa, T. Saitoh, H. Namatame, and A. Fujimori. *Electronic structure of 3d-transition-metal compounds by analysis of the 2p core-level photoemission spectra*. *Phys. Rev. B* **46** (1992)(7): 3771. 63, 147

[Brinkman and Rice(1970)] W. F. Brinkman and T. M. Rice. *Application of Gutzwiller's Variational Method to the Metal-Insulator Transition*. *Phys. Rev. B* **2** (1970)(10): 4302. 34

[Brooks(2001)] M. S. Brooks. *Thomas-Fermi screening of exchange interactions*. *J. Phys. Condens. Matter* **13** (2001)(7): L469. 13

[Brouet *et al.* (2010)] V. Brouet, F. Rullier-Albenque, M. Marsi, B. Mansart, M. Aichhorn, S. Biermann, J. Faure, L. Perfetti, A. Taleb-Ibrahimi, P. Le Fèvre, F. Bertran, A. Forget, and D. Colson. *Significant Reduction of Electronic Correlations upon Isovalent Ru Substitution of* $BaFe_2As_2$. *Phys. Rev. Lett.* **105** (2010): 087001. 116

[Bruus and Flensberg(2003)] H. Bruus and K. Flensberg. *Many-Body Quantum Theory in Condensed Matter Physics*. Oxford University Press (2003). 10, 13

[Bulla(2006)] R. Bulla. *Dynamical Mean-Field Theory - from Quantum Impurity Physics to Lattice Problems*. *Phil. Mag.* **86** (2006): 1877. 29

[Bulla *et al.* (2008)] R. Bulla, T. A. Costi, and T. Pruschke. *Numerical renormalization group method for quantum impurity systems*. *Rev. Mod. Phys.* **80** (2008)(2): 395. 32

[Campo Jr and Cococcioni(2010)] V. L. Campo Jr and M. Cococcioni. *Extended DFT+U+V method with on-site and inter-site electronic interactions*. *J. Phys. Condens. Matter* **22** (2010)(5): 055602. 67

[Capelle(2006)] K. Capelle. *A bird's-eye view of Density Functional Theory*. *Brazilian Journal of Physics* **36** (2006): 1318. 16, 18

[Carnall *et al.* (1989)] W. T. Carnall, G. L. Goodman, K. Rajnak, and R. S. Rana. *A systematic analysis of the spectra of the lanthanides doped into single crystal* LaF_3. *J. Chem. Phys.* **90** (1989): 3443. 183

[Casula *et al.* (2012a)] M. Casula, A. Rubtsov, and S. Biermann. *Dynamical screening effects in correlated materials: Plasmon satellites and spectral weight transfers from a Green's function ansatz to extended dynamical mean field theory*. *Phys. Rev. B* **85** (2012a): 035115. 55, 56, 57, 61, 107, 113, 133, 147, 191

[Casula *et al.* (2012b)] M. Casula, P. Werner, L. Vaugier, F. Aryasetiawan, T. Miyake, A. J. Millis, and S. Biermann. *Low-energy Models for Correlated Materials: Bandwidth Renormalization from Coulombic Screening*. *arXiv* **1204.4900** (2012b). 56, 57, 61, 133, 147, 191

[Ceperley and Alder(1980)] D. M. Ceperley and B. J. Alder. *Ground State of the Electron Gas by a Stochastic Method*. *Phys. Rev. Lett.* **45** (1980)(7): 566. 18

[Chamberland(1967)] B. Chamberland. *Preparation and properties of SrCrO3*. *Solid State Commun.* **5** (1967): 663. 135

[Chen *et al.* (2008a)] G. F. Chen, Z. Li, D. Wu, G. Li, W. Z. Hu, J. Dong, P. Zheng, J. L. Luo, and N. L. Wang. *Superconductivity at 41 K and Its Competition with Spin-Density-Wave Instability in Layered $CeO_{1-x}F_xFeAs$*. *Phys. Rev. Lett.* **100** (2008a): 247002. 110

[Chen *et al.* (2008b)] X. H. Chen, T. Wu, G. Wu, R. H. Liu, H. Chen, and D. F. Fang. *Superconductivity at 43 K in $SmFeAsO_{1-x}F_x$*. *Nature* **453** (2008b): 761. 110

[Chmaissem *et al.* (2001)] O. Chmaissem, B. Dabrowski, S. Kolesnik, J. Mais, D. E. Brown, R. Kruk, P. Prior, B. Pyles, and J. D. Jorgensen. *Relationship between structural parameters and the Néel temperature in $Sr1-xCaxMnO3$ and $Sr1-yBayMnO3$*. *Phys. Rev. B* **64** (2001)(13): 134412. 135

[Cococcioni and de Gironcoli(2005)] M. Cococcioni and S. de Gironcoli. *Linear response approach to the calculation of the effective interaction parameters in the LDA+U method*. *Phys. Rev. B* **71** (2005)(3): 035105. 36, 65, 66

[Cowan(1981)] R. D. Cowan. *The theory of atomic structure and spectra*. University of California Press (1981). 119, 138

[Daoud-Aladine *et al.* (2007)] A. Daoud-Aladine, C. Martin, L. C. Chapon, M. Hervieu, K. S. Knight, M. Brunelli, and P. G. Radaelli. *Structural phase transition and magnetism in hexagonal $SrMnO_3$ by magnetization measurements and by electron, x-ray, and neutron diffraction studies*. *Phys. Rev. B* **75** (2007)(10): 104417. 135, 148, 150

[de Boer *et al.* (1984)] D. K. G. de Boer, C. Haas, and G. A. Sawatzky. *Auger spectra of compounds of Sc, Ti and Cr*. *J. Phys. F* **14** (1984): 2769. 122

[de' Medici *et al.* (2011)] L. de' Medici, J. Mravlje, and A. Georges. *Janus-Faced Influence of Hund's Rule Coupling in Strongly Correlated Materials*. *Phys. Rev. Lett.* **107** (2011): 256401. 6, 35, 136, 148, 183

[Dederichs *et al.* (1984)] P. H. Dederichs, S. Blügel, R. Zeller, and H. Akai. *Ground States of Constrained Systems: Application to Cerium Impurities*. *Phys. Rev. Lett.* **53** (1984)(26): 2512. 63

[Demourgues *et al.* (2001a)] A. Demourgues, A. Tressaud, H. Laronze, P. Gravereau, and P. Macaudière. *Preparation and structural properties of new series of mixed-anion compounds: rare earth fluorosulfides*. *J. Alloys Comp.* **107** (2001a): 215. 178, 180

[Demourgues *et al.* (2001b)] A. Demourgues, A. Tressaud, H. Laronze, and P. Macaudière. *Rare earth fluorosulfides LnSF and $Ln_2AF_4S_2$ as new colour pigments*. *J. Alloys Comp.* **323-324** (2001b): 223. 177, 179

[Dieke(1968)] G. H. Dieke. *Spectra and Energy Levels of Rare Earth Ions in Crystals*. Wiley Interscience, New York (1968). 183

[Eguchi *et al.* (2006)] R. Eguchi, T. Kiss, S. Tsuda, T. Shimojima, T. Mizokami, T. Yokoya, A. Chainani, S. Shin, I. H. Inoue, T. Togashi, S. Watanabe, C. Q. Zhang, C. T. Chen, M. Arita, K. Shimada, H. Namatame, and M. Taniguchi. *Bulk- and Surface-Sensitive High-Resolution Photoemission Study of Two Mott-Hubbard Systems:* $SrVO3$ *and* $CaVO3$. *Phys. Rev. Lett.* **96** (2006)(7): 076402. 132

[Foulkes *et al.* (2001)] W. M. C. Foulkes, L. Mitas, R. J. Needs, and G. Rajagopal. *Quantum Monte Carlo simulations of solids*. *Rev. Mod. Phys.* **73** (2001)(1): 33. 21

[Franchini *et al.* (2011)] C. Franchini, T. Archer, J. He, X.-Q. Chen, A. Filippetti, and S. Sanvito. *Exceptionally strong magnetism in the 4d perovskites* $RTcO_3$ *(*$R = \mathrm{Ca}$*, Sr, Ba)*. *Phys. Rev. B* **83** (2011): 220402. 136

[Fujimori *et al.* (1992)] A. Fujimori, I. Hase, H. Namatame, Y. Fujishima, Y. Tokura, H. Eisaki, S. Uchida, K. Takegahara, and F. M. F. de Groot. *Evolution of the spectral function in Mott-Hubbard systems with* d^1 *configuration*. *Phys. Rev. Lett.* **69** (1992)(12): 1796. 133

[Georges(2004)] A. Georges. *Strongly Correlated Electron Materials : Dynamical Mean Field Theory and electronic structure. Lectures on the physics of highly correlated electron systems VI* **715** (2004): 3. 6, 29, 31, 37

[Georges *et al.* (2004)] A. Georges, S. Florens, and T. A. Costi. *A brief review of recent advances on the Mott transition: unconventional transport, spectral weight transfers, and critical behaviour*. *Journal de Physique IV* **114** (2004): 165. 167

[Georges and Kotliar(1992)] A. Georges and G. Kotliar. *Hubbard model in infinite dimensions*. *Phys. Rev. B* **45** (1992)(12): 6479. 29, 32

[Georges *et al.* (1996)] A. Georges, G. Kotliar, W. Krauth, and M. J. Rozenberg. *Dynamical mean-field theory of strongly correlated fermion systems and the limit of infinite dimensions*. *Rev. Mod. Phys.* **68** (1996)(1): 13. 28, 29, 30, 32, 47

[Georges and Krauth(1992)] A. Georges and W. Krauth. *Numerical solution of the* $d = \infty$ *Hubbard model: Evidence for a Mott transition*. *Phys. Rev. Lett.* **69** (1992)(8): 1240. 32

[Golubkov *et al.* (1995)] A. V. Golubkov, A. V. Prokofiev, and A. I. Shelykh. *Optical characteristics of* Ce_2O_3 *single crystals*. *Phys. Solid State* **37** (1995): 1028. 177

[Gomez-Abal *et al.* (2008)] R. I. Gomez-Abal, X. Li, M. Scheffler, and C. Ambrosch-Draxl. *Influence of the Core-Valence Interaction and of the Pseudopotential Approximation on the Electron Self-Energy in Semiconductors*. *Phys. Rev. Lett.* **101** (2008): 106404. 25, 69, 78

[Goubin *et al.* (2004)] F. Goubin, X. Rocquefelte, D. Pauwels, A. Tressaud, A. Demourgues, S. Jobic, and Y. Montardi. *The dielectric function of LnSF rare-earth fluorosulfides (Ln=La,Ce): experiment and theory*. *J. Solid State Chem.* **177** (2004): 2833. 180, 185

[Gull(2008)] E. Gull. *Continuous-Time Quantum Monte-Carlo Algorithms for Fermions*. Ph.D. thesis, ETH Zurich (2008). 32

[Gunnarsson(1990)] O. Gunnarsson. *Calculation of parameters in model Hamiltonians*. *Phys. Rev. B* **41** (1990)(1): 514. 63, 101

[Gunnarsson *et al.* (1989)] O. Gunnarsson, O. K. Andersen, O. Jepsen, and J. Zaanen. *Density-functional calculation of the parameters in the Anderson model: Application to Mn in CdTe*. *Phys. Rev. B* **39** (1989)(3): 1708. 63, 64

[Gutzwiller(1963)] M. C. Gutzwiller. *Effect of Correlation on the Ferromagnetism of Transition Metals*. *Phys. Rev. Lett.* **10** (1963)(5): 159. 6, 45

[Hannerz *et al.* (1999)] H. Hannerz, G. Svensson, S. Y. Istomin, and O. G. D'yachenko. *Transmission Electron Microscopy and Neutron Powder Diffraction Studies of GdFeO3 Type SrNbO3*. *Journal of Solid State Chemistry* **147** (1999)(2): 421. 136

[Hansmann *et al.* (2010)] P. Hansmann, R. Arita, A. Toschi, S. Sakai, G. Sangiovanni, and K. Held. *Dichotomy between Large Local and Small Ordered Magnetic Moments in Iron-Based Superconductors*. *Phys. Rev. Lett.* **104** (2010): 197002. 6

[Haule and Kotliar(2009)] K. Haule and G. Kotliar. *Coherence and incoherence crossover in the normal state of iron oxypnictides and importance of Hund's rule coupling*. *New Journal Of Physics* **11** (2009): 025021. 6, 110, 116

[Haule *et al.* (2008)] K. Haule, J. H. Shim, and G. Kotliar. *Correlated Electronic Structure of* $\mathrm{LaO}_{1-x}\mathrm{F}_x\mathrm{FeAs}$. *Phys. Rev. Lett.* **100** (2008): 226402. 110

[Haule *et al.* (2010)] K. Haule, C.-H. Yee, and K. Kim. *Dynamical mean-field theory within the full-potential methods: Electronic structure of* $CeIrIn_5$, $CeCoIn_5$, *and* $CeRhIn_5$. *Phys. Rev. B* **81** (2010): 195107. 41

[Haverkort(2005)] M. W. Haverkort. *Spin and orbital degrees of freedom in transition metal oxides and oxide thin films studied by soft x-ray absorption spectroscopy*. Ph.D. thesis, Universität Köln (2005). 62, 82, 153

[Haverkort *et al.* (2008)] M. W. Haverkort, I. S. Elfimov, L. H. Tjeng, G. A. Sawatzky, and A. Damascelli. *Strong Spin-Orbit Coupling Effects on the Fermi Surface of* Sr_2RuO_4 *and* Sr_2RhO_4. *Phys. Rev. Lett.* **101** (2008)(2): 026406. 152, 163

[Hedin(1965)] L. Hedin. *New Method for Calculating the One-Particle Green's Function with Application to the Electron-Gas Problem*. *Phys. Rev.* **139** (1965)(3A): A796. 24, 25

[Hee Lee and Rabe(2010)] J. Hee Lee and K. M. Rabe. *Epitaxial-Strain-Induced Multiferroicity in SrMnO3 from First Principles*. *Phys. Rev. Lett.* **104** (2010): 207204. 56

[Held(2007)] K. Held. *Electronic structure calculations using dynamical mean-field theory*. *Advances in Physics* **56** (2007): 829. 40

[Herring(1966)] C. Herring. *Magnetism*. G. T. Rado and H. Suhl, Academic, New York (1966). 122

[Hewson(1993)] A. C. Hewson. *The Kondo Problem to Heavy Fermions*. Cambridge University Press (1993). 30, 31

[Hirsch(1983)] J. E. Hirsch. *Discrete Hubbard-Stratonovich transformation for fermion lattice models*. *Phys. Rev. B* **28** (1983)(7): 4059. 32

[Hirsch and Fye(1986)] J. E. Hirsch and R. M. Fye. *Monte Carlo Method for Magnetic Impurities in Metals*. *Phys. Rev. Lett.* **56** (1986)(23): 2521. 32

[Hohenberg and Kohn(1964)] P. Hohenberg and W. Kohn. *Inhomogeneous Electron Gas*. *Phys. Rev.* **136** (1964)(3B): B864. 15

[Hsu *et al.* (2008)] F.-C. Hsu, J.-Y. Luo, K.-W. Yeh, T.-K. Chen, T.-W. Huang, P. M. Wu, Y.-C. Lee, Y.-L. Huang, Y.-Y. Chu, D.-C. Yan, and M.-K. Wu. *Superconductivity in the PbO-type structure α-FeSe*. *Proc. Natl. Acad. Sci. U.S.A.* **105** (2008): 14262. 110

[Huang *et al.* (1994)] Q. Huang, J. L. Soubeyroux, O. Chmaissem, I. Natali Sora, A. Santoro, R. J. Cava, J. J. Krajewski, and W. F. Peck. *Neutron Powder Diffraction Study of the Crystal Structures of Sr_2RuO_4 and Sr_2IrO_4 at Room Temperature and at* $10K$. *Journal of Solid State Chemistry* **112** (1994)(2): 355. 152, 165

[Hubbard(1963)] J. Hubbard. *Electron Correlations in Narrow Energy Bands*. *Proc. R. Soc. London A* **276** (1963)(1): 238. 6, 45

[Hüfner(1994)] S. Hüfner. *Electronic structure of NiO and related 3d-transition-metal compounds*. *Advances in Physics* **43** (1994): 183. 46

[Hüfner and Wertheim(1973)] S. Hüfner and G. K. Wertheim. *Estimates of the Coulomb Correlation Energy from X-Ray Photoemission Data*. *Phys. Rev. B* **7** (1973): 5086. 122

[Hussey *et al.* (1998)] N. E. Hussey, A. P. Mackenzie, J. R. Cooper, Y. Maeno, S. Nishizaki, and T. Fujita. *Normal-state magnetoresistance of* $\mathrm{Sr_2RuO_4}$. *Phys. Rev. B* **57** (1998): 5505. 152

[Hybertsen *et al.* (1989)] M. S. Hybertsen, M. Schlüter, and N. E. Christensen. *Calculation of Coulomb-interaction parameters for La_2CuO_4 using a constrained-density-functional approach*. *Phys. Rev. B* **39** (1989)(13): 9028. 63

[Şaşıoğlu *et al.* (2011)] E. Şaşıoğlu, C. Friedrich, and S. Blügel. *Effective Coulomb interaction in transition metals from constrained random-phase approximation*. *Phys. Rev. B* **83** (2011)(12): 121101. 55, 60, 89, 119, 122, 123, 126, 127, 129

[Ikeda *et al.* (2000)] S.-I. Ikeda, N. Shirakawa, H. Bando, and O. Y. *Orbital-Degenerate Paramagnetic Metal Sr_2MoO_4: An Electronic Analogue to Sr_2RuO_4*. *J. Phys. Soc. Jpn.* **69** (2000): 3162. 151

[Imada *et al.* (1998)] M. Imada, A. Fujimori, and Y. Tokura. *Metal-insulator transitions*. *Rev. Mod. Phys.* **70** (1998)(4): 1039. 5, 21, 32, 35, 132, 143, 151, 165

[Imada and Miyake(2010)] M. Imada and T. Miyake. *Electronic Structure Calculation by First Principles for Strongly Correlated Electron Systems*. *J. Phys. Soc. Jpn.* **79** (2010): 112001. 21, 133

[Isawa *et al.* (1993)] K. Isawa, J. Sugiyama, K. Matsuura, A. Nozaki, and H. Yamauchi. *Synthesis and transport properties of Sr_xNbO_3 ($0.75 \leq x \leq 0.90$)*. *Phys. Rev. B* **47** (1993)(5): 2849. 136

[Ishida *et al.* (2009)] K. Ishida, Y. Nakai, and H. Hosono. *To What Extent Iron-Pnictide New Superconductors Have Been Clarified: A Progress Report*. *J. Phys. Soc. Jpn.* **78** (2009): 062001. 110

[Jansen and Letschert(2000)] M. Jansen and H. P. Letschert. *Inorganic yellow-red pigments without toxic metals*. *Nature* **404** (2000): 980. 177

[Jiang *et al.* (2012)] H. Jiang, R. Gómez-Abal, X. Li, C. Meisenbichler, C. Ambrosch-Draxl, and M. Sheffler. *FHI-gap: A GW Code Based on Augmented Planewaves*. *(to be published)* (2012). 25, 69, 70, 71, 76, 221, 227

[Jiang *et al.* (2009)] H. Jiang, R. I. Gomez-Abal, P. Rinke, and M. Scheffler. *Localized and Itinerant States in Lanthanide Oxides United by GW@LDA+U*. *Phys. Rev. Lett.* **102** (2009)(12): 126403. 25, 69, 78, 177, 183

[Jones and Gunnarsson(1989)] R. O. Jones and O. Gunnarsson. *The density functional formalism, its applications and prospects*. *Rev. Mod. Phys.* **61** (1989)(3): 689. 15

[Kamihara *et al.* (2008)] Y. Kamihara, T. Watanabe, M. Hirano, and H. Hosono. *Iron-Based Layered Superconductor La[$O_{1-x}F_x$]FeAs ($x = 0.05 - 0.12$) with Tc = 26 K*. *J. Am. Chem. Soc.* **130** (2008): 3296. 110

[Kanamori(1963)] J. Kanamori. *Electron Correlation and Ferromagnetism of Transition Metals*. *Prog. Theor. Phys.* **30** (1963): 275. 6, 45

[Kang *et al.* (2008)] J.-S. Kang, H. J. Lee, G. Kim, D. H. Kim, B. Dabrowski, S. Kolesnik, H. Lee, J.-Y. Kim, and B. I. Min. *Electronic structure of the cubic perovskite $SrMn_{1-x}Fe_xO_3$ investigated by x-ray spectroscopies*. *Phys. Rev. B* **78** (2008)(5): 054434. 135, 148, 149

[Karlsson *et al.* (2010)] K. Karlsson, F. Aryasetiawan, and O. Jepsen. *Method for calculating the electronic structure of correlated materials from a truly first-principles LDA+U scheme*. *Phys. Rev. B* **81** (2010)(24): 245113. 56, 59

[Karolak *et al.* (2010)] M. Karolak, G. Ulm, T. Wehling, V. Mazurenko, A. Poteryaev, and A. Lichtenstein. *Double counting in LDA+DMFT - The example of NiO*. *Journal of Electron Spectroscopy and Related Phenomena : Proceedings of International Workshop on Strong Correlations and Angle-Resolved Photoemission Spectroscopy 2009* **181** (2010): 11. 40

[Kim *et al.* (2008)] B. J. Kim, H. Jin, S. J. Moon, J.-Y. Kim, B.-G. Park, C. S. Leem, J. Yu, T. W. Noh, C. Kim, S.-J. Oh, J.-H. Park, V. Durairaj, G. Cao, and E. Rotenberg. *Novel Jeff=1/2 Mott State Induced by Relativistic Spin-Orbit Coupling in Sr_2IrO_4*. *Phys. Rev. Lett.* **101** (2008)(7): 076402. 163, 173, 174

[Kim *et al.* (2009)] B. J. Kim, H. Ohsumi, T. Komesu, S. Sakai, H. Morita, T. andTakagi, and T. Arima. *Phase-Sensitive Observation of a Spin-Orbital Mott State in Sr_2IrO_4*. *Science* **323** (2009)(6): 1329. 163

[Klein and Terasaki(2008)] Y. Klein and I. Terasaki. *Insight on the electronic state of Sr_2IrO_4 revealed by cationic substitutions*. *Journal of Physics: Condensed Matter* **20** (2008)(29): 295201. 164

[Kohn(1999)] W. Kohn. *Nobel Lecture: Electronic structure of matter—wave functions and density functionals*. *Rev. Mod. Phys.* **71** (1999)(5): 1253. 15

[Kohn and Sham(1965)] W. Kohn and L. J. Sham. *Self-Consistent Equations Including Exchange and Correlation Effects*. *Phys. Rev.* **140** (1965)(4A): A1133. 10, 15, 16

[Kotani(2000)] T. Kotani. *Ab initio random-phase-approximation calculation of the frequency-dependent effective interaction between 3d electrons: Ni, Fe, and MnO*. *J. Phys. Condens. Matter* **12** (2000)(7): 2413. 55

[Kotani and van Schilfgaarde(2002)] T. Kotani and M. van Schilfgaarde. *All-electron GW approximation with the mixed basis expansion based on the full-potential LMTO method*. *Solid State Commun.* **121** (2002): 461. 70

[Kotliar *et al.* (2006)] G. Kotliar, S. Y. Savrasov, K. Haule, V. S. Oudovenko, O. Parcollet, and C. A. Marianetti. *Electronic structure calculations with dynamical mean-field theory*. *Rev. Mod. Phys.* **78** (2006)(3): 865. 29, 30, 36, 37, 41

[Kotliar *et al.* (2001)] G. Kotliar, S. Y. Savrasov, G. Pálsson, and G. Biroli. *Cellular Dynamical Mean Field Approach to Strongly Correlated Systems*. *Phys. Rev. Lett.* **87** (2001)(18): 186401. 30

[Kotliar and Vollhardt(2004)] G. Kotliar and D. Vollhardt. *Strongly Correlated Materials: Insights From Dynamical Mean-Field Theory*. *Physics Today* **57** (2004): 53. 29, 32

[Kozik *et al.* (2011)] E. Kozik, K. Van Houcke, E. Gull, L. Pollet, N. Prokof'ev, B. Svistunov, and M. Troyer. *Diagrammatic Monte Carlo for correlated fermions*. *Eur. Phys. Lett.* **90** (2011)(1): 10004. 57, 191

[Kutepov *et al.* (2010)] A. Kutepov, K. Haule, S. Y. Savrasov, and G. Kotliar. *Self-consistent GW determination of the interaction strength: Application to the iron arsenide superconductors*. *Phys. Rev. B* **82** (2010)(4): 045105. 57, 83, 216

[Lechermann *et al.* (2006)] F. Lechermann, A. Georges, A. Poteryaev, S. Biermann, M. Posternak, A. Yamasaki, and O. K. Andersen. *Dynamical mean-field theory using Wannier functions: A flexible route to electronic structure calculations of strongly correlated materials*. *Phys. Rev. B* **74** (2006)(12): 125120. 37, 38, 55, 56, 104, 123, 133

[Lee and Pickett(2009)] K.-W. Lee and W. E. Pickett. *Orbital-ordering driven structural distortion in metallic* $SrCrO3$. *Phys. Rev. B* **80** (2009)(12): 125133. 135

[Lee *et al.* (2003)] Y. S. Lee, J. S. Lee, T. W. Noh, D. Y. Byun, K. S. Yoo, K. Yamaura, and E. Takayama-Muromachi. *Systematic trends in the electronic structure parameters of the* $4d$ *transition-metal oxides* $SrMO3(M = Zr$, *Mo, Ru, and Rh)*. *Phys. Rev. B* **67** (2003)(11): 113101. 143, 165

[Levy(1982)] M. Levy. *Electron densities in search of Hamiltonians*. *Phys. Rev. A* **26** (1982)(3): 1200. 15

[Li(2008)] X. Li. *All-electron G0W0 code based on FP-(L)APW+lo and applications*. Ph.D. thesis, Fritz-Haber-Institut, Max-Planck-Gesellschaft (2008). 70, 78, 221, 227

[Lichtenstein *et al.* (1995)] A. I. Lichtenstein, V. I. Anisimov, and J. Zaanen. *Density-functional theory and strong interactions: Orbital ordering in Mott-Hubbard insulators*. *Phys. Rev. B* **52** (1995)(8): R5467. 35, 66

[Lichtenstein and Katsnelson(1998)] A. I. Lichtenstein and M. I. Katsnelson. *Ab initio calculations of quasiparticle band structure in correlated systems: LDA++ approach*. *Phys. Rev. B* **57** (1998)(12): 6884. 28, 35, 36, 41

[Lichtenstein *et al.* (2001)] A. I. Lichtenstein, M. I. Katsnelson, and G. Kotliar. *Finite-Temperature Magnetism of Transition Metals: An ab initio Dynamical Mean-Field Theory*. *Phys. Rev. Lett.* **87** (2001): 067205. 121, 124, 129

[Lieb(1983)] E. H. Lieb. *Density functionals for Coulomb systems*. *Int. J. Quantum Chem.* **24** (1983): 243. 15

[Liebsch and Lichtenstein(2000)] A. Liebsch and A. Lichtenstein. *Photoemission Quasiparticle Spectra of* Sr_2RuO_4. *Phys. Rev. Lett.* **84** (2000): 1591. 152

[Liu *et al.* (2008)] G.-Q. Liu, V. N. Antonov, O. Jepsen, and O. K. Andersen. *Coulomb-Enhanced Spin-Orbit Splitting: The Missing Piece in the Sr_2RhO_4 Puzzle*. *Phys. Rev. Lett.* **101** (2008)(2): 026408. 152, 163

[Macaudière and Demourgues(2002)] P. Macaudière and A. Demourgues. *La couleur dans les solides minéraux*. *L'actualité chimique* **251** (2002): 91. 177

[Mackenzie and Maeno(2003)] A. P. Mackenzie and Y. Maeno. *The superconductivity of Sr_2RuO_4 and the physics of spin-triplet pairing*. *Rev. Mod. Phys.* **75** (2003)(2): 657. 151, 152

[Madsen and Novák(2005)] G. K. H. Madsen and P. Novák. *Charge order in magnetite. An LDA+U study*. *Eur. Phys. Lett.* **69** (2005): 777. 63

[Maestro and Huguenin(1995)] P. Maestro and D. Huguenin. *Industrial applications of rare earths: which way for the end of the century*. *J. Alloys Comp.* **225** (1995): 520. 177

[Mahan(1990)] G. D. Mahan. *Many-Particle Physics*. Plenum Press, New York and London (1990). 12, 40, 51

[Marini *et al.* (2001)] A. Marini, G. Onida, and R. Del Sole. *Quasiparticle Electronic Structure of Copper in the GW Approximation*. *Phys. Rev. Lett.* **88** (2001): 016403. 126

[Martin(2004)] R. M. Martin. *Electronic Structure : Basic Theory and Practical Methods*. Cambridge University Press (2004). 15, 16, 22, 23

[Martins(2010)] C. Martins. *Interplay of Spin-Orbit Coupling and Electronic Coulomb Interactions in Strontium Iridate Sr_2IrO_4*. Ph.D. thesis, Ecole Polytechnique, France (2010). 165, 207

[Martins *et al.* (2011)] C. Martins, M. Aichhorn, L. Vaugier, and S. Biermann. *Reduced Effective Spin-Orbital Degeneracy and Spin-Orbital Ordering in Paramagnetic Transition-Metal Oxides: Sr_2IrO_4 versus Sr_2RhO_4*. *Phys. Rev. Lett.* **107** (2011): 266404. v, xi, 55, 56, 153, 160, 163, 164, 167, 168, 172, 190

[Marzari and Vanderbilt(1997)] N. Marzari and D. Vanderbilt. *Maximally localized generalized Wannier functions for composite energy bands*. *Phys. Rev. B* **56** (1997)(20): 12847. 37

[Massidda *et al.* (1993)] S. Massidda, M. Posternak, and A. Baldereschi. *Hartree-Fock LAPW approach to the electronic properties of periodic systems*. *Phys. Rev. B* **48** (1993): 5058. 227

[McMahan *et al.* (1988)] A. K. McMahan, R. M. Martin, and S. Satpathy. *Calculated effective Hamiltonian for La_2CuO_4 and solution in the impurity Anderson approximation*. *Phys. Rev. B* **38** (1988)(10): 6650. 63, 65

[Metzner and Vollhardt(1989)] W. Metzner and D. Vollhardt. *Correlated Lattice Fermions in $d = \infty$ Dimensions*. *Phys. Rev. Lett.* **62** (1989)(3): 324. 29

[Middey *et al.* (2011)] S. Middey, A. Kumar Nandy, P. Mahadevan, and D. D. Sarma. *Mechanism for the high Neel temperature in $SrTcO_3$*. *arXiv* **1112.5587v1** (2011). 136

[Minár *et al.* (2005)] J. Minár, L. Chioncel, A. Perlov, H. Ebert, M. I. Katsnelson, and A. I. Lichtenstein. *Multiple-scattering formalism for correlated systems: A KKR-DMFT approach*. *Phys. Rev. B* **72** (2005)(4): 045125. 41

[Miyake and Aryasetiawan(2008)] T. Miyake and F. Aryasetiawan. *Screened Coulomb interaction in the maximally localized Wannier basis*. *Phys. Rev. B* **77** (2008)(8): 085122. 55, 103, 104, 107

[Miyake *et al.* (2009)] T. Miyake, F. Aryasetiawan, and M. Imada. *Ab initio procedure for constructing effective models of correlated materials with entangled band structure*. *Phys. Rev. B* **80** (2009)(15): 155134. 55, 60, 89, 119, 122, 126, 129

[Miyake *et al.* (2010)] T. Miyake, K. Nakamura, R. Arita, and M. Imada. *Comparison of Ab initio Low-Energy Models for LaFePO, LaFeAsO, BaFe2As2, LiFeAs, FeSe and FeTe: Electron Correlation and Covalency*. *J. Phys. Soc. Jpn.* **79** (2010): 044705. 55, 57, 60, 110, 111, 112, 115

[Miyake *et al.* (2008)] T. Miyake, L. Pourovskii, V. Vildosola, S. Biermann, and A. Georges. *d- and f-Orbital Correlations in the REFeAsO Compounds*. *J. Phys. Soc. Jpn. : Supplement C* **77** (2008): 99. 54, 103, 110

[Mizokawa and Fujimori(1996)] T. Mizokawa and A. Fujimori. *Electronic structure and orbital ordering in perovskite-type 3d transition-metal oxides studied by Hartree-Fock bandstructure calculations*. *Phys. Rev. B* **54** (1996)(8): 5368. 63

[Moon *et al.* (2009)] S. J. Moon, H. Jin, W. S. Choi, J. S. Lee, S. S. A. Seo, J. Yu, G. Cao, T. W. Noh, and Y. S. Lee. *Temperature dependence of the electronic structure of the Jeff = 1/2 Mott insulator Sr_2IrO_4 studied by optical spectroscopy*. *Phys. Rev. B* **80** (2009)(19): 195110. 163, 174

[Moon *et al.* (2006)] S. J. Moon, M. W. Kim, K. W. Kim, Y. S. Lee, J.-Y. Kim, J.-H. Park, B. J. Kim, S.-J. Oh, S. Nakatsuji, Y. Maeno, I. Nagai, S. I. Ikeda, G. Cao, and T. W. Noh. *Electronic structures of layered perovskite Sr_2MO_4 (M=Ru, Rh, and Ir)*. *Phys. Rev. B* **74** (2006): 113104. 152, 163

[Morikawa *et al.* (1995)] K. Morikawa, T. Mizokawa, K. Kobayashi, A. Fujimori, H. Eisaki, S. Uchida, F. Iga, and Y. Nishihara. *Spectral weight transfer and mass renormalization in Mott-Hubbard systems $SrVO_3$ and $CaVO_3$: Influence of long-range Coulomb interaction*. *Phys. Rev. B* **52** (1995)(19): 13711. 133

[Mossanek *et al.* (2009)] R. J. O. Mossanek, M. Abbate, P. T. Fonseca, A. Fujimori, H. Eisaki, S. Uchida, and Y. Tokura. *Optical conductivity and x-ray absorption spectra of the Mott-Hubbard compounds RVO_3 (R = Sr, Ca, La, and Y).* *Phys. Rev. B* **80** (2009): 195107. 132

[Mravlje *et al.* (2012)] J. Mravlje, M. Aichhorn, and A. Georges. *Origin of the High Néel Temperature in* $\mathrm{SrTcO_3}$. *Phys. Rev. Lett.* **108** (2012): 197202. 56, 135, 136

[Mravlje *et al.* (2011)] J. Mravlje, M. Aichhorn, T. Miyake, K. Haule, G. Kotliar, and A. Georges. *Coherence-Incoherence Crossover and the Mass-Renormalization Puzzles in Sr_2RuO_4.* *Phys. Rev. Lett.* **106** (2011)(9): 096401. 41, 55, 56, 136, 152

[Müller-Hartmann(1989)] E. Müller-Hartmann. *The Hubbard model at high dimensions : some exact results and weak coupling theory.* *Zeitschrift für Physik B Condensed Matter* **76** (1989)(2): 211. 29, 34

[Nagai *et al.* (2005)] I. Nagai, N. Shirakawa, S. Ikeda, I. R., H. Nishimura, and M. Kosaka. *Highest conductivity oxide SrMoO3 grown by a floating-zone method under ultralow oxygen partial pressure.* *Appl. Phys. Lett.* **87** (2005): 024105. 136

[Nakamura *et al.* (2008)] K. Nakamura, R. Arita, and M. Imada. *Ab initio Derivation of Low-Energy Model for Iron-Based Superconductors LaFeAsO and LaFePO.* *J. Phys. Soc. Jpn.* **77** (2008): 093711. 110

[Nakamura *et al.* (2006)] K. Nakamura, R. Arita, Y. Yoshimoto, and S. Tsuneyuki. *First-principles calculation of effective onsite Coulomb interactions of* $3d$ *transition metals: Constrained local density functional approach with maximally localized Wannier functions.* *Phys. Rev. B* **74** (2006)(23): 235113. 64, 65, 122, 127

[Norman(1995)] M. R. Norman. *Calculation of effective Coulomb interaction for* Pr^{3+}, U^{4+}, *and* $\mathrm{UPt_3}$. *Phys. Rev. B* **52** (1995): 1421. 13

[Ortega-San-Martin *et al.* (2007)] L. Ortega-San-Martin, A. J. Williams, J. Rodgers, J. P. Attfield, G. Heymann, and H. Huppertz. *Microstrain Sensitivity of Orbital and Electronic Phase Separation in* $\mathrm{SrCrO_3}$. *Phys. Rev. Lett.* **99** (2007): 255701. 135

[Parcollet *et al.* (2004)] O. Parcollet, G. Biroli, and G. Kotliar. *Cluster Dynamical Mean Field Analysis of the Mott Transition.* *Phys. Rev. Lett.* **92** (2004)(22): 226402. 30

[Pauwels(2003)] D. Pauwels. *Cristallochimie des composés de terres rares à anions mixtes : propriétés d'absorption UV−visible.* Ph.D. thesis, Université Bordeaux I (2003). 177, 178, 179, 180, 185

[Pavarini *et al.* (2005)] E. Pavarini, A. Yamasaki, J. Nuss, and O. K. Andersen. *How chemistry controls electron localization in $3d^1$ perovskites: a Wannier-function study.* *New Journal Of Physics* **7** (2005): 188. 131

[Pchelkina *et al.* (2007)] Z. V. Pchelkina, I. A. Nekrasov, T. Pruschke, A. Sekiyama, S. Suga, V. I. Anisimov, and D. Vollhardt. *Evidence for strong electronic correlations in the spectra of* Sr_2RuO_4. *Phys. Rev. B* **75** (2007): 035122. 152

[Perdew *et al.* (1982)] J. P. Perdew, R. G. Parr, M. Levy, and J. L. Balduz. *Density-Functional Theory for Fractional Particle Number: Derivative Discontinuities of the Energy*. *Phys. Rev. Lett.* **49** (1982)(23): 1691. 66

[Perfetti *et al.* (2003)] L. Perfetti, A. Georges, S. Florens, S. Biermann, S. Mitrovic, H. Berger, Y. Tomm, H. Höchst, and M. Grioni. *Spectroscopic Signatures of a Bandwidth-Controlled Mott Transition at the Surface of 1T-$TaSe_2$*. *Phys. Rev. Lett.* **90** (2003): 166401. 167

[Pickett *et al.* (1998)] W. E. Pickett, S. C. Erwin, and E. C. Ethridge. *Reformulation of the LDA+U method for a local-orbital basis*. *Phys. Rev. B* **58** (1998)(3): 1201. 36, 65

[Pines and Nozière(1965)] D. Pines and P. Nozière. *Theory of Quantum Liquids*. Oxford University Press (1965). 34

[Poteryaev *et al.* (2008)] A. I. Poteryaev, M. Ferrero, A. Georges, and O. Parcollet. *Effect of crystal-field splitting and interband hybridization on the metal-insulator transitions of strongly correlated systems*. *Phys. Rev. B* **78** (2008)(4): 045115. 35

[Pourovskii *et al.* (2007)] L. V. Pourovskii, B. Amadon, S. Biermann, and A. Georges. *Self-consistency over the charge density in dynamical mean-field theory: A linear muffin-tin implementation and some physical implications*. *Phys. Rev. B* **76** (2007)(23): 235101. 41, 177

[Prokofiev *et al.* (1996)] A. V. Prokofiev, A. I. Shelykh, and B. T. Melekh. *Periodicity in the band gap variation of Ln_2X_3 (X = O, S, Se) in the lanthanide series*. *J. Alloys Comp.* **242** (1996): 41. 177

[Pruschke *et al.* (1995)] T. Pruschke, M. Jarrell, and J. K. Freericks. *Anomalous normal-state properties of high-Tc superconductors: Intrinsic properties of strongly correlated electron systems?*. *Advances in Physics* **44** (1995): 187. 32

[Qazilbash *et al.* (2009)] M. M. Qazilbash, J. J. Hamlin, R. E. Baumbach, L. Zhang, D. J. Singh, M. B. Maple, and D. N. Basov. *Electronic correlations in the iron pnictides*. *Nature Physics* **5** (2009): 647. 110

[Qian *et al.* (2011)] Y. Qian, G. Wang, Z. Li, C. Jin, and Z. Fang. *The electronic structure of a weakly correlated antiferromagnetic metal, SrCrO3: first-principles calculations*. *New Journal of Physics* **13** (2011): 053002. 135

[Ren *et al.* (2008)] Z.-A. Ren, L. Wei, Y. Jie, Y. Wei, S. Xiao-Li, Zheng-Cai, C. Guang-Can, D. Xiao-Li, S. Li-Ling, Z. Fang, and Z. Zhong-Xian. *Superconductivity at 55 K in Iron-Based F-Doped Layered Quaternary Compound Sm[$O_{1-x}F_x$]FeAs*. *Chin. Phys. Lett.* **25** (2008): 2215. 110

[Rodriguez *et al.* (2011)] E. E. Rodriguez, F. Poineau, A. Llobet, B. J. Kennedy, M. Avdeev, G. J. Thorogood, M. L. Carter, R. Seshadri, D. J. Singh, and A. K. Cheetham. *High Temperature Magnetic Ordering in the* $4d$ *Perovskite* $SrTcO3$. *Phys. Rev. Lett.* **106** (2011)(6): 067201. 136

[Rotter *et al.* (2008)] M. Rotter, M. Tegel, and D. Johrendt. *Superconductivity at 38 K in the Iron Arsenide* $Ba_{1-x}K_xFe_2As_2$. *Phys. Rev. Lett.* **101** (2008): 107006. 110

[Rozenberg *et al.* (1994)] M. J. Rozenberg, G. Kotliar, and X. Y. Zhang. *Mott-Hubbard transition in infinite dimensions. II*. *Phys. Rev. B* **49** (1994): 10181. 32

[Rozenberg *et al.* (1992)] M. J. Rozenberg, X. Y. Zhang, and G. Kotliar. *Mott-Hubbard transition in infinite dimensions*. *Phys. Rev. Lett.* **69** (1992)(8): 1236. 32

[Rubtsov *et al.* (2005)] A. N. Rubtsov, V. V. Savkin, and A. I. Lichtenstein. *Continuous-time quantum Monte Carlo method for fermions*. *Phys. Rev. B* **72** (2005)(3): 035122. 32

[Saitoh *et al.* (1995)] T. Saitoh, A. E. Bocquet, T. Mizokawa, and A. Fujimori. *Systematic variation of the electronic structure of 3d transition-metal compounds*. *Phys. Rev. B* **52** (1995)(11): 7934. 63, 135, 147

[Savrasov and Kotliar(2004)] S. Y. Savrasov and G. Kotliar. *Spectral density functionals for electronic structure calculations*. *Phys. Rev. B* **69** (2004)(24): 245101. 41

[Savrasov *et al.* (2001)] S. Y. Savrasov, G. Kotliar, and E. Abrahams. *Correlated electrons in* δ*-plutonium within a dynamical mean-field picture*. *Nature* **410** (2001): 793. 41

[Sawatzky and Allen(1984)] G. A. Sawatzky and J. W. Allen. *Magnitude and Origin of the Band Gap in NiO*. *Phys. Rev. Lett.* **53** (1984): 2339. 46, 62, 105

[Sawatzky *et al.* (2009)] G. A. Sawatzky, I. S. Elfimov, J. van den Brink, and J. Zaanen. *Heavy-anion solvation of polarity fluctuations in pnictides*. *Eur. Phys. Lett.* **86** (2009): 17006. 116

[Schleid and Grossholz(2001)] T. Schleid and H. Grossholz. *Uber Fluoridsulfide (MFS) der Lanthanide (M = La-Nd,Sm,Gd-Lu) im A-Typ mit PbFCl-Struktur*. *Z. Anorg. Allg. Chem.* **627** (2001): 2693. 178

[Sefat *et al.* (2008)] A. S. Sefat, R. Jin, M. A. McGuire, B. C. Sales, D. J. Singh, and D. Mandrus. *Superconductivity at 22 K in Co-Doped* $\mathrm{BaFe_2As_2}$ *Crystals*. *Phys. Rev. Lett.* **101** (2008): 117004. 110

[Sekiyama *et al.* (2004)] A. Sekiyama, H. Fujiwara, S. Imada, S. Suga, H. Eisaki, S. I. Uchida, K. Takegahara, H. Harima, Y. Saitoh, I. A. Nekrasov, G. Keller, D. E. Kondakov, A. V. Kozhevnikov, T. Pruschke, K. Held, D. Vollhardt, and V. I. Anisimov. *Mutual Experimental and Theoretical Validation of Bulk Photoemission Spectra of* $Sr_{1-x}Ca_xVO_3$. *Phys. Rev. Lett.* **93** (2004)(15): 156402. 56, 101, 103, 132, 133

[Sharma *et al.* (2010)] S. Sharma, A. Bharathi, S. Chandra, V. R. Reddy, S. Paulraj, A. T. Satya, V. S. Sastry, A. Gupta, and C. S. Sundar. *Superconductivity in Ru-substituted polycrystalline $BaFe_{2-x}Ru_xAs_2$*. *Phys. Rev. B* **81** (2010): 174512. 110

[Singh(1991)] D. Singh. *Ground-state properties of lanthanum: Treatment of extended-core states*. *Phys. Rev. B* **43** (1991)(8): 6388. 21

[Singh(1994)] D. J. Singh. *Planewaves, Pseudopotentials and the LAPW Method*. Kluwer Academic Publishers, Norwell, Massachusetts, USA (1994). 19, 205, 206

[Sjöstedt *et al.* (2000)] E. Sjöstedt, L. Nordström, and D. J. Singh. *An alternative way of linearizing the augmented plane-wave method*. *Solid State Communications* **114** (2000): 15. 21, 206

[Slater(1953)] J. C. Slater. *An Augmented Plane Wave Method for the Periodic Potential Problem*. *Phys. Rev.* **92** (1953)(3): 603. 19

[Slater(1960)] —. *Quantum Theory of Atomic Structure*, vol. 1. McGraw-Hill, New York (1960). 81, 215

[Solovyev(2006)] I. V. Solovyev. *First-principles Wannier functions and effective lattice fermion models for narrow-band compounds*. *Phys. Rev. B* **73** (2006)(15): 155117. 102, 103

[Solovyev *et al.* (1994)] I. V. Solovyev, P. H. Dederichs, and V. I. Anisimov. *Corrected atomic limit in the local-density approximation and the electronic structure of d impurities in Rb*. *Phys. Rev. B* **50** (1994)(23): 16861. 65

[Solovyev and Imada(2005)] I. V. Solovyev and M. Imada. *Screening of Coulomb interactions in transition metals*. *Phys. Rev. B* **71** (2005)(4): 045103. 55

[Søndenå *et al.* (2006)] R. Søndenå, P. Ravindran, S. Stølen, T. Grande, and M. Hanfland. *Electronic structure and magnetic properties of cubic and hexagonal $SrMnO_3$*. *Phys. Rev. B* **74** (2006)(14): 144102. 135

[Sorella(2001)] S. Sorella. *Generalized Lanczos algorithm for variational quantum Monte Carlo*. *Phys. Rev. B* **64** (2001): 024512. 47

[Souza *et al.* (2001)] I. Souza, N. Marzari, and D. Vanderbilt. *Maximally localized Wannier functions for entangled energy bands*. *Phys. Rev. B* **65** (2001)(3): 035109. 37

[Springer and Aryasetiawan(1998)] M. Springer and F. Aryasetiawan. *Frequency-dependent screened interaction in Ni within the random-phase approximation*. *Phys. Rev. B* **57** (1998)(8): 4364. 55

[Stollhoff *et al.* (1990)] G. Stollhoff, A. M. Oleś, and V. Heine. *Stoner exchange interaction in transition metals*. *Phys. Rev. B* **41** (1990): 7028. 127

[Sugano *et al.* (1970)] S. Sugano, Y. Tanabe, and H. Kamimura. *Multiplets of transition-metal ions in crystal*, vol. 1. Academic Press, New York London (1970). 63, 81, 82, 86, 167, 209, 210

[Sun and Kotliar(2002)] P. Sun and G. Kotliar. *Extended dynamical mean-field theory and GW method*. *Phys. Rev. B* **66** (2002)(8): 085120. 25, 28, 58

[Svane and Gunnarsson(1990)] A. Svane and O. Gunnarsson. *Transition-metal oxides in the self-interaction-corrected density-functional formalism*. *Phys. Rev. Lett.* **65** (1990): 1148. 22, 27

[Tahara and Imada(2008)] D. Tahara and M. Imada. *Variational Monte Carlo Study of Electron Differentiation around Mott Transition*. *J. Phys. Soc. Jpn.* **77** (2008): 114701. 47

[Takeda and Ohara(1974)] T. Takeda and S. Ohara. *Magnetic Structure of the Cubic Perovskite Type SrMnO3*. *J. Phys. Soc. Jpn.* **37** (1974): 275. 135

[Tamai *et al.* (2008)] A. Tamai, M. P. Allan, J. F. Mercure, W. Meevasana, R. Dunkel, D. H. Lu, R. S. Perry, A. P. Mackenzie, D. J. Singh, Z.-X. Shen, and F. Baumberger. *Fermi Surface and van Hove Singularities in the Itinerant Metamagnet* $Sr_3Ru_2O_7$. *Phys. Rev. Lett.* **101** (2008)(2): 026407. 152

[Tamai *et al.* (2010)] A. Tamai, A. Y. Ganin, E. Rozbicki, J. Bacsa, W. Meevasana, P. D. C. King, M. Caffio, R. Schaub, S. Margadonna, K. Prassides, M. J. Rosseinsky, and F. Baumberger. *Strong Electron Correlations in the Normal State of the Iron-Based* $\mathrm{FeSe_{0.42}Te_{0.58}}$ *Superconductor Observed by Angle-Resolved Photoemission Spectroscopy*. *Phys. Rev. Lett.* **104** (2010): 097002. 115

[Tomczak(2007)] J. M. Tomczak. *Spectral and Optical Properties of Correlated Materials*. Ph.D. thesis, Ecole Polytechnique, France (2007). 177

[Tomczak *et al.* (2009)] J. M. Tomczak, T. Miyake, R. Sakuma, and F. Aryasetiawan. *Effective Coulomb interactions in solids under pressure*. *Phys. Rev. B* **79** (2009)(23): 235133. 55

[Tomczak *et al.* (2012)] J. M. Tomczak, L. V. Pourovskii, L. Vaugier, S. Biermann, and A. Georges. *Colors from First Principles: Heavy-Metal vs. Rare-Earth Pigments*. *(to be published)* (2012). v, xi, 163, 177, 183, 184, 185, 190

[Torrance *et al.* (1991)] J. Torrance, L. P., A. C., and R. Metzger. *Why are some oxides metallic, while most are insulating?*. *Physica C* **182** (1991): 351. 143

[Toschi *et al.* (2012)] A. Toschi, R. Arita, P. Hansmann, G. Sangiovanni, and K. Held. *Quantum dynamical screening of the local magnetic moment in Fe-based superconductors*. *arXiv* **1112.3002v1** (2012). 6

[van den Brink and Sawatzky(2000)] J. van den Brink and G. A. Sawatzky. *Non-conventional screening of the Coulomb interaction in low-dimensional and finite-size systems*. *Eur. Phys. Lett.* **50** (2000): 447. 158

[van der Marel(1985)] D. van der Marel. *The electronic structure of embedded transition metal atoms*. Ph.D. thesis, Rijksuniversiteit Groningen (1985). 46, 63, 105, 141

[van Schilfgaarde *et al.* (2006)] M. van Schilfgaarde, T. Kotani, and S. Faleev. *Quasiparticle Self-Consistent GW Theory*. *Phys. Rev. Lett.* **96** (2006)(22): 226402. 25, 27, 57

[Vaugier *et al.* (2012a)] L. Vaugier, H. Jiang, and S. Biermann. *How Good is the Slater Parametrization in Iron-based Pnictides and Chalcogenides?. (to be published)* (2012a). v, 81, 113, 117, 118

[Vaugier *et al.* (2012b)] —. *Hubbard U and Hund's Exchange J in Oxides : Screening vs. Localization Trends from Constrained Random Phase Approximation*. *arXiv* **1206.3533v1** (2012b). v, 81, 131, 159

[Vildosola *et al.* (2008)] V. Vildosola, L. Pourovskii, R. Arita, S. Biermann, and A. Georges. *Bandwidth and Fermi surface of iron oxypnictides: Covalency and sensitivity to structural changes*. *Phys. Rev. B* **78** (2008): 064518. 113

[Wannier(1937)] G. H. Wannier. *The Structure of Electronic Excitation Levels in Insulating Crystals*. *Phys. Rev.* **52** (1937): 191. 4

[Wen *et al.* (2008)] H.-H. Wen, G. Mu, L. Fang, H. Yang, and X. Zhu. *Superconductivity at 25 K in hole-doped ($La_{1-x}Sr_x$)OFeAs*. *Eur. Phys. Lett.* **82** (2008): 17009. 110

[Werner *et al.* (2012)] P. Werner, M. Casula, T. Miyake, F. Aryasetiawan, A. J. Millis, and S. Biermann. *Satellites and large doping- and temperature-dependence of electronic properties in hole-doped $BaFe_2As_2$*. *Nature Physics* **8** (2012): 331. 57, 61, 112, 113, 116, 147, 191

[Werner *et al.* (2006)] P. Werner, A. Comanac, L. de' Medici, M. Troyer, and A. J. Millis. *Continuous-Time Solver for Quantum Impurity Models*. *Phys. Rev. Lett.* **97** (2006)(7): 076405. 32

[Werner *et al.* (2008)] P. Werner, E. Gull, M. Troyer, and M. A. J. *Spin Freezing Transition and Non-Fermi-Liquid Self-Energy in a Three-Orbital Model*. *Phys. Rev. Lett.* **101** (2008): 166405. 6

[Yeh *et al.* (2008)] K.-W. Yeh, T.-W. Huang, Y.-l. Huang, T.-K. Chen, F. Hsu, P. M. Wu, Y. C. Lee, Y.-Y. Chu, C.-L. Chen, J.-Y. Luo, D.-C. Yan, and M.-K. Wu. *Tellurium substitution effect on superconductivity of the α-phase iron selenide*. *Eur. Phys. Lett.* **84** (2008): 37002. 110

[Yin *et al.* (1977)] L. I. Yin, T. Tsang, and I. Adler. *Electron delocalization and the characterization of the L_3MM Auger spectra of $3d$ transition metals*. *Phys. Rev. B* **15** (1977)(6): 2974. 122

[Yin *et al.* (2011)] Z. P. Yin, K. Haule, and G. Kotliar. *Kinetic frustration and the nature of the magnetic and paramagnetic states in iron pnictides and iron chalcogenides*. *Nature Materials* **10** (2011): 932. 110

[Yoshida *et al.* (2009)] R. Yoshida, T. Wakita, H. Okazaki, Y. Mizuguchi, S. Tsuda, Y. Takano, H. Takeya, K. Hirata, T. Muro, M. Okawa, K. Ishizaka, S. Shin, H. Harima, M. Hirai, Y. Muraoka, and T. Yokoya. *Electronic Structure of Superconducting FeSe Studied by High-Resolution Photoemission Spectroscopy*. *J. Phys. Soc. Jpn.* **78** (2009): 034708. 115

[Yoshida *et al.* (2010)] T. Yoshida, M. Hashimoto, T. Takizawa, A. Fujimori, M. Kubota, K. Ono, and H. Eisaki. *Mass renormalization in the bandwidth-controlled Mott-Hubbard systems $SrVO_3$ and $CaVO_3$ studied by angle-resolved photoemission spectroscopy*. *Phys. Rev. B* **82** (2010): 085119. 132, 133

[Yoshida *et al.* (2005)] T. Yoshida, K. Tanaka, H. Yagi, A. Ino, H. Eisaki, A. Fujimori, and Z.-X. Shen. *Direct Observation of the Mass Renormalization in $SrVO3$ by Angle Resolved Photoemission Spectroscopy*. *Phys. Rev. Lett.* **95** (2005)(14): 146404. 133

[Zaanen *et al.* (1985)] J. Zaanen, G. A. Sawatzky, and J. W. Allen. *Band gaps and electronic structure of transition-metal compounds*. *Phys. Rev. Lett.* **55** (1985)(4): 418. 35, 132

[Zhou *et al.* (2006)] J.-S. Zhou, C.-Q. Jin, Y.-W. Long, L.-X. Yang, and J. B. Goodenough. *Anomalous Electronic State in $CaCrO3$ and $SrCrO3$*. *Phys. Rev. Lett.* **96** (2006)(4): 046408. 135